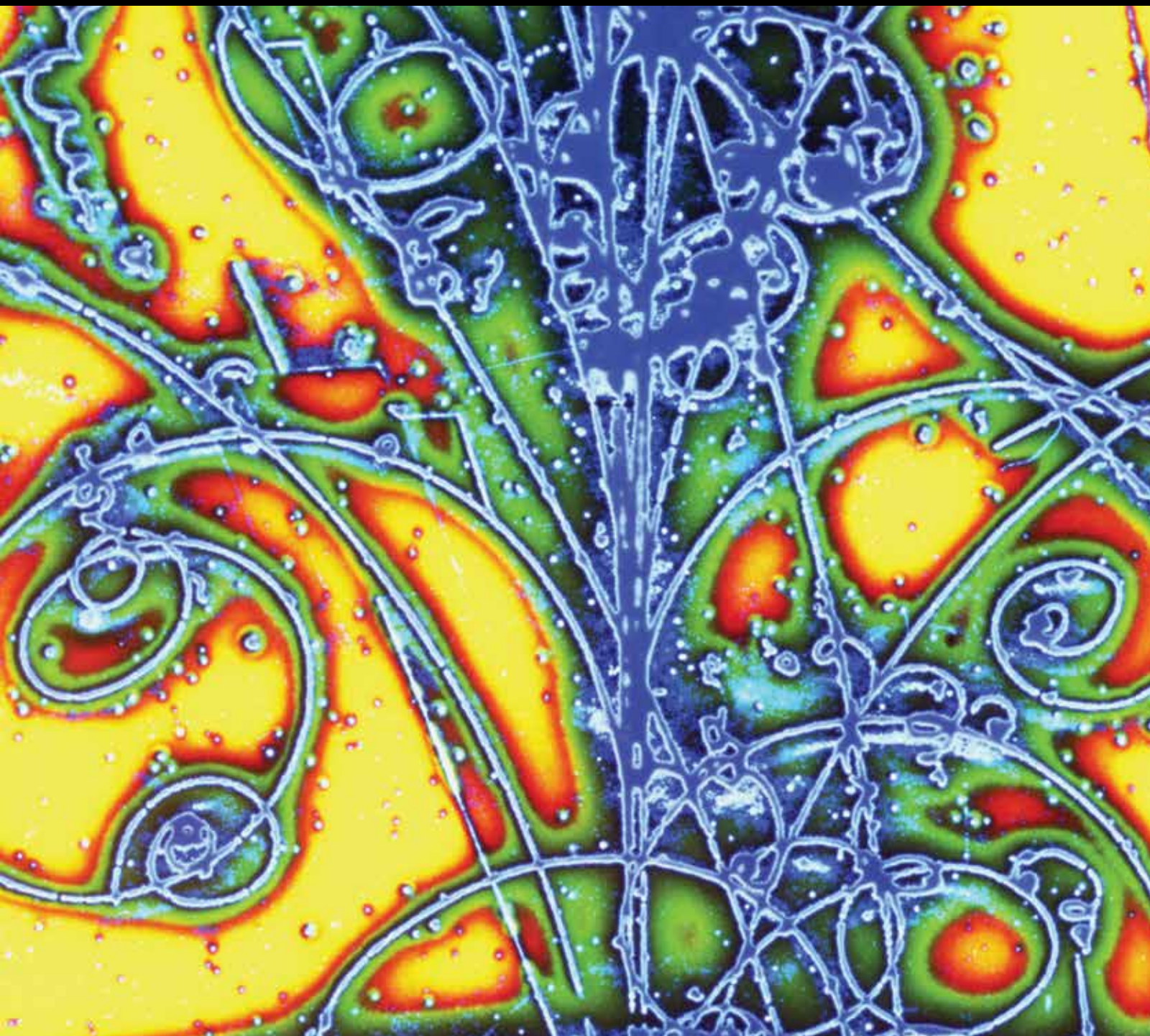


Advances in High Energy Physics

Direct Dark Matter Search

Guest Editors: Anselmo Meregaglia, Davide Franco, Marcello Messina,
Claudio Montanari, and Francesco Pietropaolo





Direct Dark Matter Search

Advances in High Energy Physics

Direct Dark Matter Search

Guest Editors: Anselmo Meregaglia, Davide Franco,
Marcello Messina, Claudio Montanari,
and Francesco Pietropaolo



Copyright © 2015 Hindawi Publishing Corporation. All rights reserved.

This is a special issue published in “Advances in High Energy Physics.” All articles are open access articles distributed under the Creative Commons Attribution License, which permits unrestricted use, distribution, and reproduction in any medium, provided the original work is properly cited.

Editorial Board

Luis A. Anchordoqui, USA
T. Asselmeyer-Maluga, Germany
Marco Battaglia, Switzerland
Botio Betev, Switzerland
Niels Bjerrum-Bohr, Denmark
Rong-Gen Cai, China
Duncan L. Carlsmith, USA
Ashot Chilingarian, Armenia
Sridhara Dasu, USA
Shi-Hai Dong, Mexico
Edmond C. Dukes, USA
Amir H. Fatollahi, Iran
Frank Filthaut, Netherlands

Chao-Qiang Geng, Taiwan
Maria Giller, Poland
Xiaochun He, USA
Filipe R. Joaquim, Portugal
Kyung K. Joo, Republic of Korea
Michal Kreps, UK
Ming Liu, USA
Enrico Lunghi, USA
Piero Nicolini, Germany
Seog H. Oh, USA
Sergio Palomares-Ruiz, Spain
Anastasios Petkou, Greece
Alexey A. Petrov, USA

Thomas Rossler, Sweden
Juan José Sanz-Cillero, Spain
Reinhard Schlickeiser, Germany
Sally Seidel, USA
George Siopsis, USA
Luca Stanco, Italy
Satyendra Thoudam, Netherlands
Smarajit Triambak, South Africa
Elias C. Vagenas, Kuwait
Nikos Varelas, USA
Kadayam S. Viswanathan, Canada
Yau W. Wah, USA

Contents

Direct Dark Matter Search, Anselmo Mereaglia, Davide Franco, Marcello Messina, Claudio Montanari, and Francesco Pietropaolo
Volume 2014, Article ID 967697, 2 pages

The DarkSide Multiton Detector for the Direct Dark Matter Search, C. E. Aalseth, P. Agnes, A. Alton, K. Arisaka, D. M. Asner, H. O. Back, B. Baldin, K. Biery, G. Bonfini, M. Bossa, A. Brigatti, J. Brodsky, F. Budano, L. Cadonati, M. Cadoni, F. Calaprice, N. Canci, A. Candela, H. Cao, M. Cariello, P. Cavalcante, A. Chepurinov, A. G. Cocco, C. Condon, L. Crippa, D. D'Angelo, M. D'Incecco, S. Davini, M. De Deo, A. Derbin, A. Devoto, F. Di Eusanio, E. Edkins, A. Empl, A. Fan, G. Fiorillo, K. Fomenko, G. Forster, M. Foxe, D. Franco, F. Gabriele, C. Galbiati, A. Goretti, L. Grandi, M. Gromov, M. Y. Guan, Y. Guardincerri, B. Hackett, K. Herner, A. Hime, P. Humble, E. Hungerford, Al. Ianni, An. Ianni, D. E. Jaffe, C. Jollet, K. Keeter, C. Kendziora, S. Kidner, V. Kobychyev, G. Koh, D. Korablev, G. Korga, A. Kurlej, P. X. Li, M. Lissia, P. Lombardi, L. Ludhova, S. Luitz, G. Lukyachenko, Y. Q. Ma, I. Machulin, A. Mandarano, S. M. Mari, J. Maricic, L. Marini, D. Markov, J. Martoff, A. Mereaglia, E. Meroni, P. D. Meyers, T. Miletic, R. Milincic, M. Montuschi, M. E. Monzani, P. Mosteiro, B. Mount, V. Muratova, P. Musico, D. Montanari, A. Nelson, S. Odrowski, A. Odrzywolek, J. L. Orrell, M. Orsini, F. Ortica, L. Pagani, M. Pallavicini, E. Pantic, S. Parmeggiano, B. Parsells, K. Pelczar, N. Pelliccia, S. Perasso, L. Perasso, A. Pocar, S. Pordes, D. Pugachev, H. Qian, K. Randle, G. Ranucci, A. Razeto, K. Recine, B. Reinhold, A. Renshaw, A. Romani, N. Rossi, B. Rossi, S. D. Rountree, D. Sablone, P. Saggese, R. Saldanha, W. Sands, S. Sangiorgio, E. Segreto, D. Semenov, E. Shields, M. Skorokhvatov, M. Smallcomb, O. Smirnov, A. Sotnikov, Y. Suvurov, R. Tartaglia, J. Tatarowicz, G. Testera, A. Tonazzo, E. Unzhakov, R. B. Vogelaar, M. Wada, S. E. Walker, H. Wang, Y. Wang, A. W. Watson, S. Westerdale, R. Williams, M. Wojcik, J. Xu, C. G. Yang, J. Yoo, B. Yu, S. Zavatarelli, W. L. Zhong, and G. Zuzel
Volume 2015, Article ID 541362, 8 pages

Astronomical Signatures of Dark Matter, Paul Gorenstein and Wallace Tucker
Volume 2014, Article ID 878203, 10 pages

The Annual Modulation Signature for Dark Matter: DAMA/LIBRA-Phase1 Results and Perspectives, Rita Bernabei, Pierluigi Belli, Fabio Cappella, Vincenzo Caracciolo, Simone Castellano, Riccardo Cerulli, Chang Jang Dai, Annelisa d'Angelo, Silio d'Angelo, Alessandro Di Marco, H. L. He, Antonella Incicchitti, H. H. Kuang, X. H. Ma, Francesco Montecchia, X. D. Sheng, Rui Guang Wang, and Zi-Piao Ye
Volume 2014, Article ID 605659, 10 pages

Searches for Dark Matter with Superheated Liquid Techniques, A. Pullia
Volume 2014, Article ID 387493, 9 pages

The WArP Experiment: A Double-Phase Argon Detector for Dark Matter Searches, Andrea Zani
Volume 2014, Article ID 205107, 17 pages

New Directions in Direct Dark Matter Searches, Paolo Panci
Volume 2014, Article ID 681312, 19 pages

Halo-Independent Comparison of Direct Dark Matter Detection Data, Eugenio Del Nobile
Volume 2014, Article ID 604914, 13 pages

Editorial

Direct Dark Matter Search

**Anselmo Merregaglia,¹ Davide Franco,² Marcello Messina,³
Claudio Montanari,⁴ and Francesco Pietropaolo⁵**

¹*IPHC, CNRS/IN2P3, 67037 Strasbourg, France*

²*APC, Université Paris Diderot, CNRS/IN2P3, CEA/IRFU, Observatoire de Paris, Sorbonne Paris Cité, 75205 Paris, France*

³*Physics Department, Columbia University, Astrophysics Laboratory, 550 W 120th Street, New York, NY 10027, USA*

⁴*INFN Sezione di Pavia, Via Bassi 6, 27100 Pavia, Italy*

⁵*INFN Sezione di Padova, Via Marzolo 8, 35131 Padova, Italy*

Correspondence should be addressed to Anselmo Merregaglia; anselmo.merregaglia@cern.ch

Received 3 July 2014; Accepted 3 July 2014

Copyright © 2015 Anselmo Merregaglia et al. This is an open access article distributed under the Creative Commons Attribution License, which permits unrestricted use, distribution, and reproduction in any medium, provided the original work is properly cited. The publication of this article was funded by SCOAP³.

About 80 years elapsed from the first postulation by Zwicky of the existence of dark matter, as consequence of the observation of the rotational curves of cluster of elliptical galaxies. Their behavior was indeed compatible with the existence of a larger amount of gravitationally interacting matter with respect to the visible matter. Nevertheless its nature is still nowadays an urgent open question for astrophysicist and cosmologists.

Promising candidates to solve the dark matter problem are the weakly interacting massive particles (WIMPs), which are expected to scatter off ordinary nuclei at very low rates ($\sim 1/\text{ton}/\text{year}$ for 10^{-47} cm^2), yielding very low energy depositions ($< 100 \text{ keV}$). Therefore, even if dark matter constitutes about 25% of the total energy of the universe, its direct detection is extremely challenging. In the near future, the Large Hadron Collider may have the chance to produce WIMPs in the laboratory. Furthermore, WIMPs of the galactic halo could be directly detected, in the near future, by presently running experiments, exploiting different technologies, like scintillating crystals, low temperature detectors, and noble liquids. The current status of art presents tensions among limits and results from different measurements. The next generation of experiments, thanks to the higher sensitivities and the technological improvements, will hopefully unravel the puzzle.

In this framework the authors have treated theoretical aspects, such as the halo-independent formalism and a new

approach to describe the dark matter-nucleus interactions. Astronomical evidences of dark matter were addressed, as well as direct detection techniques including noble gases time projection chambers, scintillating crystals, and superheated liquid techniques.

The paper “*The DarkSide multiton detector for the direct dark matter search*” by C. Aalseth et al. discusses the possible use of a liquid argon time projection chamber (LAr TPC) for the detection of WIMPs in the framework of the DarkSide experiment. The project is described with particular emphasis on the next generation experiment DarkSide-G2 which plans to use a 3.6 ton LAr TPC reaching a sensitivity as low as 10^{-47} cm^2 for WIMPs of $100 \text{ GeV}/c^2$ mass.

The paper “*Astronomical signatures of dark matter*” by P. Gorenstein and W. Tucker is a review of the different astronomical observations which led to the unambiguous indirect evidence of the existence of a much larger component of nonbaryonic matter with respect to ordinary matter in the universe.

In the paper “*The annual modulation signature for dark matter: DAMA/LIBRA-phase1 results and perspectives*” by R. Bernabei et al., the possibility of detecting dark matter using NaI scintillating crystals is described. The results obtained with the total exposure of $1.04 \text{ ton} \times \text{year}$ collected by DAMA/LIBRA-phase1 during 7 annual cycles are summarized and combined with the former DAMA/NaI data (cumulative exposure $1.33 \text{ ton} \times \text{year}$, corresponding to 14

annual cycles). An evidence at 9.3σ C.L. for the presence of dark matter particles in the galactic halo is claimed, on the basis of the exploited model independent dark matter annual modulation.

The paper “*Searches for dark matter with superheated liquid techniques*” by A. Pullia is a review of the direct dark matter detection based on superheated liquid techniques, including continuously sensitive bubble chambers, superheated droplet detectors (SDD), and Geysers.

In the paper “*The WArP experiment: a double-phase argon detector for dark matter searches*” by A. Zani the possibility of using a double-phase argon detector for the direct dark matter search is discussed in the framework of the WArP experiment. Although the experiment never performed a physics run, a technical run was taken in 2011, proving that the technology is effective in performing dark matter searches.

In the paper “*New directions in direct dark matter searches*” by P. Panci the status of direct dark matter detection is discussed in terms of dark matter interactions. A new approach to describe the dark matter-nucleus interactions in terms of a very limited number of relevant degrees of freedom is presented.

The paper “*Halo-independent comparison of direct dark matter detection data*” by E. Del Nobile is a review of the halo-independent formalism which makes it possible to compare data from different direct dark matter detection experiments without making assumptions on the properties of the dark matter halo.

*Anselmo Meregaglia
Davide Franco
Marcello Messina
Claudio Montanari
Francesco Pietropaolo*

Research Article

The DarkSide Multiton Detector for the Direct Dark Matter Search

C. E. Aalseth,¹ P. Agnes,² A. Alton,³ K. Arisaka,⁴ D. M. Asner,¹ H. O. Back,⁵ B. Baldin,⁶ K. Biery,⁶ G. Bonfini,⁷ M. Bossa,⁸ A. Brigatti,⁹ J. Brodsky,⁵ F. Budano,¹⁰ L. Cadonati,¹¹ M. Cadoni,¹² F. Calaprice,⁵ N. Canci,⁴ A. Candela,⁷ H. Cao,⁵ M. Cariello,¹³ P. Cavalcante,⁷ A. Chepurinov,¹⁴ A. G. Cocco,¹⁵ C. Condon,⁵ L. Crippa,⁹ D. D'Angelo,⁹ M. D'Incecco,⁷ S. Davini,¹⁶ M. De Deo,⁷ A. Derbin,¹⁷ A. Devoto,¹² F. Di Eusanio,⁵ E. Edkins,¹⁸ A. Empl,¹⁶ A. Fan,⁴ G. Fiorillo,¹⁵ K. Fomenko,¹⁹ G. Forster,¹¹ M. Foxe,¹ D. Franco,² F. Gabriele,⁷ C. Galbiati,⁵ A. Goretti,⁵ L. Grandi,²⁰ M. Gromov,¹⁴ M. Y. Guan,²¹ Y. Guardincerri,⁶ B. Hackett,¹⁸ K. Herner,⁶ A. Hime,¹ P. Humble,¹ E. Hungerford,¹⁶ Al. Ianni,⁷ An. Ianni,⁵ D. E. Jaffe,²² C. Jollet,²³ K. Keeter,²⁴ C. Kendziora,⁶ S. Kidner,²⁵ V. Kobychiev,²⁶ G. Koh,⁵ D. Korablev,¹⁹ G. Korga,¹⁶ A. Kurlej,¹¹ P. X. Li,²¹ M. Lissia,¹² P. Lombardi,⁹ L. Ludhova,⁹ S. Luitz,²⁷ G. Lukyachenko,¹⁴ Y. Q. Ma,²¹ I. Machulin,²⁸ A. Mandarano,¹⁰ S. M. Mari,¹⁰ J. Maricic,¹⁸ L. Marini,¹⁰ D. Markov,²⁸ J. Martoff,²⁹ A. Mereaglia,²³ E. Meroni,⁹ P. D. Meyers,⁵ T. Miletic,²⁹ R. Milincic,¹⁸ M. Montuschi,⁷ M. E. Monzani,²⁷ P. Mosteiro,⁵ B. Mount,²⁴ V. Muratova,¹⁷ P. Musico,¹³ D. Montanari,⁶ A. Nelson,⁵ S. Odrowski,⁷ A. Odrzywolek,³⁰ J. L. Orrell,¹ M. Orsini,⁷ F. Ortica,³¹ L. Pagani,¹³ M. Pallavicini,¹³ E. Pantic,^{4,32} S. Parmeggiano,⁹ B. Parsells,⁵ K. Pelczar,³⁰ N. Pelliccia,³¹ S. Perasso,² L. Perasso,¹³ A. Pocar,¹¹ S. Pordes,⁶ D. Pugachev,²⁸ H. Qian,⁵ K. Randle,¹¹ G. Ranucci,⁹ A. Razeto,⁷ K. Recine,²⁹ B. Reinhold,¹⁸ A. Renshaw,⁴ A. Romani,³¹ N. Rossi,⁷ B. Rossi,^{5,15} S. D. Rountree,²⁵ D. Sablone,¹⁶ P. Saggese,⁹ R. Saldanha,²⁰ W. Sands,⁵ S. Sangiorgio,³³ E. Segreto,⁷ D. Semenov,¹⁷ E. Shields,⁵ M. Skorokhvatov,²⁸ M. Smallcomb,³ O. Smirnov,¹⁹ A. Sotnikov,¹⁹ Y. Suvurov,⁴ R. Tartaglia,⁷ J. Tatarowicz,²⁹ G. Testera,¹³ A. Tonazzo,² E. Unzhakov,¹⁷ R. B. Vogelaar,²⁵ M. Wada,⁵ S. E. Walker,¹⁵ H. Wang,⁴ Y. Wang,²¹ A. W. Watson,²⁹ S. Westerdale,⁵ R. Williams,¹ M. Wojcik,³⁰ J. Xu,⁵ C. G. Yang,²¹ J. Yoo,⁶ B. Yu,²² S. Zavatarelli,¹³ W. L. Zhong,²¹ and G. Zuzel³⁰

¹ Pacific Northwest National Laboratory, Richland, WA 99352, USA

² APC, Université Paris Diderot, Sorbonne Paris Cité, 75205 Paris, France

³ Physics and Astronomy Department, Augustana College, Sioux Falls, SD 57197, USA

⁴ Physics and Astronomy Department, University of California, Los Angeles, CA 90095, USA

⁵ Physics Department, Princeton University, Princeton, NJ 08544, USA

⁶ Fermi National Accelerator Laboratory, Batavia, IL 60510, USA

⁷ Laboratori Nazionali del Gran Sasso, 67010 Assergi, Italy

⁸ Gran Sasso Science Institute, 67100 L'Aquila, Italy

⁹ Physics Department, Università degli Studi and INFN, 20133 Milano, Italy

¹⁰ Physics Department, Università degli Studi Roma Tre and INFN, 00146 Roma, Italy

¹¹ Physics Department, University of Massachusetts, Amherst, MA 01003, USA

¹² Physics Department, Università degli Studi and INFN, 09042 Cagliari, Italy

¹³ Physics Department, Università degli Studi and INFN, 16146 Genova, Italy

¹⁴ Skobeltsyn Institute of Nuclear Physics, Lomonosov Moscow State University, Moscow 119991, Russia

¹⁵ Physics Department, Università degli Studi Federico II and INFN, 80126 Napoli, Italy

¹⁶ Department of Physics, University of Houston, Houston, TX 77204, USA

¹⁷*Saint Petersburg Nuclear Physics Institute, Gatchina 188350, Russia*

¹⁸*Department of Physics and Astronomy, University of Hawaii, Honolulu, HI 96822, USA*

¹⁹*Joint Institute for Nuclear Research, Dubna 141980, Russia*

²⁰*Kavli Institute, Enrico Fermi Institute, and Department of Physics, University of Chicago, Chicago, IL 60637, USA*

²¹*Institute of High Energy Physics, Beijing 100049, China*

²²*Brookhaven National Laboratory, Upton, NY 11973, USA*

²³*IPHC, Université de Strasbourg, CNRS/IN2P3, 67037 Strasbourg, France*

²⁴*School of Natural Sciences, Black Hills State University, Spearfish, SD 57799, USA*

²⁵*Physics Department, Virginia Tech, Blacksburg, VA 24061, USA*

²⁶*Institute for Nuclear Research, National Academy of Sciences of Ukraine, Kiev 03680, Ukraine*

²⁷*SLAC National Accelerator Laboratory, Menlo Park, CA 94025, USA*

²⁸*National Research Centre Kurchatov Institute, Moscow 123182, Russia*

²⁹*Physics Department, Temple University, Philadelphia, PA 19122, USA*

³⁰*Smoluchowski Institute of Physics, Jagiellonian University, 30059 Krakow, Poland*

³¹*Department of Chemistry, Biology and Biotechnology, Università degli Studi and INFN, 06123 Perugia, Italy*

³²*Physics Department, University of California, Davis, CA 95616, USA*

³³*Lawrence Livermore National Laboratory, 7000 East Avenue, Livermore, CA 94550, USA*

Correspondence should be addressed to G. Fiorillo; giuliana.fiorillo@na.infn.it

Received 7 March 2014; Accepted 19 June 2014

Academic Editor: Marcello Messina

Copyright © 2015 C. E. Aalseth et al. This is an open access article distributed under the Creative Commons Attribution License, which permits unrestricted use, distribution, and reproduction in any medium, provided the original work is properly cited. The publication of this article was funded by SCOAP³.

Although the existence of dark matter is supported by many evidences, based on astrophysical measurements, its nature is still completely unknown. One major candidate is represented by weakly interacting massive particles (WIMPs), which could in principle be detected through their collisions with ordinary nuclei in a sensitive target, producing observable low-energy (<100 keV) nuclear recoils. The DarkSide program aims at the WIMPs detection using a liquid argon time projection chamber (LAR-TPC). In this paper we quickly review the DarkSide program focusing in particular on the next generation experiment DarkSide-G2, a 3.6-ton LAR-TPC. The different detector components are described as well as the improvements needed to scale the detector from DarkSide-50 (50 kg LAR-TPC) up to DarkSide-G2. Finally, the preliminary results on background suppression and expected sensitivity are presented.

1. Introduction

A wide range of astronomical evidence implies the existence of dark matter, but as yet the nature of this major component of the universe is completely unknown. A leading candidate explanation is that dark matter is composed of weakly interacting massive particles (WIMPs) formed in the early universe and gravitationally clustered together with the standard baryonic matter. Such WIMPs could in principle be detected through their collisions with ordinary nuclei in a sensitive target, producing observable low-energy (<100 keV) nuclear recoils. The predicted collision rates are very low and require ultra-low background detectors with large (0.1–10 tons) target masses, located in deep underground sites to reduce the background produced by neutrons from cosmic ray muons [1–4].

Many technologies have been developed for the direct detection of dark matter WIMPs. These include cryogenic bolometers with ionization or scintillation detection (CDMS [5], EDELWEISS [6], and CRESST [7]), sodium/cesium iodide scintillation detectors (DAMA/LIBRA [8] and KIMS [9]), bubble chambers (PICASSO [10] and COUPP [11]), a point contact germanium detector (CoGeNT [12]), detectors

using liquid xenon (XENON [13], ZEPLIN [14], LUX [15], and XMASS [16]), and detectors using liquid argon (miniCLEAN [17], DEAP [18], ArDM [19], and the experiment described in this paper, DarkSide). These detectors all share the common goal of achieving the low detection threshold energy required to observe the collisions of WIMPs with target nuclei and the low background to identify these extremely rare events as being from nonstandard sources.

To date, the LUX collaboration has obtained the most sensitive results for WIMPs, placing a limit of $8 \times 10^{-46} \text{ cm}^2$ for a WIMP mass of 33 GeV/ c^2 [15]. Evidence for a low-mass dark matter signal has been claimed by the DAMA/LIBRA and CoGeNT collaborations and may be consistent with recent observations of the CDMS collaboration using Si detectors [20]. However, these are in apparent contradiction with the XENON [13] results and a recent low-energy analysis of CDMS-Ge detectors data [21]. They also are in strong contradiction with the recent results from LUX, which *prima facie* rule out the evidences for low-mass WIMPs presented by COGENT [12] and CDMS-Si [20]. The motivation for direct WIMP searches, however, remains extremely strong, especially for high (>200 GeV/ c^2) masses not yet explored

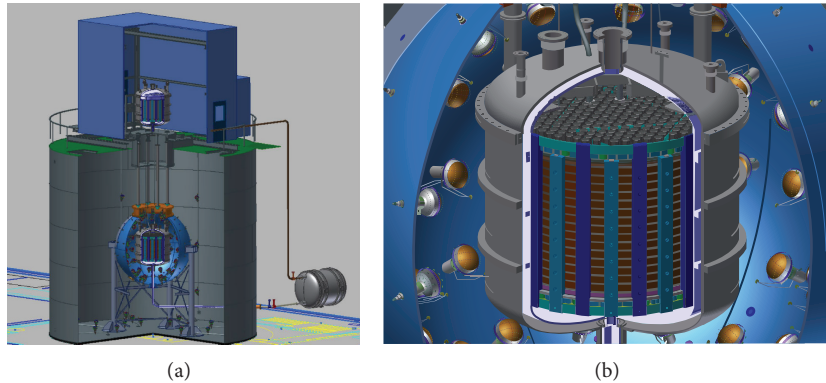


FIGURE 1: 3D model of the muon veto, neutron veto, and DarkSide-G2 LAr TPC (a), with a zoom on the TPC (b).

by the LHC and the region of low cross section ($10^{-45} \text{ cm}^2 - 10^{-47} \text{ cm}^2$) corresponding to H-mediated scattering [22].

Among the variety of detector technologies, noble liquid time projection chambers (TPCs), which detect both the scintillation light and the ionization electrons produced by recoiling nuclei, are particularly promising. Among the noble liquids, argon can effectively discriminate signal from background thanks to the time profile of the primary light signal, which depends on the interacting particle energy loss rate. In addition, liquid argon can be highly purified as demonstrated in [23] (see also references cited therein). The ability to identify, measure, and reject background makes the liquid argon TPC a key technology in dark matter searches.

The DarkSide collaboration plans to develop a multiton liquid argon TPC in the next 2-3 years. In this paper, we describe the promising results obtained with a 10 kg prototype, the current commissioning of an experiment with a 50 kg TPC, and the ongoing R&D for DarkSide-G2, the final multiton detector.

2. The DarkSide Experiment

The DarkSide project is designed for direct detection of dark matter particles, at Laboratori Nazionali del Gran Sasso (LNGS), using a two-phase TPC with liquid argon (LAr) targets. The main feature of the LAr technology is the capability to efficiently separate nuclear recoil events, as expected from WIMP interactions, from electron recoil events. In addition, the high photon yield (~ 40000 photons/MeV for \sim MeV electrons at null electric field) and the optical transparency to its own light make liquid argon an ideal medium for detecting dark matter particle interactions.

As for all the direct dark matter experiments, the success of the project mostly depends on the background control, by using ultrapure materials and purification systems, identification, and suppression. The DarkSide collaboration has dedicated a notable effort in order to meet the background requirements on internal contaminations and external background from cosmic rays, detector materials, and the surrounding rocks. A particular effort has been dedicated to ^{39}Ar , a β -decay with long half-life ($\tau_{1/2} = 269$ years and Q -value = 565 keV), intrinsic to liquid argon.

^{39}Ar is mainly formed in the atmosphere by cosmic neutron interactions on ^{40}Ar . ^{39}Ar is, indeed, present with relatively high concentrations ($\sim 10^{-15}$ with respect to ^{40}Ar) in commercial liquid argon, a distillation product of liquid air. The DarkSide collaboration identified underground argon (UAr), where the exposure to cosmic rays is naturally minimized, as solution to ^{39}Ar problem. The Princeton group successfully demonstrated that ^{39}Ar is suppressed by more than 2 orders of magnitude in UAr with respect to commercial argon of atmospheric origin (AAr) [25].

A three-stage program was designed to test both the background reduction and the liquid argon technology. In particular, the staged approach allows deeply investigating the key aspect of the experiment, its background identification capabilities. The first prototype, DarkSide-10, a 10 kg TPC installed at LNGS inside a passive shield, provided fundamental measurements, demonstrating the high light yield achievable in a liquid argon TPC (~ 9 photoelectrons/keV $_{ee}$ measured at null field averaging over calibration gammas from ^{57}Co , ^{22}Na , and ^{137}Cs) [23].

The current phase, DarkSide-50, already installed at LNGS, consists in 33 kg of liquid argon fiducial mass. It is shielded by 3500-meter water equivalent of rock and by the double veto, a spherical borated scintillator detector, housing the TPC, designed to veto neutrons and gamma rays, and a more external water Cherenkov one to detect the residual cosmic ray flux. DarkSide-50 not only will demonstrate the background suppression efficiency but also will have the potential to provide a significant physics reach of 10^{-45} cm^2 in the WIMP cross section at $100 \text{ GeV}/c^2$ mass in $0.1 \text{ ton} \times \text{year}$ exposure. The data taking of DarkSide-50 recently started and will use for the first time the UAr. This intermediate phase has already allowed the collaboration to tackle technical issues, paving the way for the following phase of the project, the so-called DarkSide-G2, a 3.6 ton TPC, with a physics goal of 10^{-47} cm^2 at $100 \text{ GeV}/c^2$ in $18 \text{ ton} \times \text{year}$ exposure. The double veto, commissioned for DarkSide-50, will also house DarkSide-G2, adding another brick towards the DarkSide final measurement. A schematic drawing of the muon veto, neutron veto, and LAr TPC is shown in Figure 1.

This review is focused on the description of the third phase of DarkSide, highlighting the already achieved progress and the future needed improvements.

3. The TPC

The WIMP signature in a LAr TPC relies on both the excitation and the ionization of the argon. The first results in a direct scintillation signal. The latter is split into two processes: a fraction of the electron-ion pairs undergoes a recombination, which deexcites by emitting photons; the remaining free electrons are drifted towards the liquid surface, by an electric field, and are extracted into the gas phase. In the so-called gas pocket, electrons, further accelerated by a stronger electric field, excite the gas atoms producing a secondary scintillation via electroluminescence. The light components emitted in liquid argon and in gas are called S1 and S2, respectively.

Interacting particles can be statistically identified exploiting two features of the liquid argon response: the ratio between S1 and S2, which depends on the recombination probability, and the S1 photoelectron time distribution, which depends on the probability of populating singlet (~ 10 ns decay time) and triplet ($\sim 1 \mu\text{s}$ decay time) states of the excited argon molecule. Both the features depend on the interacting particle stopping power. We estimate a discrimination power of $\sim 10^2$ for the S1/S2 ratio and $\sim 10^8$ for the pulse shape discrimination [26, 27].

In DarkSide-G2 the dimensions of the cryostat were designed to safely accommodate the LAr-TPC, with diameter and height of 1531 mm and 1503 mm, respectively, for a total active Ar mass of 3.8 ton. Taking into account the volume occupied by the TPC material and support structure and the 10% ullage fraction, the total Ar mass is 5.4 ton.

Both S1 and S2 signals are detected by 556 3" Hamamatsu low-background R11065-G2 PMTs, 278 each on the top and the bottom, which view the active Ar through fused silica windows. The cylindrical surface is a reflector, coated with a wavelength shifter that absorbs the 128 nm scintillation photons emitted by liquid argon. The reemitted visible photons are reflected with high efficiency. The windows at the top and bottom of the cylinder are also coated with the wavelength shifter on the inner surfaces and on both surfaces with a transparent conductive layer (indium-tin-oxide (ITO)). This allows the inner window surfaces to serve as the grounded anode (top) and HV cathode (bottom) of the LAr-TPC while maintaining their outer surfaces at the average PMT photocathode potential.

The fused silica anode window has a cylindrical rim extending downward to form the diving bell holding the 1 cm thick gas layer of the LAr-TPC. The electron drift system consists of the ITO cathode and anode planes, a field cage, and a grid that separates the drift and electron extraction regions. A high voltage is applied between the cathode and grid to produce a vertical electric field to drift the ionization electrons upward. Outside the cylindrical wall, copper rings at graded potentials make the drift field uniform throughout the active volume. An independently adjustable potential between the grid and anode creates the fields to extract

the electrons into the gas and accelerate them to create the secondary scintillation signal.

In order to build the G2 detector, however, there are still a few important points to assess. The amount of material must be as small as possible and it must have the lowest feasible radioactivity. The stainless steel for the cryostat vessel has already been identified with an acceptable radioactivity below 1 mBq/kg for ^{238}U and ^{232}Th . The main concerns come from the PMTs, since at present they have a neutron yield 6 times larger than the desired limit. The solution is within reach (see Section 6.1); however, further tests are still required.

The second important item to be tackled for the G2 scale-up is the production of UAr. As mentioned in the previous section, Princeton DarkSide group demonstrated in 2007 the extraction of low radioactivity argon from underground sources of gas [25]. The actual extraction rate is 0.5 kg/day, which was largely sufficient for the DarkSide-50 detector, but the goal for the G2 phase is to reach a production rate of about 50 kg/day. This does not represent a major problem (see Section 6.2) but some further developments on the distillation column for final separation between N_2 and UAr are needed.

A last important point related to the TPC is the choice of the electric field strength. Typically LAr TPC applies a field of about 1 kV/cm which is a compromise between a high drift velocity (about 2 mm/ μs) and technical difficulties related to the feedthroughs for very high voltages. However, the recent measurements of SCENE [28] have a crucial impact on the choice of the electric field for DarkSide-G2, since they observed a significant dependence on the drift field of liquid argon scintillation from nuclear recoils of energies in the range of interest for dark matter searches. The SCENE measurement suggests that a lower drift field is important to retain the best nuclear recoil S1 light yield in a TPC. We are already operating DarkSide-50 at a much lower drift field than our prototype studies, and it is likely that the optimum drift field for DarkSide-G2 will be in the range 100–200 V/cm. This choice will have important implications on the DarkSide program. On the one hand, the scale-up of the detector will be easier, relaxing the constraint coming from the HV. On the other hand, the drift velocity will be reduced to less than 1 mm/ μs with a drift time of the order of 1–2 ms. This means that the requirements on the target purity from electronegative components become more challenging. We expect the requirement for the electron drift lifetime in DarkSide-G2 to be about 5 ms.

4. The Neutron Veto

The DarkSide-G2 liquid scintillator neutron veto (LSV), today hosting the DarkSide-50 TPC, is a 4 m stainless steel sphere filled with liquid scintillator (see Figure 2 for an internal view).

The LSV is a highly efficient active veto for neutrons and gammas, and it complements the muon veto (see Section 5) as cosmogenic veto [29]. It is equipped with 110 low-background-glass-bulb 8-inch PMTs, mounted directly on the internal surface of the supporting sphere, for a 7%



FIGURE 2: Internal view of the LSV neutron veto from its top port.

photocathode coverage. To maximize the light collection, a high-efficiency Lumirror reflector [30] is used to cover internally the LSV.

The scintillator is a 1 : 1 mixture of trimethyl borate (TMB) and a solution of PPO in pseudocumene (PC). Neutron capture on boron, producing α 's of energy 1.47 MeV or larger, is the dominant process in the liquid, due to the large thermal neutron capture cross section on ^{10}B and its natural abundance of 20%. The fact that α 's are very short range particles is a critical point in order to have an efficient neutron detection without requiring very large veto volumes. This would not be the case for vetoes based on other dopants such as Gd that rely on detection of the γ -rays emitted in the neutron capture process.

The energy deposition in the scintillator due to a neutron capture on ^{10}B is at least 60 keV_{ee} [31], which results in a high detection efficiency. This, together with the short neutron capture time, makes it possible to operate the veto with high event rate, allowing for a direct immersion of the PMTs in the scintillator without any additional inert buffer layer.

Starting from a scintillator light yield of 12 photons/keV_{ee} and typical quantum efficiency (QE) of about 35% for the PMTs, a light yield of 0.5 PE/keV_{ee} was obtained: the resulting signal of 30 PE for a neutron capture is more than adequate to ensure very efficient neutron detection. Last but not least, faster neutrons can also be tagged, exploiting the elastic scattering of neutrons on protons [32].

5. The Muon Veto

The muon and neutron vetoes were conceived in the DarkSide-50 project in order to host the G2 upgrade without any major modification. This represents an important asset for DarkSide-G2 not only in terms of cost but also in terms of detector and BG understanding.

The muon veto is the former counting test facility (CTF) [33, 34] of the Borexino experiment [35]. It is a Cherenkov detector 10 m high with a diameter of 11 m, instrumented with 80 8-inch PMTs. It is used to identify energetic muons (and charged daughter particles) with an efficiency larger than 99% as well as acting as passive shielding for neutrons. To enhance the light collection, a reflector made of a Tyvek-Polyethylene-Tyvek sandwich, originally developed for the Daya-Bay reactor neutrino experiment, covers the inner



FIGURE 3: Internal view of the CTF muon veto.

surface of the tank and the external surface of the neutron veto.

An internal view of the CTF muon veto can be seen in Figure 3.

6. Required Improvements for the Multiton Phase

The DarkSide-50 experiment paved the way for the G2 upgrade: no modifications are needed for the muon and neutron vetoes and the TPC is almost just a scale-up by a factor of 100.

Two points need further development, as mentioned in the previous section, namely, the photosensors and the UAr extraction.

6.1. Photosensors. The baseline for the LAr-TPC PMTs of DarkSide-G2 is the 3-inch ultra-low background Hamamatsu R11065-G2, which uses the Bialkali-LT photocathode developed by Hamamatsu Photonics under contract from INFN Napoli and Princeton University. This photocathode operates down to LAr temperature with high quantum efficiency, overcoming the limitations of standard Bialkali photocathodes which exhibit poor performance at cryogenic temperatures. Thanks to the continuing R&D on photocathodes by Hamamatsu, in the latest models of the family, the average peak QE has risen to 37% at 400 nm. The R11065 family of PMTs has been very successful in enabling the achievement of high photoelectron yields (9 PE/keV_{ee} in DarkSide-10 [23]). Nonetheless, a major concern for the G2 upgrade comes from the radiopurity: the very best of the family, the R11065-20, has a neutron yield of 0.6 n/(unit \times yr), whereas our goal for the R11065-G2 is 0.1 n/(unit \times yr).

This goal is within reach thanks to the identification of the leading source of radioactivity in the R11065-20 PMTs, the ceramic feedthrough plate: we measured by GDMS a localized contamination of 3 mBq/unit ^{238}U and 1 mBq/unit ^{232}Th , clustered in the ceramic feedthrough plate.

We are pursuing two routes to resolve this problem: Hamamatsu has proposed and tested a sapphire stem in the R11065-30 obtaining a reduction in background of a factor of 5, close to the requirement of DarkSide-G2. In addition, the DarkSide collaboration has identified 99.999% ultrahigh purity alumina, whose radiopurity will allow us to reach

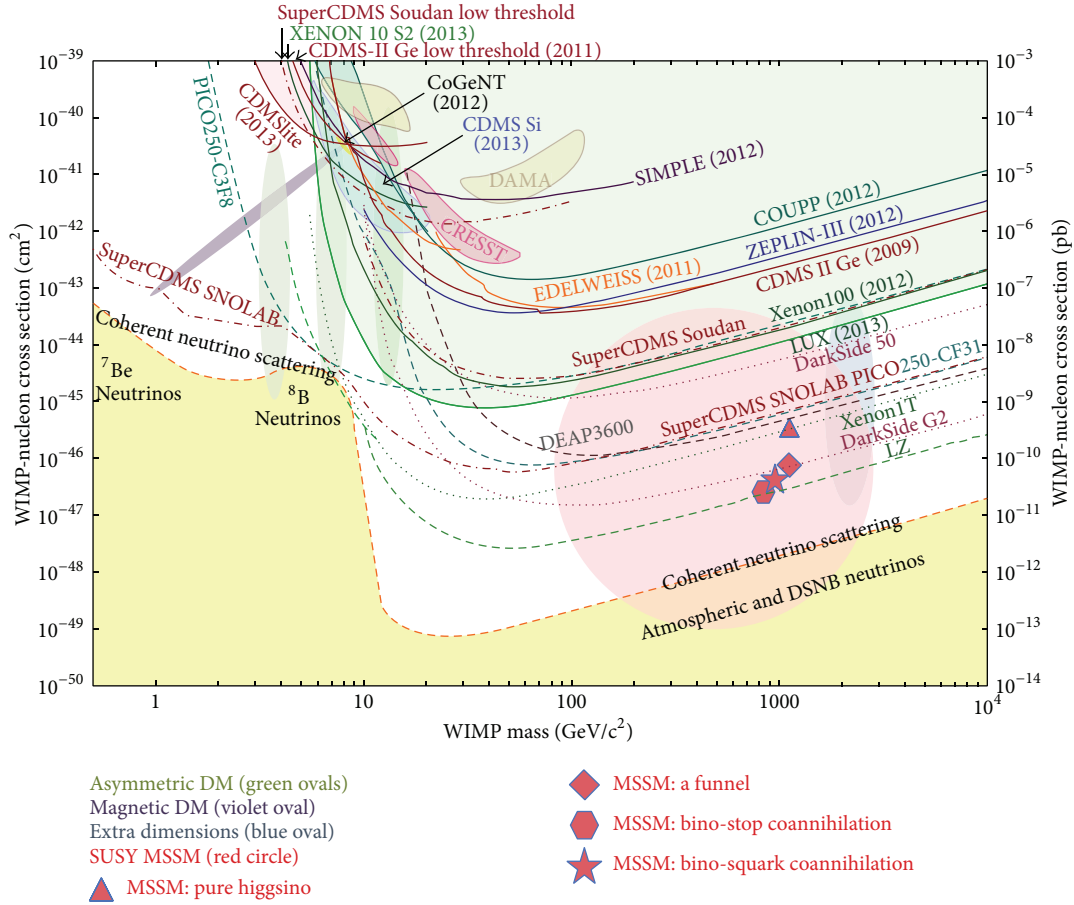


FIGURE 4: Current status of direct dark matter searches results and sensitivity of future experiments (from [24]). Shaded bounded areas represent claims for dark matter observations or regions of interest compatible with observation of a few events that could be attributed to dark matter interactions. Continuous lines show the exclusion curves by past experiments. Dashed lines show the projected sensitivity of future experiments based on various assumptions. The red dashed line shows the sensitivity of DarkSide-G2 for zero detected events in 18 tons-years.

the goal of $0.1 \text{ n}/(\text{unit} \times \text{yr})$ and is completing R&D towards its use in ultraradioclean feedthroughs.

6.2. Underground Argon Distillation. To extract low radioactivity underground argon, a large vacuum-pressure swing adsorption (VPSA) plant was installed in 2009 at Kinder Morgan Doe Canyon CO₂ facility in southwestern Colorado [36]. This accepts feed CO₂ gas with 600 ppm of Ar and produces an output stream of 4% Ar in a He and N₂ mixture. To date the VPSA plant has extracted more than 100 kg of UAr and it continues to extract it at a rate of about 0.5 kg/day.

The UAr collected in Colorado is shipped to Fermilab for further purification, using a complex purification system composed of many units, whose most important unit is a cryogenic distillation column [37]. The final obtained UAr has a contamination of ³⁹Ar lower than 0.65% compared to that in AAr [25]. At this level the DarkSide-G2 experiment will be able to operate with a very limited (<5%) fraction of events in pile-up.

The goal for DarkSide-G2 is to reach a production of 50 kg/day: to meet the goal the DarkSide Collaboration is

teaming with Kinder Morgan and Air Products. Air Products will make provisions to produce for the DarkSide-G2 collaboration a stream of N₂/UAr, originating from the tail gas of their He extraction plant, which can be treated with a cryogenic distillation column to produce detector quality UAr at the desired rate. Final separation of N₂ from UAr will be performed directly at the Kinder Morgan Doe Canyon facility in Cortez by a new cryogenic distillation column based on the successful design of the unit currently operating at FNAL (the present distillation column at Fermilab has demonstrated the ability to separate a 40–60 Ar-N mix at a rate of 20 kg/day).

7. Sensitivity

In order to observe a signal rate of the order of 1 event per ton per year (assuming a cross section of 10^{-47} cm^2), an exceptional background reduction is needed.

The sources of background are β/γ giving an electron recoil misidentified as a nuclear recoil and cosmogenic or radiogenic neutrons that produce a nuclear recoil which can

not be distinguished from a WIMP one. The strategy for an efficient background reduction relies therefore on extreme radiopurity of materials, an efficient nuclear and electron recoil discrimination, and the active external volumes to veto and suppress the neutrons reaching the TPC.

The background due to the cosmogenic neutrons can be completely eliminated using the neutron and muon vetoes. Details of the simulation studies can be found in [38], where a lifetime of 36 years was simulated and no events were found reaching the TPC active volume without triggering at least one of the two veto detectors.

The main source of radiogenic neutrons (mainly from (α, n) reactions) is the radioactivity in the PMTs and in the cryostat. Cross sections for (α, n) reactions result in one in every 10^5 – 10^7 α -decays producing a low-energy neutron [39].

Radioactive daughters of ^{222}Rn plate out on surfaces and are the major contributors to surface α activity. The α -decays on the inner surface of the detector are particularly dangerous for another reason: about half the time, the α goes deeper into the surface, and the daughter nucleus recoils into the active volume, mimicking a WIMP recoil.

Hence, the surface contamination in DarkSide-G2 will be significantly reduced by carrying out precision cleaning and assembly in the two Rn-suppressed clean room appositely conceived, with a Rn contamination of less than 5 mBq/m^3 .

Recoils from the remaining surface activity can be further suppressed by position reconstruction and a fiducial volume cut.

After the fiducial volume cut, the energy selection window of 55–240 keV_e, and the rejection of events with multiple energy depositions, we obtain less than 0.1 events from radiogenic neutrons for an exposure of 18 tons \times year.

Concerning the β/γ background, the main source is the ^{39}Ar in the sensitive volume, from which we expect 4.2×10^8 events in the dark matter energy window at the upper limit of ^{39}Ar activity for an 18-ton-year exposure. In order to achieve less than 0.1 background event in the WIMP search, the requisite reduction factor is 2×10^{-10} between 55 and 240 keV_e. Pulse shape discrimination (PSD) is the major attack on this background. Preliminary data from DarkSide-50, with the same threshold, indicate that the experiment will remain background-free for the full exposure of DarkSide-G2 and with ^{39}Ar in UAr at the measured upper limit concentration [40]. Further data from DarkSide-50 are forthcoming and promise to directly test the PSD capability in LAr at the statistical level needed for DarkSide-G2.

A summary of the expected BG rate can be found in Table 1.

Based on our calculated backgrounds, the projected (90% C.L.) sensitivity is $2 \times 10^{-47} \text{ cm}^2$ for 100 GeV WIMPs, as shown in Figure 4. We note that the analysis on which we base this estimate of the sensitivity uses conservative assumptions on background rejection (DarkSide-50 data with minimal cuts and noise levels achieved at the beginning of the run, no use of S2/S1 or of x - y fiducialization yet). Possible improvements in background rejection may result in lower threshold and improved sensitivity.

TABLE 1: A summary of the expected nuclear and electron recoil backgrounds depositing 55–240 keV_e in an 18-ton-year exposure of DarkSide-G2. We assume ^{39}Ar at our recently measured limit [25]. For PMTs, we use the expected background in the R11065-G2s based on measurements reported by Hamamatsu and our ongoing R&D. For the cryostat, we use detailed measurements of the steel used for the DarkSide-50 cryostat. After cuts include fiducial, energy, and multihit cuts.

Detector element	Electron recoil BG after PSD and cuts	Radiogenic neutron BG after cuts
^{39}Ar (<6.5 mBq/kg)	<0.1	—
R11065-G2 PMTs	<0.01	0.05
Cryostat and insulation	<0.01	0.05
Total	<0.1	0.1

8. Conclusions

WIMPs are a leading candidate to explain the nature of dark matter. They could be observed detecting low-energy nuclear recoils, and among the existing techniques, noble liquid TPCs are today the most promising technology.

The DarkSide program aims at the WIMPs detection using a two-phase argon TPC. The first demonstration phase of DarkSide-10 is now over and DarkSide-50 is running preliminary calibrations. The measurements taken with the two active vetoes, the borated scintillator and the water Cherenkov detectors, will allow better constraints on the background rejection efficiency of DarkSide-G2.

Conflict of Interests

The authors declare that there is no conflict of interests regarding the publication of this paper.

References

- [1] Committee on the Physics of the Universe, Board on Physics and Astronomy, and Division on Engineering and Physical Sciences of the National Research Council of the National Academies, *Connecting Quarks with the Cosmos: Eleven Science Questions for the New Century*, National Academies Press, 2003.
- [2] National Science and Technology Council, *Committee on Science, A 21st Century Frontier of Discovery*, The Physics of the Universe, 2004.
- [3] The Dark Matter Scientific Assessment Group, Report on the Direct Detection and Study of Dark Matter, 2007.
- [4] The Particle Astrophysics Scientific Assessment Group, “Report of the HEPAP Particle Astrophysics Scientific Assessment Group (PASAG),” 2009.
- [5] Z. Ahmed, D. S. Akerib, S. Arrenberg et al., “Search for inelastic dark matter with the CDMS II experiment,” *Physical Review D*, vol. 83, Article ID 112002, 2011.
- [6] E. Armengaud, C. Augier, A. Benoît [EDELWEISS Collaboration] et al., “Search for low-mass WIMPs with EDELWEISS-II heat-and-ionization detectors,” *Physical Review D*, vol. 86, Article ID 051701, 2012.
- [7] G. Angloher, M. Bauer, I. Bavykina et al., “Results from 730 kg days of the CRESST-II Dark Matter search,” *European Physical Journal C*, vol. 72, no. 4, pp. 1–22, 2012.

- [8] R. Bernabei, P. Belli, F. Cappella et al., “New results from DAMA/LIBRA,” *The European Physical Journal C*, vol. 67, no. 1-2, pp. 39–49, 2010.
- [9] S. C. Kim, H. Bhang, J. H. Choi et al., “New limits on interactions between weakly interacting massive particles and nucleons obtained with CsI(Tl) crystal detectors,” *Physical Review Letters*, vol. 108, Article ID 181301, 2012.
- [10] S. Archambault, F. Aubin, M. Auger et al., “Dark matter spin-dependent limits for WIMP interactions on 19F by PICASSO,” *Physics Letters, Section B: Nuclear, Elementary Particle and High-Energy Physics*, vol. 682, no. 2, pp. 185–192, 2009.
- [11] E. Behnke, J. Behnke, S. J. Brice et al., “Improved limits on spin-dependent WIMP-proton interactions from a two liter CF3I bubble chamber,” *Physical Review Letters*, vol. 106, no. 2, Article ID 021303, 2011.
- [12] C. E. Aalseth, P. S. Barbeau, N. S. Bowden [CoGeNT Collaboration] et al., “Results from a search for light-mass dark matter with a p -type point contact germanium detector,” *Physical Review Letters*, vol. 106, Article ID 131301, 2011.
- [13] E. Aprile, M. Alfonsi, K. Arisaka et al., “Dark matter results from 225 live days of XENON100 data,” *Physical Review Letters*, vol. 109, Article ID 181301, 1813.
- [14] G. J. Alner, H. M. Araújo, A. Bewick et al., “First limits on WIMP nuclear recoil signals in ZEPLIN-II: a two-phase xenon detector for dark matter detection,” *Astroparticle Physics*, vol. 28, no. 3, pp. 287–302, 2007.
- [15] D. S. Akerib, X. Bai, H. M. Araujo et al., “First results from the LUX dark matter experiment at the Sanford Underground Research Facility,” *Physical Review Letters*, vol. 112, Article ID 091303, 2014.
- [16] <http://www-sk.icrr.u-tokyo.ac.jp/xmass/>.
- [17] A. Hime, “The MiniCLEAN dark matter experiment,” in *Proceedings of the DPF Conference Proceedings*, 2011.
- [18] M. G. Boulay, “DEAP-3600 dark matter search at SNOLAB,” *Journal of Physics: Conference Series*, vol. 375, Article ID 012027, 2012.
- [19] A. Rubbia, “ArDM: a ton-scale liquid Argon experiment for direct detection of Dark Matter in the Universe,” *Journal of Physics: Conference Series*, vol. 39, no. 39, article 129, 2006.
- [20] R. Agnese, Z. Ahmed, A. J. Anderson et al., “Silicon detector dark matter results from the final exposure of CDMS II,” *Physical Review Letters*, vol. 111, Article ID 251301, 2013.
- [21] R. Agnese, A. J. Anderson, M. Asai et al., “CDMSlite: a search for low-mass WIMPs using voltage-assisted calorimetric ionization detection in the superCDMS experiment,” *Physical Review Letters*, vol. 112, Article ID 041302, 2014.
- [22] K. Zurek, “Theoretical results on Dark Matter,” in *Proceedings of the 26th International Symposium on Lepton Photon Interactions at High Energies*, San Francisco, Calif, USA, June 2013.
- [23] T. Alexander, D. Alton, K. Arisaka et al., “Light yield in DarkSide-10: a prototype two-phase argon TPC for dark matter searches,” *Astroparticle Physics*, vol. 49, pp. 44–51, 2013.
- [24] P. Cushman, C. Galbiati, D. N. McKinsey et al., “Snowmass CFI summary: WIMP dark matter direct detection,” <http://arxiv.org/abs/1310.8327>.
- [25] J. Xu, F. Calaprice, C. Galbiati et al., “A study of the residual ^{39}Ar content in argon from underground sources,” <http://arxiv.org/abs/1204.6011>.
- [26] P. Benetti, R. Acciarri, F. Adamo et al., “First results from a dark matter search with liquid argon at 87 K in the Gran Sasso underground laboratory,” *Astroparticle Physics*, vol. 28, no. 6, pp. 495–507, 2008.
- [27] M. G. Boulay and A. Hime, “Technique for direct detection of weakly interacting massive particles using scintillation time discrimination in liquid argon,” *Astroparticle Physics*, vol. 25, pp. 179–182, 2006.
- [28] T. Alexander, H. O. Back, H. Cao et al., “Observation of the dependence on drift field of scintillation from nuclear recoils in liquid argon,” *Physical Review D*, vol. 88, Article ID 092006, 2013.
- [29] A. Wright, P. Mosteiro, B. Loer, and F. Calaprice, “A highly efficient neutron veto for dark matter experiments,” *Nuclear Instruments and Methods in Physics Research A: Accelerators, Spectrometers, Detectors and Associated Equipment*, vol. 644, no. 1, pp. 18–26, 2011.
- [30] http://www.toray.us/products/electronics/ele_003.html.
- [31] R. Greenwood and N. R. Chellev, “Improved ^{10}B -loaded liquid scintillator with pulse-shape discrimination,” *Review of Scientific Instruments*, vol. 50, p. 466, 1979.
- [32] M. Flaska and S. A. Pozzi, “Digital pulse shape analysis for the capture-gated liquid scintillator BC-523A,” *Nuclear Instruments and Methods in Physics Research A: Accelerators, Spectrometers, Detectors and Associated Equipment*, vol. 599, no. 2-3, pp. 221–225, 2009.
- [33] G. Alimonti, G. Anghloherd, C. Arpesella et al., “Ultra-low background measurements in a large volume underground detector,” *Astroparticle Physics*, vol. 8, no. 3, pp. 141–157, 1998.
- [34] G. Alimonti, C. Arpesella, G. Bacchiocchi et al., “A large-scale low-background liquid scintillation detector: the counting test facility at Gran Sasso,” *Nuclear Instruments and Methods in Physics Research A: Accelerators, Spectrometers, Detectors and Associated Equipment*, vol. 406, no. 3, pp. 411–426, 1998.
- [35] G. Alimonti, C. Arpesella, H. Back et al., “The Borexino detector at the Laboratori Nazionali del Gran Sasso,” *Nuclear Instruments and Methods in Physics Research A*, vol. 600, no. 3, pp. 568–593, 2009.
- [36] H. O. Back, F. Calaprice, C. Condon et al., “First large scale production of low radioactivity argon from underground sources,” <http://arxiv.org/abs/1204.6024>.
- [37] H. O. Back, T. Alexander, A. Alton et al., “First commissioning of a cryogenic distillation column for low radioactivity underground argon,” <http://arxiv.org/abs/1204.6061>.
- [38] A. Empl, R. Jasim, E. Hungerford, and P. Mosteiro, “Study of cosmogenic neutron backgrounds at LNGS,” Submitted, <http://arxiv.org/abs/1210.2708>.
- [39] R. Heaton, H. Lee, P. Skensved, and B. C. Robertson, “Neutron production from thick-target (α, n) reactions,” *Nuclear Instruments and Methods in Physics Research A*, vol. 276, no. 3, pp. 529–538, 1989.
- [40] R. Agnese, T. Alexander, A. Alto et al., “First results from the darkside-50 dark matter experiment at Laboratori Nazionali del Gran Sasso,” <http://arxiv.org/abs/1410.0653>.

Review Article

Astronomical Signatures of Dark Matter

Paul Gorenstein and Wallace Tucker

Harvard-Smithsonian Center for Astrophysics, 60 Gardens Street, MS-4, Cambridge, MA 02138, USA

Correspondence should be addressed to Paul Gorenstein; pgorenstein@cfa.harvard.edu

Received 11 February 2014; Accepted 13 May 2014; Published 26 June 2014

Academic Editor: Anselmo Meregaglia

Copyright © 2014 P. Gorenstein and W. Tucker. This is an open access article distributed under the Creative Commons Attribution License, which permits unrestricted use, distribution, and reproduction in any medium, provided the original work is properly cited. The publication of this article was funded by SCOAP³.

Several independent astronomical observations in different wavelength bands reveal the existence of much larger quantities of matter than what we would deduce from assuming a solar mass to light ratio. They are very high velocities of individual galaxies within clusters of galaxies, higher than expected rotation rates of stars in the outer regions of galaxies, 21 cm line studies indicative of increasing mass to light ratios with radius in the halos of spiral galaxies, hot gaseous X-ray emitting halos around many elliptical galaxies, and clusters of galaxies requiring a much larger component of unseen mass for the hot gas to be bound. The level of gravitational attraction needed for the spatial distribution of galaxies to evolve from the small perturbations implied by the very slightly anisotropic cosmic microwave background radiation to its current web-like configuration requires much more mass than is observed across the entire electromagnetic spectrum. Distorted shapes of galaxies and other features created by gravitational lensing in the images of many astronomical objects require an amount of dark matter consistent with other estimates. The unambiguous detection of dark matter and more recently evidence for dark energy has positioned astronomy at the frontier of fundamental physics as it was in the 17th century.

1. Introduction

Astronomy and physics have had a mutually beneficial partnership. The late 16th century astronomical observations of planetary positions as a function of time by the Danish astronomer Tycho Brahe were analyzed and interpreted by Johannes Kepler. Three laws relating planetary motion and distance from the Sun were abstracted from Kepler's analysis. Galileo's telescopic observations of the Sun and planets in the early 17th century established the connection between Kepler's analysis and the validity of the Copernican view of the solar system. With that knowledge in late 17th century Isaac Newton founded modern theoretical physics by explaining Kepler's findings in the context of Galileo's physical picture with his three laws of classical mechanics and the law of universal gravitational attraction.

Aside from the synergy between solar/stellar and laboratory atomic spectroscopy, from that time until the turn of the 20th century, astronomy and fundamental physics did not forge any more connections with such significance. Classifying and cataloging stars, noting their positions, color,

and spectra, observing the occurrence of eclipses and the comings and goings of comets, all in accordance with Newton's laws, were the preoccupations of astronomers. In fact, Simon Newcomb the most distinguished American astronomer of his era, founding member and first president of the American Astronomical Society said in 1888, "*We are probably nearing the limit of all we can know about astronomy.*" This proved to be as accurate as the belief of many physicists—buoyed by the great success of Maxwell's equations at the turn of the 20th century, prior to the discovery of X-rays and radioactivity, that the only things left to do in fundamental physics was design better measuring devices and build faster computational aids to facilitate applications of Newton's laws and Maxwell's equations [1, 2].

Beginning with the 20th century, profound changes in both astronomy and laboratory physics, plus the development of Einstein's special and general theories of relativity, would bring the two disciplines together again at the frontiers of fundamental physics. Astronomy underwent a great expansion in scope thanks to the construction of new tools such as very large optical telescopes, solid state image sensors, large radio

telescopes, and with access to space above the absorption of the atmosphere, far infrared, ultraviolet, X-ray and gamma-ray telescopes. This capability led to the discovery of neutron stars and black holes, objects whose existence could be explained by theoretical physicists following their discovery. Astronomers have also discovered evidence for dark matter, which seems to be primarily nonbaryonic and an even more enigmatic entity known as dark energy. At the current time the total mass-energy content of the known universes described by the so-called Lambda-Cold Dark Matter model is believed to be 5% ordinary matter, 23% dark nonbaryonic matter, and 72% “dark energy.”

Dark matter has been discussed by many authors. Trimble reviews our understanding of dark matter from an elegant historical perspective describing events up to 1987. She includes early indications of the existence of dark matter whose significance was not widely recognized at the time [3]. The cosmological connection is described by, for example, Bergstrom [4].

2. Evidence for the Existence of Dark Matter

A variety of independent lines of evidence indicate that galaxies and clusters of galaxies contain much more gravitating matter than the total amount that has been detected across the entire electromagnetic spectrum. The excess is called dark matter (DM). The evidence includes galactic rotation curves, large oxygen-rich halos of star-forming galaxies, the velocity dispersions of stars in elliptical galaxies and of galaxies in clusters of galaxies, gravitational lensing, the confinement of hot gas in galaxy clusters, the pattern of acoustic oscillations in the power spectrum of the cosmic microwave background (CMB), and the imprint of these oscillations on the relative strength, and shape of the galaxy-distribution power spectrum at large wave numbers. The collective evidence suggests that dark matter comprises some twenty-three percent of the energy density of the universe today, ($\Omega_{\text{dm}} = 0.23$) with a precision of a few percent.

2.1. Baryonic Dark Matter. Some baryons are tied up in dark forms, such as extremely low mass stars or black holes. The Hubble Space Telescope detected large (150 kiloparsec) halos of ionized oxygen surrounding star-forming galaxies. They contain a substantial amount of heavy elements and gas, perhaps exceeding the reservoirs of gas within the galaxies [5]. However, only a small fraction of DM can be baryonic. The ratio of the acoustic peaks in the CMB radiation spectrum, as well as calculations of the nuclear synthesis processes that took place following the Big Bang (prior to any star formation), when compared to the observed ratios of D/H, He/H and Li/H, indicate that the normalized mass-energy density of baryonic matter is $\Omega_b = 0.0456 \pm 0.0016$ [6]. At high redshifts ($z > 2$), most of the baryonic matter in the universe resides outside of galaxies in diffuse filamentary photoionized intergalactic clouds. Their presence has been revealed through the detection of hydrogen absorption lines in the spectra of distant quasars. Each individual cloud, which

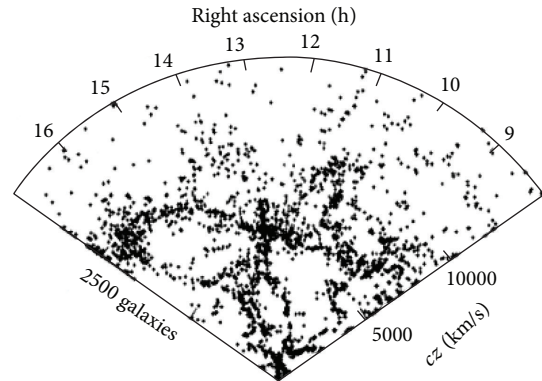


FIGURE 1: The web-like spatial distribution of galaxies reported by Geller and Huchra [8].

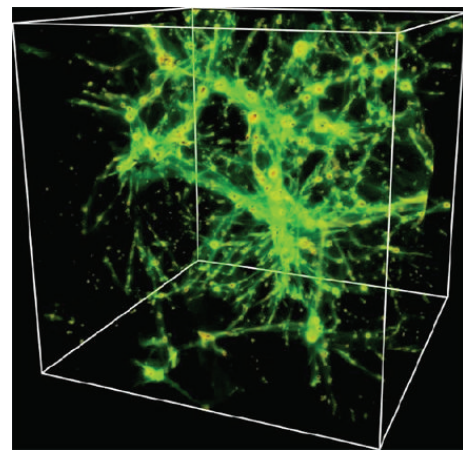


FIGURE 2: The spatial distribution of hot baryons in the model of Cen and Ostriker [9] and Davé et al. [10].

in general has a different redshift, leaves its Lyman-alpha fingerprint as an absorption feature at a different wavelength in the observed optical spectrum of a distant quasar. Collectively the Lyman-alpha clouds impose a complex of absorption lines known as the “Lyman-alpha forest” on the visible light spectrum of the distant quasar [7]. With time, gravity causes a fraction of gas in the intergalactic clouds to condense and form galaxies.

On a large scale, the spatial distribution of relatively nearby galaxies (Figure 1) [8] exhibits a web-like structure with regions of high and low density concentrations of galaxies. Hydrodynamic simulations of the evolution of structure of the intergalactic medium under the influence of gravity can reproduce the Lyman-alpha forest and the observed web-like structure of galaxies (see Figure 2). The models show that, by the present day, approximately half of all baryons should have become incorporated into galaxies, and a hot intracluster medium in galaxy clusters. The remaining $\sim 50\%$ is predicted to be in a warm-hot intergalactic medium (WHIM) [10] that was shock-heated by gravitational collapse to temperatures in the range $0.1 \text{ MK} < T < 10 \text{ MK}$.

The simulations show that the temperature of the baryonic portion of the clouds increases with time. This implies

that clouds closer to the observer and further from a distant background quasar are warmer. The higher temperature hydrogen in nearby clouds is ionized and not capable of causing Lyman-alpha absorption. The clouds also contain heavier elements, for example, carbon and oxygen with abundance $\sim 10^{-3}$ hydrogen. Warm oxygen in a cloud along the line of sight absorbs ~ 0.6 keV (2 nm wavelength) X-rays in the spectrum of a quasar or other type active galaxy. Because we do not know the distance and temperature of the X-ray absorbing cloud and the degree of ionization of the oxygen atoms, the exact wavelengths of the absorption lines are not known a priori.

The most promising method for detecting the hot part of the WHIM is through absorption of far-ultraviolet (FUV) and X-radiation from a background source. Over the last few years, detections have been reported by a number of authors, but these have been biased toward the strongest systems, or trace extreme galaxy overdensity regions, and therefore may not be representative. Chandra grating spectrometers, combined with earlier XMM-Newton and Chandra observations, gave a 4σ detection of the OVII $K\alpha$ absorption line in the spectrum of a background blazar (a bright nonthermal source thought to be powered by accretion onto a supermassive black hole) at redshift $z = 0.165$ behind the SculpterWall, a large superstructure of galaxies at $z = 0.03$ [11]. Because the redshift of the SculpterWall is known, absorption signatures can be regarded as significant even if they are less prominent than those found in a random search. For a metallicity $Z = 10\%$ of the solar value the implied overdensity is consistent with cosmological simulations. A dedicated X-ray mission with much larger area and much better spectral resolution is needed to trace the bulk of the WHIM. The current status of intergalactic soft X-ray absorption line spectroscopy is described in a special section of the journal Science [12].

2.2. The Velocity Dispersion of Galaxies in Large Clusters of Galaxies. Papers by Zwicky in the 1930s [13, 14] were early indications of the existence of dark matter. Zwicky noted that the radial velocities of the galaxies in the Coma Cluster of galaxies (Figure 3) were much larger than what would be expected by assuming that the galaxies have the same ratio of mass to light, M/L , as the Sun. The Coma Cluster of galaxies is one of largest structures in the universe and therefore an excellent sample of its constituents. The virial theorem states that $\langle W \rangle = -\langle U \rangle/2$, where $\langle W \rangle$ is the time average of the total kinetic energy and $\langle U \rangle$ is the time average of the total potential energy. It applies to a stable system consisting of particles, bound by potential forces, with the total potential energy U . Because it is not a young object, it is reasonable to assume that the galaxies in the Coma Cluster are in equilibrium within a stable system.

Applying the virial theorem to the observed kinetic energy indicates that the potential energy and consequently the mass of the Coma Cluster is much larger than the mass obtained by assuming a solar-like mass to light ratio. The popular term for this disparity became known as the “missing mass.” Although there were other indications of a discrepancy between the solar mass to light ratio and the

mass of some other objects, it took thirty years for other types of measurements to confirm the existence of dark matter as convincingly as had Zwicky’s measurements of the Coma Cluster.

Zwicky and his contemporaries did not know that the Coma Cluster contains a halo of hot, $\sim 10^8$ K gas whose mass is ~ 5 times larger than the mass of the stars in the galaxies. That became known some forty years later after X-ray telescopes were launched into space. Although the baryonic mass becomes much larger after taking the hot gas into account, it is still a factor ~ 6 too small to explain the high velocities of the galaxies. Also the existence and presumably the stability of the hot gas halo is also an indication that a larger quantity of mass is present. Determining the mass of an object by measuring the parameters of a hot gas halo is discussed in more detail in Section 2.4. There are modern investigations of dark matter using Zwicky’s methods [15].

A 1959 theoretical paper by Kahn and Woltjer showed that the Local Group of galaxies can be dynamically stable only if contains an appreciable amount of intergalactic matter that is not seen [16]. At the time visible light images were thought to define the limits of the galaxy so their extended dark halos could satisfy the need for dark matter. They did not address the issue of whether and not the intergalactic dark matter was baryonic. Measurements with the Hubble Space Telescope of the velocity vector of neighbor galaxy M31 towards the Milky Way confirm that the Local Group of galaxies has a much larger mass to light ratio than the Sun [17], confirming the theoretical work of Kahn and Woltjer. The RAVE survey of high velocity stars constrains the local galactic escape speed to within a range that demonstrates the presence of the Galaxy’s dark halo [18].

2.3. The Flatness of the Rotation Curve of Galaxies. As was first discovered a hundred years ago, the stars and clouds of a spiral galaxy are generally rotating about the galaxy’s center. A measurement of the orbital velocities of stars as a function of distance from the center of rotation in spiral galaxies yields the mass interior to the stars’ positions. Rubin and her colleagues studied the rotation of several spiral galaxies including the Milky Way and the Andromeda galaxy, M31 [19, 20]. The orbital, or circular velocities of stars and clouds, V_c were measured in visible light and by others in radio. According to simple Newtonian mechanics $V_c^2 = GM/r$, the rotation curve $V_c(r)$ should first rise (because more mass is being included with increasing radius) and then decrease inversely with distance beyond the radius where the mass ends. But the rotation curves of the observed galaxies, after first rising and then falling, almost invariably flatten out. This behavior continues well beyond the edge of the disk as traced by the 21 cm line of atomic hydrogen with even more confidence [21]. The failure of galactic rotation curves to fall off as theoretically expected is perhaps the strongest evidence for the widespread belief that disk galaxies are all embedded in massive DM halos. This is shown in Figure 4(a), as actually measured and, in Figure 4(b), pictorially.

These optical and radio observers did not claim that the dark matter was nonbaryonic. However there were others

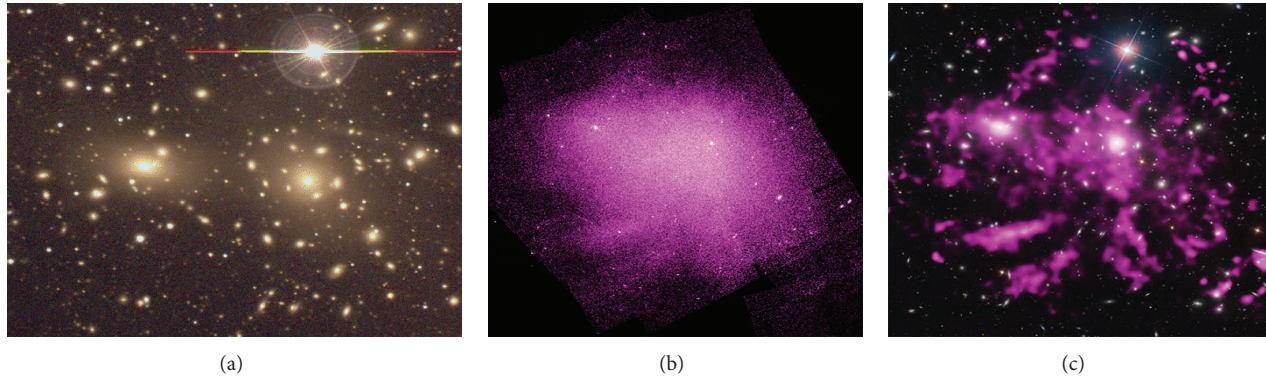


FIGURE 3: The Coma Cluster of galaxies. An optical image (a) shows two giant galaxies near the center plus a number of smaller galaxies. The raw X-ray image (b) was taken by the Chandra X-Ray Observatory. The size of the optical and X-ray fields shown is about 600 kpc (2 million light years). (c) is an overlay of the optical image with a high contrast X-ray image that displays the regions with high X-ray surface brightness around two giant elliptical galaxies that dominate the cluster.

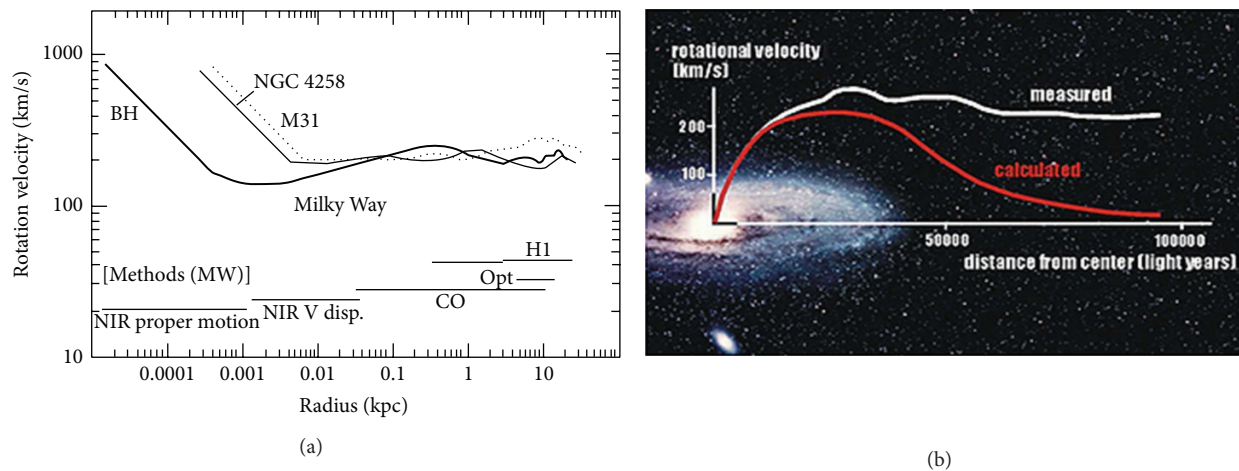


FIGURE 4: (a) shows the rotational velocity of stars as a function of distance from the center for three galaxies, the Milky Way, M31, and NGC 4258. (b) is a pictorial representation [20, 22].

who claimed that indeed the halo mass contained a nonbaryonic component [23].

The same general analysis applied to elliptical galaxies, with the dispersion of the stellar velocities replacing the circular velocities, also provides evidence for the existence of dark matter. Dwarf spheroidals (dSphs) are small galaxies, with $M_{\text{tot}} \sim 10^7$ solar masses, and relatively large dispersion velocities. In some extreme cases the deduced amount of dark matter is an order of magnitude or higher than that deduced for spiral galaxies, implying that dark matter constitutes more than 95% of the matter in these galaxies [24]. One possible explanation for the extreme dark matter content of dwarf spheroidal galaxies is that heating, by supernovae or some other process, has driven most of the baryonic matter out of these galaxies.

A modification of Newtonian dynamics (MOND), according to which the acceleration term in Newton's second law become nonlinear for very small accelerations, corresponding to large distances, has been offered as an alternative explanation for the flattening of the rotation

curves of galaxies [25]. A general-relativistic version was described later [26]. When it was introduced MOND was as good an explanation for the high rotation rates as assuming that the galaxy had a dark matter corona. However, it is not clear that it is possible to find a single version of MOND that can explain all the phenomena that have been associated with dark matter.

2.4. The Hot Gas Coronas of Large Elliptical Galaxies. M87 is a giant elliptical galaxy with an extended corona of X-ray emitting hot gas and two opposing jets projecting out from a giant black hole at the center. The mass of M87's giant central black hole is 3×10^9 solar, where the solar mass is 2×10^{33} grams [27]. It is small compared to the visible mass and much smaller than the DM in M87. A Chandra X-Ray Observatory image of M87 is shown in Figure 5. The hot gaseous corona is likely to be in hydrostatic equilibrium.

From the equation of hydrostatic equilibrium shown below, the total mass, $M(< r)$ can be determined almost

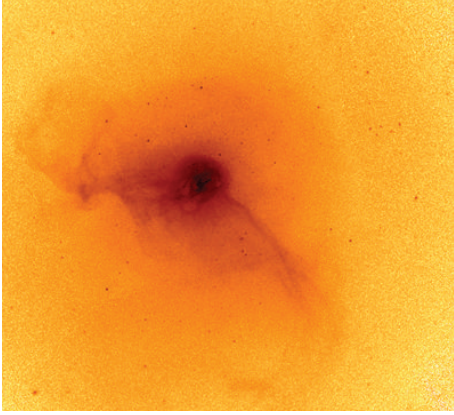


FIGURE 5: A Chandra X-Ray Observatory image of the giant elliptical galaxy M87 in the constellation Virgo. (provided by W. Forman of CfA). There is a large X-ray halo as well as features created by episodic outbursts emanating from a giant black hole at the center [28]. The field is about 10 arc minutes. The distance to M87 is about 16.4 Mpc (53 million light years).

independent of the model by measuring the density and temperature gradients as a function of radius, assuming spherical symmetry, and taking in account that we are observing M87 projected onto a plane:

$$M(<r) = \frac{-kT_{\text{gas}}}{G_{\mu}M_H} \left(\frac{d \log \rho_{\text{gas}}}{d \log r} + \frac{d \log T_{\text{gas}}}{d \log r} \right) r. \quad (1)$$

Within a radius of 87 kpc, or 275 million light years, (20 arc minutes) the optical luminosity is 6.6×10^{10} solar (solar luminosity = 2×10^{33} ergs/sec), the mass of the gas $M_{\text{gas}} = 2.1 \times 10^{11}$ solar (solar mass = 2×10^{33} g), and the total mass including DM is $M_{\text{tot}} = 1.3 \times 10^{13}$ solar, with a model dependent uncertainty of a factor of 2 due to errors in chemical abundances and assumptions made in deprojecting the X-ray image [29]. At larger radii the visible light does not increase much more and the ratio of mass of DM to the gas is larger. M87 is in the Virgo cluster of galaxies so there is a limit to how much further from the center can be studied without encountering another galaxy.

These results are confirmed, within the uncertainties, by observing the velocities of 161 globular clusters orbiting M87 [30]. A globular cluster is a gravitationally bound aggregate of up to a million stars usually in the halo of a galaxy. They act as test particles, whose positions and velocities can be measured. Planetary nebular are another set of test particles. They are observed in M87's halo up to a radial distance of 150 kpc [31].

The X-ray measuring technique has been widely applied, especially to data from the Chandra X-Ray Observatory, to measure the baryonic and dark matter content of many hydrodynamically relaxed galaxy clusters, with the general result that the mass of dark matter in galaxy clusters is ~ 5 to 10 times that of the baryonic matter [32, 33]. If, as seems reasonable, large galaxy clusters are representative of the universe as a whole, this can be taken to be the cosmic value of the ratio of dark to baryonic matter [34].



FIGURE 6: Gravitational arc from a distant galaxy behind a foreground galaxy cluster [36]. Credit: NASA, ESA, and A. Gonzalez (University of Florida, Gainesville), A. Stanford (University of California, Davis and Lawrence Livermore National Laboratory), and M. Brodwin (University of Missouri-Kansas City and Harvard-Smithsonian Center for Astrophysics) The giant arc, an incomplete Einstein Ring shown is an example of strong gravitational lensing. The more typical effect is weak gravitational lensing [37]. The process is described in more detail by Massey et al. [38].

2.5. Gravitational Lensing. Gravitational lensing is a technique that uses the distorted images of distant galaxies as a tracer of dark matter in a foreground object. The patterns of the distortions reflect the density of matter along the line of sight. The process is essentially the same as that which Arthur Eddington used for measuring the change in positions of stars when their positions are close to the solar disk, as observed during a solar eclipse. After applying some corrections, Eddington reported that the changes in stellar positions were in agreement with the predictions of General Relativity. On a cosmic scale the same process can be used to map the distribution of matter in a foreground object by observing the distorted and often multiple images of a distant point source. The geometry is far more complex because unlike the Sun the foreground lens is not a simple sphere but a cluster of galaxies. Figure 6 is one of the Hubble Space Telescope images that show the effect [35].

One of the most significant examples of utilizing gravitational lensing to trace the location of mass is shown in Figure 7. Two clusters of galaxies collided ~ 100 Myr ago and appear to be passing through each other to create the “Bullet Cluster” [39]. The clusters are believed to be moving in the plane of the figure. The gaseous halos are lagging behind. Analysis of weak gravitational lensing effects in the image shows that the mass, which is mostly DM, is associated with the galaxies and not with the hot gas [40].

Since the discovery of the Bullet Cluster, a half dozen or so other examples have been found, establishing cluster mergers as important cosmic laboratories for the study of the constraints on the cross-section for dark matter self-interactions. At present the best constraints are still from the Bullet Cluster.

2.6. The Cosmic Microwave Background and the Evolution of Structure. The 2.73 K thermal CMB is the strongest evidence that our universe was indeed created in a Big Bang. The



FIGURE 7: A composite X-ray/optical image of the galaxy cluster 1E 0657-56, also known as the “Bullet Cluster.” This cluster was formed following the collision of two large clusters of galaxies. The X-ray image, pink, is from the Chandra X-Ray Observatory. The optical image is from the Magellan telescope and the Hubble Space Telescope; the galaxies are orange and white. The distribution of mass as determined by gravitational lens analysis is blue.

general picture is that quantum fluctuations caused the newborn post-Big Bang ionized matter to be slightly nonuniform. These fluctuations were frozen-in by a sudden inflation or expansion in volume, which has been described as a change in state [41]. About four hundred thousand years after the Big Bang ($z \sim 1000$) the universe had cooled enough for the electrons and protons to combine into neutral atoms that decoupled from the radiation. Following recombination the small nonuniformities ($\delta T/T \sim 10^{-5}$) in the background radiation did not change as it cooled from the infrared to the microwave band, while the universe was expanding.

The current structure of the microwave background radiation represents the structure of the universe as it was 4×10^5 years after the Big Bang. The amount of mass needed to provide the level of gravitational attraction required for the structure of the universe as it was 4×10^5 years ago to evolve into the web-like structure of the galaxies, clusters of galaxies, and the voids we observe today is much larger than what we can detect over the entire electromagnetic spectrum, and it is consistent with other measurements of the amount of dark matter. Although this conclusion is based entirely upon theoretical considerations it is one of the strongest pieces of evidence for the existence of dark matter. However, it provides no direct indication of whether the matter is baryonic or nonbaryonic. Light element abundances and models of Big Bang nuclear synthesis point to the latter (Section 2.1).

Three spacecraft with increasing resolution and sensitivity were launched to map the cosmic microwave background. The first was NASA’s Cosmic Background Explorer (COBE) launched in 1989. It was followed by NASA’s Wilkinson Microwave Anisotropy Probe (WMAP) in 2001 and ESA’s Planck in 2009. A collection of papers on the results of Planck are available online [42]. Figure 8 is the Planck map and a chart of the power in its multipole components.

Analysis of the Planck data is ongoing following a new release in May, 2013. Methods of accounting for terrestrial, solar system, or galactic foreground radiation are being refined, but these corrections are unlikely to change the basic conclusions on the amount of dark matter in the Universe [43].

Simulation by computation of complex hydrodynamic and magnetodynamic processes that cannot be studied in the laboratory or observed in the cosmos with any type of telescope has become an important tool in astrophysics, indeed virtually a separate branch of astrophysics on a par with theory and observation. It is being applied to studying the evolution of structure in the universe under the influence of gravity. For example, starting with the structure of the microwave background, which represents the universe as it was 4×10^5 years after the Big Bang determining what is required for it to evolve to the web-like structure it has today with the correct number of spiral and elliptical galaxies and the observed quantities of dark matter and baryonic matter. This effort has been occurring over a period of two decades at various institutions. The most recent and the most detailed simulation so far is the work of the *Illustris* collaboration reported in Nature [44]. This work demonstrates that the Lambda-Cold Dark Matter can correctly describe the evolution of the universe to the web-like structure it has today with the correct number of spiral and elliptical galaxies, as well as a variety of observational data on small and large scales.

2.7. The Cosmic High Energy Positron and Gamma-Ray Spectra. Some models of the decay of DM predict that high energy positrons will be produced [45]. Indeed, several observations—the positron fraction as measured by the Alpha Magnetic Spectrometer [46] aboard the Space Station and the PAMELA magnetic spectrometer (aboard the Russian Resurs DK-1 spacecraft) [47] plus an excess of gamma-rays, presumably from positron annihilation, seen by the Fermi Gamma-ray Space Telescope [48]—indicate a positron fraction considerably higher than expected from ordinary cosmic ray production. However, there are possible astrophysical sources such as pulsars and the acceleration region of supernova remnants, whose rates of positron production have not been quantified. The positron fraction has been measured up to 300 GeV and is still rising from a minimum at ~ 7 GeV. While the rising positron flux with energy is not necessarily a positive indication of DM because of other possible cosmic production modes, the results can be interpreted as upper limits upon the rates of decay of a DM particle into positrons.

Another investigator team presents evidence of a 110–140 GeV gamma-ray emission feature from the inner galaxy where dark matter is expected to be enhanced, in the Fermi data [49]. This is expected in some models of the decay of a dark matter particle. However, the statistics are poor and there is the possibility that the emission is from known astrophysical processes. The HESS array of ground based very high energy ($> \text{TeV}$) gamma-ray telescopes in Namibia also searched the galactic center region, without success so far [50].

3. Identity of Dark Matter

3.1. Introduction. We consider the possible identities of dark matter only in general terms. If an element of dark matter is a particle we do not provide a specific description of its

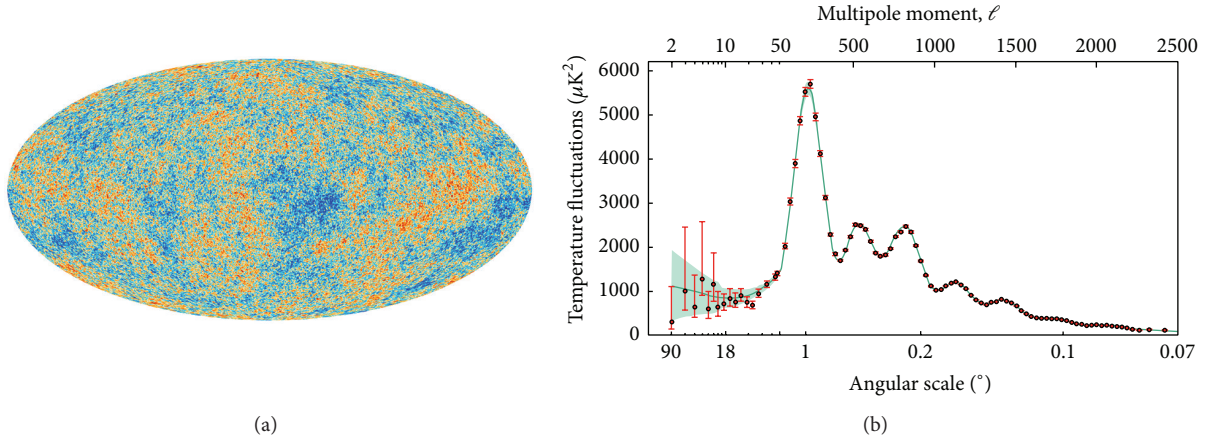


FIGURE 8: Planck all-sky map of the intensity of the cosmic microwave background radiation is shown in (a). (b) is an analysis of its angular structure and multipole components.

properties or attempt to find a place for it within the Standard Model of subatomic particles. It would not be one of those already detected in the laboratory. Other articles in this issue are likely to address this, as has a recent paper by Bergstrom [51] and references in the following paragraphs.

As discussed in Section 2.1, the dark matter is primarily nonbaryonic. That excludes as candidates such very low luminosity stars whose emission is below the detection threshold and isolated planetary objects, also known as “Massive Compact Halo Objects” or MACHOs, although they could account for a small fraction of DM. When a compact object in the halo of our galaxy passes in front of a source star in a nearby dwarf galaxy, the image of a source star experiences a temporary magnification due to gravitational microlensing [52]. MACHOs have been eliminated as accounting for all the dark matter by an unsuccessful search for long-duration microlensing events toward the Large Magellanic Cloud. The observations of the MACHO and EROS collaboration showed that objects whose mass is less than 30 solar masses contribute less than 40% of the dark matter [53]. However the teams did detect a microlensing effect near the center of the galaxy [54]. That effect could be attributed to a region containing many stars plus Sgr A*, the black hole at the center of the Milky Way.

It has been long thought that dark matter could be explained by an as yet undiscovered massive, weakly interacting elementary particle (WIMP), that is, a thermal relic of the Big Bang. Initially the early Universe was dense and hot, and all particles were in thermal equilibrium. The Universe then cooled to temperatures below the pair creation of dark matter particles with mass m_{DM} and the number of dark matter particles would have dropped exponentially once $kT \ll m_{\text{DM}}c^2$. In addition to cooling, the Universe was also expanding. Eventually, the Universe would have become so large and the gas of dark matter particles would have become so dilute that they cannot have found each other to annihilate. The dark matter particles then have “frozen out,” with their number asymptotically approaching

their thermal relic density. These considerations imply that a weakly interacting particle that makes up all of dark matter is predicted to have mass in the range ~ 100 GeV to 1 TeV [55]. However, if the annihilation cross-section is much less than the weak interaction cross-section, this mass constraint can be relaxed, and dark matter candidates which satisfy the relic density and Big Bang nucleosynthesis constraints successfully can have masses in the keV to TeV range [56].

Observations of large-scale cosmological structures imply that dark matter must be stable, or at least metastable, on Gyr time scales. This rules out all unstable Standard Model particles. Furthermore, the observation that galaxies formed at redshifts $z \sim 10$ –20 implies that dark matter cannot be “hot,” that is, have a large thermal velocity, at the redshift at which it decouples from matter in the cooling early Universe. For thermal relics, this criterion selects the mass of the dark candidate as well, so that colder particles are heavier. However, alternative nonthermal production scenarios can exist and very light particles can also act as cold dark matter, as in the case of the axion.

Another line of investigation into the nature of dark matter is to look for its effects in the X-ray spectra of cosmic sources. One class of dark matter candidates is called axion-like particles (ALPs). The presence of a magnetic field is predicted to induce conversions of photons into ALPs. The absence of anomalous irregularities in the Chandra X-ray spectrum of the Hydra A cluster produces the most stringent constraint to date in the range of very low mass ALPs, with mass $< 10^{-11}$ eV [57]. The archive of 70 Chandra observations of the central region of M31 were used to effectively rule out canonical oscillation-based sterile neutrinos as a viable dark matter candidate in the 2.5–10 keV range, although other mechanisms for producing sterile neutrinos are still possible. Phase-space constraints derived from optical observations of dwarf galaxies in the Local Group have closed the window at lower energies [58].

3.2. *MOND, No Dark Matter.* One possibility is that there is no such thing as dark matter. The effects described in

Section 2 would then be entirely due to deviations from Newton's law. The model is Modification of Newtonian Dynamics (MOND). MOND was proposed as an alternative to DM to explain the rotation rates of stars far from the center of the galaxy as described in Section 3.3. The same version of MOND can perhaps also explain the existence of massive hot gaseous halos around M87 and other giant elliptical galaxies, but it is not clear that the same version of MOND can also explain the effects attributed to gravitational lensing by DM in complex geometries like the Bullet Cluster [59]. While a single version of MOND may be able to explain several effects attributed to dark matter, it may not be able to offer an explanation for the growth of structure. Perhaps this could be accomplished by a modified version of MOND that weakens the effects of gravity on the scale of a galaxy to explain the large rotation rates of stars in the gaseous coronas of certain galaxies and modifies the Newtonian dynamics again at the largest distances to explain gravitational lenses and the growth of structure [60]. However, MOND still has a significant number of proponents and its originator has recently offered more evidence in its support [61].

3.3. Primordial Black Holes. The limits on the baryonic mass-energy density rule out black holes created through the process of star formation and evolution. However, it is possible that primordial black holes were created in the very early universe and thereby evades Big Bang nucleosynthesis and CMB constraints. Primordial black holes with masses much less than $\sim 10^{15}$ g ($= 2 \times 10^{-18}$ solar mass) will have evaporated into gamma-rays [62] but more massive black holes could survive until the present epoch [63]. The negative results of the MACHO/EROS collaborative search for microlensing events concluded that objects within the mass range from 3×10^{-8} to 30 solar masses cannot account for more than 40% of dark matter. The lower limit was reduced to 10^{-9} solar masses (2×10^{24} g) by an analysis of Kepler microlensing data [64]. Constraints from the Fermi Observatory of the lack of observed femto-lensing in gamma-ray bursts rule out the range 5×10^{17} – 10^{20} g [65]. That left a narrow window of masses in the range 10^{20} – 10^{24} g for primordial black holes as viable dark matter candidates. However, an analysis of the capture rate of primordial black holes by neutron stars by Pani & Loeb suggests that primordial black holes with masses between 10^{15} and 10^{24} grams cannot exist in sufficient numbers to explain dark matter [66]. Otherwise tidal capture of primordial black holes by neutron stars followed by rapid accretion into the black hole would have led to the disruption of all the neutron stars in the Galaxy and the Large Magellanic Cloud. If confirmed, this result would severely narrow the window on the possibility that primordial black holes can explain a significant amount of the observed dark matter.

4. Conclusions

As in the 16th and 17th centuries, the interests of astronomers, now more appropriately called astrophysicists, and laboratory physicists are converging upon the same issue at the frontier of fundamental physics, identifying the source and nature

of the elusive dark matter. Astronomers are developing a new generation of tools including ground optical based telescopes with 28 to 40 m segmented apertures provided with adaptive optics to correct for atmospheric jitter. Large area optics will be stationed in both the northern and southern hemispheres. The Large Synoptic Survey Telescope (LSST) is likely to find numerous examples of gravitational lenses that will shed light upon dark matter. There will be a second generation space telescope, the James Webb Space telescope (JWST), with extended infrared sensitivity to view objects at very large redshift, which are closer in time to the first generation of star formation and perhaps unveiling the condition of dark matter at that epoch. Radio telescopes can reach even further back in time to study structure at earlier times by mapping the redshifted ubiquitous 21 cm hydrogen line. Radio astronomers are constructing the low frequency array (LOFAR), an international partnership led by The Netherlands. LOFAR will be able to map redshifted 21 cm lines that reveal structure at earlier epochs. Radio astronomers are also planning the Square Kilometer Array. The European Space Agency has approved "Athena," an X-ray telescope system that will have a much larger aperture and much better spectroscopic resolution than the currently orbiting Chandra X-Ray Observatory and XMM-Newton. It will be capable of detecting and measuring the mass of the WHIM by observing oxygen and other elemental absorption lines by foreground clouds in the spectra of quasars with orders of magnitude more sensitivity and better resolution than Chandra and XMM-Newton.

These astronomical facilities will no doubt improve our knowledge about the behavior of dark matter, but a definitive resolution of what the dark matter particles actually are and where they fit in the Standard Model of fundamental particles, if they do indeed fit within, or upset the Standard Model, will ultimately require a positive detection of individual particles either in a debris of particles created by the Large Hadron Collider or by a ground, subterranean or deep oceanic based large area detector array.

Conflict of Interests

The authors declare that there is no conflict of interests regarding the publication of this paper.

References

- [1] M. Planck, "When I began my physical studies [in Munich in 1874] and sought advice from my venerable teacher Philipp von Jolly...he portrayed to me physics as a highly developed, almost fully matured science...Possibly in one or another nook there would perhaps be a dust particle or a small bubble to be examined and classified, but the system as a whole stood there fairly secured, and theoretical physics approached visibly that degree of perfection which, for example, geometry has had already for centuries," 1924, <http://www.goodreads.com/quotes/tag/johann-philipp-gustav-von-jolly>.
- [2] J. Al-Khali, "Where science is going," *International New York Times*, vol. 15, 2013.

- [3] V. Trimble, "Existence and nature of dark matter in the universe," *Annual Review of Astronomy and Astrophysics*, vol. 25, pp. 425–472, 1987.
- [4] L. Bergström, "Cosmology and the dark matter frontier," *Physica Scripta*, vol. 2013, Article ID 014014, 2013.
- [5] J. Tumlinson, C. Thom, J. K. Werk et al., "The large, oxygen-rich halos of star-forming galaxies are a major reservoir of galactic metals," *Science*, vol. 334, no. 6058, pp. 948–952, 2011.
- [6] G. Steigman, "Primordial nucleosynthesis in the precision cosmology era," *Annual Review of Nuclear and Particle Science*, vol. 57, pp. 463–491, 2007.
- [7] July 2013, <http://www.astr.ua.edu/keel/agn/forest.html>.
- [8] M. J. Geller and J. P. Huchra, "Mapping the universe," *Science*, vol. 246, no. 4932, pp. 897–903, 1989.
- [9] R. Cen and J. P. Ostriker, "Where are the baryons?" *The Astrophysical Journal*, vol. 514, no. 1, pp. 1–6, 1999.
- [10] R. Davé, R. Cen, J. P. Ostriker et al., "Baryons in the warm-hot intergalactic medium," *The Astrophysical Journal*, vol. 552, no. 2, pp. 473–483, 2001.
- [11] T. Fang, D. A. Buote, P. J. Humphrey et al., "Confirmation of X-ray absorption by warm-hot intergalactic medium in the sculptor wall," *The Astrophysical Journal*, vol. 714, no. 2, pp. 1715–1724, 2010.
- [12] F. Nicastro, S. Mathur, and M. Elvis, "Perspective: missing baryons and the warm-hot intergalactic medium," *Science*, vol. 319, no. 5859, pp. 55–57, 2008.
- [13] F. Zwicky, "Die Rotverschiebung von extragalaktischen Nebeln," *Helvetica Physica Acta*, vol. 6, pp. 110–127, 1933.
- [14] F. Zwicky, "On the masses of nebulae and of clusters of nebulae," *The Astrophysical Journal*, vol. 86, pp. 217–246, 1937.
- [15] A. B. Newman, T. Treu, R. S. Ellis, and D. J. Sand, "The density profiles of massive, relaxed galaxy clusters. II. Separating luminous and dark matter in cluster cores," *The Astrophysical Journal*, vol. 765, no. 1, article 25, 12 pages, 2013.
- [16] F. D. Kahn and L. Woltjer, "Intergalactic matter and the Galaxy," *The Astrophysical Journal*, vol. 130, pp. 705–717, 1959.
- [17] R. P. van der Marel, M. Fardal, G. Besla et al., "The M31 velocity vector. II. Radial orbit toward the milky way and implied local group mass," *The Astrophysical Journal*, vol. 753, no. 1, article 8, 14 pages, 2012.
- [18] M. C. Smith, G. R. Ruchti, A. Helmi et al., "The RAVE survey: constraining the local Galactic escape speed," *Monthly Notices of the Royal Astronomical Society*, vol. 379, no. 2, pp. 755–772, 2007.
- [19] V. C. Rubin, D. Burstein, W. K. Ford Jr., and N. Thonnard, "Rotational velocities of 16 Sa galaxies and a comparison of Sa, Sb, and Sc rotation properties," *The Astrophysical Journal*, vol. 289, pp. 81–104, 1985.
- [20] Y. Sofue and V. Rubin, "Rotation curves of spiral galaxies," *Annual Review of Astronomy and Astrophysics*, vol. 39, no. 1, pp. 137–174, 2001.
- [21] A. Bosma, "21-cm line studies of spiral galaxies. II. The distribution and kinematics of neutral hydrogen in spiral galaxies of various morphological types," *Astronomical Journal*, vol. 86, pp. 1845–1846, 1981.
- [22] November 2013, <http://cdn.physorg.com/newman/gfx/news/hires/2011/coulddarkmat.jpg>.
- [23] D. J. Hegyi and K. A. Olive, "A case against baryons in galactic halos," *The Astrophysical Journal*, vol. 303, pp. 56–65, 1986.
- [24] R. R. Muñoz, J. L. Carlin, P. M. Frinchaboy, D. L. Nidever, S. R. Majewski, and R. J. Patterson, "Exploring halo substructure with giant stars: the dynamics and metallicity of the dwarf spheroidal in Boötes," *The Astrophysical Journal Letters*, vol. 650, no. 1, pp. L51–L54, 2006.
- [25] M. Milgrom, "A modification of the newtonian dynamics as a possible alternative to the hidden mass hypothesis," *The Astrophysical Journal*, vol. 270, pp. 365–370, 1983.
- [26] J. D. Bekenstein, "The modified Newtonian dynamics—MOND and its implications for new physics," *Contemporary Physics*, vol. 47, no. 6, pp. 387–403, 2006.
- [27] T. di Matted, S. W. Allen, A. C. Fabian, A. S. Wilson, and A. J. Young, "Accretion onto the supermassive black hole in M87," *The Astrophysical Journal*, vol. 582, no. 1, pp. 133–140, 2003.
- [28] W. Forman, C. Jones, E. Churazov et al., "Filaments, bubbles, and weak shocks in the gaseous atmosphere of M87," *The Astrophysical Journal*, vol. 665, no. 2, pp. 1057–1066, 2007.
- [29] D. Fabricant and P. Gorenstein, "Further evidence for M87's massive dark halo," *The Astrophysical Journal*, vol. 267, pp. 535–546, 1983.
- [30] X. Wu and S. Tremaine, "Deriving the mass distribution of M87 from globular clusters," *The Astrophysical Journal*, vol. 643, no. 1, pp. 210–221, 2006.
- [31] A. Longobardi, M. Arnaboldi, O. Gerhard, L. Coccatto, S. Okamura, and K. C. Freeman, "The planetary nebula population in the halo of M87," *Astronomy & Astrophysics*, vol. 558, p. A42, 2013.
- [32] A. Vikhlinin, A. Kravtsov, W. Forman et al., "Chandra sample of nearby relaxed galaxy clusters: mass, gas fraction, and mass-temperature relation," *The Astrophysical Journal*, vol. 640, no. 2, pp. 691–709, 2006.
- [33] L. P. David, C. Jones, and W. Forman, "The universal gas mass fraction in clusters of galaxies," *The Astrophysical Journal*, vol. 748, no. 2, article 120, 8 pages, 2012.
- [34] R. W. Schmidt and S. W. Allen, "The dark matter haloes of massive, relaxed galaxy clusters observed with Chandra," *Monthly Notices of the Royal Astronomical Society*, vol. 379, no. 1, pp. 209–221, 2007.
- [35] November 2013, <http://hubblesite.org/newscenter/archive/releases/exotic/gravitational%20lens/2012/08/image/a/format/large-web/>.
- [36] <http://hubblesite.org/newscenter/archive/releases/2012/19/full/>.
- [37] D. M. Wittman, J. A. Tyson, D. Kirkman, I. Dell'Antonio, and G. Bernstein, "Detection of weak gravitational lensing distortions of distant galaxies by cosmic dark matter at large scales," *Nature*, vol. 405, no. 6783, pp. 143–148, 2000.
- [38] R. Massey, T. Kitching, and J. Richard, "The dark matter of gravitational lensing," *Reports on Progress in Physics*, vol. 73, Article ID 086901, 26 pages, 2010.
- [39] M. Markevitch, A. H. Gonzalez, L. David et al., "A textbook example of a bow shock in the merging galaxy cluster 1E 0657-56," *The Astrophysical Journal Letters*, vol. 567, no. 1, pp. L27–L31, 2002.
- [40] D. Clowe, A. Gonzalez, and M. Markevitch, "Weak-lensing mass reconstruction of the interacting cluster 1E 0657-558: direct evidence for the existence of dark matter," *The Astrophysical Journal*, vol. 604, no. 2, pp. 596–603, 2004.
- [41] A. H. Guth and S.-Y. Pi, "Fluctuations in the new inflationary universe," *Physical Review Letters*, vol. 49, no. 15, pp. 1110–1113, 1982.

- [42] December 2013, <http://planck.caltech.edu/publications2013Results.html>.
- [43] D. Spergel, R. Flauger, and R. Hlozek, "Planck data reconsidered," <http://arxiv.org/abs/1312.3313>.
- [44] M. Vogelsberger, S. Genel, V. Springel et al., "Properties of galaxies reproduced by a hydrodynamic simulation," *Nature*, vol. 509, pp. 177–182, 2014.
- [45] M. S. Turner and F. Wilczek, "Positron line radiation as a signature of particle dark matter in the halo," *Physical Review D*, vol. 42, no. 4, pp. 1001–1007, 1990.
- [46] L. Bergstrom, T. Bringmann, I. Cholis, and D. Hooper, "New limits on dark matter annihilation from alpha magnetic spectrometer cosmic ray positron data," *Physical Review Letters*, vol. 111, Article ID 171101, 5 pages, 2013.
- [47] O. Adriani, G. C. Barbarino, G. A. Bazilevskaya et al., "The cosmic-ray positron energy spectrum measured by PAMELA," *Physical Review Letters*, vol. 111, Article ID 081102, 2013.
- [48] D. Hooper and L. Goodenough, "Dark matter annihilation in the Galactic Center as seen by the Fermi Gamma Ray Space Telescope," *Physics Letters B*, vol. 697, no. 5, pp. 412–428, 2011.
- [49] M. Su and D. P. Finkbeiner, "Strong evidence for gamma-ray line emission from the inner galaxy," <http://arxiv.org/abs/1206.1616>.
- [50] A. Abramowski, F. Acero, F. Aharonian et al., "Search for photon-lineline signatures from dark matter annihilations with H.E.S.S.," *Physical Review Letters*, vol. 110, no. 4, Article ID 041301, 2013.
- [51] L. Bergstrom, "Cosmology and the dark matter frontier," *Physica Scripta*, vol. 2013, no. T158, Article ID 014014, 2013.
- [52] B. Paczynski, "Gravitational microlensing by the galactic halo," *The Astrophysical Journal*, vol. 304, pp. 1–5, 1986.
- [53] C. Alcock, R. A. Allsman, D. R. Alves et al., "Macho project limits on black hole dark matter in the 1–30 M_{\odot} range," *The Astrophysical Journal Letters*, vol. 550, no. 2, pp. L169–L172, 2001.
- [54] C. Alcock, R. A. Allsman, D. R. Alves et al., "Direct detection of a microlens in the Milky Way," *Nature*, vol. 414, no. 6864, pp. 617–619, 2001.
- [55] J. L. Feng, "Dark matter candidates from particle physics and methods of detection," *Annual Review of Astronomy and Astrophysics*, vol. 48, pp. 495–545, 2010.
- [56] S. Gardner and G. M. Fuller, "Dark matter studies entrain nuclear physics," *Progress in Particle and Nuclear Physics*, vol. 71, pp. 167–184, 2013.
- [57] D. Wouters and P. Brun, "Constraints on axion-like particles from X-ray observations of the hydra galaxy cluster," *The Astrophysical Journal*, vol. 772, no. 1, article 44, 2013.
- [58] S. Horiuchi, P. J. Humphrey, J. Oñorbe, K. N. Abazajian, M. Kaplinghat, and S. Garrison-Kimmel, "Sterile neutrino dark matter bounds from galaxies of the Local Group," *Physical Review D*, vol. 89, Article ID 025017, 2013.
- [59] G. W. Angus, B. Famaey, and H. S. Zhao, "Can MOND take a bullet? Analytical comparisons of three versions of MOND beyond spherical symmetry," *Monthly Notices of the Royal Astronomical Society*, vol. 371, no. 1, pp. 138–146, 2006.
- [60] S. Dodelson and M. Liguori, "Can cosmic structure form without dark matter?" *Physical Review Letters*, vol. 97, no. 23, Article ID 231301, 2006.
- [61] M. Milgrom, "Testing MOND over a wide acceleration range in X-ray ellipticals," *Physical Review Letters*, vol. 109, no. 13, Article ID 131101, 2012.
- [62] D. N. Page and S. W. Hawking, "Gamma-rays from primordial black holes," *The Astrophysical Journal*, vol. 206, pp. 1–7, 1976.
- [63] B. J. Carr, K. Kohri, Y. Sendouda, and J. Yokoyama, "New cosmological constraints on primordial black holes," *Physical Review D*, vol. 81, no. 10, Article ID 104019, 33 pages, 2010.
- [64] K. Griest, A. M. Cieplak, and M. J. Lehner, "New limits on primordial black hole dark matter from an analysis of Kepler source microlensing data," *Physical Review Letters*, vol. 111, Article ID 181302, 15 pages, 2013.
- [65] A. Barnacka, J.-F. Glicenstein, and R. Moderski, "New constraints on primordial black holes abundance from femtolensing of gamma-ray bursts," *Physical Review D*, vol. 86, no. 4, Article ID 043001, 6 pages, 2012.
- [66] P. Pani and A. Loeb, "Exclusion of the remaining mass window for primordial black holes as the dominant constituent of dark matter," <http://arxiv.org/abs/1401.3025>.

Research Article

The Annual Modulation Signature for Dark Matter: DAMA/LIBRA-Phase1 Results and Perspectives

Rita Bernabei,^{1,2} Pierluigi Belli,² Fabio Cappella,^{3,4} Vincenzo Caracciolo,⁵ Simone Castellano,⁵ Riccardo Cerulli,⁵ Chang Jang Dai,⁶ Annelisa d'Angelo,^{3,4} Silio d'Angelo,^{1,2} Alessandro Di Marco,^{1,2} H. L. He,⁶ Antonella Incicchitti,⁴ H. H. Kuang,⁶ X. H. Ma,⁶ Francesco Montecchia,^{2,7} X. D. Sheng,⁶ Rui Guang Wang,⁶ and Zi-Piao Ye^{6,8}

¹ Dipartimento di Fisica, Università di Roma "Tor Vergata", 00133 Rome, Italy

² INFN, sez. Roma "Tor Vergata", 00133 Rome, Italy

³ Dipartimento di Fisica, Università di Roma "La Sapienza", 00185 Rome, Italy

⁴ INFN, sez. Roma, 00185 Rome, Italy

⁵ Laboratori Nazionali del Gran Sasso, INFN, 67100 Assergi, Italy

⁶ Institute of High Energy Physics, Chinese Academy of Sciences, P.O. Box 918-3, Beijing 100049, China

⁷ Dipartimento di Ingegneria Civile e Ingegneria Informatica, Università di Roma "Tor Vergata", 00133 Rome, Italy

⁸ Maths & Physics College, Jingtangshan University, Jián 343009, China

Correspondence should be addressed to Pierluigi Belli; pierluigi.belli@roma2.infn.it

Received 13 January 2014; Accepted 19 March 2014; Published 24 June 2014

Academic Editor: Anselmo Meregaglia

Copyright © 2014 Rita Bernabei et al. This is an open access article distributed under the Creative Commons Attribution License, which permits unrestricted use, distribution, and reproduction in any medium, provided the original work is properly cited. The publication of this article was funded by SCOAP³.

The results obtained with the total exposure of $1.04 \text{ ton} \times \text{yr}$ collected by DAMA/LIBRA-phase1 deep underground at the Gran Sasso National Laboratory (LNGS) of the I.N.F.N. during 7 annual cycles are summarized. The DAMA/LIBRA-phase1 and the former DAMA/NaI data (cumulative exposure $1.33 \text{ ton} \times \text{yr}$, corresponding to 14 annual cycles) give evidence at 9.3σ C.L. for the presence of Dark Matter (DM) particles in the galactic halo, on the basis of the exploited model independent DM annual modulation signature by using highly radiopure NaI(Tl) target. The modulation amplitude of the *single-hit* events in the (2–6) keV energy interval is $(0.0112 \pm 0.0012) \text{ cpd/kg/keV}$; the measured phase is (144 ± 7) days and the measured period is $(0.998 \pm 0.002) \text{ yr}$; values are in a good well in agreement with those expected for DM particles. No systematic or side reactions able to mimic the exploited DM signature have been found or suggested by anyone over more than a decade. Some of the perspectives of the presently running DAMA/LIBRA-phase2 are outlined.

1. Introduction

The presently running DAMA/LIBRA [1–11] experiment, as the former DAMA/NaI [12–41], has the main aim to investigate the presence of DM particles in the galactic halo by exploiting the model independent DM annual modulation signature (originally suggested in [42, 43]). Moreover, the developed highly radiopure NaI(Tl) target-detectors [1] assure as well sensitivity to a wide range of DM candidates, interaction types, and astrophysical scenarios.

As a consequence of the Earth's revolution around the Sun, the Earth should be crossed by a larger flux of DM particles around ≈ 2 June and by a smaller one around ≈ 2 December. This DM annual modulation signature is very distinctive since the effect induced by DM particles must simultaneously satisfy all the following requirements: (1) the rate must contain a component modulated according to a cosine function (2) with one year period and (3) a phase that peaks roughly ≈ 2 June; (4) this modulation must only be found in a well-defined low energy range, where DM particle

induced events can be present; (5) it must apply only to those events in which just one detector of many actually “fires” (*single-hit* events), since the DM particle multi-interaction probability is negligible; (6) the modulation amplitude in the region of maximal sensitivity must be $\approx 7\%$ for usually adopted halo distributions (see, e.g., [8, 23, 24]), but it can be larger in case of some possible scenarios such as, for example, those in [44–48] (even up to $\approx 30\%$). Thus, this signature is model-independent, is very effective, and, in addition, it allows the test of a large range of cross sections and of halo densities.

This DM signature might be mimicked only by systematic effects or side reactions able to account for the whole observed modulation amplitude and to simultaneously satisfy all the requirements given above. No one is available [1–3, 7, 8, 22–24].

The full description of the DAMA/LIBRA setup during phase1 and other related arguments have been discussed in detail in [1–4, 8] and references therein. Here, we just remind the reader that the sensitive part of this setup is made of 25 highly radiopure NaI(Tl) crystal scintillators (5 rows by 5-column matrix) having 9.70 kg mass each one. In each detector two 10 cm long UV light guides (made of Suprasil B quartz) act also as optical windows on the two end faces of the crystal and are coupled with two low background photomultipliers (PMTs) working in coincidence at single photoelectron level. The low background 9265-B53/FL and 9302-A/FL PMTs, developed by EMI-Electron Tubes with dedicated R&Ds, were used in the phase1; for details, see [1, 21, 23] and references therein. The detectors are housed in a sealed low-radioactive copper box installed in the center of a low-radioactive Cu/Pb/Cd-foils/polyethylene/paraffin shield; moreover, about 1 m concrete (made from the Gran Sasso rock material) almost fully surrounds (mostly outside the barrack) this passive shield, acting as a further neutron moderator. A threefold-level sealing system prevents the detectors from being in contact with the environmental air of the underground laboratory [1]. The light response of the detectors during phase1 typically ranges from 5.5 to 7.5 photoelectrons/keV, depending on the detector. The hardware threshold of each PMT is at single photoelectron, while a software energy threshold of 2 keV electron equivalent (hereafter keV) is used [1, 21]. Energy calibration with X-rays/ γ sources are regularly carried out in the same running condition down to few keV [1]; in particular, double coincidences due to internal X-rays from ^{40}K (which is at ppt levels in the crystals) provide (when summing the data over long periods) a calibration point at 3.2 keV close to the software energy threshold (for details, see [1]). The radiopurity, the procedures, and details are discussed in [1–4, 8] and references therein.

2. The Results of DAMA/LIBRA-Phase1 and DAMA/NaI

The total exposure of DAMA/LIBRA-phase1 is 1.04 ton \times yr in seven annual cycles; when including also that of the first generation DAMA/NaI experiment, it is 1.33 ton \times yr,

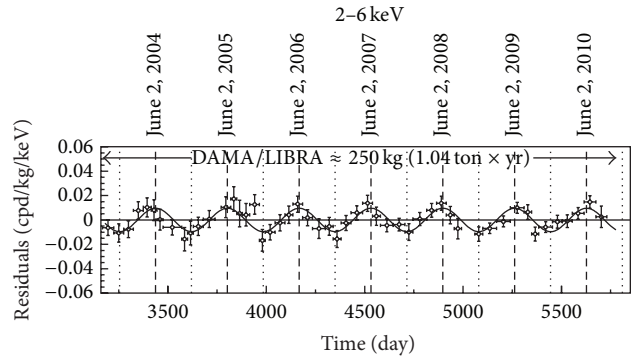


FIGURE 1: Experimental residual rate of the *single-hit* scintillation events measured by DAMA/LIBRA-phase1 in the (2–6) keV energy interval as a function of the time. The data points present the experimental errors as vertical bars and the associated time bin width as horizontal bars. The superimposed curves are the cosinusoidal functions behaviour $A \cos \omega(t - t_0)$ with a period $T = 2\pi/\omega = 1$ yr, a phase $t_0 = 152.5$ day (June 2nd) and modulation amplitudes, A , equal to the central values obtained by best fit on the data points of the entire DAMA/LIBRA-phase1. The dashed vertical lines correspond to the maximum expected for the DM signal (June 2nd), while the dotted vertical lines correspond to the minimum.

corresponding to 14 annual cycles. The variance of the cosine $(\alpha - \beta^2) = (\langle \cos^2 \rangle - \langle \cos \rangle^2)$, where the averages $\langle \dots \rangle$ are taken over the periods in which the data taking was on, is 0.518 during the DAMA/LIBRA-phase1, showing that the setup has been operational evenly throughout the years (the expectation value for full-year data taking is $(\alpha - \beta^2) = 0.5$). For details, see [2–4, 8].

The total number of events collected for the routine calibrations during the entire DAMA/LIBRA-phase1 is about 9.6×10^7 , while about 3.5×10^6 events/keV have been collected for the evaluation of the acceptance window efficiency for noise rejection near energy threshold [1]. The duty cycle of the experiment is high [4]; the routine calibrations and, in particular, those related to the acceptance windows efficiency mainly affect it.

Figure 1 shows the time behaviour of the experimental residual rates of the *single-hit* scintillation events in the (2–6) keV energy interval for DAMA/LIBRA-phase1. The residuals of the DAMA/NaI data (0.29 ton \times yr) are given in [2, 8, 23, 24]. We remind the reader that these residual rates are calculated from the measured rate of the *single-hit* events after subtracting the constant part: $\langle r_{ijk} - \text{flat}_{jk} \rangle_{jk}$. Here, r_{ijk} is the rate in the considered i th time interval for the j th detector in the k th energy bin, while flat_{jk} is the rate of the j th detector in the k th energy bin averaged over the cycles; it is of order of ≤ 1 cpd/kg/keV [1, 2, 49]. The average is made on all the detectors (j index) and on all the energy bins (k index) which constitute the considered energy interval. The weighted mean of the residuals must obviously be zero over one cycle.

The χ^2 test excludes the hypothesis of absence of modulation in the data: $\chi^2/\text{d.o.f.} = 83.1/50$ and the P value is $P = 2.2 \times 10^{-3}$ for the (2–6) keV energy interval. When fitting

the *single-hit* residual rate of DAMA/LIBRA-phase1 (Figure 1) together with the DAMA/NaI ones, with the function, $A \cos \omega(t - t_0)$, considering a period $T = 2\pi/\omega = 1$ yr and a phase $t_0 = 152.5$ day (June 2nd) as expected by the DM annual modulation signature, the following modulation amplitude is obtained: $A = (0.0110 \pm 0.0012)$ cpd/kg/keV corresponding to 9.2σ C.L. (χ^2 of the fit is 70.4 over 86 d.o.f.).

When the period and the phase are kept free in the fitting procedure, the modulation amplitude is (0.0112 ± 0.0012) cpd/kg/keV (9.3σ C.L.), the period $T = (0.998 \pm 0.002)$ year, and the phase $t_0 = (144 \pm 7)$ day. The period and the phase are well compatible with expectations for a DM annual modulation signal. In particular, the phase is consistent with about June 2nd and is fully consistent with the value independently determined by Maximum Likelihood analysis (see later). For completeness, we recall that a slight energy dependence of the phase could be expected in case of possible contributions of nonthermalized DM components to the galactic halo, such as, for example, the SagDEG stream [26, 50–54] and the caustics [55]. For more details, see [4].

The modulation amplitudes singularly calculated for each annual cycle of DAMA/NaI and DAMA/LIBRA-phase1 are compatible among them and are normally fluctuating around their best fit values [2–4]. In particular, for the (2–6) keV energy interval, the χ^2 is 10.8 over 13 d.o.f. corresponding to an upper tail probability of 63%, while the *run test* yields a lower tail probability of 23%. This analysis confirms that the data collected in all the annual cycles with DAMA/NaI and DAMA/LIBRA-phase1 are statistically compatible and can be considered together, on the contrary of the statements in [56].

The DAMA/LIBRA-phase1 *single-hit* residuals of Figure 1 and those of DAMA/NaI have also been investigated by a Fourier analysis. The data analysis procedure has been described in detail in [8]. A clear peak corresponding to a period of 1 year (see Figure 2) is evident for the (2–6) keV energy interval; the same analysis in the (6–14) keV energy region shows instead only aliasing peaks. No other structure at different frequencies has been observed (see also [8]).

Absence of any other significant background modulation in the energy spectrum has been verified in energy regions not of interest for DM. (In fact, the background in the lowest energy region is essentially due to “Compton” electrons, X-rays, and/or Auger electrons, muon induced events, etc., which are strictly correlated with the events in the higher energy region of the spectrum. Thus, if a modulation detected in the lowest energy region was due to a modulation of the background (rather than to a signal), an equal or larger modulation in the higher energy regions should be present.) For example, the measured rate integrated above 90 keV, R_{90} , as a function of the time has been analysed [4]. Similar result is obtained when comparing the *single-hit* residuals in the (2–6) keV with those in other energy intervals; for example, Figure 3 shows the *single-hit* residuals in the (2–6) keV and in the (6–14) keV energy regions for the entire DAMA/LIBRA-phase1 data as if they were collected in a single annual cycle (i.e., binning in the variable time from the Jan 1st of each annual cycle). It is worth noting that the obtained results account for whatever kind of background and, in

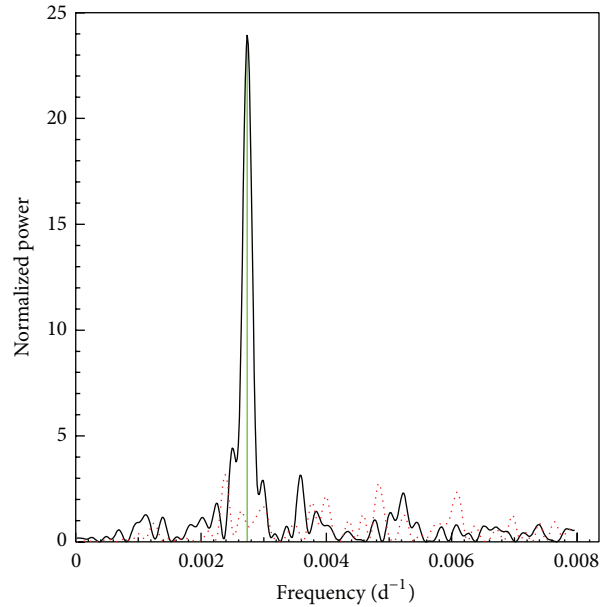


FIGURE 2: Power spectrum of the measured *single-hit* residuals in the (2–6) keV (solid lines) and (6–14) keV (dotted lines) energy intervals calculated according to [8], including also—as usual in DAMA analyses—the treatment of the experimental errors and of the time binning. The data refer to DAMA/NaI and DAMA/LIBRA-phase1. As it can be seen, the principal mode present in the (2–6) keV energy interval corresponds to a frequency of $2.737 \times 10^{-3} \text{ d}^{-1}$ (vertical lines), corresponding to a period of ≈ 1 year. A similar peak is not present in the (6–14) keV energy interval.

addition, no background process able to mimic the DM annual modulation signature (that is able to simultaneously satisfy all the peculiarities of the signature and to account for the measured modulation amplitude) is available (see also discussions, for example, in [1–4, 7, 8, 49, 57–62]).

A further relevant investigation in the DAMA/LIBRA-phase1 data has been performed by applying the same hardware and software procedures, used to acquire and to analyse the *single-hit* residual rate, to the *multiple-hit* one. (A *multiple-hit* event is defined when more scintillating pulses arrive within a time window of about 600 ns.) In fact, since the probability that a DM particle interacts in more than one detector is negligible, a DM signal can be present just in the *single-hit* residual rate. Thus, the comparison of the results of the *single-hit* events with those of the *multiple-hit* ones corresponds practically to compare between them the cases of DM particles beam-on and beam-off. This procedure also allows an additional test of the background behaviour in the same energy interval where the positive effect is observed. In particular, in Figure 4, the residual rates of the *single-hit* events measured over the DAMA/LIBRA-phase1 annual cycles are reported, as collected in a single cycle, together with the residual rates of the *multiple-hit* events, in the (2–6) keV energy interval. While, as already observed, a clear modulation, satisfying all the peculiarities of the DM annual modulation signature, is present in the *single-hit* events, the fitted modulation amplitude for the *multiple-hit* residual rate is well compatible with zero: $-(0.0005 \pm 0.0004)$ cpd/kg/keV

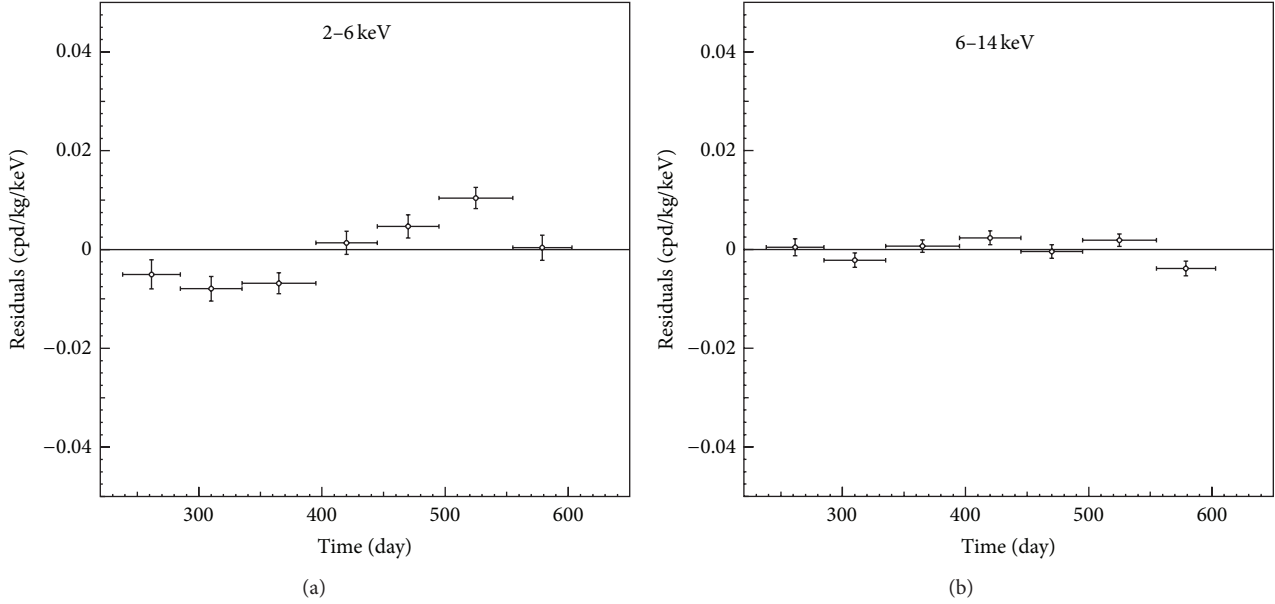


FIGURE 3: Experimental *single-hit* residuals in the (2–6) keV and in the (6–14) keV energy regions for the entire DAMA/LIBRA-phase1 data as if they were collected in a single annual cycle (i.e., binning in the variable time from the Jan 1st of each annual cycle). The data points present the experimental errors as vertical bars and the associated time bin width as horizontal bars. The initial time of the figures is taken at August 7th. A clear modulation satisfying all the peculiarities of the DM annual modulation signature is present in the lowest energy interval with $A = (0.0088 \pm 0.0013)$ cpd/kg/keV, while it is absent just above $A = (0.00032 \pm 0.00076)$ cpd/kg/keV.

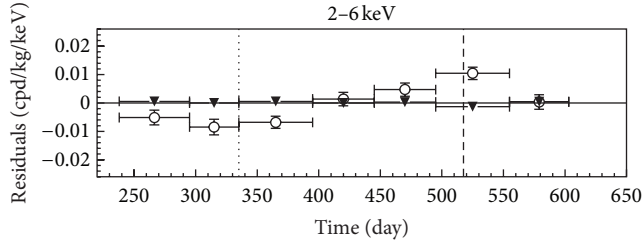


FIGURE 4: Experimental residual rates of DAMA/LIBRA-phase1 *single-hit* events (open circles), class of events to which DM events belong, and, for *multiple-hit* events (filled triangles), class of events to which DM events do not belong. They have been obtained by considering for each class of events the data as collected in a single annual cycle and by using in both cases the same identical hardware and the same identical software procedures. The initial time of the figure is taken on August 7th. The experimental points present the errors as vertical bars and the associated time bin width as horizontal bars. Analogous results were obtained for the DAMA/NaI data [24].

in the energy region (2–6) keV. Thus, again evidence of annual modulation with proper features as required by the DM annual modulation signature is present in the *single-hit* residuals (events class to which the DM particle induced events belong), while it is absent in the *multiple-hit* residual rate (event class to which only background events belong). Similar results were also obtained for the last two annual cycles of the DAMA/NaI experiment [24]. Since the same identical hardware and the same identical software procedures have been used to analyse the two classes of events, the obtained

result offers an additional strong support for the presence of a DM particle component in the galactic halo.

The annual modulation present at low energy can also be pointed out by depicting—as a function of the energy—the modulation amplitude, $S_{m,k}$, obtained by maximum likelihood method over the data considering $T = 1$ yr and $t_0 = 152.5$ day. For such purpose, the likelihood function of the *single-hit* experimental data in the k th energy bin is defined as $\mathbf{L}_k = \prod_{ij} e^{-\mu_{ijk}} (\mu_{ijk}^{N_{ijk}} / N_{ijk}!)$, where N_{ijk} is the number of events collected in the i th time interval (hereafter 1 day), by the j th detector and in the k th energy bin. N_{ijk} follows a Poisson's distribution with expectation value $\mu_{ijk} = [b_{jk} + S_{ik}]M_j\Delta t_i\Delta E\epsilon_{jk}$. The b_{jk} are the background contributions, M_j is the mass of the j th detector, Δt_i is the detector running time during the i th time interval, ΔE is the chosen energy bin, ϵ_{jk} is the overall efficiency (for details, see, e.g., [1]). Moreover, the signal can be written as $S_{ik} = S_{0,k} + S_{m,k} \cdot \cos \omega(t_i - t_0)$, where $S_{0,k}$ is the constant part of the signal and $S_{m,k}$ is the modulation amplitude. The usual procedure is to minimize the function $y_k = -2 \ln(\mathbf{L}_k) - \text{const}$ for each energy bin; the free parameters of the fit are the $(b_{jk} + S_{0,k})$ contributions and the $S_{m,k}$ parameter. Hereafter, the index k is omitted for simplicity.

In Figure 5, the obtained S_m are shown in each considered energy bin (there $\Delta E = 0.5$ keV) when the data of DAMA/NaI and DAMA/LIBRA-phase1 are considered. It can be inferred that positive signal is present in the (2–6) keV energy interval, while S_m values compatible with zero are present just above. In fact, the S_m values in the (6–20) keV energy interval have random fluctuations around zero with χ^2 equal to 35.8 for 28

TABLE 1: Best fit values for the (2–6) and (6–14) keV energy intervals (1σ errors) for S_m versus Z_m and Y_m versus t^* , considering the cumulative exposure of DAMA/NaI and DAMA/LIBRA-phase1. See also Figure 6.

E (keV)	S_m (cpd/kg/keV)	Z_m (cpd/kg/keV)	Y_m (cpd/kg/keV)	t^* (day)
2–6	(0.0106 ± 0.0012)	$-(0.0006 \pm 0.0012)$	(0.0107 ± 0.0012)	(149.5 ± 7.0)
6–14	(0.0001 ± 0.0007)	(0.0000 ± 0.0005)	(0.0001 ± 0.0008)	Undefined

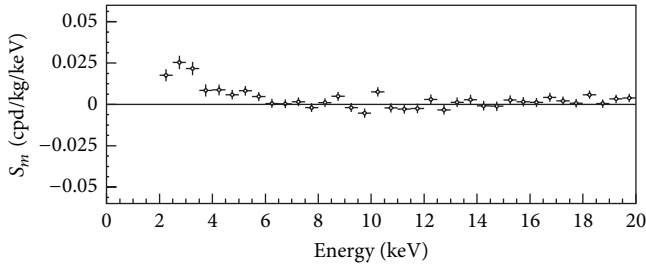


FIGURE 5: S_m variable as a function of the energy for the total cumulative exposure $1.33 \text{ ton} \times \text{yr}$. The energy bin is 0.5 keV . A clear modulation is present in the lowest energy region, while S_m values compatible with zero are present just above. In fact, the S_m values in the (6–20) keV energy interval have random fluctuations around zero with χ^2 equal to 35.8 for 28 degrees of freedom (upper tail probability of 15%).

degrees of freedom (upper tail probability of 15%). All this confirms the previous analyses.

As described in [2–4, 8], the observed annual modulation effect is well distributed in all the 25 detectors at 95% C.L.

Among further additional tests, the analysis of the modulation amplitudes as a function of the energy separately for the nine inner detectors and the remaining external ones has been carried out for the entire DAMA/LIBRA-phase1. The obtained values are fully in agreement; in fact, the hypothesis that the two sets of modulation amplitudes as a function of the energy belong to the same distribution has been verified by χ^2 test, obtaining $\chi^2/\text{d.o.f.} = 3.9/4$ and $8.9/8$ for the energy intervals (2–4) and (2–6) keV, respectively ($\Delta E = 0.5 \text{ keV}$). This shows that the effect is also well shared between inner and outer detectors.

Let us, finally, release the assumption of a phase $t_0 = 152.5$ day in the procedure to evaluate the modulation amplitudes. In this case, the signal can be written as

$$\begin{aligned} S_{ik} &= S_{0,k} + S_{m,k} \cos \omega(t_i - t_0) + Z_{m,k} \sin \omega(t_i - t_0) \\ &= S_{0,k} + Y_{m,k} \cos \omega(t_i - t^*). \end{aligned} \quad (1)$$

For signals induced by DM particles, one should expect the following: (i) $Z_{m,k} \sim 0$ (because of the orthogonality between the cosine and the sine functions); (ii) $S_{m,k} \simeq Y_{m,k}$; (iii) $t^* \simeq t_0 = 152.5$ day. In fact, these conditions hold for most of the dark halo models; however, as mentioned above, slight differences can be expected in case of possible contributions from nonthermalized DM components, such as, for example, the SagDEG stream [26, 50–54] and the caustics [55].

Considering cumulatively the data of DAMA/NaI and DAMA/LIBRA-phase1 (exposure $1.33 \text{ ton} \times \text{yr}$) the obtained

2σ contours in the plane (S_m, Z_m) for the (2–6) keV and (6–14) keV energy intervals are shown in Figure 6(a), while in Figure 6(b) the obtained 2σ contours in the plane (Y_m, t^*) are depicted. The best fit values for the (2–6) and (6–14) keV energy intervals (1σ errors) for S_m versus Z_m and Y_m versus t^* are reported in Table 1.

Finally, setting S_m in (1) to zero, the Z_m values as function of the energy have also been determined by using the same procedure. The values of Z_m as a function of the energy is reported in Figure 7; they are expected to be zero. The χ^2 test applied to the data supports the hypothesis that the Z_m values are simply fluctuating around zero; in fact, for example, in the (2–14) keV and (2–20) keV energy region the $\chi^2/\text{d.o.f.}$ are equal to 23.0/24 and 46.5/36 (probability of 52% and 11%), respectively.

The behaviour of the phase t^* variable as function of energy is shown in Figure 8 for the cumulative exposure of DAMA/NaI and DAMA/LIBRA-phase1 ($1.33 \text{ ton} \times \text{yr}$). No modulation is present above 6 keV and the phase is undetermined.

Sometimes naive statements were put forward as the fact that, in nature, several phenomena may show some kind of periodicity. It is worth noting that the point is whether they might mimic the annual modulation signature in DAMA/LIBRA (and former DAMA/NaI), that is, whether they might be not only quantitatively able to account for the observed modulation amplitude but also able to contemporaneously satisfy all the requirements of the DM annual modulation signature. The same is also for side reactions. This has already been deeply investigated in [1–4] and references therein; the arguments and the quantitative conclusions, presented there, also apply to the entire DAMA/LIBRA-phase1 data. Additional arguments can be found in [7, 8, 49, 57–62].

Firstly, in order to continuously monitor the running conditions, several pieces of information are acquired with the production data and quantitatively analysed. In particular, all the time behaviour of the running parameters, acquired with the production data, have been investigated. Table 2 shows the modulation amplitudes obtained for each annual cycle when fitting the time behaviour of the values of the main parameters including a cosine modulation with the same phase and period as for DM particles. As can be seen, all the measured amplitudes are well compatible with zero.

No modulation has been found in any possible source of systematics or side reactions; thus, cautious upper limits (90% C.L.) on possible contributions to the DAMA/LIBRA measured modulation amplitude are summarized in Table 3 (also see [2–4]). It is worth noting that they do not quantitatively account for the measured modulation amplitudes and also are

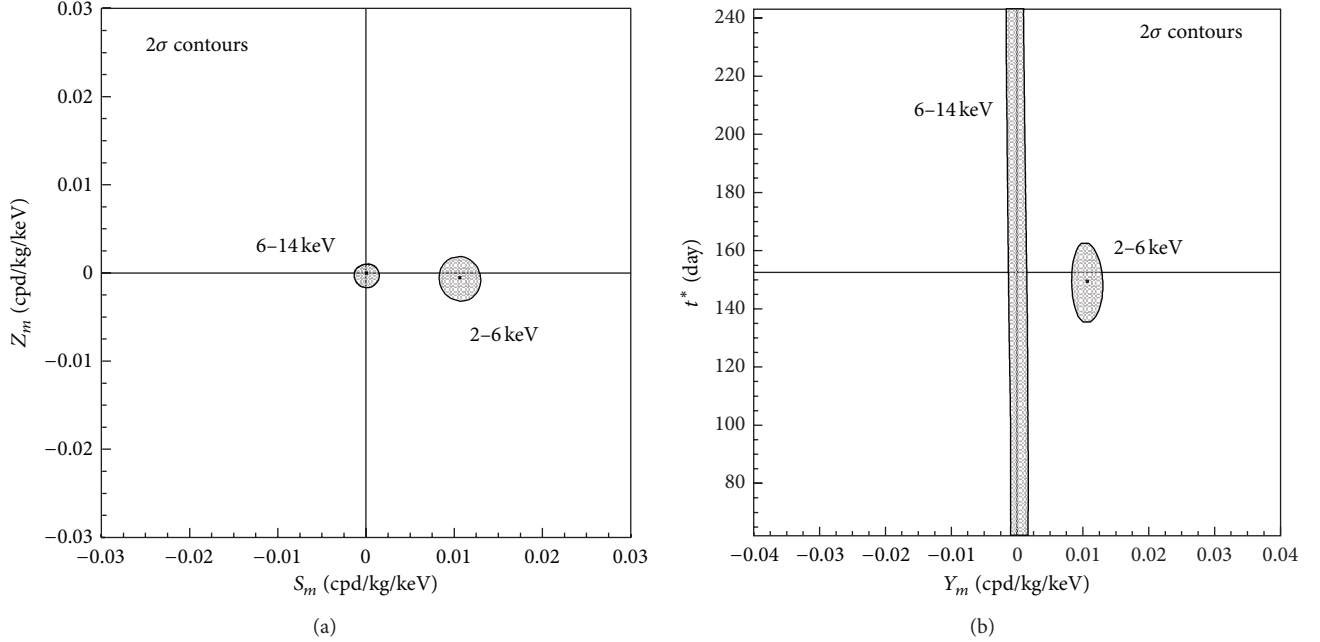


FIGURE 6: 2σ contours in the plane (S_m, Z_m) (a) and in the plane (Y_m, t^*) (b) for the (2–6) keV and (6–14) keV energy intervals. The contours have been obtained by the maximum likelihood method, considering the cumulative exposure of DAMA/NaI and DAMA/LIBRA-phase1. A modulation amplitude is present in the lower energy intervals and the phase agrees with that expected for DM induced signals. See text.

TABLE 2: Modulation amplitudes (1σ error) obtained by fitting the time behaviours of the main running parameters including a possible annual modulation with phase and period as for DM particles. These running parameters, acquired with the production data are (i) the operating temperature of the detectors; (ii) the HP Nitrogen flux in the inner Cu box housing the detectors; (iii) the pressure of the HP Nitrogen atmosphere of the inner Cu box housing the detectors; (iv) the environmental Radon in the inner part of the barrack from which the detectors are, however, excluded; (v) the hardware rate above single photoelectron threshold. All the measured amplitudes are compatible with zero.

	DAMA/LIBRA-1	DAMA/LIBRA-2	DAMA/LIBRA-3	DAMA/LIBRA-4
Temperature ($^{\circ}\text{C}$)	$-(0.0001 \pm 0.0061)$	(0.0026 ± 0.0086)	(0.001 ± 0.015)	(0.0004 ± 0.0047)
Flux (L/h)	(0.13 ± 0.22)	(0.10 ± 0.25)	$-(0.07 \pm 0.18)$	$-(0.05 \pm 0.24)$
Pressure (10^{-3} mbar)	(15 ± 30)	$-(13 \pm 25)$	(22 ± 27)	(1.8 ± 7.4)
Radon (Bq/m^3)	$-(0.029 \pm 0.029)$	$-(0.030 \pm 0.027)$	(0.015 ± 0.029)	$-(0.052 \pm 0.039)$
Hardware rate (10^{-2} Hz)	$-(0.20 \pm 0.18)$	(0.09 ± 0.17)	$-(0.03 \pm 0.20)$	(0.15 ± 0.15)
	DAMA/LIBRA-5	DAMA/LIBRA-6	DAMA/LIBRA-7	
Temperature ($^{\circ}\text{C}$)	(0.0001 ± 0.0036)	(0.0007 ± 0.0059)	(0.0000 ± 0.0054)	
Flux (L/h)	$-(0.01 \pm 0.21)$	$-(0.01 \pm 0.15)$	$-(0.00 \pm 0.14)$	
Pressure (10^{-3} mbar)	$-(0.8 \pm 1.2)$	(0.7 ± 1.3)	$-(2.6 \pm 5.5)$	
Radon (Bq/m^3)	(0.021 ± 0.037)	$-(0.028 \pm 0.036)$	(0.012 ± 0.047)	
Hardware rate (10^{-2} Hz)	(0.03 ± 0.14)	(0.08 ± 0.11)	(0.06 ± 0.10)	

not able to simultaneously satisfy all the many requirements of the signature. Similar analyses have also been done for the seven annual cycles of DAMA/NaI [23, 24].

In conclusion, the model-independent DAMA results give evidence (at 9.3σ C.L. over 14 independent annual cycles) for the presence of DM particles in the galactic halo.

In order to perform corollary investigation on the nature of the DM particles, model-dependent analyses are necessary; thus, many theoretical and experimental parameters and models are possible and many hypotheses must also be exploited.

In particular, the obtained DAMA model independent evidence is compatible with a wide set of scenarios regarding the nature of the DM candidate and related astrophysical, nuclear, and particle Physics. For example, some given scenarios and parameters are discussed in [2, 8, 13–20, 22, 23, 26]. Further large literature is available on the topics (see e.g., in [8]). Moreover, both the negative results and all the possible positive hints, achieved so far in the field, are largely compatible with the DAMA model-independent DM annual modulation results in many scenarios considering also the existing experimental and theoretical uncertainties; the same

TABLE 3: Summary of the results obtained by investigating possible sources of systematics or side processes [1–4, 7, 8, 49, 57–62]. None able to give a modulation amplitude different from zero has been found; thus, cautious upper limits (90% C.L.) on the possible contributions to the measured modulation amplitude have been calculated and are shown here for DAMA/LIBRA-phase1 as done before for the seven annual cycles of DAMA/NaI [23, 24].

Source	Main comment	Cautious upper limit (90% C.L.)
Radon	Sealed Cu Box in HP Nitrogen atmosphere, 3 levels of sealing	$<2.5 \times 10^{-6}$ cpd/kg/keV
Temperature	Air conditioning + huge heat capacity	$<10^{-4}$ cpd/kg/keV
Noise	Efficient rejection	$<10^{-4}$ cpd/kg/keV
Energy scale	Routine + intrinsic calibrations	$<1 - 2 \times 10^{-4}$ cpd/kg/keV
Efficiencies	Regularly measured	$<10^{-4}$ cpd/kg/keV
Background	No modulation above 6 keV; no modulation in the (2–6) keV <i>multiple-hit</i> events; this limit includes all possible sources of background	$<10^{-4}$ cpd/kg/keV
Side reactions	From muon flux variation measured by MACRO	$<3 \times 10^{-5}$ cpd/kg/keV
In addition: no effect can mimic the signature		

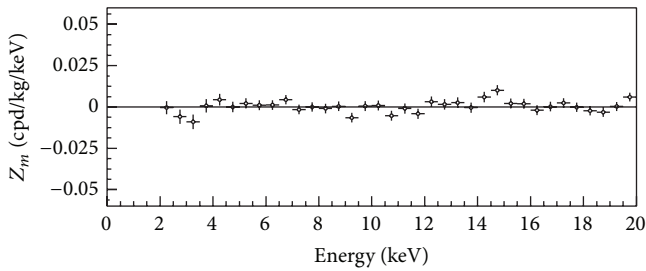


FIGURE 7: Z_m variable as a function of the energy for the cumulative exposure of DAMA/NaI and DAMA/LIBRA-phase1, once setting S_m in (1) to zero. The energy bin is 0.5 keV. The Z_m values are expected to be zero. The χ^2 test applied to the data supports the hypothesis that the Z_m values are simply fluctuating around zero. See text.

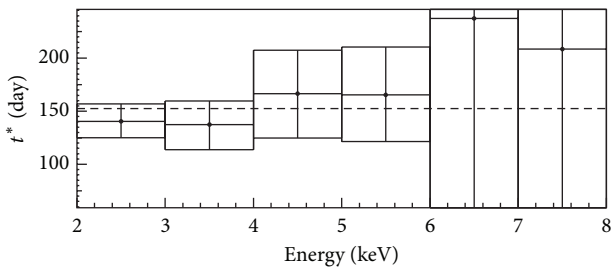


FIGURE 8: Phase t^* as a function of the energy for the total exposure; here, the errors are at 2σ . The vertical scale spans over \pm a quarter of period around 2 June; other intervals are replica of it. An annual modulation effect is present in the lower energy intervals up to 6 keV and the phase agrees with that expected for DM induced signals. No modulation is present above 6 keV and thus the phase is undetermined. See text.

holds for indirect approaches; see, for example, arguments in [8] and references therein. As an example in Figure 9, there are allowed regions shown for DM candidates interacting by elastic scattering on target-nuclei with spin-independent coupling, including also some of the existing uncertainties [5].

3. DAMA/LIBRA-Phase2 and Perspectives

A first upgrade of the DAMA/LIBRA setup was performed in September 2008. One detector was recovered by replacing a broken PMT and a new optimization of some PMTs and HVs was done; the transient digitizers were replaced with new ones (the U1063A Acqiris 8-bit IGS/s DC270 High-Speed cPCI Digitizers) having better performances and a new DAQ with optical readout was installed. The DAMA/LIBRA-phase1 concluded its data taking in this configuration on 2010.

A further and more important upgrade has been performed at the end of 2010 when all the PMTs have been replaced with new ones having higher quantum efficiency (Q.E.), realized with a special dedicated development by HAMAMATSU Co. Details on the developments and on the reached performances in the operative conditions are reported in [6]. Just as example, Figure 10 shows the values of the Q.E. of the new 50 HAMAMATSU PMTs installed in DAMA/LIBRA both at peak and at the λ of the NaI(Tl) scintillation light. We remind the reader that up to October 2010 low background PMTs, developed by EMI-Electron Tubes with dedicated R&D, were used (Q.E. \approx 30% at $\lambda = 380$ nm [1, 6, 21]); the light yield and other response features already allowed a software energy threshold of 2 keV in the data analysis. The feasibility to decrease the software energy threshold below 2 keV in the new configuration has been demonstrated [6].

Since the fulfillment of this upgrade, the DAMA/LIBRA-phase2 is continuously running in order (1) to increase the experimental sensitivity lowering the software energy threshold of the experiment, (2) to improve the corollary investigation on the nature of the DM particle and related astrophysical, nuclear, and particle physics arguments, and (3) to investigate other signal features. This requires long and heavy full time dedicated work for reliable collection and analysis of very large exposures.

Another upgrade at the end of 2012 was successfully concluded: new-concept preamplifiers were installed, with suitable operative and electronic features; in particular, they allow the direct connection of the signal to the relative channel of the Transient Digitizer (TD).

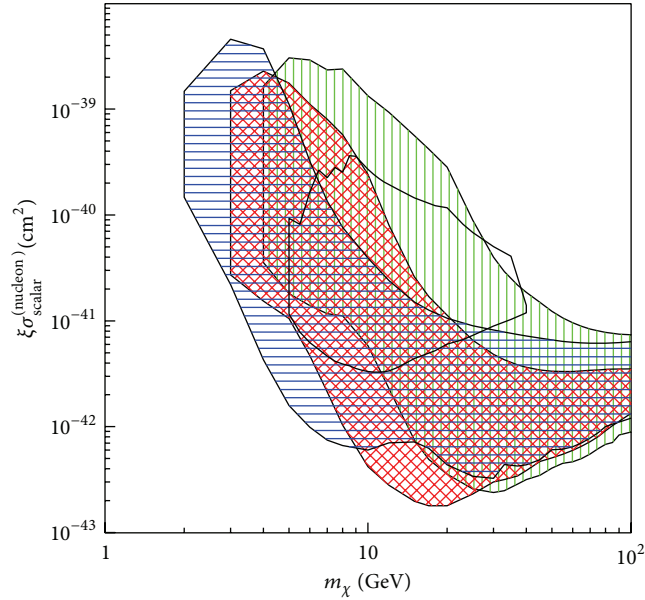


FIGURE 9: Regions in the nucleon cross section versus DM particle mass plane allowed by DAMA for a DM candidate interacting via spin-independent elastic scattering on target-nucleus; three different instances for the Na and I quenching factors have been considered: (i) without including the channeling effect [(green) vertically hatched region], (ii) by including the channeling effect [(blue) horizontally hatched region], and (iii) without the channeling effect considering energy dependence of Na and I quenching factors [5] [(red) crosshatched region]. The velocity distributions and the same uncertainties as in [23, 24] are considered here. These regions represent the domain where the likelihood-function values differ more than 7.5σ from the null hypothesis (absence of modulation). The allowed region obtained for the CoGeNT experiment, including the same astrophysical models as in [23, 24] and assuming for simplicity a fixed value for the Ge quenching factor and a Helm form factor with fixed parameters, is also reported by a (black) thick solid line. This region includes configurations whose likelihood-function values differ more than 1.64σ from the null hypothesis (absence of modulation). For details, see [5].

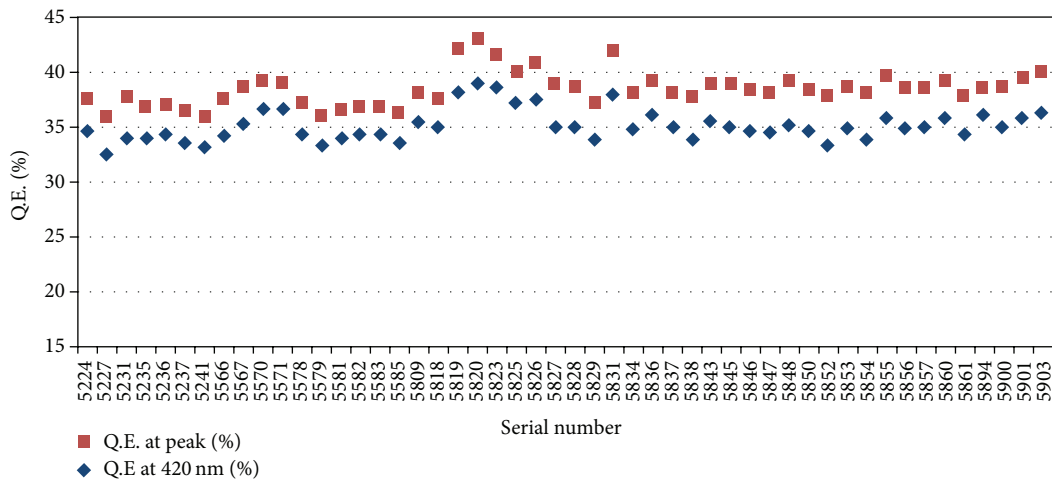


FIGURE 10: Q.E. at peak and at 420 nm of each one of the 50 high Q.E. PMTs, installed in DAMA/LIBRA-phase2. The averages (RMS) are 38.5% (1.6%) and 35.1% (1.4%), respectively; the RMS show that the Q.E. spread in the PMTs production is well limited.

Moreover, further improvements are planned. In particular, new trigger modules have been prepared and ready to be installed.

In the future, DAMA/LIBRA will also continue its study on several other rare processes [9–11] as also the former DAMA/NaI apparatus did [31–40].

Finally, further improvements to increase the sensitivity of the setup can be considered; in particular, the use of high

Q.E. and ultra-low background PMTs directly coupled to the NaI(Tl) crystals is an interesting possibility. (However, this would require the disassembling of the detectors since the light guides act at present also as optical windows.) This possible configuration can allow a further large improvement in the light collection and a further lowering of the software energy threshold. Moreover, efforts towards a possible highly radiopure NaI(Tl) “general purpose” experiment

(DAMA/1ton) having full sensitive mass of 1 ton (we already proposed in 1996 as a general purpose setup) have been continued in various aspects.

4. Conclusions

The data of DAMA/LIBRA-phase1 have further confirmed a peculiar annual modulation of the *single-hit* events in the (2–6) keV energy region satisfying all the many requirements of the DM annual modulation signature; the cumulative exposure by the former DAMA/NaI and DAMA/LIBRA-phase1 is $1.33 \text{ ton} \times \text{yr}$.

In fact, as required by the DM annual modulation signature: (1) the *single-hit* events show a clear cosine-like modulation as expected for the DM signal; (2) the measured period is equal to $(0.998 \pm 0.002) \text{ yr}$ well compatible with the 1 yr period as expected for the DM signal; (3) the measured phase, $(144 \pm 7) \text{ days}$, is compatible with $\approx 152.5 \text{ days}$ as expected for the DM signal; (4) the modulation is present only in the low energy (2–6) keV interval and not in other higher energy regions, consistently with expectation for the DM signal; (5) the modulation is present only in the *single-hit* events, while it is absent in the *multiple-hit* ones as expected for the DM signal; (6) the measured modulation amplitude in NaI(Tl) of the *single-hit* events in the (2–6) keV energy interval is $(0.0112 \pm 0.0012) \text{ cpd/kg/keV}$ ($9.3\sigma \text{ C.L.}$). No systematic or side processes able to simultaneously satisfy all the many peculiarities of the signature and to account for the whole measured modulation amplitude are available.

DAMA/LIBRA is continuously running in its new configuration (named DAMA/LIBRA-phase2) with a lower software energy threshold aiming to improve the knowledge on corollary aspects regarding the signal and on second order effects as discussed, for example, in [8].

Conflict of Interests

The authors declare that there is no conflict of interests regarding the publication of this paper.

References

- [1] R. Bernabei, P. Belli, A. Bussolotti et al., “The DAMA/LIBRA apparatus,” *Nuclear Instruments and Methods in Physics Research A*, vol. 592, no. 3, pp. 297–315, 2008.
- [2] R. Bernabei, P. Belli, F. Cappella et al., “First results from DAMA/LIBRA and the combined results with DAMA/NaI,” *The European Physical Journal C*, vol. 56, no. 3, pp. 333–355, 2008.
- [3] R. Bernabei, P. Belli, F. Cappella et al., “New results from DAMA/LIBRA,” *The European Physical Journal C*, vol. 67, no. 1-2, pp. 39–49, 2010.
- [4] R. Bernabei, P. Belli, F. Cappella et al., “Final model independent result of DAMA/LIBRA-phase1,” *The European Physical Journal C*, vol. 73, article 2648, 2013.
- [5] P. Belli, R. Bernabei, A. Bottino et al., “Observations of annual modulation in direct detection of relic particles and light neutralinos,” *Physical Review D*, vol. 84, no. 5, Article ID 055014, 2011.
- [6] R. Bernabei, P. Belli, A. Bussolotti et al., “Performances of the new high quantum efficiency PMTs in DAMA/LIBRA,” *Journal of Instrumentation*, vol. 7, no. 3, Article ID P03009, 2012.
- [7] R. Bernabei, P. Belli, F. Cappella et al., “No role for muons in the DAMA annual modulation results,” *The European Physical Journal C*, vol. 72, article 2064, 2012.
- [8] R. Bernabei, P. Belli, S. d’Angelo et al., “Dark matter investigation by DAMA at Gran Sasso,” *International Journal of Modern Physics A*, vol. 28, no. 16, Article ID 1330022, 2013.
- [9] R. Bernabei, P. Belli, F. Cappella et al., “New search for processes violating the Pauli exclusion principle in sodium and in iodine,” *The European Physical Journal C*, vol. 62, no. 2, pp. 327–332, 2009.
- [10] R. Bernabei, P. Belli, F. Cappella et al., “Search for charge non-conserving processes in ^{127}I by coincidence technique,” *The European Physical Journal C*, vol. 72, article 1920, 2012.
- [11] R. Bernabei, P. Belli, F. Cappella et al., “New search for correlated e^+e^- pairs in the α decay of ^{241}Am ,” *The European Physical Journal A*, vol. 49, article 64, 2013.
- [12] P. Belli, R. Bernabei, C. Bacci, A. Incicchitti, R. Marcovaldi, and D. Prospero, DAMA proposal to INFN Scientific Committee II, 1990.
- [13] R. Bernabei, P. Belli, V. Landoni et al., “New limits on WIMP search with large-mass low-radioactivity NaI(Tl) set-up at Gran Sasso,” *Physics Letters B*, vol. 389, no. 4, pp. 757–766, 1996.
- [14] R. Bernabei, P. Belli, F. Montecchia et al., “Searching for WIMPs by the annual modulation signature,” *Physics Letters B*, vol. 424, no. 1-2, pp. 195–201, 1998.
- [15] R. Bernabei, P. Belli, F. Montecchia et al., “On a further search for a yearly modulation of the rate in particle dark matter direct search,” *Physics Letters B*, vol. 450, no. 4, pp. 448–455, 1999.
- [16] P. Belli, R. Bernabei, C. J. Dai et al., “Quest for electron decay $e^- \rightarrow \nu_e \gamma$ with a liquid xenon scintillator,” *Physical Review D*, vol. 61, no. 11, Article ID 117301, 2000.
- [17] R. Bernabei, P. Belli, R. Cerulli et al., “Search for WIMP annual modulation signature: results from DAMA/NaI-3 and DAMA/NaI-4 and the global combined analysis,” *Physics Letters B*, vol. 480, no. 1-2, pp. 23–31, 2000.
- [18] R. Bernabei, M. Amato, P. Belli et al., “Investigating the DAMA annual modulation data in a mixed coupling framework,” *Physics Letters B*, vol. 509, no. 3-4, pp. 197–203, 2001.
- [19] R. Bernabei, P. Belli, R. Cerulli et al., “Investigating the DAMA annual modulation data in the framework of inelastic dark matter,” *The European Physical Journal C*, vol. 23, no. 1, pp. 61–64, 2002.
- [20] P. Belli, R. Cerulli, N. Fornengo, and S. Scopel, “Effect of the galactic halo modeling on the DAMA-NaI annual modulation result: an extended analysis of the data for weakly interacting massive particles with a purely spin-independent coupling,” *Physical Review D*, vol. 66, no. 4, Article ID 043503, 2002.
- [21] R. Bernabei, P. Belli, F. Montecchia et al., “Performances of the $\approx 100 \text{ kg}$ NaI(Tl) set-up of the DAMA experiment at Gran Sasso,” *Il Nuovo Cimento A*, vol. 112, no. 6, pp. 545–575, 1999.
- [22] R. Bernabei, P. Belli, R. Cerulli et al., “On the investigation of possible systematics in WIMP annual modulation search,” *The European Physical Journal C*, vol. 18, no. 2, pp. 283–292, 2000.
- [23] R. Bernabei, P. Belli, F. Cappella et al., “Dark matter search,” *Rivista del Nuovo Cimento*, vol. 26, no. 1, pp. 1–73, 2003.
- [24] R. Bernabei, P. Belli, F. Cappella et al., “Dark matter particles in the galactic halo: results and implications from DAMA/NaI,” *International Journal of Modern Physics D*, vol. 13, no. 10, pp. 2127–2159, 2004.

- [25] R. Bernabei, P. Belli, F. Montecchia et al., “Investigating pseudoscalar and scalar dark matter,” *International Journal of Modern Physics A*, vol. 21, no. 7, pp. 1445–1469, 2006.
- [26] R. Bernabei, P. Belli, F. Montecchia et al., “Investigating halo substructures with annual modulation signature,” *The European Physical Journal C*, vol. 47, no. 1, pp. 263–271, 2006.
- [27] R. Bernabei, P. Belli, F. Montecchia et al., “On electromagnetic contributions in WIMP quests,” *International Journal of Modern Physics A*, vol. 22, no. 19, pp. 3155–3168, 2007.
- [28] R. Bernabei, P. Belli, F. Montecchia et al., “Possible implications of the channeling effect in NaI(Tl) crystals,” *The European Physical Journal C*, vol. 53, no. 2, pp. 205–213, 2008.
- [29] R. Bernabei, P. Belli, F. Montecchia et al., “Investigating electron interacting dark matter,” *Physical Review D*, vol. 77, Article ID 023506, 2008.
- [30] R. Bernabei, P. Belli, F. Cappella et al., “Investigation on light dark matter,” *Modern Physics Letters A*, vol. 23, no. 26, pp. 2125–2140, 2008.
- [31] R. Bernabei, P. Belli, F. Montecchia et al., “Search for non-paulian transitions in ^{23}Na and ^{127}I ,” *Physics Letters B*, vol. 408, no. 1–4, pp. 439–444, 1997.
- [32] P. Belli, R. Bernabei, C. J. Dai et al., “New experimental limit on the electron stability and non-paulian transitions in Iodine atoms,” *Physics Letters B*, vol. 460, no. 1–2, pp. 236–241, 1999.
- [33] R. Bernabei, P. Belli, R. Cerulli et al., “Extended limits on neutral strongly interacting massive particles and nuclearites from NaI(Tl) scintillators,” *Physical Review Letters*, vol. 83, no. 24, pp. 4918–4921, 1999.
- [34] P. Belli, R. Bernabei, C. J. Dai et al., “New limits on the nuclear levels excitation of ^{127}I and ^{23}Na during charge nonconservation,” *Physical Review C*, vol. 60, no. 6, Article ID 065501, 1999.
- [35] R. Bernabei, P. Belli, R. Cerulli et al., “Investigation on possible diurnal effects induced by dark matter particles,” *Il Nuovo Cimento A*, vol. 112, pp. 1541–1552, 1999.
- [36] R. Bernabei, P. Belli, R. Cerulli et al., “Search for solar axions by Primakoff effect in NaI crystals,” *Physics Letters B*, vol. 515, no. 1–2, pp. 6–12, 2001.
- [37] F. Cappella et al., *The European Physical Journal C*, vol. 14, p. 1, 2002.
- [38] R. Bernabei, P. Belli, F. Cappella et al., “Search for spontaneous transition of nuclei to a superdense state,” *The European Physical Journal A*, vol. 23, no. 1, pp. 7–10, 2005.
- [39] R. Bernabei, P. Belli, F. Cappella et al., “A search for spontaneous emission of heavy clusters in the 127I nuclide,” *The European Physical Journal A*, vol. 24, no. 1, pp. 51–56, 2005.
- [40] R. Bernabei, P. Belli, W. Di Nicolantonio et al., “A multiton low activity NaI(Tl) detector for underground physics,” *Astroparticle Physics*, vol. 4, no. 1, pp. 45–54, 1995.
- [41] R. Bernabei, *The Identification of Dark Matter*, World Scientific, Singapore, 1997.
- [42] K. A. Drukier, K. Freese, and D. N. Spergel, “Detecting cold dark-matter candidates,” *Physical Review D*, vol. 33, p. 3495, 1986.
- [43] K. Freese, J. Frieman, and A. Gould, “Signal modulation in cold-dark-matter detection,” *Physical Review D*, vol. 37, no. 12, pp. 3388–3405, 1988.
- [44] D. Smith and N. Weiner, “Inelastic dark matter,” *Physical Review D*, vol. 64, Article ID 043502, 2001.
- [45] D. Tucker-Smith and N. Weiner, “Status of inelastic dark matter,” *Physical Review D*, vol. 72, Article ID 063509, 2005.
- [46] D. P. Finkbeiner, T. Lin, and N. Weiner, “Inelastic dark matter and DAMA/LIBRA: an experimentum crucis,” *Physical Review D*, vol. 80, Article ID 115008, 2009.
- [47] K. Freese, P. Gondolo, and H. J. Newberg, “Detectability of weakly interacting massive particles in the Sagittarius dwarf tidal stream,” *Physical Review D*, vol. 71, Article ID 043516, 2005.
- [48] K. Freese, P. Gondolo, H. J. Newberg, and M. Lewis, “Effects of the Sagittarius dwarf tidal stream on dark matter detectors,” *Physical Review Letters*, vol. 92, no. 11, Article ID 11301, 2004.
- [49] R. Bernabei, P. Belli, F. Cappella et al., “Technical aspects and dark matter searches,” *Journal of Physics: Conference Series*, vol. 203, no. 1, Article ID 012040, 2010.
- [50] K. Freese, P. Gondolo, and H. J. Newberg, “Detectability of weakly interacting massive particles in the Sagittarius dwarf tidal stream,” *Physical Review D*, vol. 71, Article ID 043516, 2005.
- [51] P. Gondolo, K. Freese, H. J. Newberg, and M. Lewis, “A dark matter stream through the solar neighborhood,” *New Astronomy Reviews*, vol. 49, no. 2–6, pp. 193–197, 2005.
- [52] K. Freese, P. Gondolo, H. J. Newberg, and M. Lewis, “The effects of the Sagittarius dwarf tidal stream on dark matter detectors,” *Physical Review Letters*, vol. 92, Article ID 111301, 2004.
- [53] K. Freese, P. Gondolo, and H. J. Newberg, “Detectability of weakly interacting massive particles in the Sagittarius dwarf tidal stream,” *Physical Review D*, vol. 71, Article ID 043516, 2005.
- [54] G. Gelmini and P. Gondolo, “Weakly interacting massive particle annual modulation with opposite phase in late-infall halo models,” *Physical Review D*, vol. 64, Article ID 023504, 2001.
- [55] F. S. Ling, P. Sikivie, and S. Wick, “Diurnal and annual modulation of cold dark matter signals,” *Physical Review D*, vol. 70, no. 12, Article ID 123503, 2004.
- [56] J. Beringer, J.-F. Arguin, R. M. Barnett et al., “Review of particle physics,” *Physical Review D*, vol. 86, Article ID 010001, 2012.
- [57] R. Bernabei, P. Belli, F. Cappella et al., “Particle dark matter and DAMA/LIBRA,” *AIP Conference Proceedings*, vol. 1223, p. 50, 2010.
- [58] R. Bernabei, P. Belli, F. Cappella et al., “Particle dark matter in DAMA/LIBRA,” in *Proceedings of the Frontier Objects in Astrophysics and Particle Physics*, p. 157, Vulcano, Italy, May 2010, <http://arxiv.org/abs/1007.0595>.
- [59] R. Bernabei, P. Belli, F. Montecchia et al., “Particle dark matter in the galactic halo: recent results from DAMA/LIBRA,” *Canadian Journal of Physics*, vol. 89, no. 1, pp. 141–152, 2011.
- [60] R. Bernabei, P. Belli, A. Di Marco et al., “DAMA/LIBRA at Gran Sasso,” *Physics Procedia*, vol. 37, pp. 1095–1104, 2012.
- [61] R. Bernabei, P. Belli, F. Cappella et al., “Comment on ‘on an unverified nuclear decay and its role in the DAMA experiment,’” <http://arxiv.org/abs/1210.6199>.
- [62] R. Bernabei, P. Belli, F. Cappella et al., “A few final comments to arXiv: 1210.7548 [hep-ph],” <http://arxiv.org/abs/1211.6346>.

Review Article

Searches for Dark Matter with Superheated Liquid Techniques

A. Pullia

Department of Physics and I.N.F.N., University of Milano-Bicocca, Piazza della Scienza 3, 20135 Milano, Italy

Correspondence should be addressed to A. Pullia; antonino.pullia@mib.infn.it

Received 5 March 2014; Accepted 25 April 2014; Published 12 June 2014

Academic Editor: Anselmo Mereaglia

Copyright © 2014 A. Pullia. This is an open access article distributed under the Creative Commons Attribution License, which permits unrestricted use, distribution, and reproduction in any medium, provided the original work is properly cited. The publication of this article was funded by SCOAP³.

This is a short review of the detectors based on the superheated liquid techniques, including continuously sensitive bubble chambers, superheated droplet detectors (SDD) and Geysers.

1. Introduction

One of the most celebrated detectors operating at accelerators is the bubble chamber [1]; very important discoveries were done employing this technology during the sixties and seventies.

Bubble chambers were divided into two categories (hydrogen and heavy liquid bubble chambers); the former ones (like the “80 cm,” BEBC, 15-foot Flab, Argonne 30 inches, etc.) had the advantage that the target was well defined and static; the latter ones (Gargamelle, BP3, 15-foot Bubble Chamber, SKAT, etc.) had a bigger stopping power and were particularly suited to identify the nature of the secondary produced particles like electrons, gamma rays, and pions and kaons decays. Many discoveries were done by bubble chambers: several resonances, the neutral currents, leptonic and semileptonic, the Ω^- , and so forth.

Their use decreased with the birth of the “electronic detectors” capable of performing automatic event selection and scanning and collecting and analysing much more events.

However the expansion of the bubble chamber was linked to the beam passage: the switching off of the acceleration of the primary particles was used to command it.

So the bubble chambers were commanded by the beam passage and the used liquid reached a metastable equilibrium state which occurs when the pressure of the liquid was lowered adiabatically: the substance remains in the liquid state despite the vapor pressure or the boiling point temperature.

The metastability of the liquid makes it possible to detect charged particles. When the liquid is brought to

a temperature and pressure, where, according to its phase diagram, it should be gaseous but maintains the liquid phase, it is said to be “superheated.” The difference in pressure between the vapor pressure and the operating pressure of a bubble chamber is known as “degree of superheat.”

The higher this degree is, the less stable the liquid is, but at high degree of superheat the bubble chamber becomes more sensitive to lower energy particles that can interact with the nuclei giving lower energy recoils and becomes sensitive to electrons, γ rays, high energy muons, and so forth.

These particles are an important background for the search of dark matter, so, in order to exploit superheated detectors for direct detection of dark matter, the operation technique had to be changed [2–4].

2. Bubble Nucleation in Superheated Liquids

The phenomena describing the formation of a bubble in a superheated liquid are the nucleation and the growing of the bubble.

The nucleation and the growing are described by the theory of Seitz [5–7] which is briefly summarized in the following.

A charged particle loses energy along its trajectory through a superheated liquid via ionization, collision, and radiation.

Thus the primary particle leads to a temporary thermal excitation along its track; the temperature of the gas created is hotter than that of the surrounding liquid. The Seitz model is named as “hot spike” model of bubble nucleation.

If the pressure of the hot gas is sufficient, a protobubble will overcome the surface tension and the bubble grows. Its growth is due to its internal pressure which is the vapor pressure of the liquid at the current temperature P_v (this pressure is greater than the pressure outside the bubble P_e by definition of superheated liquid); in this case the bubble becomes visible. To reach this condition the radius of the protobubble must be as follows:

$r_c > (2\lambda)/(\Delta P)$, where $\Delta P = P_v - P_e$ and λ is the surface tension of the liquid. Furthermore the stopping power must be $dE/dx > E_c/(2r_c)$, where

$$E_c = 4\pi r_c^2 \left(\lambda - \frac{Td\lambda}{dT} \right) + \left(\frac{4\pi r_c^3}{3} \right) \left(\left(\frac{\rho_v h_{fg}}{M} \right) - \Delta P \right), \quad (1)$$

ρ_v is the saturated vapor density, h_{fg} is the latent heat of vaporization per mole, and M is the molecular mass [8].

If $E < E_c$ and the relation $dE/dx > E_c/(2r_c)$ is not fulfilled, $r < r_c$ and then the protobubble created is smaller than the critical radius; it will collapse and disappear.

3. Application of Superheated Devices to WIMP Searches

To be useful as dark matter detectors the bubble formation devices needed several changes to fulfil three important constraints:

- (i) to be more stable than traditional high energy physics bubble chamber (reaching a quasicontinuously sensitive operation);
- (ii) to be triggered when a dark matter particle crosses the detector and interacts with it;
- (iii) to have a strong rejection of the principal backgrounds that can simulate a dark matter interaction with the ordinary matter. The rarity of the interactions also changes the nature of the bubble devices from that of a tracking device (full of multiple tracks of small bubbles from different particle crossing the detector) to a counting device.

This different way to use a bubble detector as a counting detector brought the interested physicists in three directions:

- (1) new type of bubble chambers;
- (2) SDD which are superheated droplet detectors;
- (3) the Geyser detectors.

In this paper I concentrate on the three directions mentioned above and I summarize the most relevant results and the proposals for the future.

In the following, I will focus on weakly interacting massive particle (WIMP) as the most plausible candidate for dark matter.

WIMPs interact not only with gravitational fields but also weakly; in this case indeed the search of their direct

interaction is not without hope. Many experimental methods have been studied and realized to detect directly WIMPs. They include the use of scintillators NaI [9], liquid argon [10], xenon chamber [11], cryogenic semiconductors [12], and detectors based on the nucleation of bubbles [2–4]. The results obtained with these detectors are in some case in contradiction and need a supplement of work to make clear the situation; the development of alternative and complementary techniques is thus particularly motivated.

4. Bubble Chamber

The experiments with bubble chambers are concentrated on the work of the Collaboration COUPP (Chicagoland Observatory for Underground Particle Physics).

4.1. 2 kg Chamber (1L) Filled with CF₃I (Experiment T945). The first dark matter limits SD [13, 14] produced by COUPP was achieved with a 2 kg (1L) prototype which produced the best spin-dependent (SD) proton limits at the time over a significant mass range. This chamber was built at the University of Chicago and tested at the Laboratory for Astrophysics and Space Research (LASR) at a depth of six m.w.e.; the results are reported in Figure 1.

4.2. Modified 2 kg Chamber (1L). Due to the very high background from Radon filtering an O-ring, the first version of the chamber was modified: substitution of the O-ring and replacement of the quartz jar with a new, acid-etched, and precision cleaned jar; data were taken in NUMI (NeUtrinos at Main Injector) at Fermilab.

4.3. 4 kg Chamber (2L) (Figure 2 and [13, 14]). This chamber worked in two phases which are

- (a) filled with CF₃I;
- (b) filled with C₃F₈;

phase (a): the preliminary results are reported in the talk of Ardid at Trieste [15, 16] (see Figure 3).

phase (b): 4 kg filled with C₃F₈.

Excellent sensitivity was obtained for low energy recoils (3 keV) at SNOLAB [15, 16], but this phase is in progress and no definitive results were reported up to now.

4.4. The Big Bubble Chamber (30 L = 60 kg) [17]. This chamber is working in SNOLAB filled at the moment with 37 kg of CF₃I; the installation was completed in June 2013; a run collecting 50000 kg-days data is foreseen in the future, with a possible increase of the detector's mass.

No results have been yet reported for the moment; the sensitivity of this chamber is shown in Figure 4.

4.5. Proposal for a 500 kg Bubble Chamber. For the future the collaboration PICO (which joints the expertise of COUPP

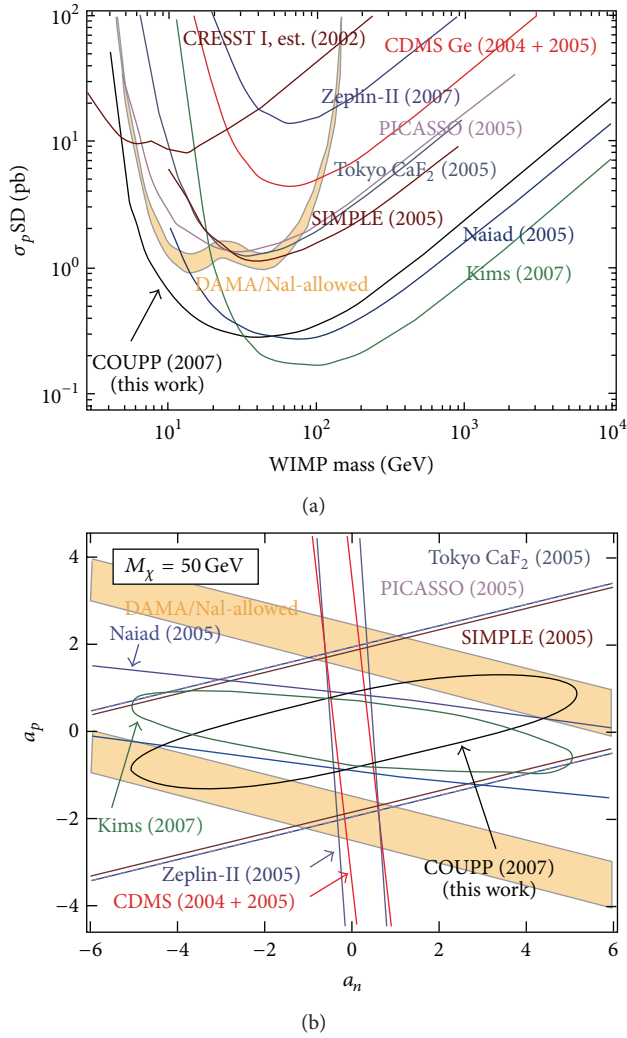


FIGURE 1: COUPP, 2 kg bubble chamber: (a) limits (90% C.L.) on spin-dependent (SD) WIMP-proton cross section (picobarns) from COUPP; (b) similar limits for the SD parameters a_p and a_n .

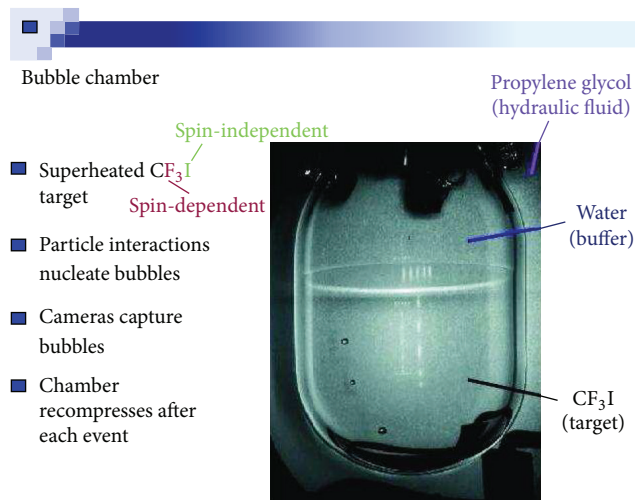


FIGURE 2: Peter Cooper CERN PH Seminar on July 10, 2012: the 4 kg COUPP bubble chamber.

and PICASSO) plans to build a new bubble chamber on the scale of tons [18].

The conceptual design is well developed. If the results from COUPP-4 and COUPP-60 are scaled up, the expected sensitivities are reported in Figures 5 and 6 for a filling of C₃F₈.

5. Superheated Droplet Detectors

Superheated droplet detectors (SDD) are also based on the technique of the superheated bubble formation.

In contrast to bubble chambers used in high energy physics, which are based on the same principle, SDD are basically continuously sensitive, since one droplet at a time undergoes phase transition. Only occasionally, for instance, every few days the detector medium is set under pressure in order to transform gas bubbles back to liquid droplets.

The rupture of metastability by radiation has been used as a method in particle detection. The most important application was the bubble chamber. Apfel [19] extended this concept in the form of SDD in which small drops of the superheated liquid are uniformly dispersed in a gel or viscoelastic medium: it isolates the fragile metastable system from vibrations and convections currents that occur in bubble chambers; in Figure 7 a sketch of a detector exposed to a neutron flux is shown.

The lifetime of the superheated state becomes very long, allowing applications of the SDD as neutron dosimeters and detectors for dark matter.

Two experiments have used SDD for searches of direct interaction of WIMP with ordinary matter: SIMPLE and PICASSO.

SIMPLE is superheated instrument for massive particle.

PICASSO is Project in Canada to Search for Super-symmetric Objects.

SIMPLE obtained the first important results (see Figure 8); the limit curve in function of the WIMP mass is shown in [8, 20].

For PICASSO, see Figure 9 for technical procedures and [21] for results.

In comparison with the bubble chamber the SDD technique has at least the following advantages:

- (1) stability for much longer times;
- (2) lower cost (0.19 k\$/kg);
- (3) much less impurities (γ , α , and β due to the avoided contact with the wall of the vessel and with the buffer liquid),

and the following disadvantages:

- (1) very poor quantity of sensitive matter (maximum 3% of the gel). This makes impossible a competition with the proposals at the ton scale for different detectors (see Table 1).

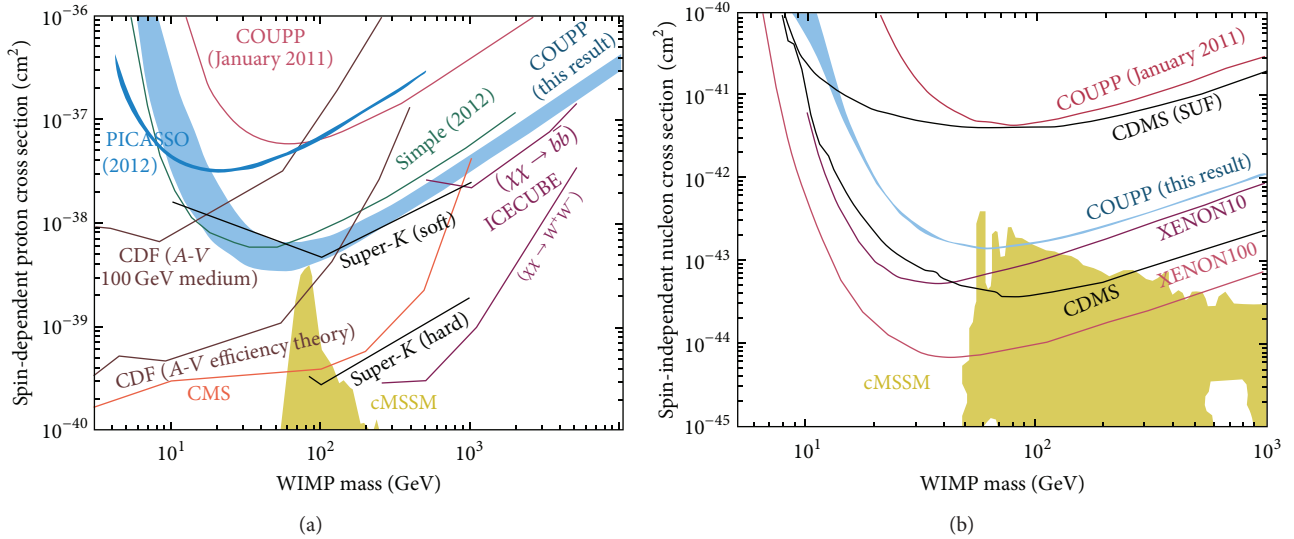


FIGURE 3: Preliminary results of the 4 kg bubble chamber: from Ardid [15], Italy, on August 26, 2013.

TABLE 1: Comparison between different techniques.

	SIMPLE (SDD)	PICASSO (SDD)	Bubble chamber (COUPP)
Detector construction	House	Industry	House
Liquid	C_2ClF_5	$C_2ClF_5; C_4F_8$	$CF_3I; C_3F_8$
Installation (m.w.e.)	GESA (1500)	SNOLAB (6010)	LASR (6), NUMI (300), and SNOLAB (6010)
Results	Figure 8	Figure 9 and [21]	Figure 5

6. Trigger of SDD and Bubble Chambers

R&D within SDD detectors brought an interesting feature into light: the sound emitted at the bubble formation [22] is different if the bubble is due to a recoiling nucleus (as happens for an interaction of neutron or WIMP) or if the bubble is induced by an α decay [23].

Energetic charged particles traversing liquids or solids produce acoustic waves during their passage (see ANTARES and ICECUBE [24, 25] experiments in the PeV range of energy). However, for processes useful for dark matter (in the range of 10–100 keV), the emitted sound predicted by the thermoacoustic effect is not detectable. Nevertheless particle interactions in stressed or superheated liquids produce detectable acoustic signal that is characteristic of the nature or the extension of the primary event.

This suggests that the superheated liquids provide an intrinsic amplification mechanism with a gain of 10^5 .

In Figure 10 [23] and Figure 11 typical spectra are reported for recoils induced by neutrons from an “Am-Be” source.

Ions from nuclear recoils indeed have ranges with sub- μm length; on the contrary the α emitter (inside the superheated liquid) can provide two sources of ionizations (the α itself with a track length of about 40 μm for an energy of 5 MeV and the daughter nucleus.) In Figure 11 [23] such an effect is shown.

The sound signal must be transformed to electronic signals by transducers accompanying the detector, studied with a Fourier analysis and described by an acoustic energy

parameter. The success of this possible separation of the α background has quickly stimulated COUPP and this technique was applied to the bubble chambers; the level of the rejection of this background is now $<10^{-3}$, still keeping an acceptance for recoiling nuclei of 98% [21].

7. The Geyser or Condensation Chamber

Two groups are interested in a new technique called “Geyser”:

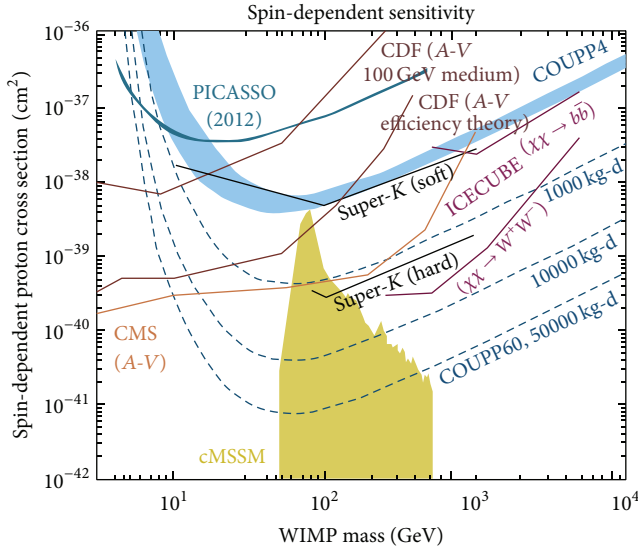
- (1) the Milano-Bicocca group MOSCAB [26, 27];
- (2) the PICO group [28].

This technique is a variant of the superheated liquid technique of extreme simplicity.

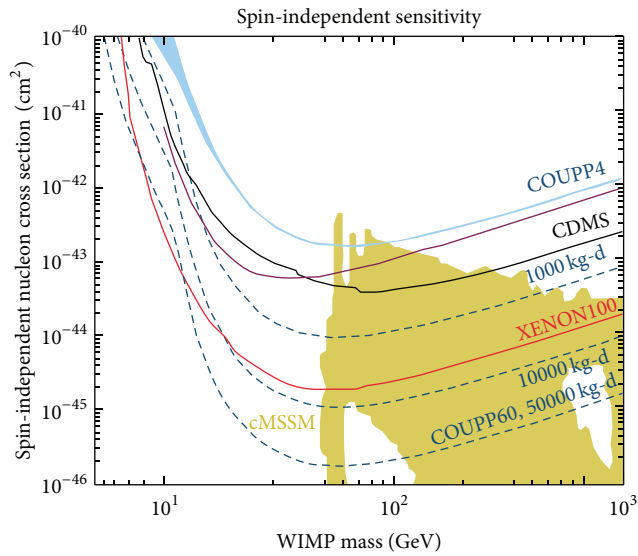
The main volume of the target liquid (C_3F_8 , e.g.,) is kept in a thermal bath at a constant temperature T_L .

The vapour above the liquid is kept at a temperature $T_V < T_L$ by cooling the top of the vessel by a circulating liquid (water).

The equilibrium vapour pressure above the liquid is P_V so the liquid is in a state of underpressure and therefore a superheat of $\Delta p = P_V - P_L$, where $P_V = P_{\text{Sat}}(T_L)$ and $P_L = P_{\text{Sat}}(T_V)$. A local energy release of energy due to, for instance, a recoiling ion induced by a WIMP interaction can produce a vapour bubble which can grow (if over a threshold in energy) to visible size. This vapour bubble rises in the liquid and pushes up part of the liquid in the neck (this is the reason of the name Geyser). When equilibrium pressure



(a)



(b)

FIGURE 4: Sensitivity of the 60 kg bubble chamber: from Ardid [15], Italy, on August 26, 2013.

is reached, the hot vapour in the top of the vessel recondenses and the liquid is recovered into the main volume. The original metastable state is recovered in a few seconds and the system is ready to record a new event. The system does not require external intervention or recompression.

In Figure 12 a drawing of the principal parts of the MOSCAB Geyser is shown.

The figure represents a vertical section of a cylinder, so the coils used as sources of heat are represented by small circles.

In the top part of the same figure the pressure equalizers are shown; they are constituted by two elastic membranes that push the external water when the pressure of the freon gas increases and acts also in the reverse sense.

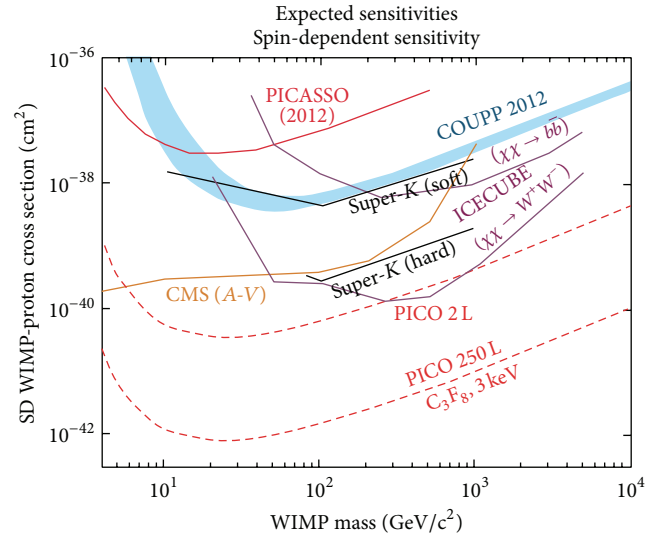


FIGURE 5: Expected sensitivity for the PICO proposal of a 500 kg detector (SD): from Ardid [15], Italy, on August 26, 2013.

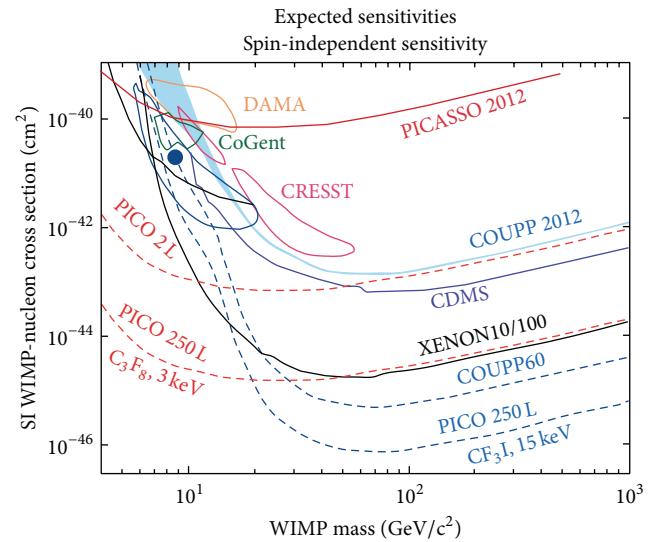


FIGURE 6: Expected sensitivity for the PICO proposal of a 500 kg detector (SI): from Ardid [15], Italy, on August 26, 2013.

In Figure 13 there is a picture of the apparatus built in Milano. In the bottom the liquid freon is shown; the buffer liquid glycol that separates the liquid freon from the vapour is also shown. The degree of superheat applied must exclude the detection of minimum ionizing particles (electrons and γ rays) and on the contrary it must allow the detection with high efficiency of the recoiling ions.

The principal advantages of the Geyser (and of the bubble chamber) are the following.

- (1) The strong rejection of the particles at minimum ionization (electrons and γ) is an advantage.

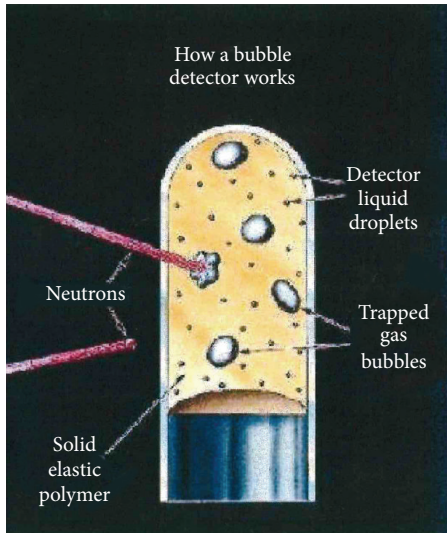


FIGURE 7: SDD for neutron's detectors.

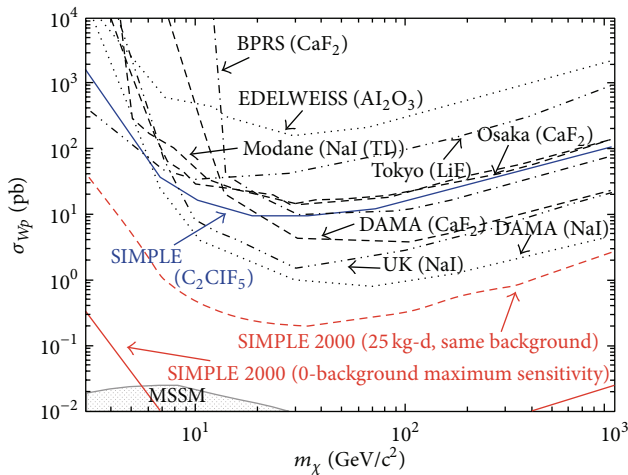
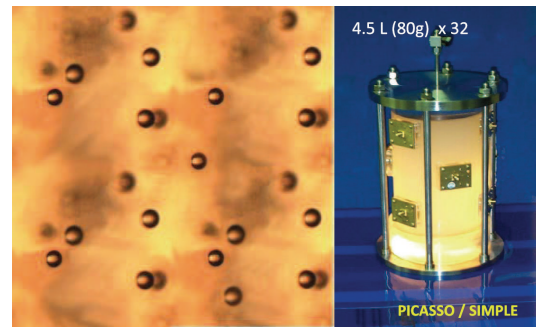


FIGURE 8: SIMPLE 2000: 95% C.L. limits from only 0.19 kg days SDD exposure compared with other experiments; the red lines indicate the expected sensitivity after an exposure of 25 kg days.

- (2) The simplicity of the mechanical construction, also for large size detectors, and therefore low cost are an advantage.
- (3) The very interesting possibility of counting multiple neutron interactions and hence subtract the neutron background (the interaction length of a neutron is of the order of (6–20) cm in liquid freon) is an advantage. The double or triple interaction in the same frame can be used statistically to evaluate the number of events with a single interaction due to neutrons.
- (4) The possibility of distinguishing the spin-dependent interaction of WIMP from spin-independent by changing the liquid used is an advantage.
- (5) Only for the Geyser, the reset of the detector is automatic and has a very short time (few seconds).

Technical realizations



Droplet detectors

- 150 μm superheated droplets of C_4F_{10} dispersed in polymerised gel
- Droplets superheated at ambient T and P ($T_b = -1.7^\circ\text{C}$)
- Bubble explosion recorded by piezoelectric transducers
- Repressurization (6b) returns bubbles into droplets
- Operating temperature determines energy threshold

FIGURE 9: The PICASSO-droplet detector.

A prototype of the Geyser with a mass of 0.5 kg has been constructed in Milano-Bicocca University and INFN [26, 27].

With reference to Figure 12 the quartz vessel of 0.33 liters is immersed in a water bath and it is surrounded by Cu coils with an internal circulating water at the two fixed temperatures.

It contains freon C_3F_8 around 25°C at a pressure of about 6 bars.

The hot freon is separated from the cold freon vapour by the neck of the vessel filled with a buffer liquid (glycol) with thermal capacity greater than that of the water.

In fact in the original Geyser of Hahn and Reist [29] no buffer liquid was used, but we found that it improves greatly the stability of the device.

The temperature of the two regions of water is kept fixed by two thermostats with a precision of 0.1 degrees and the two regions are separated by a loosely fitting rubber washer.

The temperature of the cold vapour was varied between 15°C and 21°C .

Everything is surrounded by a cylindrical vessel of plexi-glass of thickness of 1.5 cm, filled with a water/glycol mixture.

In order that the flask undergoes only a small overpressure with respect to the water an automatic pressure equalizer using rubber membranes is used.

The freon is illuminated by diffuse light, coming from LEDs.

To summarize, the Geyser is essentially a vessel constituted by a “flask” containing the overheated liquid (e.g., some kind of freon) and a “neck” (containing partially a separation liquid and partially the freon vapour).

The scattered ions, after an interaction with a neutral particle like a neutron or a WIMP, deposit their energy in very small regions (size of the order of 0.05–0.1 micron).

In these conditions a bubble can grow and reach a few mm of radius (well visible).

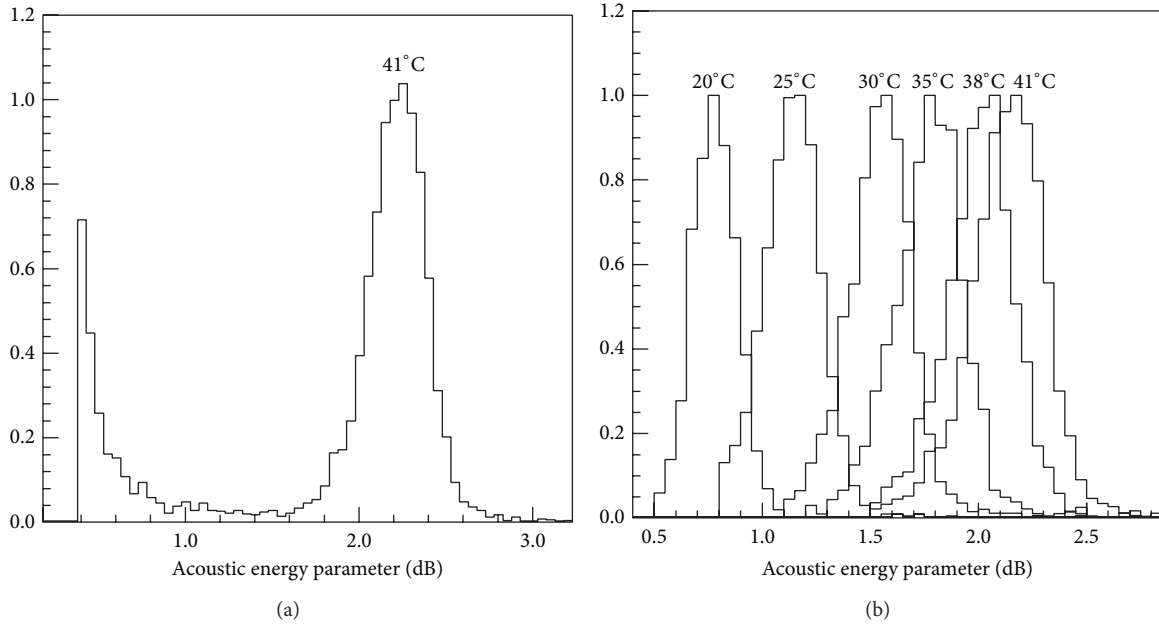


FIGURE 10: Distribution of the acoustic energy parameter recorded in calibrations with neutrons from Am-Be source; neutron recoils show up an ion peak; this peak is well separated from acoustic and electronic noise (a) and shifts with increasing temperature to larger signal intensities (b).

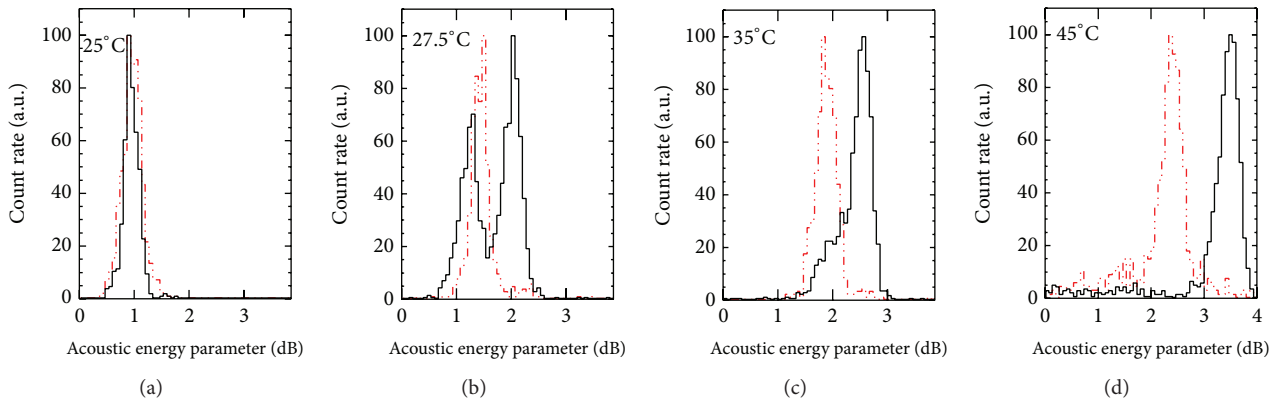


FIGURE 11: Distribution of the acoustic energy parameter obtained with α decays as a function of temperature; the dotted red histograms indicate the location of recoil events obtained with a neutron source; at low temperature the two peaks coincide, and at higher temperature a second peak appears on the high side for the α .

Two professional digital cameras monitor in a continuous way at 50 frames per second (fps) the volume in the freon vessel.

Some pixels undergo a change of luminosity when a bubble is generated.

At this point a trigger is launched and a stream of pictures is registered (between -50 and $+50$ frames starting from the trigger); in Figure 14 the evolution of a typical bubble observed in our detector is shown.

The time sequence (period = 20 ms) starts in the bottom of this figure (right hand), where it is possible to see a small bubble; the sequence continues toward the left and passes to the third line (right); the bubble increases its volume and reaches the surface of the liquid freon (second line); here it

produces a small Geyser (left side of the second line); in the first line the passage of the bubble in the lower layers of glycol is shown.

A local energy release, due to, for instance, a recoiling ion induced by a neutron or by a WIMP interaction, can produce a vapour bubble which can grow (if over a threshold in energy) to visible size. This vapour bubble rises in the liquid and pushes up part of the liquid in the neck. When equilibrium pressure is reached the hot vapour in the top of the vessel recondenses and the liquid is recovered into the main volume. The system returns to equilibrium after a few seconds and it is ready to record new events. The system does not require external intervention or recompression.

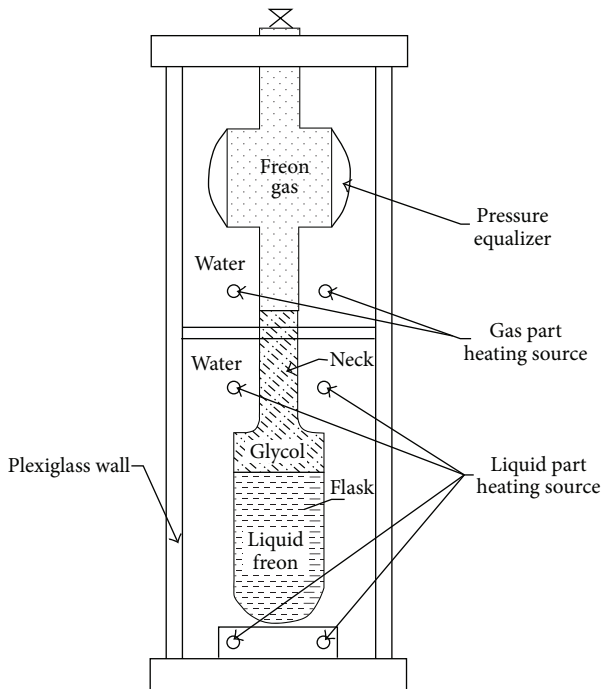


FIGURE 12: Sketch of a vertical section of the Geysier.



FIGURE 13: Internal Geysier's view.

The degree of superheat applied must exclude the detection of minimum ionizing particles (electrons and γ rays) and on the contrary it must allow the detection with high efficiency of the recoiling ions.

A small prototype (0.3 L) of this kind of detector has been realized in Milano-Bicocca University and INFN [26, 27].

For the future the MOSCAB group wants to construct a bigger detector (27 L) which could be competitive with other experiments and with other techniques and work in the Laboratory of the Gran Sasso (INFN).

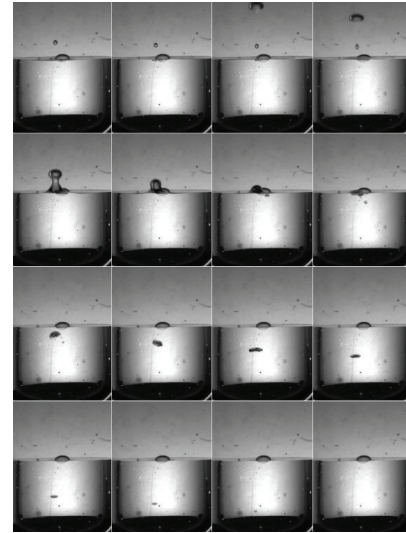


FIGURE 14: Evolution of a bubble.

The transition from a small detector to a very big one requires a lot of new technologies, for the mechanical support, the thermostats, the quartz's vessel, the trigger, the dramatic reduction of the impurities contained in the materials surrounding the detector, and so forth.

However, in particular, information on the spin-dependent interaction with protons is poor. On the contrary, fluorine based detectors offer excellent opportunities in this field.

The PICASSO and now PICO groups have produced a detailed proposal for the construction of a big detector (0.5 tons) [28]. The expected sensitivity for one-year run (0.5 tons per year) with a supposed 0 background is shown in Figures 5 and 6.

The future of this kind of detectors depends on the possibilities of extrapolating the data from small prototypes to a very big detector and from the existing residual background in the LNGS and SNOLAB underground laboratories.

8. Conclusion

In this short review I have shown that detectors based on the superheated liquid technique have played a relevant role in the search of dark matter. The new generation of ton scale detectors is complementary and competitive with projects employing other techniques. Hopefully, in a few years the mystery of the dark matter will be revealed.

Conflict of Interests

The author declares that there is no conflict of interests regarding the publication of this paper.

References

- [1] D. A. Glaser, "Some effects of ionizing radiation on the formation of bubbles in liquids," *Physical Review*, vol. 87, no. 4, p. 665, 1952.

- [2] V. Zacek, "Search for dark matter with moderately superheated liquids," *Il Nuovo Cimento A*, vol. 107, no. 2, pp. 291–298, 1994.
- [3] J. Collar, "Superheated microdrops as cold dark matter detectors," *Physical Review D*, vol. 54, no. 2, pp. R1247–R1251, 1996.
- [4] L. Baudis, "Direct dark matter searches-rapporteur talks," in *Proceedings of the New Opportunities in the Physics Landscape at CERN*, CERN, May 2009.
- [5] F. Seitz, "On the theory of the bubble chamber," *Physics of Fluids*, vol. 1, no. 1, pp. 2–13, 1958.
- [6] G. Jungman, M. Kamionkowski, and K. Griest, "Supersymmetric dark matter," *Physics Reports*, vol. 267, pp. 195–373, 1996.
- [7] E. Behnke, T. Benjamin, S. J. Brice et al., "Direct measurement of the bubble nucleation energy threshold in a CF_3I bubble chamber," *Physical Review D*, vol. 88, no. 2, Article ID 021101(R), 2013.
- [8] J. I. Collar, J. Puiasset, T. A. Girard, D. Limagne, H. S. Miley, and G. Waysand, "Prospects for SIMPLE 2000: a large-mass, low-background superheated droplet detector for WIMP searches," *New Journal of Physics*, vol. 2, pp. 14.1–14.14, 2000.
- [9] R. Bernabei, P. Belli, F. Cappella et al., "New results from DAMA/LIBRA," *European Physical Journal C*, vol. 67, no. 1-2, pp. 39–49, 2010.
- [10] P. Benetti, R. Acciarri, F. Adamo et al., "First results from a dark matter search with liquid argon at 87 K in the Gran Sasso underground laboratory," *Astroparticle Physics*, vol. 28, no. 6, pp. 495–507, 2008.
- [11] E. Aprile and T. Doke, "Liquid xenon detectors for particle physics and astrophysics," *Reviews of Modern Physics*, vol. 82, no. 3, pp. 2053–2097, 2010.
- [12] D. S. Akerib, M. J. Attisha, C. N. Bailey et al., "Characterization, performance, and future advanced analysis of detectors in the cryogenic dark matter search (CDMS-II)," *Nuclear Instruments and Methods in Physics Research A: Accelerators, Spectrometers, Detectors and Associated Equipment*, vol. 559, no. 2, pp. 387–389, 2008.
- [13] E. Behnke, J. I. Collar, P. S. Cooper et al., "Spin-dependent WIMP limits from a bubble chamber," *Science*, vol. 319, no. 5865, pp. 933–936, 2008.
- [14] P. Cooper, CERN PH Seminar, July 2012.
- [15] M. Ardid, ICTP Trieste, 2013.
- [16] A. Sonnenschein, Private communication.
- [17] J. Collar, E. Behnke, P. Cooper et al., COUPP—A Proposal to Operate the COUP-60 Bubble Chamber at SNOLAB, 2009.
- [18] J. Collar, E. Behnke, P. Cooper et al., COUPP-500 A Proposal for a Ton Scale Bubble Chamber for Dark Matter Detection, 2010.
- [19] R. E. Apfel, "The superheated drop detector," *Nuclear Instruments and Methods*, vol. 162, no. 1-3, pp. 603–608, 1979.
- [20] M. Felizardo, "Final analysis and results of the phase II SIMPLE dark matter search," *Physical Review Letters*, vol. 108, no. 20, Article ID 201302, 2012.
- [21] V. Zacek, Proposal for a 0.5 Ton Dark Matter Experiment at SNOLAB, 2012.
- [22] Y. N. Martynyuk and N. S. Smirnova, *Soviet Physics: Acoustics*, vol. 37, p. 376, 1991.
- [23] S. Archambault, F. Aubin, M. Auger et al., "New insights into particle detection with superheated liquids," *New Journal of Physics*, vol. 13, Article ID 043006, 4 pages, 2011.
- [24] S. Adrian-Martinez, A. Albert, M. André et al., "Searches for clustering in the time integrated sky map of the ANTARES neutrino telescope," *Journal of Cosmology and Astroparticle Physics*, vol. 2014, no. 5, article 001, 2014.
- [25] M. G. Aartsen, "Evidence for high-energy extraterrestrial neutrinos at the IceCube detector," *Science*, vol. 342, no. 6161, Article ID 1242856, 2013.
- [26] R. Bertoni, F. Chignoli, D. Chiesa et al., "A new technique for direct investigation of dark matter," *Nuclear Instruments and Methods in Physics Research A: Accelerators, Spectrometers, Detectors and Associated Equipment*, vol. 744, pp. 61–68, 2014.
- [27] A. Pullia, in *Proceedings of the VILLA OLMO International Conference 2013—ICATPP Conference*, September 2013.
- [28] V. Zacek, in *Proceedings of the VILLA OLMO International Conference 2013—ICATPP Conference*, 2013.
- [29] B. Hahn and W. W. Reist, *Proceedings of the 5th International Conference on High-Energy Physics Nuclear Structure*, 1973.

Review Article

The WArP Experiment: A Double-Phase Argon Detector for Dark Matter Searches

Andrea Zani

Pavia University and INFN Pavia, Via Bassi 6, 27100 Pavia, Italy

Correspondence should be addressed to Andrea Zani; andrea.zani@pv.infn.it

Received 5 December 2013; Accepted 19 February 2014; Published 30 April 2014

Academic Editor: Claudio Montanari

Copyright © 2014 Andrea Zani. This is an open access article distributed under the Creative Commons Attribution License, which permits unrestricted use, distribution, and reproduction in any medium, provided the original work is properly cited. The publication of this article was funded by SCOAP³.

Cryogenic noble liquids emerged in the previous decade as one of the best media to perform WIMP dark matter searches, in particular due to the possibility to scale detector volumes to multiton sizes. The WArP experiment was then developed as one of the first to implement the idea of coupling Argon in liquid and gas phase, in order to discriminate β/γ -interactions from nuclear recoils and then achieve reliable background rejection. Since its construction, other projects spawned, employing Argon and Xenon and following its steps. The WArP 100l detector was assembled in 2008 at the Gran Sasso National Laboratories (LNGS), as the final step of a years-long R&D programme, aimed at characterising the technology of Argon in double phase for dark matter detection. Though it never actually performed a physics run, a technical run was taken in 2011, to characterise the detector response.

1. Introduction

Recent results on cosmic microwave background by the Planck space observatory have brought further confirmation that an important component of our Universe comes in the form of nonbaryonic dark matter, with an abundance far higher than that of known baryonic matter. According to the latest Planck results, it is $\Omega_{\text{DM}} \approx 26.8\%$ and $\Omega_B \approx 4.9\%$ [1, 2].

Several theories have been developed in the past to describe the nature of dark matter (DM) [3], and one interesting class of candidates is the so-called weakly interactive massive particles (WIMPs). In the past years the preferred candidate of this class of theories came from supersymmetric extensions of the Standard Model [4]. According to these models, experiments on Earth surface can detect elastic scatterings on target nuclei by crossing WIMPs that are part of the dark halo surrounding our Galaxy [5]. The energies of the recoiling nuclei should range from few to a hundred keV. The cross sections and rates depend on many parameters: the chosen WIMP candidate and nuclear model, the target material, and the distribution of velocities of the DM particles in the halo surrounding our galaxy. The variety of theories

implies that allowed regions by theoretical models in the parameter space, characterised by the mass (m) and WIMP-nucleon cross section (σ) of these particles, span many orders of magnitude.

So far, most experiments have tried to detect the signatures of the interaction, in the form of light, charge, or heat. More recent experiments choose to detect simultaneously two signatures, which allow performing particle discrimination and rejecting backgrounds not due to nuclear recoils. Most recent negative results come from XENON100 (2012) [6, 7] and LUX (2013) [8], which pushes the limit on spin-independent, WIMP-nucleon cross section below 10^{-45} cm^2 . This is in contrast with experiments searching for a seasonal modulation in the spectrum of recoils, which is ascribed to the Earth variation of relative velocity with respect to the DM halo, during its revolution around the Sun. The DAMA [9] and CoGeNT [10, 11] Collaborations reported positive detection of an annual modulation. Only one experiment searching for a double interaction signature (in this case light emission and heat depositions) reported a positive result as well, that is, the CRESST-II experiment in Gran Sasso [12]. A definitive answer to the identification

of dark matter is however yet to come, as the allowed regions in the parameters spaces, selected by these experiments, were all excluded by mentioned LUX latest data [8].

The WArP (Wimp Argon Programme) experiment represents one of the first attempts to use liquefied noble gases as target for the interaction. The use of noble liquids implies the need to operate at cryogenic temperatures (87 K Argon, 165 K Xenon), but they behave as scintillators, which means that any ionising particle in the medium produces both light and charge. The implementation of the double-phase (described in the next section) is then introduced, to exploit simultaneously the charge/light signatures and to probe the low recoil-energy range predicted by the theories. The WArP Collaboration carried on years of studies on liquid Argon and double-phase technologies: this led to the operation of a 2.3 l prototype (Section 3.1), which successfully tested the new detection technique, and to the implementation of a full-scale 100 l detector, aimed at dark matter searches (Section 3.2).

2. Liquid Argon

The WArP technology was developed through years of R&D studies, started at CERN in the 1990s, as part of the activities related to the ICARUS experiment [13]. First studies to discriminate between nuclear recoils and β/γ -induced events were performed in liquid Xenon [14], but later the decision was made to employ Argon instead, coupled to the concept of a double-phase chamber [15].

Noble liquids are scintillators, with energies of the order of tens of eV required to produce a scintillation photon. For example, a relativistic electron needs to deposit about 20 eV in Argon to produce a scintillation photon; the value increases for heavier, slower particles. First tests were performed on Xenon: the reason is that it has slightly better physical properties with respect to Argon, like higher electron mobility, density, and boiling point. On the other hand, Argon is more commonly found in atmosphere, and state-of-the-art technology to obtain, store, and purify it is already available and cheap. This makes it possible to scale detectors up to multiton volumes.

A further physical significant advantage of Argon over Xenon is related to light emission. Scintillation light in Argon is emitted in the vacuum ultraviolet (VUV) region, at 128 nm, from deexcitation of Ar_2^* dimers. These can be produced either by excitation of the medium, or following recombination after production of electron-ion pairs. The energy required to produce a pair is dependent on the nature of the interacting particle. For a wide range of particles, from relativistic ions and electrons to α 's, it is measured to be 23.6 eV [16, 17]. The value increases for heavy slow ion recoils ($\beta < 0.01$), due to the decreasing efficiency of the ionization process. The description of the mechanism in this energy range was first suggested by Lindhard et al. [18, 19]. The first experimental confirmations of the theory came in the 1960s [20, 21]; later, the WArP collaboration tested independently the model for the case of Argon nuclei recoiling in LAr [22], confirming its validity.

TABLE 1: Relative fast-to-slow signal intensity ratio in LAr for different particles in zero-field conditions [23]. LET increases from electrons to fission fragments, and I_f/I_s increases as well.

Ionising particle	I_f/I_s
Rel. electrons	0.3
α -Particles	1.3
Fission fragments	3.0

In general, the amount of produced scintillation light and ionization depends on the way particles deposit their energy in the medium, that is, the *Linear Energy Transfer (LET)*. Therefore, both light and charge can be used to perform particle identification, based on the characteristics of the collected signals.

Both luminescence processes discussed above are characterised by two components with different decay times. The fast one has a decay-constant $\tau_f \approx 6$ ns, while the other is far slower, with $\tau_s \approx 1200$ –1500 ns. Such a large difference in the values of the time constants is related to the characteristics of the excited states in which the Argon dimers appear, and it shows no dependence on the particle LET. However, it has been demonstrated [23] that it is the relative intensity of the two components (fast-to-slow, I_f/I_s) to be heavily dependent on LET, with their ratio increasing with it (see Table 1). Therefore, different particles produce light signals characterised by different shapes and profiles as a function of time: in particular electrons are expected to produce signals dominated by the slow light component, while α 's and nuclear recoils, characterised by a higher LET, induce much faster signals. An analysis of the pulse shape, applied to the collected signals, allows recognising distinct particles interacting in LAr, therefore providing a powerful method to reject backgrounds. As mentioned, this is made possible only by the fact that Argon light decay constants are very well separated in magnitude: the same is not applicable to, for example, Xenon, which has both decay-time constants in range of few ns–few tens of ns.

A drawback of Argon is the contamination of ^{39}Ar . It is a β^- -emitter with half-life of 269 y and end-point at 565 keV; its activity was measured by the WArP Collaboration as (1.01 ± 0.08) Bq per kg of natural Argon, corresponding to a concentration of $(8.0 \pm 0.6) \cdot 10^{-16}$ g(^{39}Ar)/g(^{nat}Ar) [24]. ^{39}Ar is produced by interaction of cosmic rays with the atmosphere, and it is naturally present in commercial Argon; however, it was recently discovered [25] that underground Argon pockets contain very low levels of ^{39}Ar , due to their isolation from Earth surface and atmospheric radiation. The extraction technology is not yet perfected, and costs are high, therefore this solution is still not any more convenient than using liquid Xenon.

The choice of the target material is also dependent on the need to enhance as much as possible the interaction rate of WIMPs, characterised by weak cross sections. The integrated cross section for elastic scatterings on a nucleus is proportional to A^2 , with A being the mass number, due to the coherence effect. Then Argon is expected to have

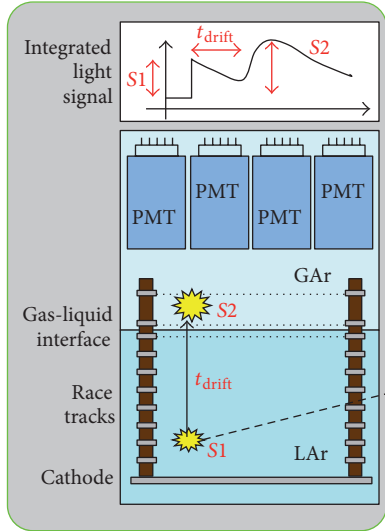


FIGURE 1: Working scheme of the inner detector.

a lower integrated cross section, with respect to “heavier” materials like Xenon or Germanium; however, the spectra of these elements are suppressed at higher energies by the nuclear form factor [22]. Then, by assuming a low recoil energy threshold at around 30 keV, the integrated rates of the considered materials will be similar in magnitude.

In conclusion, taking into account the availability at cheap cost of large quantities of highly purified Argon, the expected rates of interaction, and its scintillation light properties, LAr can be considered as a preferred medium for future large-volume dark matter experiments.

2.1. Double Phase Technology. The characteristics of liquid Argon are coupled, for dark matter searches, to the innovative concept of a double-phase chamber ([15], see Figure 1), which derives from the time projection chamber (TPC) design [26].

In this new implementation, a gaseous Argon (GAr) pocket is coupled to a liquid volume, in which a uniform electric field is applied. Interactions taking place in the liquid produce both a primary scintillation light signal (s_1) and ionization electrons. The light is collected by means of cryogenic photomultipliers (PMTs); the charge is drifted to the liquid surface by a uniform electric field. There, a grid system provides electron extraction into the gas phase and acceleration, in order to produce secondary light emission (s_2), which is proportional to the initially produced charge. The amount of collected light (light yield, LY) is expressed in phe/keV, that is, number of collected photoelectrons per keV of energy deposited in the liquid.

As already discussed in Section 2, the relative intensity of primary scintillation and ionization is dependent on the particle nature; therefore, it is expected that distinct particles will produce different values of the ratio s_2/s_1 . The same can be stated for the fraction of fast component (s_f) present in the primary signal: once again this is dependent on which particle is interacting in LAr. These two features can be exploited to recognise particles, through the analysis of light

signals shapes and intensities. Figure 2 depicts real events recorded with a prototype chamber used during the R&D of the WArP project: it can be seen as in particular integrated signals show the difference between the response produced, following an interaction by a fast, light particle (electron, left) and a nuclear recoil (right). Different particles will produce distinct signal shapes and intensities, allowing performing particle identification, and thus rejection of events not due to nuclear recoils.

Numerous technical issues were to be investigated when the WArP Collaboration first came out with this solution, and the necessary activities were carried out by the various groups of the collaboration [27].

The processes of electron extraction and multiplication in the gas phase were investigated, along with the proportionality of secondary light to the emitted charge [28]. The solution eventually adopted within the collaboration consists in a system of three metallic wire grids independently fed. The first grid is put beneath the liquid surface, while the other two are in the gas volume. The region between the first and second grid is where extraction and acceleration are performed, by means of an electric field. The field region between the second and third grid is instead configured to collect all the electrons on the last plane, in order to protect the PMTs that are placed behind it. The study of the extraction/multiplication fields was carried on with a 2.3l prototype chamber [22].

The issue of light collection was also heavily investigated: first of all it is necessary to employ a wavelength shifter, in order to shift the scintillation VUV photons produced in Argon into the visible range. Then, as the detector is designed to have photomultipliers on a single side (facing the gas pocket), all other internal surfaces must be covered with a reflecting material, in order not to lose light. The solution chosen by the collaboration, after a series of tests performed both at CERN and LNGS, is to use VM2000, a dielectric reflector from 3M (not affected by the electric field), on which tetraphenyl-butadiene (TPB), that shifts VUV photons to 430 nm, is deposited through vacuum evaporation. TPB is also deposited in a thin toluene film on the PMTs windows, so that all produced photons can undergo shifting before reaching the detectors. The choice of materials and of the method of deposition for TPB on VM2000 was achieved after dedicated tests carried out at CERN. Vacuum evaporation on all inner detector surfaces was chosen as it proved to be the deposition method least affecting TPB properties (in particular it is hygroscopic). In the same way photomultiplier behaviour at LAr temperature was heavily tested both by the supplier and the collaboration.

Light and charge transport in LAr is a delicate matter as well. Substances like O_2 , H_2O , CO_2 , and N_2 are commonly found even in pure 6.0 commercial Argon, as well as in most building materials (mainly plastics). The first three substances are electronegative, so that they can attach drifting ionization electrons, thus quenching the charge yield. On the other hand nitrogen and oxygen can also produce light losses, by nonradiative interactions with Argon dimers before their decay. The WArP Collaboration has carried on dedicated studies on the effects of N_2 [29] and O_2 [30] contamination in liquid Argon, as a part of its R&D program. The dependence

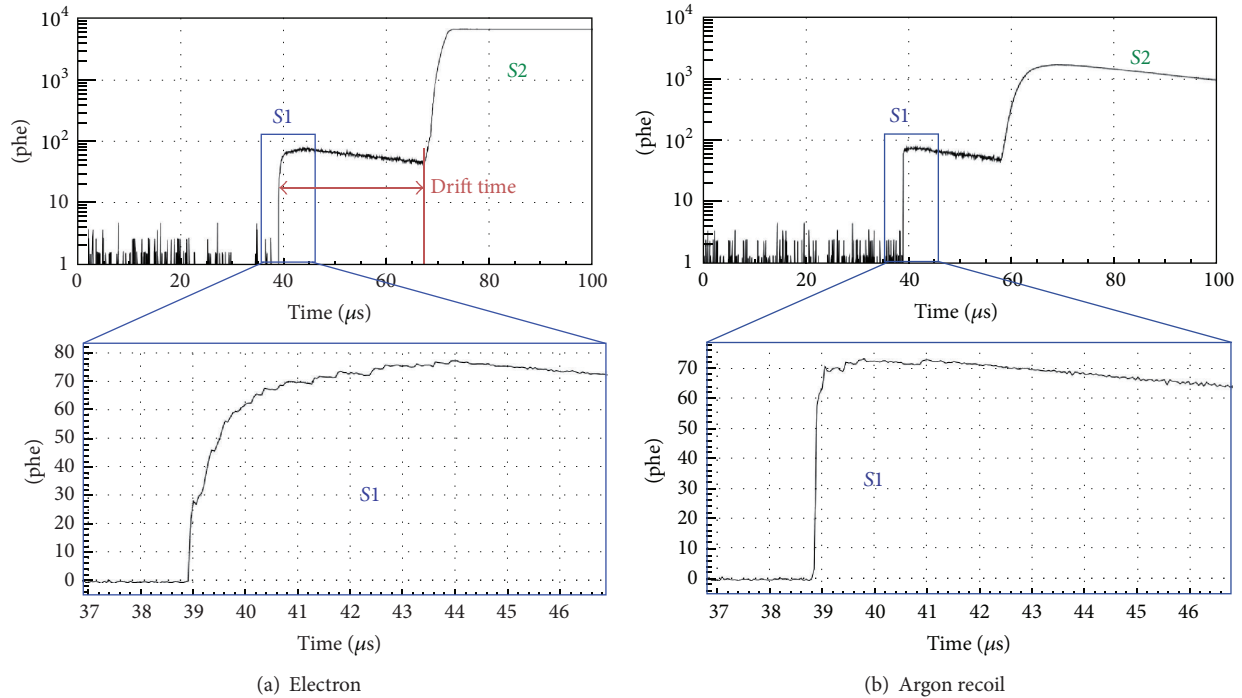


FIGURE 2: Example of collected integrated signals, due to electrons (a) and nuclear recoils (b). The difference in the magnitude of the secondary signal s_2 and in the rise time of the primary pulse (related to the fraction of fast light component sf) is clearly visible for the two classes of events.

of the long-lived light decay-constant and of electron life time on impurity concentration was demonstrated [30]. However, this effect sets in from values of the order of 0.1–1 ppm, which are far higher than the one needed to correctly operate a detector (order of ppb for O_2 ; see discussion below about impurity concentration control). O_2 has a far higher interaction rate and affects both light and charge, but it can be extracted from LAr with dedicated filters; on the other hand, N_2 affects only light, but it cannot be removed. To study the effects of N_2 and O_2 , two chambers were employed, the 2.3l prototype and a 0.7l dedicated cell, where it was possible to inject predetermined amounts of impurities.

In an actual detector, impurity concentration has to be kept under strict control: highly purified commercial Argon has an impurity concentration below 0.1 ppm O_2 equivalent, which can still affect both light and charge yield. Standard operating procedure to further lower the impurity levels is to implement a liquid and gaseous recirculation system where Argon is periodically extracted from the main volume and passed to a combination of purifiers. The solution devised for the ICARUS detector [13] implies the use of standard commercial filters such as *Hydrosorb* and *Oxysorb*. The first is a mechanical porous filter used to stop large molecules like H_2O and CO_2 , while the second is a chemical filter used to stop small nonpolar substances like O_2 . In the WArP experiment a variation is introduced by employing *Hopkalite* rather than *Oxysorb*, as it is known to introduce less radiochemical contaminants. The combined use of the filters can reduce the overall impurity concentration up to a factor 1000. However, they are not sufficient to maintain purity over

long time periods. As a matter of fact further contaminants can enter the sensitive volume, either from possible small leaks from the outside or from *outgassing* of the inner walls. The main impurities introduced in such way are water and oxygen; the effect is more important in the gas phase, as in liquid the molecules can freeze out on the wall surface and practically not diffuse into the sensitive volume. For this reason, in order to maintain a high level of Argon purity over long periods of time, a recirculation system is needed. The purity of the system then results from the balance between the inflow (leaks, outgassing) and the outflow (recirculation, filters) of impurities in the sensitive volume.

3. The WArP Experiment

The Wimp Argon Programme, as already mentioned in Section 2, started in the 1990s from ICARUS studies on the possibility to use scintillation light in noble liquids to perform separation between β/γ -induced events and nuclear recoils ([13–15]). Following and complementing the R&D activities discussed in the previous section, in 2000 the assembly of a 2.3l demonstrator chamber was started, with the aim of testing and characterising the detection technique [22]. This chamber has been used widely so far, also to provide the first results on WIMP parameters within the WArP project [28], and later to test new materials and devices for further steps of the program [31]. Other than that, smaller chambers (order of 0.5 ÷ 1 l LAr) were built, to carry on dedicated tests on new materials and photomultipliers [31]. Finally in



FIGURE 3: 3D layout of the 2.31 prototype, configuration for LNGS physics run. Details in text.

2005 there was the start of activities related to a full scale, 100 litres physics detector, aimed at performing a physics run and upgradable to larger volumes in case of program success. The detector was constructed and commissioned, but the mentioned problems in operation finally redirected the project scope to a technical run, useful to characterise the detection technology at the level of a full-scale detector.

3.1. 2.31 Prototype Results. The 2.31 chamber [22, 28] was first developed and tested with a single 8'' photomultiplier (*Electron Tubes 9357FLA*), at sea level in Pavia, Italy. The chamber was immersed in a LAr bath, and it was structured as a Teflon cylinder surmounting an inverted truncated cone; all inner surfaces were covered by a layer of VM2000 reflector, with TPB deposited on it. The chamber contained a liquid volume capped by a gas pocket; the drift field in the liquid was set at 1kV/cm, while a system of 3 grids around the liquid-gas interface assured electron extraction and multiplication. Geometry and dimensions details are reported in [22, 28].

The chamber was mainly used to evaluate the light collection efficiency and to test the production of secondary signals. It first demonstrated that different events can be reliably discriminated on the base of their $s2/s1$ ratio: indeed low-ionising particles (e.g., electrons) produce small ionization density, and a lot of ionization electrons are extracted from the original interaction region, thus not recombining. Then a large secondary signal is produced. On the other hand, α 's and recoiling Argon nuclei produce high ionization density that enhances recombination, independently of the field strength. Therefore, few electrons are extracted and the resulting secondary signal is reduced.

In the same way it was shown that the shape of primary signals is different according to the particle nature: this is due to the ratio between the fast and slow scintillation light intensity, which depends on the interacting particle, as

discussed in Section 2. The measurements led to evaluate a probability of wrong particle recognition of 10^{-4} for each investigated technique ($s2/s1$ and pulse shape discrimination). As the two rejection techniques are independent and evaluated separately, an overall 10^{-8} rejection power can be estimated [22].

Later, the chamber configuration was modified, and the 8'' PMT was replaced with seven 2'' photo-tubes, ETL D757-UFLA (such implementation is shown in Figure 3). It was transferred at LNGS in 2005 to operate underground [28]. There it was first employed to study backgrounds in the underground laboratory, with particular attention to the ^{39}Ar spectrum and its specific activity. The light yield of the chamber for nuclear recoil events was evaluated, with a field of 1kV/cm. This was done by studying the recoil energy spectrum of neutron interactions, both from environmental radiation and from a dedicated Am-Be source. The collected data were compared with a GEANT4-based Monte Carlo simulation: as a result in both configurations the experimental spectrum could be reproduced by a constant light yield [28],

$$\begin{aligned} LY_{\text{env}} &\approx 1.55 \pm 0.40 \text{ phe/keV}; \\ LY_{\text{AmBe}} &= 1.26 \pm 0.15 \text{ phe/keV}. \end{aligned} \quad (1)$$

The errors on the data are mainly systematic, deriving from uncertainties in the determination of the MC neutron flux induced inside the chamber.

The study of the proportional signal was again performed with events induced by electrons, α 's from ^{222}Rn and nuclear recoils. Electron-induced events result in a large ionization signal, while α 's produce a much lower one, as discussed above. Nuclear recoils $s2/s1$ -ratio instead is found to depend on the recoil energy, and it is modelled by an empirical ($a + b/E_R$) function, related to the recoil energy spectrum of the used source [22]. At high energies the ratio tends to the α -particles value.

The activities on the 2.31 chamber ended with an underground physics run at LNGS, during which $2.8 \cdot 10^7$ triggers were collected, with a total exposure of 96.5 kg d. By using the information from $s2/s1$ ratio and the pulse shape analysis, nuclear recoil events were searched for. In the energy region below 55 keV, 8 events survived cuts, while nothing was detected at higher energies. The nature of these events was not understood: they could be of spurious origin, namely, residual neutrons or misrecognized e-like events, surviving cuts due to some inefficiency in the rejection. 90% C.L. upper limits were set on the WIMP (m, σ) parameter space, for the case of no events observed at $E > 55$ keV. In the plot shown in Figure 4, WARP limits are reported, along with contemporary CRESST [32], EDELWEISS [33], and CDMS [34–36] ones. Though present limits are 3 orders of magnitude better [6–8], it can be seen how the demonstrator limits were comparable to those of contemporary, full-scale experiments. The allowed region for DAMA [9] was excluded as well.

The collected data were extrapolated to the upcoming 100l detector, by correcting for the PMT quantum efficiencies, different photocathodic coverage, and dimensions;

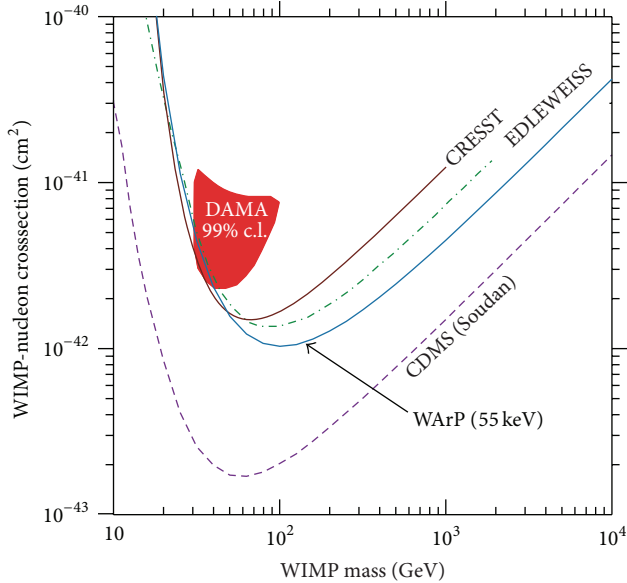


FIGURE 4: 90% C.L. spin-independent limit for WARP-2.31 (solid blue line), compared with previous limits [28] available at the time.

as a result, a light yield value of ≈ 3.5 phe/keV in the inner detector (no field) was expected. It was estimated that the new detector sensitivity would have allowed to probe the region down to cross sections of the order of 10^{-45} cm² in the mass region of 50–100 GeV, that is, the same order of magnitude of the limits reached today by Xenon100 [6, 7].

3.2. WARP 100 l Detector. The 100 l detector is the last iteration of the project: it consists of an inner double-phase chamber, which is surrounded by a larger volume of LAr, instrumented with photomultipliers as well. This serves as anticoincidence to reject all those events producing a signal in both volumes, and it is a unique feature first introduced by the WARP programme, to effectively eliminate spurious nuclear-recoil signals, produced by neutron elastic scatterings. The detector has been housed underground in Hall B of the Gran Sasso laboratories, in order to minimise its exposure to cosmic and environmental radiation.

The inner detector is a double-phase chamber, with a volume of 100 l (140 kg) of Liquid Argon topped by a gas pocket, read by 37 PMTs (Figure 5(a)). The drift region is delimited at the bottom by an Oxygen-Free Copper cathode (3 mm thick, 580 mm wide); the side walls are constituted by Oxygen-Free Copper field-shaping strips (race-tracks, 1 cm wide, 1 cm pitched), printed on a *Kapton* substrate. The system ensures a uniform field within the drift region; the strips are arranged in a truncated conical shape, to avoid trapping of ionization electrons between race-tracks themselves. The drift volume is closed at the top by the first of a three-grid system. Each grid is made by a stainless steel ring (5 mm thick, 580 mm external diameter, 500 mm internal) holding stainless steel wires (4 mm pitch, 150 μ m diameter) enrolled on gold-plated bushes and mechanically tensioned to 750 g. They are supported by PEEK annular

insulators, connected to the main structure. The described design defines a *maximum drift length* of 600 mm. A resistive divider chain distributes supply voltage from the cathode, through the race-track system, to the first grid. The second and third grids are independently fed, which allows to (i) tune the field in the extraction/multiplication region, (ii) maximize the transparency of first and second grids, and (iii) achieve complete charge collection on the third one. The plane of the light-collecting photomultipliers is positioned 25 mm above the third grid: they are kept in place by the last layer of the PEEK structure that also sustains the race tracks and the grids. The PMTs and the gas pocket are enclosed in a stainless steel cap, vacuum insulated and fixed on the PEEK structure. A set of small resistors is placed just below the liquid surface: they assure continuous boiling of the liquid. Excess gas is evacuated through small holes in the cap, positioned at the desired level of the liquid-vapour interface (5 mm above the first grid), which is thus precisely set. The 37 PMTs, (31, 3'' ETL D750-UKFLA and 6, 2'' ETL D757-UFLA) are deployed in a hexagonal shape. This arrangement is chosen to maximise the photocathodic coverage, to a value of 10%. The internal walls of the detector are covered with TPB evaporated on VM2000, which ensures conversion of VUV photons into visible light and minimises light losses. PMT windows are also treated with TPB. The whole inner detector structure is enclosed by a foil of copper, put to ground to isolate the internal volume and ensure that no field is present in the outer veto region.

The inner detector is immersed in a liquid Argon bath and surrounded by the active shield or veto (Figure 5(b)). This is a large ellipsoidal structure (5600 l volume) separating the internal detector from the cryostat and passive shield walls. It is made by a thin tile structure connected to a Copper superstructure. This is made to sustain the active shield weight during construction and its buoyancy after immersion in LAr. Each of the tiles is in copper, covered by a TPB+reflector layer; they have holes to house photomultipliers: in total 300 (36, 2'' and 264, 3'') PMTs are in place in the veto, yielding a 7% photocathodic coverage.

The inner detector and the veto are contained in the main cryostat, made of *AISI 304L* stainless steel, chosen for its low radioactive content (for a detailed list of contaminants, see, e.g., [37]). The structure double walls are vacuum superinsulated. It is closed by a top flange from which the copper superstructure hangs, sustaining both the inner and veto volumes, which then make a single object (see Figure 5(b)). On the dewar inner walls, a 10 cm polyethylene shield is mounted, used to moderate the neutrons produced by the radio-contaminants present in the cryostat walls. The dewar inner volume is 30 m³, of which 23 are filled with LAr.

The cryostat is surrounded by an external shielding system, to protect the detector from γ and neutron radiation, as well as to serve as further container, in case of significant cryostat spills. It is made by a 10 cm thick lead layer, contained in stainless steel boxes, followed by 70 cm of polyethylene. The shield was not completed during the actual technical run of the detector. An external antiseismic structure, made of carbon steel, sustains the external shielding.

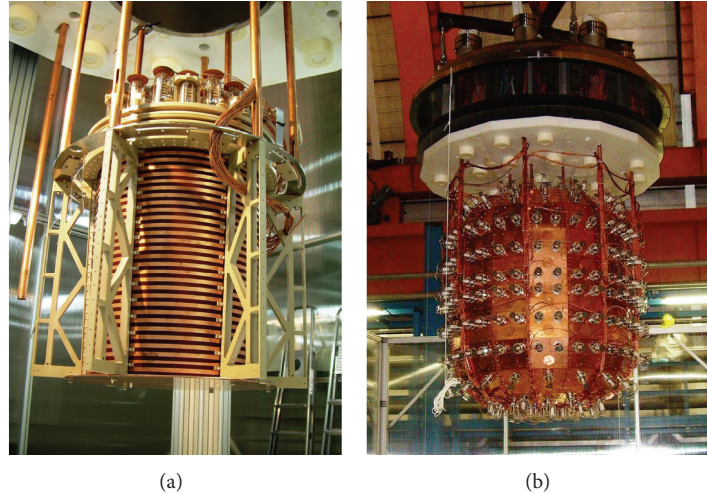


FIGURE 5: (a) Picture of the inner detector, completed in the clean room. (b) Completed WArP 1001 detector, ready to be inserted in its cryostat. The veto is visible, hanging from the cryostat top flange; the inner detector is inside.

The cryogenic system of the experiment consists in the main dewar, the filters for Argon purification, and the filling/recirculation units. The filling unit is used during data taking for cryostat periodical refills from an external storage dewar, connected to the main one through a *Hydrosorb-Hopkalite* cartridge immersed in a LAr bath. During 2011 run, the consumption of Argon was measured in 900 l/day. The gas recirculation unit is used to counter the effect of outgassing: once extracted from the detector top, gaseous Argon is then made to pass through three standard filters in parallel and then recondensed and injected at the bottom of the cryostat. Nominal recirculation speed is 5 l/h. A further pump for liquid recirculation was later mounted, but it was only briefly used during 2011 data taking, normally keeping only the gas recirculation operational.

The inner and veto photomultipliers are managed by two different types of electronics: the signals from the veto PMTs are sent to 40, 8-channel, N914 CAEN boards. The analog sums of the signals are then sent to 5 CAEN V1724 digitisers, with sampling frequency of 100 MHz and resolution of 14 bits. The signals of the 37 inner detector photomultipliers are sent to 19 Aquiris Boards, DP235 Dual-Channel PCI Digitizer Card, with a sampling up to 1 GS/s and 8 bit dynamic range.

3.2.1. Trigger Configuration. The data acquisition (DAQ) system of the WArP detector is based on a double-level trigger specific of the inner volume that can be coupled to the trigger of the veto. The two systems are completely independent and can be operated separately to study the performance of the two devices. The overall system is managed by a dedicated LabView interface.

In principle the veto should operate in conjunction with the inner detector; however, when operated alone for tests, its trigger system is made to start the acquisition when the sum of the integrated signals from all the PMTs overcomes an overall threshold of 100 phe, set a priori.

The inner detector first-level trigger is a simple lower threshold on the signal height, which must be overcome by a minimum number of PMTs in coincidence, in order for the signal to be registered. The minimum number of coincident photomultipliers (multiplicity), as well as the threshold value, had to be set in order to effectively reject noise, without losing too many real signals. After test runs, the multiplicity was set to four and the threshold to 15 ADC counts (ADCc).

The second-level trigger consists in a live integration of the signal, starting with a short delay (100 ns) after its onset. Electron-induced pulses, dominated by the slow light component, are mostly integrated, while fast, recoil signals are almost completely skipped. By setting an upper threshold for the integrated pulses not to overcome, slow events are rejected, whereas fast events are accepted.

True rejection efficiency achieved with this procedure has yet to be evaluated, as it was not regularly implemented during data taking. Instead, only the first-level trigger was used, in order to collect electron-recoil data, mainly from ^{39}Ar decay, to test the detector response. A few dedicated runs were performed with the second-level trigger enabled, during which the acquisition rate was significantly lowered from 30–40 Hz to 12 Hz. Visual inspection of the collected data shows a significant depression of the ^{39}Ar spectrum, but not its complete disappearance. While quantitative analyses on this on-line rejection power have yet to be performed, the comparison of spectra already confirms the possibility of achieving at least partial background rejection *online*.

3.2.2. Detector History. The activities on WArP 1001 [38] started in 2005 when, prior to the detector construction, all the building materials were selected and tested for low radioactivity requirements. The inner detector and the veto were preassembled in Pavia laboratory, to test and qualify assembly procedures and mechanical tolerances. Later, the detector was disassembled and the components underwent special cleaning by an external industry before

being sent to LNGS. Meanwhile photomultipliers were heavily tested, both at room and LN_2 temperature. Manufacturer tests were followed by additional custom measurements. The tests regarded stability at room and LN_2 temperature, intrinsic noise evaluation, and compliance to specifications.

Main assembly started in LNGS Hall B in 2007: the external structures and the cryostat were mounted, while the detector was assembled in a dedicated clean room. In parallel PMT preassembly was carried on, as well as TPB evaporation on the inner surfaces. Final assembly took place in the clean room from June to December 2008. After all the PMTs had been tested in dark conditions, the detector was moved into the cryostat. Figure 5(b) shows the assembled detector ready to be inserted into the cryostat. The external cooling and purification systems were first installed in January 2009. At the same time the external lead shield walls were put in place; the installation of the lateral polyethylene external shield was started as well, but it was not completed.

The WArP 1001 detector experienced some technical issues, mainly related to HV distribution, which severely hindered operation in double-phase mode with a stable electric field in the liquid. The nominal operating drift field should have been of 1kV/cm. The detector first started commissioning in 2009, right after assembly was concluded, but a short circuit problem on the supply chain prevented its operation. Similarly, in 2010 detector was commissioned, but another HV failure again stopped its operation, after only two days of activity. Before attempting a novel start, some elements underwent further checks, due to detected instabilities on the photomultipliers: the elements of the PMT bases (resistors, capacitors) were again tested for stability at low temperature, and the veto PMTs were optically decoupled with *Kapton* foils.

After that, a third commissioning was started in 2011. All the internal volumes were evacuated starting in early April 2011. Vacuum pumping lasted about two months: once target pressure less than 10^{-4} mbar had been reached, pumping continued to ensure outgassing on the internal surfaces. During this phase, repeated washings with gaseous Argon were performed, to further lower water contaminations.

Vacuum pumping was stopped on May 25th, with a measured internal pressure of 1.4×10^{-5} mbar. Cooling phase then began, with the use of a liquid Argon serpentine, installed between the internal and external walls of the main cryostat. At the end of this phase, the measured residual pressure of water was around 3×10^{-9} mbar, while oxygen and nitrogen concentrations were, respectively, 10 and 100 times higher.

Within five days, below-zero temperature was reached uniformly inside the cryostat, and the filling phase began. Initial filling was performed during a two-day period, May 30th to June 1st, with 6.0 commercial liquid Argon. The load liquid was further purified before injection, by passing through an external *Hopkalite* filter immersed in a LAr bath. Initially the liquid was used to further cool down the inner volume; one of the Argon lines was left open to

vent the produced excess gas; after this first phase, filling proceeded at a speed of 500l/h. This last stage ended after the inner polyethylene shield had been submerged. Right after completion, the GAR recirculation unit was turned on; later also the liquid recirculation pump was put into operation. Finally the voltage supply for the veto and inner detector photomultipliers was turned on, successfully ending commissioning.

Data acquisition took place from July 24th to November 21st. The first tests on HV supply were carried on one week after filling, down to -45 kV without problems (i.e., discharges). At the beginning of July, the official raise of the field was started. Foreseen to reach -60 kV in two days, the procedure was stopped at -20 kV, when an instability occurred, followed by an anomalous current flow. This prevented the achievement of nominal field conditions at 1kV/cm. Despite this problem, data taking with electric field began, starting with -10 kV supplies.

Later, HV supply could be slowly raised, and the highest *stable* field reached during data taking was 270 V/cm, that is, a voltage of -25 kV. Runs were also taken at -27 , -30 kV, but discharges were usually experienced. The system seemed to deteriorate under continued stress, as back-to-back runs caused higher rate of discharges with time. Acquiring data in zero-field conditions for a time led to more stable conditions, allowing running steadily without further discharges. After the decommissioning, the inner detector was extracted and opened: a deterioration of the insulation of the HV cable was found, as well as a temperature-probe cable disconnected and floating free in the liquid inner volume. The HV problems led to the early end of the 2011 run and to ultimate closure of the WArP programme.

4. 2011 Data Analysis

During the 2011 campaign 151 runs were acquired in zero-field conditions. Of them, 121 are in “standard mode,” that is, with a 15 ADCc threshold for the signal registered by the single PMTs and with acquisition triggered by coincident firing (multiplicity) of 4 units. The remaining 30 runs are not considered here, as they were expressly used to test different thresholds, multiplicities, and the second level trigger. 13.718.000 total events were collected.

On the other hand, 66 runs were taken in nonzero field conditions, for a total of 1.059.000 events, although in different configurations. The second and third grids (G2 and G3), independently fed, were always kept at $V(G2) = +900$ V, $V(G3) = -700$ V, to provide, respectively, electron extraction/multiplication and then collection on G3. HV supply was brought from -10 to -30 kV, for a corresponding drift field ranging from 90 to 330 V/cm. Electron drift velocity in these field conditions lies in the range $0.499 \div 1.297$ mm/ μ s [39, 40].

4.1. Background Sources. The 1001 detector has been described by Monte Carlo simulations, both with FluKa [41] and GEANT4 [42] packages, before its actual construction [22, 27]. The main goal of these simulations was to evaluate

the main sources of background expected during data taking and then to estimate the minimum rejection power needed to eliminate the spurious signals.

Two main sources of background are present:

- (i) electron recoils produced by β/γ emitters, which may be misrecognized as nuclear recoils;
- (ii) nuclear recoils produced by elastic scattering of neutral particles like neutrons and, possibly, neutrinos.

As regards electrons, the main elements to be considered are Argon isotopes (^{39}Ar , ^{41}Ar , ^{42}Ar), ^{85}Kr , and ^{42}K , all β^- decaying. Calculations show that all contributions are negligible with respect to ^{39}Ar , which produces, in the acceptance energy window of the experiment, some 10^7 events in 100 days of acquisition. To be able to exclude these events, it is necessary to apply the combined analysis on pulse shape and $s2/s1$ ratio. Electron events can also be produced by γ -emitters from the U, Th, K chains, trapped in the building materials. While such events can be rejected by exploiting both pulse shape discrimination and $s2/s1$ ratio, as for β^- decays, further means are available in this case: it is expected that low energy γ 's ($E < 30\text{ keV}$) would interact via photoelectric effect near the detector walls (where they are produced). Then volume cuts should allow to get rid of such events. On the other hand, γ 's with higher energy ($E > 30\text{ keV}$) could produce multiple Compton scatterings: in this case rejection can be achieved by resolution of multiple events.

Neutrons sources are varied: they are produced in fission or (α, n) reactions of the radioactive contaminants in the building/surrounding materials, or following cosmic rays interactions. Moreover, a component from environmental radioactivity is expected: the measured neutron flux (for energies above 1 MeV) in LNGS [43] is $6 \times 10^{-7}\text{ cm}^{-2}\text{ s}^{-1}$; the external polyethylene shield is expected from simulations to reduce this flux by a factor 5×10^4 . Neutron-induced nuclear recoils mimic WIMP interactions; however, they are likely to produce multiple interactions, due to their much higher cross section. Simulations were used to evaluate the amount of neutron events that cannot be rejected, according to the radioactive content of the building materials and as a function of the signal thresholds used for the veto and inner detector. The best way to reject these events is to detect double interactions, either in the inner volume alone or both there and in the veto. Thus, the active shield threshold should be in principle as low as possible. The expected values of light yield for the 100 l detector, extrapolated before construction from the 2.3 l data in zero-field conditions, were 3.5 (3.0) phe/keV in the inner detector (veto) for electron events and ≈ 0.65 phe/keV in both volumes for nuclear recoils. With these values and assuming thresholds of 30 keV in the two detectors, simulations reported that the main source of background neutrons came from inner photomultipliers; with the help of veto and resolution of multiple interactions, the number of residual unvetoes events was estimated to be around 3/year.

Finally, neutrino-nucleus elastic scatterings (from solar and cosmic-ray neutrinos) can induce recoil events in the

same energy region selected for WIMPs. Given the weak cross sections involved in this case, passive/active shielding is of no use and this background is *irreducible*. However, the cosmic neutrino flux at LNGS is estimated in $\approx 11.5\text{ cm}^{-2}\text{ s}^{-1}$ [44], yielding an event rate in the energy range of interest of the order of 10^{-6} event/day. Such a rate is negligible over a data-taking period of a few years.

In the original WArP proposal, the goal for background rejection was set at a limit of *1 event in 100 days* wrongly recognised. The tests on the 2.3 l chamber [22, 28] show that at least it is possible to achieve a 10^{-4} rejection power for electron events for each of the two, independent analysis techniques. Given that the strongest source of electron background events was evaluated in some 10^7 event in 100 days within the detector acceptance window, as mentioned, the evaluated combined rejection power should allow reaching the requested goal.

The operation of the 100 l detector in 2011 showed lower values of light yield (discussed in the next sections); then background evaluations need to be rerun to correctly fit the new acceptance windows of the detector, in terms of collected photoelectrons. This has been possible thanks to a new, recently developed simulation [37], able to reproduce the light yield data of the 2.3 l prototype and of a 0.7 kg chamber used for PMT testing. The code has been validated on both chambers and it can now be applied to the 100 l detector with two main objectives: (i) rerun, as said, the background evaluation, possibly in parallel with older codes to check results and (ii) study the effect of growing detector dimensions on light loss and collection (i.e., variations in light yield, given the same used materials and photocathode coverage).

A further source of background is related to α -emission. This is mainly due to ^{222}Rn which, with a half-life of 3.82 d, should rapidly disappear from the data (as demonstrated in [22] for the 2.3 l prototype). However, in the 2011 campaign a significant presence of such events was steadily recorded, meaning a source of Radon was present inside the detector, continuously contaminating it. The presence of Radon is a very dangerous background for the experiment, as α -particle signals share similarities with nuclear recoils (mostly regarding the primary pulse shape). Unfortunately, so far it has not been possible to identify the source of Radon contamination inside the detector and act to remove it.

4.2. Data Code. The data analysis code for the 100 l detector has been developed on the 2.3 l prototype data. It basically operates in two steps: first, for each run the initial 5000 collected triggers are used to produce the single electron response (SER) of each photomultiplier that is then saved in a database. This represents the response of the PMT to single impinging photons and it is used to calibrate the instrument [45].

Later, single triggers are analysed: the start of primary pulse on each PMT waveform is searched for and then checks for signal saturation are performed. Baseline and noise information (RMS and peak-to-peak) is calculated in the pretrigger window ($2\ \mu\text{s}$ wide). The waveform is then reversed

(positive edge) and the baseline is set to zero. To obtain the primary pulse amplitude, an integration of the waveform over $7 \mu\text{s}$ after trigger is done, while the fast component is set as the fraction of signal integrated in the first 80 ns after onset. If the primary signal is not saturated, then a secondary pulse is searched for and reconstructed as well. This is done for each PMT; then the signal intensity is normalized to the respective SER, to be expressed in phe. Finally, the summed up signals (s_1 and s_2) are calculated. An example of summed signals is shown in Figure 6 for the different cases of electron-driven events and α -particles ones.

Ancillary routines allow then to (i) visually inspect each single PMT waveform, to check reconstruction problems; (ii) perform more detailed analyses on single waveform, like Fast Fourier Transform (FFT) to study noise sources; (iii) create an average waveform for the run: according to the measurements performed on N_2 contamination [29], the fitted value for the slow decay-time constant τ_s can be used to estimate the amount of light-quenching impurities.

The code was developed on 2.31 prototype data; then it had to be slightly adapted to the different conditions of the 1001 detector. This was also due to the nonstandard conditions of operation: a far lower drift field than planned, meaning longer drift times, and an unidentified source of noise at 250 kHz in the data. This only slightly affected primary reconstruction but could hinder reconstruction of long waveforms containing secondary pulse. The code has been modified during and after data taking (for details see [37]), and now it should be possible to recover field-on data affected by this noise superimposed on the waveforms.

4.3. Veto Data. The veto has been operated mainly independently during data taking. The response of the detector in terms of light yield has been evaluated through analysis of both electron recoils and α -induced signals. Calibration to electron recoils was done with a ^{60}Co source inserted in the detector next to the inner structure: two gamma lines were detected (though not resolved) at 1.17 and 1.33 MeV. On the other hand, calibration to α -particles was possible due to the presence of events from the ^{222}Rn chain: peaks from ^{222}Rn (5.59 MeV), ^{218}Po (6.11 MeV), and ^{214}Po (7.83 MeV) were identified in the background spectrum. The analysis of both sources, after correcting for the difference in response between α -particles and electrons, led to a corresponding light yield evaluation of

$$LY_{\text{veto}} \sim 0.53 \text{ phe/keV}. \quad (2)$$

This result is approximately 6 times smaller than extrapolations from the 2.31 prototype. The reason of this is yet to be fully understood, the main possibilities under investigation being a lower-than-evaluated quantum efficiency of the PMTs of the veto and/or an underestimated effect of the increasing detector dimensions on light survival. A new simulation of the 1001 detector, with the mentioned newer code used to reproduce the prototype chambers results, could possibly help verifying such hypotheses.

TABLE 2: Summary of light yield measurements from calibration lines (gamma sources) and background measurements, performed in November 2011. Errors from fits are negligible. Errors on LY for γ -sources are taken as the sigma of the photo-peak distribution.

Nuclide	γ -Energy (keV)	LY (phe/keV)
^{60}Co	1173	1.54 ± 0.10
^{60}Co	1335	1.57 ± 0.06
^{133}Ba	356	1.55 ± 0.14
^{137}Cs	662	1.54 ± 0.09
Bkg	Endpoint (keV)	LY (phe/keV)
^{39}Ar	565	1.58

4.4. Inner PMTs Characterization. The data collected with the inner detector in zero-field conditions were firstly used to characterise the 37 photomultipliers and to inspect the system stability over time [37, 46]. Data from 22 August to 21 November are considered, for a total of 92 live days. For each PMT three parameters are investigated, namely:

- (i) the gain, derived from the SER peak information: it measures the number of charges collected at the anode of the PMT per photoelectron produced at the cathode [45];
- (ii) the noise, root-mean-square (RMS) and peak-to-peak (PP), evaluated in the pretrigger window;
- (iii) the counting rate, evaluated in the waveform region 8 to $13 \mu\text{s}$ after the primary signal onset.

Five of the 37 PMTs were found to be nonworking at the start of data taking; therefore, in that case only the noise parameter was evaluated.

The gain data reveal an overall stable behaviour for most channels, centred on a value of $2 \times 10^6 e^-/\text{phe}$. Few variations can be explained by changes in the DAQ configuration (e.g., reevaluation of some baselines). Only one channel shows significant instability, which can be ascribed to a malfunctioning of the PMT itself.

Noise values vary between the different channels, ranging from 0.15 to 0.3 mV for RMS and from 1.1 to 2 mV for peak-to-peak. However, there is a remarkable correspondence between RMS and PP behaviors for each PMT, which ensures that no spurious peaks are wrongly labelled as good signals; moreover, very similar values are obtained for consecutive even-odd channels (e.g., 0-1, 2-3) which are read by the same acquisition board. This means that the detected noise can be related also to the boards themselves rather than only to the PMTs.

The rate data show a wide range of values, from 1-2 kHz to ≈ 20 kHz. However, each PMT has a quite stable behaviour, only interrupted by a significant increase during a 15-day period, when the detector underwent a lot of stress, with repeated insertions of γ -calibration sources and several attempts to run in field-on conditions. After this period the rates lower again, demonstrating that the PMTs felt the changes but were able to recover later. Moreover, no corresponding decrease in gain was registered, which means that light collection system worked properly and the detector

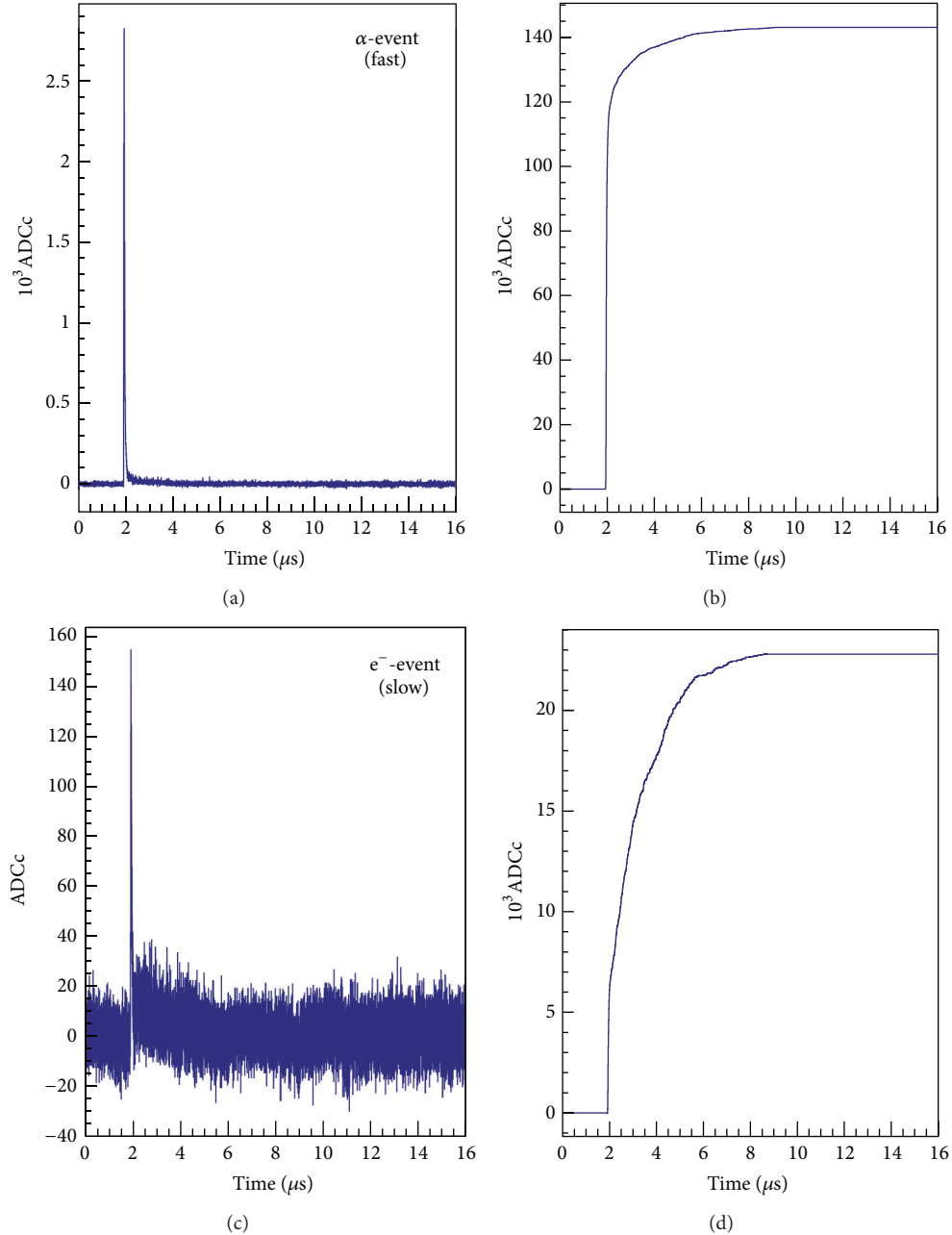


FIGURE 6: ((a), (b)) Total reconstructed waveform (sum of 37 PMTs, (a)) and integrated signal (b) for an α -induced event in the inner detector. ((c), (d)) The same for an electron event. The difference in the relative weight of the fast and slow light components in the two classes of events is clearly visible in the rise times of the integrated signals, with the upper one being much smaller than the lower one (i.e., dominating fast component for the α -particle event).

was able to recover from solicitations, allowing for a years-long data taking period.

4.5. Inner Data, Zero Field. Runs in zero-field conditions were also used to study the detector response to different particles, in terms of light yield. Response to electron-like events was obtained by fitting the peaks of various γ -calibration sources and the β -spectrum of ^{39}Ar , as shown in

Table 2. An average value of $1.4 \div 1.6$ phe/keV was measured over the whole acquisition period, slightly increasing with time. The value is compatible with the few measurements made on ^{39}Ar 2010 data (1.6 phe/keV). The evolution of light yield was investigated in the same period chosen for PMT characterization. As mentioned, a slight increase is detected over time, which is ascribed to a stabilisation of the detector with time, despite the technical HV problems. A 15-day period shows higher LY ~ 1.75 phe/keV, corresponding to

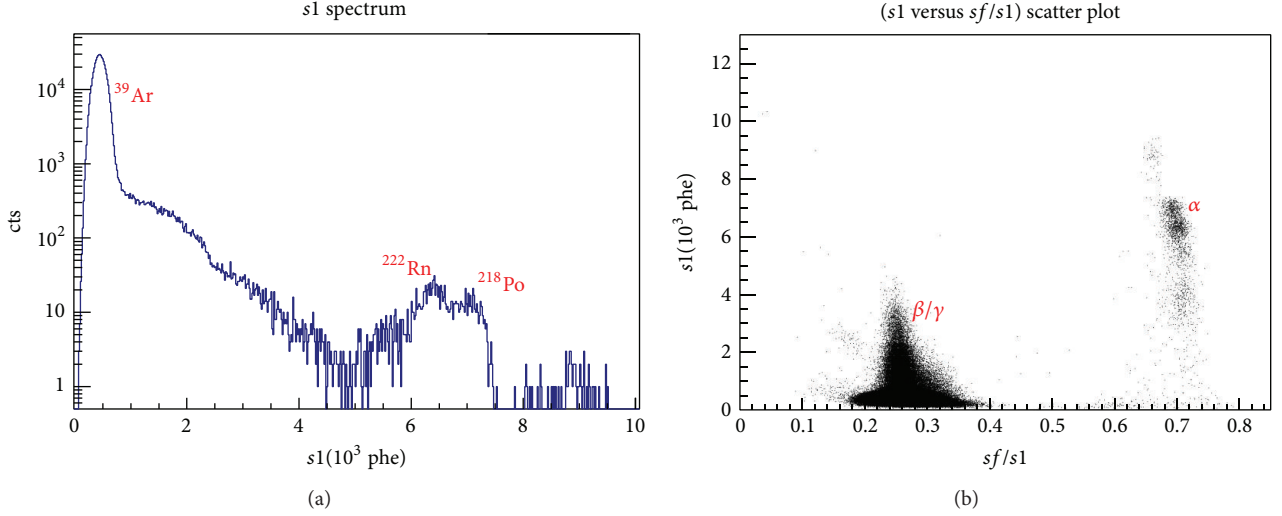


FIGURE 7: Primary signals collected with the WArP 100l detector in 2011: (a) primary energy spectrum in units of phe. The low energy region is dominated by the ^{39}Ar β -spectrum, then at higher energies signals from other radioactive contaminants are present. The α -peaks of ^{222}Rn and ^{218}Po are visible at $6\text{--}7 \times 10^3$ phe; (b) ($s1$ versus $sf/s1$) scatter plot, showing the separation between slow events, induced by β/γ radiation, and fast ones, mostly due to α -decays.

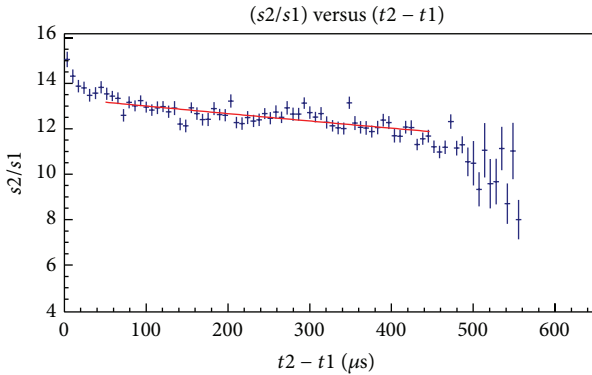


FIGURE 8: $s2/s1$ ratio as a function of drift time ($t2 - t1$). The region used for an exponential fit (red line) allows estimating the electron life time. The decrease of the $s2/s1$ value for the highest drift times is related to few badly reconstructed events near the cathode.

runs acquired with a higher single PMT threshold (25 ADCc instead of 15).

The reason of this could be due to the fact that, with a 15 ADCc threshold, noise rejection is not perfected, which could slightly lower the estimated response of the single PMTs and then the overall system response. However, the higher value of the threshold also increased the low-energy threshold of the recorded spectrum, cutting away most of the interesting window for WIMP interactions; therefore, the single PMT threshold was brought back to its original value, which represents a value of compromise.

In the data, the α -peaks of the ^{222}Rn chain can be recognised, as in the veto (see Figure 7(a)), but the signals are mostly saturated; therefore, no reliable evaluation of light yield could be performed in this case.

4.5.1. Pulse Shape Analysis. By studying the fraction of fast signal component per event versus the total pulse, it is possible to check the discrimination achieved for different classes of interacting particles: as seen in Figure 7(b), two distinct populations can be recognised. The one with $sf/s1 \sim 0.3$ represents events dominated by the *slow* scintillation light component; they are mainly due to ^{39}Ar decay and γ -background events. On the other hand, the population at $sf/s1 \sim 0.7$ is instead due to *fast* events, and it can be roughly divided in three groups. The events with >6000 phe are mainly due to ^{222}Rn chain α -decays. The region around $3000\text{--}4000$ phe shows a group of events not yet identified, but which could be due to low energy α -decays of the Thorium chain. Finally in the region around 100 phe there is a group of events that could be due to background neutrons or α -decay byproducts of contaminants in the detector walls. 3D localization is necessary to resolve the nature of this group. The recognition of a population of neutrons would be useful to test the detector to nuclear recoils, as there has not been, during the 2011 campaign, the possibility to insert neutron calibration sources.

4.6. Inner Data, Field-On. To verify the dependence on $\mathcal{E}_{\text{drift}}$ of the recombination process in Argon, the value of the light yield was measured with different field configurations, on ^{39}Ar spectra. A decrease was expected in the collected primary light (light yield), due to more ionization electrons being drifted away by the electric field. Indeed it was registered, at a field of 330 V/cm, a 32% reduction of primary light output, with respect to zero-field conditions. This is in agreement with previous studies on light/charge yield variations, as a function of the drift field intensity [47].

Field-on data can of course also be used to study the $s2/s1$ ratio and the possibility to perform particle discrimination

TABLE 3: Effective electron lifetime and signal attenuation (for particles travelling the whole volume) estimated for two-field values in WARp 100 l.

$\mathcal{E}_{\text{drift}}$ (V/cm)	210	330
Drift time t_{drift} (μs)	544 ± 2	462 ± 1
$\langle s2/s1 \rangle$	7	13
Fitted τ_e (μs)	≈ 1400	≈ 3800
e^- signal attenuation	33%	12%

based on this. As mentioned above, the original analysis code was usually characterised by a bad reconstruction of secondary events. Modifications were carried on since then. Presently, only a small fraction of the available data has been correctly reanalyzed; however, preliminary analyses have been performed.

The behaviour of $s2/s1$ as a function of drift time (indicated as $t2 - t1 = t_{\text{drift}}$) has been studied for electron recoils, and it is shown in Figure 8. Extremely pure Argon would result in a stable $s2/s1$ ratio for signals from the whole chamber; on the other hand, a decrease of the ratio as a function of the distance from the liquid surface is the evidence of the presence of the mentioned electronegative impurities (O_2 , H_2O) that can attach drifting electrons (see Section 2.1). The distance to the surface is directly proportional to the drift time through the electron drift velocity. In Table 3 the obtained average values of $s2/s1$ are shown for electron recoils, along with estimates for the effective electron life time, τ_e , and the corresponding signal attenuation within the chamber.

Electron life time is inversely proportional to impurity concentration, through a *rate constant* (see [30]) that is slightly decreasing with increasing field. However, here one should also take into account the effect of the issues in reconstruction of secondary signals: while an increase of τ_e with the field is expected, the difference between the reported values is also dependent on the mentioned dispersion of reconstructed data. This implies a significant uncertainty on the measurements, which should be taken as evaluations.

4.6.1. 3D Localization. In principle, 3D localization can be performed on secondary signals, as they are generated next to the photomultipliers: then the amount of direct light hitting the PMTs is much higher than the diffuse component resulting from reflections on the walls. The situation is inverted for primary signals. A correct reconstruction of $s2$ is fundamental to obtain reliable localization.

An algorithm has been developed and tested on Monte-Carlo-generated secondary signals [48], with the aim of reconstructing the position of the simulated pulse in the plane of the photomultipliers (x, y plane). It is essentially based on the formula used to calculate the barycentre of the light signals, starting from the relative weights of the amount of photons collected by the single PMTs. As a first precaution, an ‘‘artificial’’ signal has to be assigned to nonworking PMTs as, even if we do not read their signal, we must assume that photons arrive also on them. To do this, it was decided to assign to these PMTs an amount of

light that resulted from the mean of the light collected by surrounding photomultipliers. After the rough position is reconstructed, two main corrections have to be applied: first, the amount of light collected by the external PMTs has to be rescaled, because it contains a significant amount of the reflected component that in an ideally infinite system would end up in farther devices. Such correction has been evaluated on its own and it has been later applied to all rings of PMTs, which receive less and less reflected light, from the outermost to the central one.

The second correction is related to the fact that, to calculate the event position, the central coordinates of the PMTs are used. Therefore, reconstructed positions tend to accumulate on these points, and there are no events outside the external ring of PMT centres. To correct this, detector slices of 5° in the angular variable have been defined. For each of these slices, the correlation function between the reconstructed (R_{rec}) and the MC-generated (R_{MC}) radial positions of the events has been derived. Ideally, for perfect reconstruction, the function $R_{\text{rec}}(R_{\text{MC}})$ should be a straight line with angular coefficient equal to 1; the use of central PMT coordinates to calculate the event position and the fact that the system is finite, however, introduce deviations in this function, especially in the outermost region. By inverting the obtained relation and applying it to the reconstructed MC data, it is possible to correct the bias in the distribution of positions, so that the dimensions and circular shape of the detector are well reproduced. The error on the reconstructed positions, evaluated on MC data after corrections, was estimated to be ≈ 1 cm, to be compared with the PMT minimal diameter, 4.6 cm. In Figure 9 the distribution of errors in the reconstruction for the MC data is shown: on the left the error before corrections is displayed, on the right after corrections.

The algorithm was then applied to a sample of reanalyzed events (25000), from a run taken with $\mathcal{E}_{\text{drift}} = 330$ V/cm: actual data must also be corrected for the different response of the single PMTs (in terms of phe). A small convergence on PMT centres is still visible and not removable; moreover, the reconstructed plane maintains a hexagonal-like shape (see Figure 10), which disappears in the MC data after the discussed corrections are applied. The hexagon is rotated with respect to the shape obtained before the radial correction, which is related to the PMTs positions. This is due to the reflector foils on the inner walls: the foils are fixed in six points and could have contracted during the cooling down at LAr temperature. The absence of nonworking PMTs is well visible, in Figure 10(b), for pairs 5, 11 and 31, 26, which are next to each other: in these cases regions of lower density of points are visible. PMT 33, though being on the border, is completely surrounded by working devices, and the distribution of reconstructed position clusters on its central coordinates, much like for working PMTs.

The information related to the drift coordinate (z) can then be obtained from the knowledge of the drift time and velocity. The error on this value is estimated in 3 mm, deriving from the propagation of the uncertainties on $t1$, $t2$ onsets (≈ 300 ns) and on the liquid level position (2 mm). The uncertainty on v_{drift} , which was measured in [39, 40], is instead negligible. By adding the z information, it has

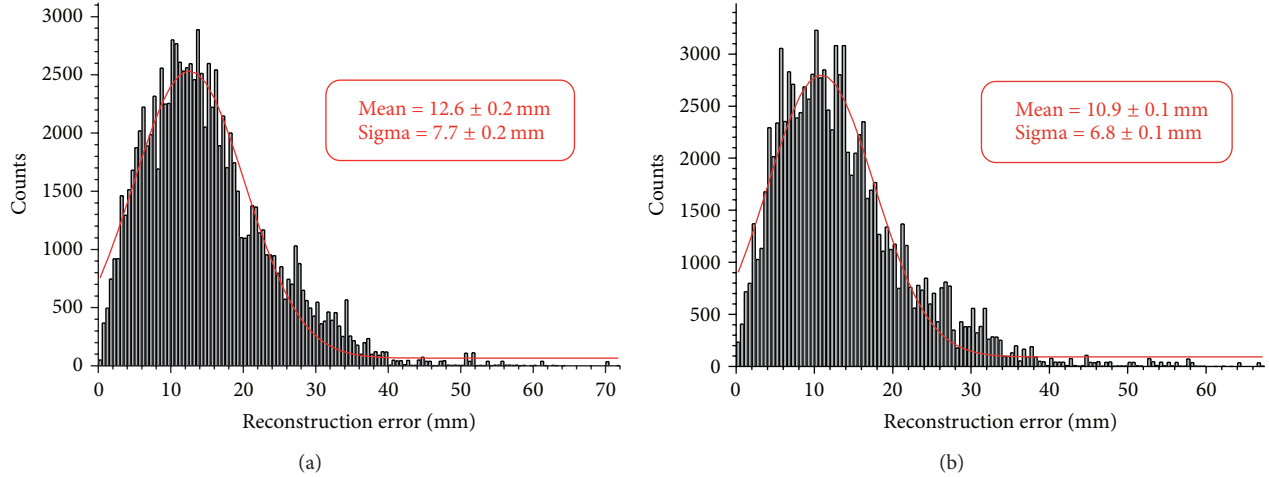


FIGURE 9: (a) Distribution of errors on reconstruction of the event position, for the sample of MC data, before corrections. (b) The same, after corrections. The error is the absolute difference between the real and reconstructed position.

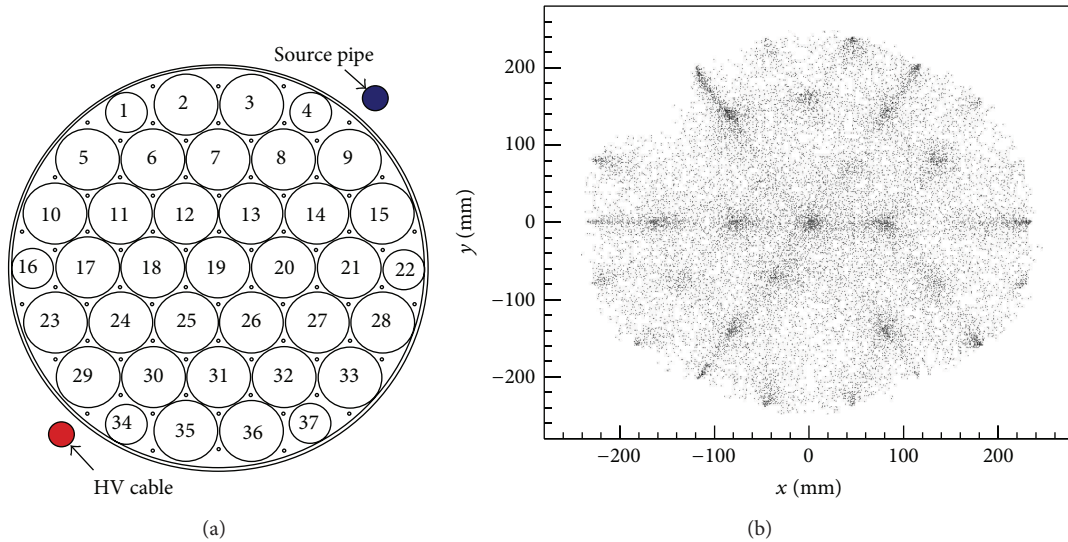


FIGURE 10: Reconstructed positions of 25000 events from the 2011 WArP run (b), to be compared with the actual PMT disposition (a). Nonworking PMTs are numbers 5, 11, 26, 31, and 33.

been verified that the detector profile is correctly reproduced: this is visible in Figure 11(a). In Figure 11(b) the distribution of events wrongly reconstructed outside the detector is reported, as a function of the distance from the wall. These events show a slightly larger tail than the estimated resolution for two reasons: first, the plot is a 1D projection of the detector external conical profile, which causes some smearing of the distribution. Secondly, external events lack, by definition, a farther outer ring of PMTs which would help calculating the correct position of the event with the adopted method: it is expected that in this boundary region errors could be slightly larger than in the inner part of the detector.

5. Conclusions

The WArP programme represents one of the first attempts to exploit the properties of scintillating noble liquids in double

phase, as a means to discriminate β/γ -interactions from nuclear recoils, in order to perform dark matter searches. A powerful, years-long R&D program, concentrated on Argon, has been carried on over the years, to study cryogenic detectors and materials and the background rejection technique based on signals produced in Argon (Sections 2.1 and 3.1). The R&D program led to the construction and operation of a 2.3l chamber, which demonstrated the high rejection power achievable with the mentioned techniques and was used to perform a physics run at the Gran Sasso laboratories. This was used to set limits on the WIMP (m, σ) parameter space, excluding the DAMA positive results.

The next step of the program was a 100l detector, whose projected sensitivity was expected to almost match present best results in the field. The detector was built and operated at LNGS, but issues related to HV distribution hindered the possibility of performing a physics run. This ultimately led to

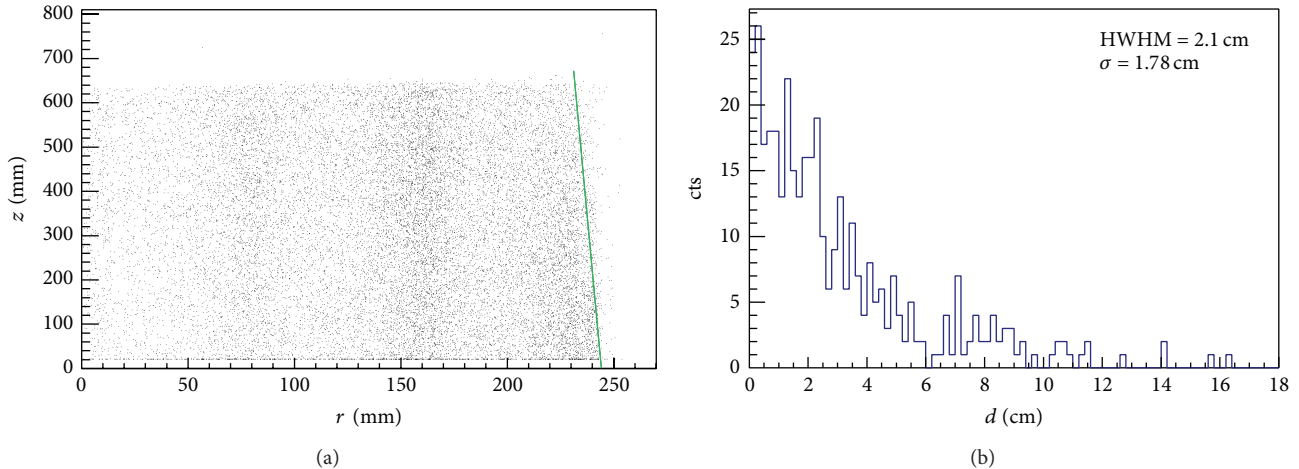


FIGURE 11: (a) Distribution of real events positions in the (z, r) plane, where z is the distance from the liquid level and r is the reconstructed radial coordinate, as derived from (x, y) information. The truncated-cone shape of the detector is well reproduced (upside-down in this view): the real slope, $s_r = -62$, is to be compared with the one fitted from the data, $s_{rec} = -61 \pm 1.4$. Denser regions correspond once again to the radial positions of the photomultipliers. (b) Distribution of events wrongly reconstructed outside the detector walls, as a function of their distance d from the walls (details in text).

the program premature closure. Anyway in 2011 a five-month technical run was performed: data are still being analysed to characterise the detector response from a technical point of view. The analysis of the primary signals shows stability of the light collection system (PMTs), though with a measured light output lower than expectations; it is also tested the PMTs ability to recover from solicitations (due to HV problems). In the same way the analysis of secondary signals shows that they can be used to perform precise 3D localization of the events position. Preliminary analyses show that discrimination based on pulse shape analysis on primary signals can be achieved and used to partially reject *online* electron-induced events. Quantitative evaluation of the rejection power for the full-scale, 100 l detector is still to be performed.

Though the response of the detector in terms of collected light (Light Yield) is lower than predicted, the work carried on so far suggests that it can be a reliable instrument. Mentioned issues on HV stability are not related to the proposed detection technique. The technology was proven to be an effective means to perform dark matter searches (see Section 3.1); the use of Argon that couples pulse shape analysis to the s_2/s_1 discrimination, also used in Xenon-based experiments, can lead to more stringent background rejection with respect to other techniques. Indeed, the implemented technology and gathered experience during the life of the WArP project can prove useful to the community for the successful outcome of other present and future LAr-based experiments, like, for example, ArDM [49] and DarkSide [50].

Conflict of Interests

The author declares that there is no conflict of interests regarding the publication of this paper.

Acknowledgments

This document summarises all the years of work and efforts by the members of the WArP Collaboration, as well as the results obtained during this period; it is written on behalf of the collaboration. The author wishes to thank the INFN for the support given to the program during its lifespan and the Gran Sasso Laboratories which made facilities and staff available during the periods of operation. This experiment started as a spinoff of the major technological advances provided by the ICARUS Collaboration, without whom this work could not have been carried on. The WArP programme has been supported since March 2006 by the National Science Foundation under Grant no. PHY-0603376. Funding from the NSF allowed developing upgraded electronics, which permitted obtaining the presented results on pulse shape discrimination. The author wishes to acknowledge the dedication and professionalism of the personnel of the sections of the INFN mechanical and electronics workshops that have designed and built the components of the 2.3 l and 100 l detectors. The author also acknowledges all the people of the LNGS staff that collaborated in the construction and installation of the detectors, from the underground operations to the chemical, mechanical, and electronics services.

References

- [1] Full list of Planck papers can be found at ESA site, A&A, <http://www.rssd.esa.int/index.php?project=planck>.
- [2] Planck Collaboration, Planck 2013 results. XVI. Cosmological parameters, 2013, <http://arxiv.org/abs/1303.5076>.
- [3] J. Beringer, J. F. Arguin, and Particle Data Group, "Review of particle physics," *Physical Review D*, vol. 86, Article ID 010001, 2012.

- [4] G. Jungman, M. Kamionkowski, and K. Griest, "Supersymmetric dark matter," *Physics Report*, vol. 267, no. 5-6, pp. 195–373, 1996.
- [5] J. D. Lewin and P. F. Smith, "Review of mathematics, numerical factors, and corrections for dark matter experiments based on elastic nuclear recoil," *Astroparticle Physics*, vol. 6, no. 1, pp. 87–112, 1996.
- [6] E. Aprile, M. Alfonsi, XENON Collaboration et al., "Dark matter results from 100 live days of XENON100 data," *Physical Review Letters*, vol. 107, Article ID 131302, 2011.
- [7] E. Aprile et al., "Dark matter results from 225 live days of XENON100 data," *Physical Review Letters*, vol. 109, Article ID 181301, 2012.
- [8] D. S. Akerib, H. M. Araujo, X. Bai et al., "First results from the LUX dark matter experiment at the Sanford underground research facility," *Physical Review Letters*, vol. 112, Article ID 091303, 2014.
- [9] R. Bernabei, P. Belli, F. Cappella et al., "DAMA/LIBRA results and perspectives," *Journal of Physics: Conference Series*, vol. 375, Article ID 012002, 2012.
- [10] CoGeNT Collaboration, C. E. Aalseth, P. S. Barbeau et al., "Results from a search for light-mass dark matter with a p -type point contact germanium detector," *Physical Review Letters*, vol. 106, Article ID 131301, 2011.
- [11] CoGeNT Collaboration, C. E. Aalseth, P. S. Barbeau et al., "Search for an annual modulation in a p -type point contact germanium dark matter detector," *Physical Review Letters*, vol. 107, Article ID 141301, 2011.
- [12] G. Angloher, G. M. Bauer, I. Bavykina et al., "Results from 730 kg \cdot days of the CRESST-II dark matter search," *The European Physical Journal C*, vol. 72, article 1971, 2012.
- [13] Amerio, S. S. Amoroso, and M. Antonello, "Design, construction and tests of the ICARUS T600 detector," *Nuclear Instruments and Methods in Physics Research A: Accelerators, Spectrometers, Detectors and Associated Equipment*, vol. 527, no. 3, pp. 329–410, 2004.
- [14] P. Benetti, E. Calligarich, R. Dolfini et al., "Dolfini Detection of energy deposition down to the keV region using liquid xenon scintillation," *Nuclear Instruments and Methods in Physics Research A: Accelerators, Spectrometers, Detectors and Associated Equipment*, vol. 327, no. 1, pp. 203–206, 1993.
- [15] D. Cline, A. Curioni, A. Lamarin et al., "A WIMP detector with two-phase xenon," *Astroparticle Physics*, vol. 12, no. 4, pp. 373–377, 2000.
- [16] M. Miyajima, T. Takahashi, S. Konno et al., "Average energy expended per ion pair in liquid Argon," *Physical Review A*, vol. 9, article 1438, 1974.
- [17] T. Takahashi, M. Miyajima, S. Konno, and T. Hamada, "The W -value of liquid Argon," *Physics Letters A*, vol. 44, no. 2, pp. 123–124, 1973.
- [18] J. Lindhard, V. Nielsen, and M. Scharff, "Integral equations governing radiation effects," *Matematisk-Fysiske Meddelelser, Udgivet af Det Kongelige Danske Videnskabernes Selskab*, vol. 33, no. 10, p. 1.
- [19] J. Lindhard, V. Nielsen, and M. Scharff, "Range concepts and heavy ion ranges," *Matematisk-Fysiske Meddelelser, Udgivet af Det Kongelige Danske Videnskabernes Selskab*, vol. 33, no. 14, p. 1.
- [20] P. J. William and J. Sadauskis, "Alpha-particle ionization in pure gases and the average energy to make an ion pair," *Physical Review Letters*, vol. 90, p. 1120, 1953.
- [21] G. L. Cano, "Total ionization and range of low-energy recoil particles in pure and binary gases," *Physical Review Letters*, vol. 169, p. 277, 1968.
- [22] L. Grandi, *WARP: an Argon double phase technique for dark matter search [Ph.D. thesis]*, 2005.
- [23] A. Hitachi, T. Takahashi, N. Funayama et al., "Effect of ionization density on the time dependence of luminescence from liquid Argon and xenon," *Physical Review B*, vol. 27, article 5279, 1983.
- [24] P. Benetti, F. Calaprice, E. Calligarich et al., "Measurement of the specific activity of ^{39}Ar in natural Argon," *Nuclear Instruments and Methods in Physics Research A*, vol. 574, pp. 83–88, 2007.
- [25] D. Acosta-Kane, R. Acciarri, and O. Amaize, "Discovery of underground Argon with low level of radioactive ^{39}Ar and possible applications to WIMP dark matter detectors," *Nuclear Instruments and Methods in Physics Research A*, vol. 587, p. 46, 2008.
- [26] C. Rubbia, "The liquid-Argon time projection chamber: a new concept for neutrino detectors," Tech. Rep. CERN-EP/77-08, 1977.
- [27] WARP Collaboration, <http://warp.lngs.infn.it>.
- [28] P. Benetti, R. Acciarri, WARP Collaboration et al., "First results from a dark matter search with liquid Argon at 87 K in the Gran Sasso underground laboratory," *Astroparticle Physics*, vol. 28, no. 6, pp. 495–507, 2008.
- [29] WARP Collaboration, R. Acciarri, M. Antonello et al., "Effects of nitrogen contamination in liquid Argon," *Journal of Instrumentation*, vol. 5, Article ID 06003, 2010.
- [30] R. Acciarri, M. Antonello, WARP Collaboration et al., "Oxygen contamination in liquid Argon: combined effects on ionization electron charge and scintillation light," *Journal of Instrumentation*, vol. 5, Article ID 05003, 2010.
- [31] R. Acciarri, M. Antonello, F. Boffelli et al., "Demonstration and comparison of photomultiplier tubes at liquid Argon temperature," *Journal of Instrumentation*, vol. 7, Article ID 01016, 2012.
- [32] F. Pröbst, "Results of CRESST phase I," *Nuclear Physics B*, vol. 110, no. 2, pp. 67–69.
- [33] EDELWEISS Collaboration, V. Sanglard, A. Benoit et al., "Final results of the EDELWEISS-I dark matter search with cryogenic heat-and-ionization Ge detectors," *Physical Review D*, vol. 71, Article ID 122002, 2005.
- [34] CDMS Collaboration, D. S. Akerib, J. Alvaro-Dean et al., "New results from the cryogenic dark matter search experiment," *Physical Review D*, vol. 68, Article ID 082002, 2003.
- [35] D. Abrams, D. S. Akerib, and M. S. Armel-Funkhouser, "Exclusion limits on the WIMP-nucleon cross section from the cryogenic dark matter search," *Physical Review D*, vol. 66, Article ID 122003, 2002.
- [36] D. S. Akerib, J. Alvaro-Dean, M. S. Armel-Funkhouser et al., "First results from the cryogenic dark matter search in the Sudan underground laboratory," *Physical Review Letters*, vol. 93, Article ID 211301, 2004.
- [37] A. Zani, *Development and operation of large volume Liquid Argon detectors for rare events detection [Ph.D. thesis]*, 2013.
- [38] Acciarri, R. M. Antonello, B. Baibussinov et al., "The WARP experiment," *Journal of Physics: Conference Series*, vol. 203, Article ID 012006, 2010.
- [39] ICARUS Collaboration, S. Amoroso, M. Antonello et al., "Analysis of the liquid Argon purity in the ICARUS T600 TPC,"

- Nuclear Instruments and Methods in Physics Research A: Accelerators, Spectrometers, Detectors and Associated Equipment*, vol. 516, pp. 68–79, 2004.
- [40] W. Walkowiak, “Drift velocity of free electrons in liquid Argon,” *Nuclear Instruments and Methods in Physics Research A: Accelerators, Spectrometers, Detectors and Associated Equipment*, vol. 449, no. 1-2, pp. 288–294, 2000.
- [41] A. Ferrari, P. R. Sala, A. Fassó, and J. Ranft, “FLUKA: a multi-particle transport code,” Tech. Rep. CERN-2005-10, 2005, INFN/TC-05-11, SLAC-R-773.
- [42] GEANT4 Collaboration, S. Agostinelli, J. Allison et al., “Geant4—a simulation toolkit,” *Nuclear Instruments and Methods in Physics Research A: Accelerators, Spectrometers, Detectors and Associated Equipment*, vol. 506, no. 3, pp. 250–303, 2003.
- [43] H. Wulandari, J. Jochum, W. Rau, and F. von Feilitzsch, “Neutron flux at the Gran Sasso underground laboratory revisited,” *Astroparticle Physics*, vol. 22, no. 3-4, pp. 313–322, 2004.
- [44] G. Battistoni, A. Ferrari, T. Montaruli, and P. R. Sala, “The FLUKA atmospheric neutrino flux calculation,” *Astroparticle Physics*, vol. 19, no. 2, pp. 269–290, 2003.
- [45] W. R. Leo, *Techniques for Nuclear and Particle Physics Experiments*, Springer, Berlin, Germany, 1987.
- [46] L. Cavallero, *Functional parameter analysis of the liquid Argon dark matter detector working in double-phase WArP 100I [M.S. thesis]*, 2012.
- [47] S. Kubota, A. Nakamoto, T. Takahashi et al., “Recombination luminescence in liquid Argon and in liquid xenon,” *Physical Review B*, vol. 17, Article ID 2762, 1978.
- [48] A. Falcone, *Localization of events in the WArP 100 detector [M.S. thesis]*, 2012.
- [49] A. Badertscher, F. Bay, The ArDM Collaboration et al., “Status of the ArDM experiment: first results from gaseous Argon operation in deep underground environment,” <http://arxiv.org/abs/1307.0117>.
- [50] T. Alexander, D. Akimov, K. Arisaka et al., “Light yield in darkside-10: a prototype two-phase liquid Argon TPC for dark matter searches,” <http://arxiv.org/abs/1204.6218>.

Review Article

New Directions in Direct Dark Matter Searches

Paolo Panci

Institut d'Astrophysique, CNRS, UMR 7095 & Université Pierre et Marie Curie, 98 bis Boulevard Arago, 75014 Paris, France

Correspondence should be addressed to Paolo Panci; pancipaolo@gmail.com

Received 9 January 2014; Accepted 3 February 2014; Published 16 April 2014

Academic Editor: Anselmo Meregaglia

Copyright © 2014 Paolo Panci. This is an open access article distributed under the Creative Commons Attribution License, which permits unrestricted use, distribution, and reproduction in any medium, provided the original work is properly cited. The publication of this article was funded by SCOAP³.

I present the status of direct dark matter detection with specific attention to the experimental results and their phenomenological interpretation in terms of dark matter interactions. In particular I review a new and more general approach to study signals in this field based on nonrelativistic operators which parametrize more efficiently the dark matter-nucleus interactions in terms of a very limited number of relevant degrees of freedom. Then I list the major experimental results, pointing out the main uncertainties that affect the theoretical interpretation of the data. Finally, since the underlying theory that describes both the dark matter and the standard model fields is unknown, I address the uncertainties coming from the nature of the interaction. In particular, the phenomenology of a class of models in which the interaction between dark matter particles and target nuclei is of a long range type is discussed.

1. Introduction

One of the most exciting open questions at the interface between particle physics and cosmology is the nature of Dark Matter (DM). The first person who provided evidence and inferred the presence of DM was a Swiss-American astrophysicist, Fritz Zwicky. He applied the virial theorem to the Coma cluster of galaxies and obtained evidence of unseen mass. Roughly 40 years following the discoveries of Zwicky and others, Vera Rubin and collaborators conducted an extensive study of the rotation curves of isolated spiral galaxies. They announced the discovery that the rotational curves of stars in spiral galaxies exhibit a characteristic flat behaviour at large distance in contrast with Kepler's law. Many other evidence of unseen mass on distance scales of the size of galaxies and clusters of galaxies appeared throughout the years, but the most precise measurement of the total amount of DM comes from cosmological scales. In particular, the measurements of modern precision cosmology (the Cosmic Microwave Background (CMB) and the surveys of the Large Scale Structure (LSS) of the Universe) provide the current most relevant evidence. Apart from the qualitative agreement, it is the quantitative fitting of the wealth of available data that allows the amount of DM to be one of the cosmological parameters now most precisely measured

($\Omega_{\chi} h^2 = 0.1199 \pm 0.0027$; see [1, Table 2]). Therefore, we have compelling evidence of unseen mass, but the microscopic features of this new kind of matter remain unknown yet. Direct and indirect searches may shed light on the nature of DM, and therefore a careful study of their phenomenology is fundamental. For a pedagogical review on this subject, see, for example, [2].

Direct searches for DM aim at detecting the nuclear recoils arising from scattering between DM particles and target nuclei in underground detectors. DM direct detection experiments are providing exciting results in terms of measured features which have the right properties to be potentially ascribed to a DM signal. For example in addition to the long-standing DAMA results, nowadays there are other experiments, such as CoGeNT, CRESST-II, and CDMS-Si that start to see some anomalies in their counting rates. On the other hand, the situation in this field is extremely unclear and confusing, because, on top of these positive result experiments, the constraints coming from null results, like XENON100, COUPP, PICASSO and very recently LUX, are very stringent and put the interpretation of the anomalies in terms of a DM interaction in serious trouble. Nevertheless, there are at least two main caveats when the results from the experiments commented upon above are interpreted. The first is that one has to

treat with great care the fine experimental details associated with the results quoted by each experiment. The second caveat is instead associated with the interpretation of the data within a very simple-minded DM model. For instance, the DM-nucleus spin independent contact interaction is just a benchmark example. Upon relaxing some of these assumptions, the current complicated experimental puzzle can probably be solved.

The *scope of this work* is to present the *status* of direct DM detection with specific attention to the experimental results and their phenomenological interpretation in terms of DM interaction. In particular in Section 2, I review a new and more general approach to study signals in this field based on nonrelativistic operators which parameterize most efficiently the DM-nucleus interactions in terms of a very limited number of relevant degrees of freedom. In Section 3, I review the experimental results and their interpretation in terms of the “standard” spin independent (SI) interaction. I list then the main uncertainties that affect the theoretical interpretation of the data: this is a very promising area of research since only major advancements here can probably reconcile the complicated puzzle showed by the experiments up. Finally in Section 4, I pose my attention on the uncertainties coming from the nature of the interaction. In particular the phenomenology of a class of models in which the interaction between DM particles and target nuclei is of a long range type is discussed.

2. Basics of Direct Detection Computations

2.1. Kinematics. As already stated, when a DM particle scatters off a nucleus, depending on the DM properties, one can envision at least two distinct kinematics, the elastic and the inelastic one. The elastic scattering is represented by

$$\chi + \mathcal{N}(A_{\mathcal{N}}, Z_{\mathcal{N}})_{\text{at rest}} \longrightarrow \chi + \mathcal{N}(A_{\mathcal{N}}, Z_{\mathcal{N}})_{\text{recoil}}, \quad (1)$$

while the inelastic is

$$\chi + \mathcal{N}(A_{\mathcal{N}}, Z_{\mathcal{N}})_{\text{at rest}} \longrightarrow \chi' + \mathcal{N}(A_{\mathcal{N}}, Z_{\mathcal{N}})_{\text{recoil}}. \quad (2)$$

In (1) and (2), χ and χ' are two DM particle states, and $A_{\mathcal{N}}, Z_{\mathcal{N}}$ are, respectively, the mass and atomic numbers of the nucleus \mathcal{N} .

We know, thanks to rotational curves data, that the velocity of χ in the vicinity of the Earth is of the order of $10^{-3}c$. Hence the scattering between a DM particle with velocity v and mass m_{χ} and a nucleus at rest with mass $m_{\mathcal{N}}$ occurs in deeply nonrelativistic regime. This is analogous with the collision between two billiard balls and therefore the recoil energy can be simply obtained by considering energy and

momenta conservation separately. In the detector rest frame, such scattering would end up into a nuclear recoil of energy:

$$E_R = \frac{2\mu_{\chi\mathcal{N}}^2}{m_{\mathcal{N}}} v^2 \left(\frac{1 - (v_t^2/2v^2) - \sqrt{1 - (v_t^2/v^2)} \cos \theta}{2} \right),$$

$$v_t = 0, \text{ elastic scattering,}$$

$$v_t \neq 0, \text{ inelastic scattering,} \quad (3)$$

where $\mu_{\chi\mathcal{N}} = m_{\chi}m_{\mathcal{N}}/(m_{\chi} + m_{\mathcal{N}})$ is the DM-nucleus reduced mass, θ as usual is the scattering angle in the center-of-mass frame, and $v_t = \sqrt{2\delta/\mu_{\chi\mathcal{N}}}$ is a threshold velocity. Here $\delta = m'_{\chi} - m_{\chi}$ is the mass splitting between χ and χ' , and the equation above holds for $\delta \ll m'_{\chi}, m_{\chi}$. Elastic scattering occurs for $\delta = 0$, while $\delta \neq 0$ implies inelastic scattering. The minimal DM velocity providing the E_R recoil energy can be then obtained by putting $\theta = -\pi$ in (3). One gets

$$v_{\min}(E_R) = \sqrt{\frac{m_{\mathcal{N}}E_R}{2\mu_{\chi\mathcal{N}}^2}} \left(1 + \frac{\mu_{\chi\mathcal{N}}\delta}{m_{\mathcal{N}}E_R} \right). \quad (4)$$

2.2. Formalism of Nonrelativistic Operators. Having a disposal the basic quantity v_{\min} that fully describes the kinematics of the DM-nucleus scatterings in (1) and (2) and the differential rate of nuclear recoil expected in a given detector can be achieved by weighting the differential cross section $d\sigma_{\mathcal{N}}/dE_R$ with the DM velocity distribution $f_E(\vec{v})$ in the velocity range allowed by the kinematics. It reads as follows:

$$\frac{dR_{\mathcal{N}}}{dE_R} = \frac{\xi_{\mathcal{N}}}{m_{\mathcal{N}}} \frac{\rho_{\odot}}{m_{\chi}} \int_{v_{\min}(E_R)}^{v_{\text{esc}}} d^3v v f_E(\vec{v}) \frac{d\sigma_{\mathcal{N}}}{dE_R}(v, E_R), \quad (5)$$

where $\xi_{\mathcal{N}}$ are the mass fractions of different nuclides ($\xi_{\mathcal{N}} = 10^3 N_A m_{\mathcal{N}} \zeta_{\mathcal{N}} / \text{kg } \bar{A}$, where $N_A = 6.022 \times 10^{23}$ is Avogadro's number, $\zeta_{\mathcal{N}}$ are the numeric abundances and $\bar{A} \equiv \sum_{\mathcal{N}} \zeta_{\mathcal{N}} A_{\mathcal{N}}$), and $\rho_{\odot} \simeq 0.3 \text{ GeV/cm}^3$ is the DM energy density at the Earth's location. This is the canonical value routinely adopted in the literature (see, e.g., [2–4]). Recent computations have found a higher central value of it, still subject for some debate [5–7]. The integral in the right-hand side of the equation above is a key ingredient because it contains all the information related to the geometry of the DM halo, the nature of the DM-nucleus interaction, and in turn the nuclear response of the target. In the following we present the formalism of nonrelativistic (NR) operators and then we describe how to write down the main observables in terms of it.

(i) As already stated, the weight of the velocity integral is the DM velocity distribution $f_E(\vec{v})$. In the rest frame of our Galaxy it can be roughly approximated with a Maxwell-Boltzmann distribution due to the fact, as pointed out in [8], that the violent relaxation of the gravitational potential at the formation of the Milky Way leads to fast mixing of the DM

phase space elements. Therefore, DM particles were basically frozen in high-entropy configuration which are indeed Maxwell-Boltzmann-like. This has been roughly confirmed by some recent numerical simulation, but as one can see in [9, Figure 2], there are some deviations due to the DM assembly history of the Milky Way. Indeed one can see different features both at low and high velocities that of course are not present in the case of a Maxwell-Boltzmann distribution. Furthermore the geometry of the halo predicted by this kind of numerical simulation is not exactly spherical but tends to a triaxial configuration (see, e.g., [10]).

Keeping in mind that this is not the truth because we have not directly measured the properties of the DM halo yet, what we know for sure is that, since we are setting in the Earth laboratory frame, one has to boost the DM-nucleus relative velocity with the drift velocity of the Sun around the galactic center and the Earth's orbital velocity projected in the galactic plane. Therefore the DM velocity distribution $f_E(\vec{v})$ in the Earth frame is related to the DM velocity distribution in the galactic one $f_G(\vec{w})$ by the Galilean velocity transformation $f_E(\vec{v}) = f_G(\vec{v} + \vec{v}_E(t))$, where

$$\vec{v}_E(t) = \vec{v}_\odot + \vec{v}_\oplus(t). \quad (6)$$

Here $\vec{v}_\odot = \vec{v}_G + \vec{v}_S$ is the sum of the galactic rotational velocity of the local system $\vec{v}_G = (0, v_0, 0)$ (here $v_0 = 220 \pm 50$ km/s is the local DM velocity) and the Sun's proper motion $\vec{v}_S = (10, 13, 7)$ km/s with absolute value $v_\odot = 233 \pm 50$ km/s, while $\vec{v}_\oplus(t)$ is the time dependent Earth's orbital velocity with period of one year, phase around June 2nd (when it is aligned to \vec{v}_\odot), and size $v_\oplus = 30$ km/s, and it is inclined of an angle $\gamma \approx 60^\circ$ with respect to the galactic plane. More details can be found in [11–13]. Since in (6) the Earth's orbital velocity projected in the galactic plane $v_\oplus \cos \gamma$ is relatively small compared to v_\odot , we can approximate $\vec{v}_E(t)$ with its component directed toward the galactic center. We can then write

$$v_E(t) \approx v_\odot + \Delta v \cos \left[\frac{2\pi(t - \phi)}{\tau} \right], \quad (7)$$

where $\Delta v = v_\oplus \cos \gamma \approx 15$ km/s. Here $\phi \approx 152.5$ days (June 2nd) is the phase and $\tau \approx 365$ days is the period of the Earth motion around the Sun.

Therefore, in general, it is expected an annual modulation in the counting rate of direct detection experiment, as the incoming flux of DM particles toward us contains small oscillatory terms due to the Earth's proper motion around the Sun during the years. More details on this model independent signature can be found, for instance, in [14, 15]. It is worth stressing that looking for an annual modulation of the counting rate in direct detection is very challenging from the experimental point of view, simply because the modulus of the time dependent component of the velocity

is relatively small compared to the constant one; in better words, the size of the modulated signal that experiments like DAMA and CoGeNT are looking for is suppressed with respect to the unmodulated one, due basically to the collective motion of the Solar system around the galactic center.

- (ii) In the nonrelativistic limit the differential cross section can be written in the usual form:

$$\frac{d\sigma_{\mathcal{N}}}{dE_R}(v, E_R) = \frac{1}{32\pi} \frac{1}{m_\chi^2 m_{\mathcal{N}}} \frac{1}{v^2} |\overline{\mathcal{M}_{\mathcal{N}}}|^2, \quad (8)$$

where $|\overline{\mathcal{M}_{\mathcal{N}}}|^2$ is the DM-nucleus matrix element that encodes all the information related to the nuclear physics and the nature of the interactions. Since, as already stated, the velocity of the DM particles in the vicinity of the Earth is much smaller than the speed of light, the framework of relativistic quantum field theory is not too much appropriate to study signals in this field, especially if we do not have any clue about the underlying theory that describes the DM-quark interactions. A more useful and general framework is actually the one based on nonrelativistic operators. Indeed, since, for the elastic scattering, the relevant degrees of freedom are the DM-nucleon relative velocity \vec{v} , the exchanged momentum \vec{q} , the nucleon spin \vec{s}_N ($N = p, n$ can be proton or neutron), and the DM one \vec{s}_χ (if different from zero), the scattering amplitude will then be a rotationally invariant function of these variables. In this regard, with \vec{v} , \vec{q} , \vec{s}_N , and \vec{s}_χ [16], we can construct a basis for 16 operators, which includes all possible spin configurations (the complete list and the numbering of the nonrelativistic operators can be found in [17–19]). The DM-nucleon matrix element can then be written as a linear combination of these operators, with coefficients that may depend on the momenta only through the q^2 or v^2 scalars (DM models feature a long range interaction with the Standard Model fermions provide perhaps the most notable example. Indeed, in this case, the differential cross section is enhanced at smaller exchanged momenta, due to the negative power dependence of q . A specific realization is offered by models in which DM particles can carry small but nonzero electric charge, electric dipole moment, or magnetic one. Their phenomenology in the context of DM direct searches has been studied in [20–31] and references therein.). In particular it reads

$$\mathcal{M}_N = \sum_{i=1}^{16} c_i^N(\lambda, m_\chi) \mathcal{O}_i^{\text{NR}}, \quad (9)$$

where the coefficients c_i^N are functions of the free parameters of the underlying relativistic theory, such as mediator masses, mixing angles, and couplings constants (collectively denoted by λ), and the DM mass m_χ . For instance, if the interaction between

a fermionic DM χ and the nucleon N is described by the “standard” SI Lagrangian $g_N/\Lambda^2 \bar{\chi}\chi \bar{N}N$, the only nonrelativistic operator involved will be the identity ($\mathcal{O}_1^{\text{NR}} = \mathbb{1}$). Before moving on, it is worth stressing that the operators above, which entirely describe the nonrelativistic physics of the DM-nucleus scattering, are many and they can either depend on the exchanged momenta \vec{q} or the relative velocity \vec{v} . As a consequence, focussing on just one operator (e.g., $\mathcal{O}_1^{\text{NR}}$) is not the most model independent way to study signals in direct DM searches, since theories can predict several operators entering together with the possibility that some of them may even interfere.

Since now the nucleus is of course made of protons and neutrons, one has to correct the DM-nucleon matrix element (9) with the nuclear responses, which are a sort of form factors that take account of the finite size of the target nuclei. According to [17, Equation (55)] we can then write the spin-averaged amplitude squared for scattering off a target nucleus \mathcal{N} with mass $m_{\mathcal{N}}$ as

$$|\overline{\mathcal{M}_{\mathcal{N}}}|^2 = \frac{m_{\mathcal{N}}^2}{m_N^2} \sum_{i,j=1}^{16} \sum_{N,N'=p,n} c_i^N c_j^{N'} F_{i,j}^{(N,N')}. \quad (10)$$

The $F_{i,j}^{(N,N')}(v, E_R, \mathcal{N})$ are the nuclear responses and they depend critically on the type of scattering nucleus \mathcal{N} : they are also functions of m_χ , v , and the nuclear recoil energy $E_R = q^2/2m_{\mathcal{N}}$. In Figure 1, the nuclear responses for both light element (on the left panel) and heavy one (on the right panel), considering two completely different kinds of interactions, are depicted. On a more specific level, in thick red the total nuclear response for the standard SI interaction is shown. As we can see, in the energy range of interest in direct DM experiments (few keV), it is enhanced by the canonical $A_{\mathcal{N}}^2$ factor: this is due to the fact that, in this case, the incoming DM particles see the nucleus as a point-like object with $A_{\mathcal{N}}$ scatter centers. On the other hand, we show in blue the nuclear responses of a completely different type of interaction which is both momenta and spin dependent ($\mathcal{O}_6^{\text{NR}} = (\vec{s}_\chi \cdot \vec{q})(\vec{s}_N \cdot \vec{q})$). This type of interaction can give rise if the DM-nucleus interaction is mediated by a pseudoscalar particle. We can see that the nuclear responses are dominated by the scattering with protons, simply because neither the fluorine nor the iodine has unpaired neutrons and moreover the interaction goes to zero in the small momenta transferred limit.

A complete set of these nuclear responses for each pair of nucleons (N, N') , each pair of nonrelativistic operators (i, j) , and for several target nuclei \mathcal{N} has been provided in the appendices of [17]. This is extremely useful because, for the first time, different

types of interactions can be studied in a more general ground. However, since this kind of computations is quite new, the uncertainties, especially for the spin, momenta, and velocity dependent interactions, are still quite large.

Having a disposal the general relation of the DM-nucleus matrix element (10), the differential cross section (8), and in turn the rate of nuclear recoil (5) can be rewritten, following [32], in a very general way. It reads

$$\frac{dR_{\mathcal{N}}}{dE_R} = X \xi_{\mathcal{N}} \sum_{i,j=1}^{16} \sum_{N,N'=p,n} c_i^N(\lambda, m_\chi) \times c_j^{N'}(\lambda, m_\chi) \mathcal{F}_{i,j}^{(N,N')}(E_R, \mathcal{N}), \quad (11)$$

where we defined

$$X \equiv \frac{\rho_\odot}{m_\chi} \frac{1}{32\pi} \frac{1}{m_\chi^2 m_N^2}, \quad (12)$$

$$\begin{aligned} \mathcal{F}_{i,j}^{(N,N')}(E_R, \mathcal{N}) &\equiv \int_{v_{\min}(E_R)}^{v_{\text{esc}}} d^3v \frac{1}{v} f_G(\vec{v} + \vec{v}_E(t)) F_{i,j}^{(N,N')}(v, E_R, \mathcal{N}). \end{aligned} \quad (13)$$

2.2.1. “Standard” SI Contact Interaction. To give a concrete example, in the following the coefficient and the nuclear responses for the “standard” SI contact interaction are showed explicitly. In particular, when experiments present results in terms of this interaction, they implicitly assume (probably inspired by supersymmetric neutralino scattering) the following DM-nucleon effective Lagrangian:

$$\mathcal{L}_{\text{SI}}^N = \lambda_{\text{SI}}^N \bar{\chi}\chi \bar{N}N. \quad (14)$$

From this the DM-nucleon matrix element can be obtained by contracting (14) with initial and final states of the scattering. Performing then the nonrelativistic limit one gets

$$\mathcal{M}_{\text{SI}}^N \equiv \langle \chi N | \mathcal{L}_{\text{SI}}^N | \chi N \rangle \simeq 4\lambda_{\text{SI}}^N m_\chi m_N \mathcal{O}_1^{\text{NR}}, \quad (15)$$

where $\mathcal{O}_1^{\text{NR}} = \mathbb{1}$ is the operator that describes the nonrelativistic limit of (14) and the coefficient is obviously given by $c_1^N(\lambda_{\text{SI}}^N, m_\chi) = 4\lambda_{\text{SI}}^N m_\chi m_N$.

For the SI scattering, DM-proton and DM-neutron couplings are customarily assumed to be equal and thus $\lambda_{\text{SI}}^p = \lambda_{\text{SI}}^n \equiv \lambda_{\text{SI}}$ (isospin violating process is not taken into account). Plugging back then the coefficient in the general equation (11) and defining $\sigma_{\text{SI}} = \lambda_{\text{SI}}^2/\pi \cdot \mu_N^2$ (μ_N is the DM-nucleon reduced mass) to make contact with the usual physical cross sections, the differential rate of nuclear recoil reduces to the very well-know compact form:

$$\frac{dR_{\mathcal{N}}}{dE_R} = \frac{\xi_{\mathcal{N}}}{m_{\mathcal{N}}} \frac{\rho_\odot}{m_\chi} \left[\frac{m_{\mathcal{N}}}{2\mu_N^2} \sigma_{\text{SI}} F_{\mathcal{N}}^{\text{tot}}(E_R) \mathcal{J}(E_R) \right], \quad (16)$$

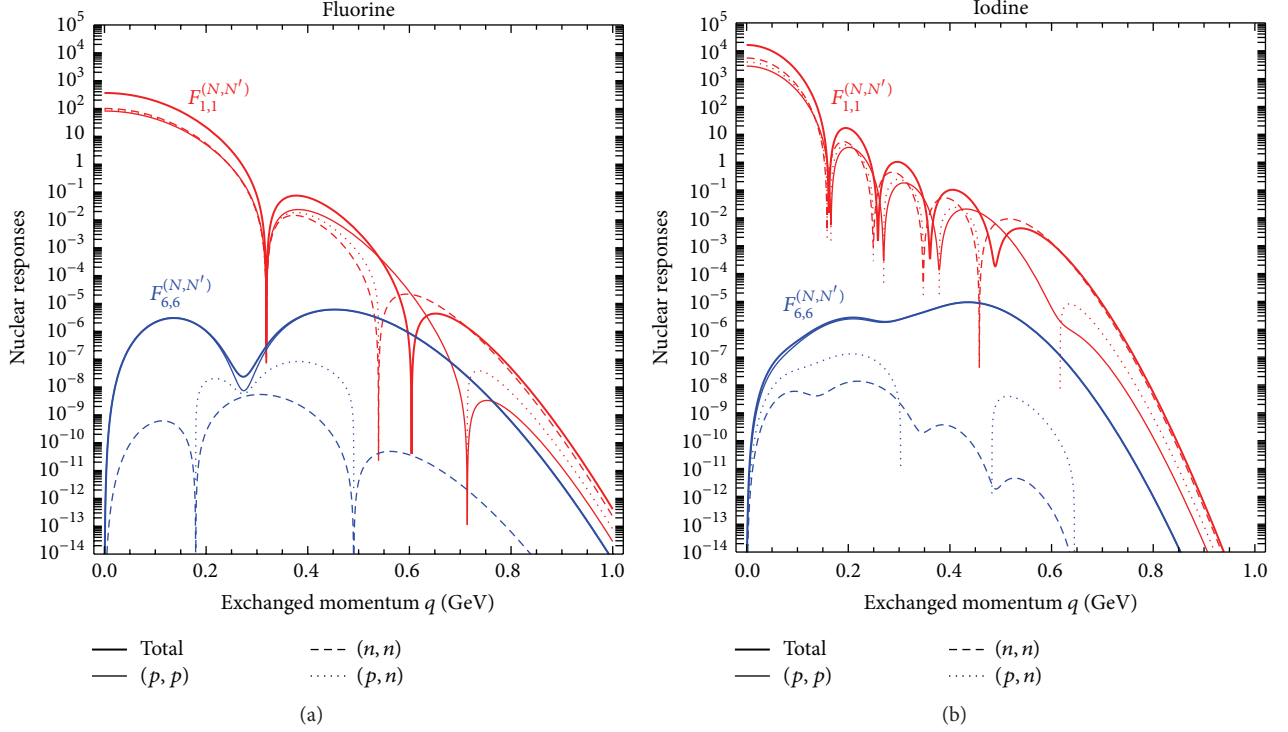


FIGURE 1: *Nuclear responses* of the fluorine (a) and the iodine (b) targets considering two completely different types of interactions. On a more specific level, we show, in red, the nuclear responses for the “standard” SI contact interaction, while in blue those for another kind of interaction described in the nonrelativistic limit by the operator $\mathcal{O}_6^{\text{NR}} = (\vec{s}_\chi \cdot \vec{q})(\vec{s}_N \cdot \vec{q})$. The different hatching refers instead to the possible choices of nucleon pairs in the nucleus. In particular, the solid, dashed, and dotted lines are for (p, p) , (n, n) , and (p, n) pairs, while the thick ones are obtained by summing over all of them (total nuclear responses). Notice that the total nuclear responses for the “standard” SI contact interaction (thick red lines) reduce to $A_{\mathcal{N}}^2 F_{\text{Helm}}^2(q)$, where $F_{\text{Helm}}^2(q)$ is the customary Helm form factor [33].

where we define the total SI nuclear response as

$$F_{\mathcal{N}}^{\text{tot}}(E_R) = \sum_{N, N' = p, n} F_{1,1}^{(N, N')} (E_R, \mathcal{N}). \quad (17)$$

Here, since $\lambda_{\text{SI}}^p = \lambda_{\text{SI}}^n$, the total nuclear response reduces to the square of the customary Helm form factor [33] multiplied by the coherent enhancement of the cross section $A_{\mathcal{N}}^2$. In particular it reads $F_{\mathcal{N}}^{\text{tot}}(E_R) = A_{\mathcal{N}}^2 F_{\text{Helm}}^2(E_R)$. The function $\mathcal{J}(E_R) = \int_{v_{\text{min}}}^{v_{\text{esc}}} d^3v f_G(\vec{v} + \vec{v}_E(t))/v$ is instead the velocity integral encountered many times in the literature. It is worth noticing that $\mathcal{J}(E_R)$ can be written in this way because in the “standard” SI interaction the operator that describes the nonrelativistic limit of the effective Lagrangian does not carry any dependences on the relative velocity \vec{v} . In Section 3.2 the interpretation of the experimental results in terms of the “standard” SI interaction is briefly reviewed.

2.3. Experimental Observables. Since, as already stated, the Earth’s orbital velocity projected in the galactic plane is relatively small compared to the drift velocity of the Sun, we can then expand the recoil rate (11), assuming that the velocity

distribution is not strongly anisotropic. Then, by means then of (7), one gets

$$\frac{dR_{\mathcal{N}}}{dE_R}(t) \simeq \left. \frac{dR_{\mathcal{N}}}{dE_R} \right|_{v_E=v_\odot} + \frac{\partial}{\partial v_E} \left. \frac{dR_{\mathcal{N}}}{dE_R} \right|_{v_E=v_\odot} \Delta v \cos \left[\frac{2\pi(t - \phi)}{\tau} \right]. \quad (18)$$

In order now to properly reproduce the experimental rate of nuclear recoil and in turn the expected number of events in a certain energy bin, one should take into account the response of the detectors as well. It can be done by the following energy convolution and transformation:

$$\frac{dR}{dE'} = \sum_{\mathcal{N}} \epsilon(E') \int_0^\infty dE_R \mathcal{K}_{\mathcal{N}}(q_{\mathcal{N}} E_R, E') \frac{dR_{\mathcal{N}}}{dE_R}(E_R), \quad (19)$$

where E' is the detected energy and the functions $\mathcal{K}_{\mathcal{N}}(q_{\mathcal{N}} E_R, E')$ and $\epsilon(E')$ are the energy resolution centered in $q_{\mathcal{N}} E_R$ and the detector’s efficiency, respectively. Here the sum runs over the different species of the detectors (e.g., DAMA is a multiple target experiment composed by crystal of sodium and iodine) and $q_{\mathcal{N}}$ is the so-called

quenching factor that takes account of the partial recollection of the released energy in the detector. After convolving with all the experimental effects, (19) must be averaged over the energy bins of the detector. For each energy bin k , we then obtain the number of the unmodulated events N_{0k}^{th} and of the modulated ones N_{mk}^{th} as

$$N_{0k}^{\text{th}} = w_k \int_{\Delta E_k} dE' \left. \frac{dR}{dE'} \right|_{v_E=v_0}, \quad (20)$$

$$N_{mk}^{\text{th}} = w_k \Delta v \int_{\Delta E_k} dE' \left. \frac{\partial}{\partial v_E} \frac{dR}{dE'} \right|_{v_E=v_0}, \quad (21)$$

where w_k is the exposure (expressed kilograms per day) and ΔE_k is the width of the k th-esime energy bin. N_{0k}^{th} and N_{mk}^{th} are the relevant quantities that one can use for the analysis of the experiments which address the annual modulation effect, namely, DAMA and CoGeNT. For the other experiments, only N_{0k}^{th} is instead relevant.

Collecting all the elements in the previous equations we expand (20) and (21) and write

$$N_{0k}^{\text{th}} = X \sum_{i,j=1}^{16} \sum_{N,N'=p,n} c_i^N(\lambda, m_\chi) c_j^{N'}(\lambda, m_\chi) \times \left. \widetilde{\mathcal{F}}_{i,j}^{(N,N')} (m_\chi, k) \right|_{v_E=v_0}, \quad (22)$$

$$N_{mk}^{\text{th}} = X \Delta v \sum_{i,j=1}^{16} \sum_{N,N'=p,n} c_i^N(\lambda, m_\chi) c_j^{N'}(\lambda, m_\chi) \frac{\partial}{\partial v_E} \times \left. \widetilde{\mathcal{F}}_{i,j}^{(N,N')} (m_\chi, k) \right|_{v_E=v_0}.$$

Here $\widetilde{\mathcal{F}}_{i,j}^{(N,N')} (m_\chi, k)$ is a sort of *integrated form factor* that encapsulates all the information related to nuclear physics, astrophysics, and the detector dependency of the rate. There is one of these factors for each energy bin k of each experiment under consideration and for each choice of the operators pair (i, j) and nucleons pair (N, N') . It reads explicitly

$$\begin{aligned} & \widetilde{\mathcal{F}}_{i,j}^{(N,N')} (m_\chi, k) \\ &= w_k \sum_{\mathcal{N}} \xi_{\mathcal{N}} \int_{\Delta E_k} dE' \epsilon(E') \\ & \quad \times \int_0^\infty dE_R \mathcal{K}_T(q_{\mathcal{N}} E_R, E') \\ & \quad \times \mathcal{F}_{i,j}^{(N,N')} (E_R, \mathcal{N}). \end{aligned} \quad (23)$$

It is worth noticing that the linearity of the expected number of events in the *integrated form factors* is a fundamental ingredient. This, indeed, lets us parametrize the model dependent part of the rate from the model independent one, encapsulated in the function $\widetilde{\mathcal{F}}_{i,j}^{(N,N')} (m_\chi, k)$. Therefore, if the experimental collaborations, instead of presenting the experimental results in terms of a specific DM model,

release all of this finite number of *integrated form factors*, one will be easily able to obtain the expected number of events for any kind of interactions, whose particle physics is completely encapsulated in the coefficient c_i^N . A first example of the potentiality of such parametrization has been presented in [32]. In particular the authors provide a self-contained set of numerical tools based on the *integrated form factors* above, to derive the bounds from some current direct detection experiments on virtually any arbitrary model of DM elastically scattering on target nuclei.

3. Direct Detection Status

3.1. Experimental Landscape. The elusive nature of DM particles makes their detection a challenge for experimentalist: in fact, considering typical atomic masses for the target nuclei of $m_{\mathcal{N}} = 100$ GeV and typical properties for the DM halo (Maxwell-Boltzmann distribution with dispersion velocity $v_0 = 220$ km/s), DM particles should induce tiny nuclear recoil in the range $1 \div 10^3$ keV with a total rate lower than 1 cpd/kg/keV (here cpd refers to counts per days). Due to this rare phenomenon, the experimental priorities in this field are as follows:

- (i) the detectors must work deeply underground in order to avoid the high rate interaction induced by cosmic rays scattering off on target nuclei,
- (ii) they must use active shields and very clean materials against the residual radioactivity in the tunnel (mostly α -particles, neutrons, and photons),
- (iii) they must distinguish multiple scattering, simply because DM particles do not interact twice in the detector, being of course weakly interacting particles.

A variety of different experimental techniques with the aim of measuring the tiny energy released by a DM interaction have been developed. In the following the main channels by which the scattered nucleus can deposit energy in the detectors are summarized as follows.

- (i) *Scintillation detection*: a particle interacting within a scintillating target induces the emission of light produced by the deexcitation of exited atoms. This light can be detected by appropriate photomultipliers. Typically NaI(Tl) and xenon are used as scintillators.
- (ii) *Ionization detection*: a particle interacting inside a target produces an amount of free electron-ion pairs that can be detected with a collecting drift field and a device sensitive to the electric charge.
- (iii) *Phonon detection*: a particle interacting inside a detector releases a tiny energy deposition with a subsequently increase of the temperature. Cryogenic apparatus working at very low temperature (around few mK) are able to measure this small variation making this detection technique possible.

Since various types of interacting particles release a different amount of energy in the channels commented upon above, for a better rejection of the background events, most

of the experiments are designed to be sensitive to more than one of them. Indeed, thanks to this ability, the ratio between two channels can be used to distinguish between nuclear (due to a DM interaction) and electromagnetic recoils.

The only two experiments that do not use this kind of experimental technique are DAMA and CoGeNT that, perhaps not coincidentally, were the only two detectors (until the CRESST-II and recently the CDMS-Si results) observing an excess in their counting rate. In particular, since both the experiments are not able to disentangle the nuclear recoil signals from the electromagnetic ones, they infer the presence of DM in our halo by exploiting the model independent annual modulation signature in the counting rate. As follows, I review the most important experiments in this field.

3.1.1. DAMA. The DAMA experiment, located at the National Laboratory of Gran Sasso, is an observatory for rare processes made of highly radiopure scintillators (NaI(Tl) crystals). In particular the former DAMA/NaI and the current DAMA/Libra experiments have the main aim of investigating the presence of DM particles in the galactic halo by exploiting the model independent annual modulation induced by a DM interaction.

The DAMA detector is only able to measure the fraction of energy deposited in scintillation light, while the phonon excitation due to multiple nuclear interactions is not detected. This effect, as commented upon in Section 2.3, is taken into account by the so-called quenching factor. In particular, for NaI(Tl) crystals, one normally considers $q_{\text{Na}} \approx 0.3$ and $q_{\text{I}} \approx 0.09$ [34]. It is, however, known [34–36] that some scattered nuclei can travel long distances along the crystallographic axes and planes without colliding with other nuclei. This process is called channeling effect, and since no phonon excitation is produced, the scattered nuclei deposit all the energy in the detector electromagnetically ($q_{\mathcal{N}} \approx 1$). The fraction of channeling depends on the nucleus itself, on the recoil energy and strongly on the temperature. It has been calculated, for instance, in [35] and, in particular, it has been found that, for low energy recoiling Na and I ions, the fraction of channeled events can be relatively large. Nevertheless, this result has not been confirmed by other theoretical [37–39] and experimental studies [40], which instead suggest that the channeling effect in NaI crystals is negligible.

The DAMA collaboration published results of the combined DAMA/NaI and DAMA/Libra experiments [41, 42], corresponding to an exposure of 1.17 ton-yr for a target. They observed a cosine-like modulation, present only in the *single-hit* events, with a measured period $\tau = (0.999 \pm 0.002)$ yr and a phase $t' = (146 \pm 7)$ days well compatible with the roughly 152.30 days expected for DM signals (see the previous section). The modulation is present only in the low energy window (2–6) keVee (here, keVee refers to electron equivalent recoil energy. This must be converted with the quenching factor in order to get the total energy released to the nucleus by the scattering process ($E_R [\text{keV}] \equiv E_R [\text{keVee}]/q_{\mathcal{N}}$) and its amplitude $N_m^{\text{exp}}(2-6)$ is equal to (0.0116 ± 0.0013) cpd/(kg-keV) at 8.9σ CL [42].

3.1.2. CoGeNT. The CoGeNT experiment employs p-type point-contact Germanium detectors operating in the Soudan Underground Laboratory.

Like DAMA, the experiment performs just one of the techniques commented upon above; namely, the p-type point-contact germanium detectors only measure the fraction of energy deposited by incident particles in the form of ionization. The lack of energy measured is again taken into account by the quenching factor that can be extracted through the following empirical relation $E_{\text{det}} = 0.2E_R^{1.12}$ [43]. By virtue of its low energy threshold (0.4 keVee) and the ability to reject surface backgrounds, this type of detector is particularly sensitive to light DM candidates, although large background contamination may be present for these low energies.

In 2010 the collaboration has reported a step rise of nuclear recoil spectrum at low energy which is not directly explainable in terms of known radioactive background [44]. The energy region probed by CoGeNT partially overlaps with the one in which the DAMA apparatus reported the annual modulation signal, and therefore it is natural to interpret the excess at low energy due to a DM interaction. In view of that, fifteen months of cumulative CoGeNT data (442 live days) have been also examined in order to look for an annual modulation signature [45]. In particular the CoGeNT data seem to favor a cosine-like modulation slightly shifted in phase with respect to the one measured by DAMA. The modulation is again only present at low energy with a statistical significance of 2.8σ CL, limited by the short exposure.

Very recently, the collaboration presented a 3.4-year data taking, with an improved analysis that allows a better discrimination between pure bulk and pure surface events [46, 47]. In the same energy region, where in 2010 they observed a step rise of the nuclear recoil spectrum, they still reported a preference for an annual modulation in the pure bulk counting rate. Although the statistical significance of the modulation is modest (2.2σ CL), the phase is compatible with the one observed by DAMA.

3.1.3. CRESST-II. The CRESST-II cryogenic dark matter experiment, located at the national laboratory of Gran Sasso, employs 300 g of scintillating CaWO₄ crystals.

In particular the eight moduli of the experiments measure the deposited energy in the form of phonons and scintillation light. The former provides a precise measure of the energy deposited, while the ratio between them gives an excellent rejection of the background events.

In 2011 the collaboration completed a 730 kg-day data taking [48]. In particular, 67 events were found in the DM acceptance region with an expected background contributions in the same band which is not sufficient to explain all the observed events. The resulting statistical significance, at which the background-only hypothesis is rejected, is roughly 4.5σ CL.

3.1.4. CDMS. The CDMS experiment, located at the Soudan Underground Laboratory, is composed by germanium and silicon cryogenic detectors.

In particular 19 germanium and 11 silicon detectors measure the deposited energy in the form of phonons and ionization through superconducting technology. Thanks to the ability of detecting these two signals, the rejection of the electromagnetic recoils can be obtained by the ratio among them.

In 2009 the CDMS collaboration [49] has reported no significant evidence for DM interaction. In particular, only germanium detectors were used with an exposure of 612 kg-days. The collaboration observed two events in the signal region with energy 12.3 keVnr and 15.5 keVnr (here, keVnr refers to nuclear recoil energy. Unlike the electron equivalent recoil energy, it already represents the total energy released to the nucleus by the scattering process (E_R [keV] $\equiv E_R$ [keVnr])), against an expected background of radiogenic neutrons, cosmogenic neutrons, and misidentified surface events equal to roughly 0.9 events.

More recently, the collaboration has also presented results based on the silicon analysis [50, 51]. In [51], a blind analysis of 140.2 kg-days revealed three DM candidate events in the signal region with an expected background of roughly 0.62 events. A profile likelihood ratio statistical test of the three events yields a 0.19% probability when the known-background-only hypothesis is tested, against the alternative DM + background hypothesis.

3.1.5. Xenon Experiments. Direct detection experiments based on liquid/gaseous xenon have done stunning progresses in the last decade. Indeed, thanks to the advantage in scale ability and to the good reconstruction of the three-dimensional coordinates, these experiments are among the largest in terms of fiducial mass.

Discrimination between nuclear and electromagnetic recoils is achieved by the ratio between the scintillation signal due to a particle interaction in the liquid xenon and the subsequent ionization signal in the gas phase of the detector. Furthermore, the large mass number of the xenon nuclei makes them an excellent target for the detection of DM particles with SI interaction. However, the experiments based on liquid xenon are also sensitive to the n -DM spin dependent interaction, by virtue of the unpaired neutron of the ^{129}Xe and ^{131}Xe isotopes.

In the following the results of the main experiments using the double-phase xenon technology are summarized.

- (i) *XENON experiment:* the XENON detector is a two-phase time projection chamber located at the national laboratory of Gran Sasso. The first stage of the experiment was installed underground during March 2006, and it searched for DM interactions until October 2007. In 2008 the collaboration reported a blind analysis with an exposure of 5.4×58.6 kg-days, which yields no significance evidence for DM interactions [52].

More recently the XENON10 experiment has been superseded by XENON100 with more than one order of magnitude improvement in sensitivity. In [53], the collaboration reported the results of the last

run, a blind analysis with an exposure of 34×224.6 kg-days which again yielded no evidence for DM interactions. In particular, the two observed events in the predefined nuclear recoil energy range of 6.6–43.3 keVnr were consistent with the background expectation of roughly 1 event.

- (iii) *LUX experiment:* the LUX experiment is a dual-phase xenon time-projection chamber operated at the Sanford Underground Research Facility in South Dakota. Like the XENON100 experiment, it measures both the scintillation light and the ionization in the gas phase to disentangle the nuclear recoils from the electromagnetic ones. In [54], a nonblind analysis was performed on data, collected with an exposure of 118.3×85.3 kg-days. After cuts, 160 events were found within the signal energy region. The collaboration found that all of these events are compatible with the expected electron recoil background.

3.1.6. COUPP. The COUPP experiment operating at SNO-LAB in Ontario is a 4 kg CF_3I bubble chamber. By virtue of its unpaired proton, the fluorine nucleus gives an excellent sensitivity for p -DM spin-dependent interactions, while the iodine enhances the sensitivity for the SI ones.

Particles entering the liquid in the superheated phase create an ionization tracks, around which the liquid vaporizes, forming microscopic bubbles. Bubbles grow in size as the chamber expands, making the detector able to record them both photographically and by pressure and acoustic measurements. The discrimination between nuclear and electromagnetic recoils can be achieved by choosing an appropriate chamber pressure and temperature. Indeed, under this condition, the abundant gamma-ray and beta-decay backgrounds do not nucleate bubbles.

In [55], data obtained for an effective exposure to single recoil events of 437.4 kg-days (taking into account the 79.1% detection efficiency) were presented. Twenty single nuclear recoil events passing all the analysis cuts were observed over the three energy bins. Due to uncertainties in the neutron background estimation, the collaboration has not attempted any background subtraction and instead has treated all of them as DM events.

3.2. Interpretation in Terms of the “Standard” SI Interaction.

There are many studies in literature that try to analyze the implications of the results of DAMA and the anomalies in CoGeNT and CRESST-II and recently in CDMS-Si together with the null results from other experiments in terms of specific DM models and interactions. A routine way to compare results from different DM experiments is by assuming a particular DM velocity distribution and a certain type of DM-nucleus interaction. The customary choices that can often be found in literature are (i) a truncated Maxwell-Boltzmann velocity distribution with isotropic velocity dispersion $v_0 = 220$ km/s and (ii) DM particles coupling through a contact SI interaction with equal strength to the protons and neutrons. In this case one customarily chooses the total DM-nucleon cross section σ_{SI}

defined in Section 2.2.1 together with the DM mass m_χ as free parameters, since the bounds and the allowed regions from different experiments can be compared on the same plot.

In Figure 2 a compilation of the allowed regions of the positive results experiments and the constraints coming from null results taken from different experimental collaborations are shown. Without entering in the details of the different analysis, we summarize the interpretation of the datasets of the positive results experiments listed above in terms of the “standard” SI contact interaction as follows.

- (i) The DAMA modulation signal effect has been shown to be compatible with two areas in the $(m_\chi, \sigma_{\text{SI}})$ parameter space, due to the different kinematics experienced by the two targets in the scintillator. In particular, a region pointing towards DM masses in the 10 GeV ballpark and towards a cross section $\sigma_{\text{SI}} \approx 2 \times 10^{-40} \text{ cm}^2$ can be associated with a DM particle scattering off with sodium (see, e.g., the red contour in the top left-handed plot of Figure 2 denoted by DAMA/Na). Another region around DM masses of roughly 60 GeV is instead due to the scattering with the iodine. In this case the cross section is enhanced by a larger coherent factor and indeed the favored value is $\sigma_{\text{SI}} \approx 10^{-41} \text{ cm}^2$ (red contour denoted by DAMA/I).
- (ii) The modulation in CoGeNT is mostly concentrated in the first two energy bins, close to the lower threshold of the detector. If this anomaly is interpreted in terms of SI contact interaction, it will be fitted by light DM candidates (around 9 GeV) with a total SI cross section $\sigma_{\text{SI}} \approx 3 \times 10^{-41} \text{ cm}^2$ (see, e.g., the red contour in the top right-handed plot of Figure 2).
- (iii) Like DAMA, the CRESST-II experiment is a multiple target detector and therefore more than one allowed region is in general expected. In particular, as one can see in Figure 2, the region pointing towards light DM masses (around 12 GeV) and $\sigma_{\text{SI}} \approx 5 \times 10^{-41} \text{ cm}^2$ is due to the scattering with oxygen and calcium. On the other hand, the one pointing towards heavier DM mass (around 30 GeV) and cross section $\sigma_{\text{SI}} \approx 10^{-42} \text{ cm}^2$ can be associated with a DM particle scattering off with tungstenum. These regions are, for instance, denoted as gray contours in the top left-handed plot of Figure 2.
- (iv) Very recently, also the 11 silicon detectors of the CDMS experiment reported an excess in their counting rate. Again, if the anomaly is interpreted in terms of SI contact interaction, it will be fitted by light DM particles (around 9 GeV) with a SI total cross section $\sigma_{\text{SI}} \approx 2 \times 10^{-41} \text{ cm}^2$ (blue regions in the bottom left-handed plot of Figure 2).

The interesting feature is that all the experiments employing light target nuclei seem to be compatible with a DM interpretation, which, for the “standard” SI contact interaction, pin-points the properties of the DM particle quite precisely; namely, it leads to DM masses in the 10 GeV ballpark and total cross section in the range $(2 \times 10^{-41} \text{ cm}^2 - 2 \times 10^{-40} \text{ cm}^2)$.

On the other hand, the constraints coming from null results are very stringent, and in particular the XENON100 and recently the LUX results severely exclude the allowed parameter space of the positive results experiments. On a more specific level, before LUX, the XENON100 experiment provided the most stringent constraints for a DM mass above roughly 8 GeV, with a minimum of $\sigma_{\text{SI}} \approx 1.8 \times 10^{-44} \text{ cm}^2$ (see, e.g., the thick blue line in the top left-handed plot of Figure 2). Nowadays this bound has been beat out by the one of LUX by a factor ~ 2.5 (see the blue line in the bottom right-handed plot of Figure 2). Other relevant analyses can be found in [56–68].

3.3. *Uncertainties.* Nevertheless, since the actual range of masses and cross section critically depends on several assumptions, one always bears in mind all the uncertainties that enter in this field when interpreting the data in terms of a specific DM interaction.

- (i) A first class of uncertainties comes from the poor knowledge of the properties of the DM halo. The often used Maxwell-Boltzmann halo with isotropic velocity dispersion is only a benchmark choice, not the physical description of it. Other possible choices (spherical halo with nonisotropic velocity dispersion, axisymmetric halo, triaxial halo, and the possibility to have corotating halo with different number densities) must be taken into account, in order to have a much better idea of how the velocity distribution affects the final results. In particular, it has been recently demonstrated that the uncertainties on the astrophysical part of the rate can be removed by comparing different experimental results in the v_{min} space (see, e.g., [69–77]). In this way one can, for instance, relax a bit the tension between the positive results and the constraints showed in Figure 2 up. However, this is not still sufficient to reconcile the complicated puzzle the experimental data have left to us (see, e.g., [77–80]).
- (ii) A second class of uncertainties comes from the experimental side. For instance, the direct measurements of quenching factor are performed with reference detectors, and thus the systematic uncertainties, important for all the detectors in direct DM searches, could be larger than what we normally assumed. These must be carefully investigated, because they produce a significant shift of the allowed regions in the total cross section/DM mass plane.
- (iii) Together with these main uncertainties, the third and perhaps the most important class of them comes from the nature of the DM interaction and in turn from the nuclear responses of the target nuclei. Most of the models tested in recent years are based on the assumption that the mechanism of interaction is realized through a contact interaction. Deviations from this standard phenomenological approach are interesting to study, since, from more general conditions, the DM parameter space can be analyzed.

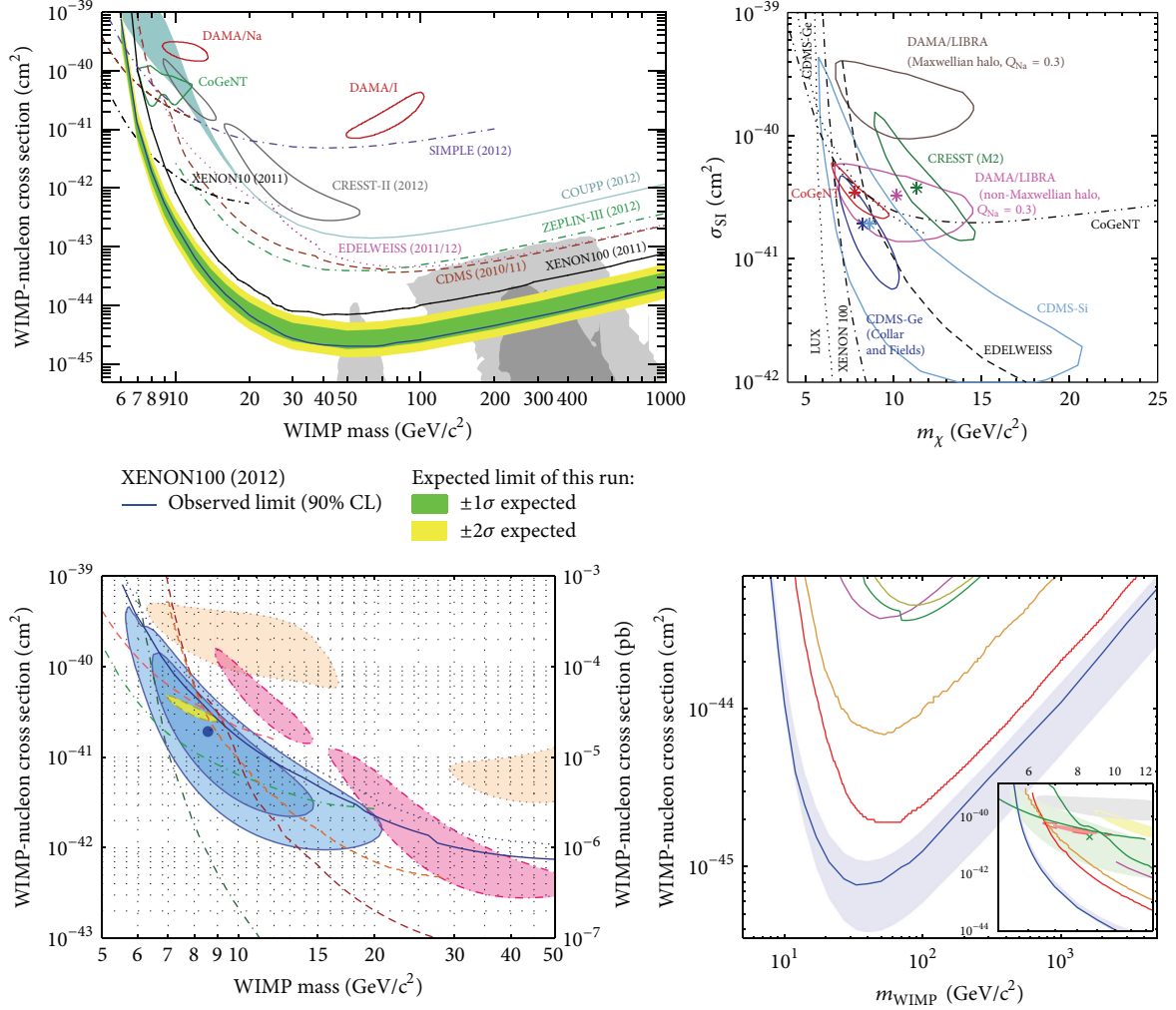


FIGURE 2: A compilation of the allowed regions and the constraints for the “standard” SI contact interaction in the $(m_\chi, \sigma_{\text{SI}})$ plane. The plots on the top row are taken from [53] (left) and from [46] (right), while those in the bottom row are taken from [51] (left) and from [54] (right). The galactic halo has been assumed in the form of an isothermal sphere with velocity dispersion $v_0 = 220$ km/s and local DM energy density $\rho_\odot = 0.3$ GeV/cm³.

In particular, there is a concrete possibility to remove the uncertainties coming from the nature of interaction thanks to the formalism of nonrelativistic operator reviewed in Section 2.2. On a more specific level, if the experimental collaborations, in addition to presenting the results in terms of a specific DM-nucleus interaction, also provide all the model independent *integrated form factors*, it will be extremely useful for the community. Indeed, in this way one can easily compute the expected number of events for any kind of interactions (e.g., including isospin violating interactions, momentum-dependent form factors, and velocity dependent form factors) and compare it directly with the experimental results.

Therefore the data must be treated very prudently with a maximally conservative attitude, simply because slightly modification of the assumptions summarized above can affect the theoretical interpretation of the experimental results in

a relevant way. In the next section, I will focus on the uncertainties coming from the nature of interaction and in particular I am going to show how the allowed regions and constraints are modified, if an exchanged momentum dependent DM-nucleus interaction is taken into account.

4. Long Range Interaction

So far, the LHC has not reported any evidences of physics beyond the standard model. An optimistic point of view is that the new physics threshold is truly around the corner. A pessimistic and maybe more realistic point of view is that the LHC results are instead telling us that the TeV scale is not a fundamental energy scale for new physics and therefore all the new theories beyond the standard model are, let us say, unnatural. Within this picture there is not any particular reason to expect new particles in the TeV mass range weakly interacting with ordinary matter. Therefore it

should be time to ask ourselves whether there are other indications of the relevant energy scale. DM may play a central role in this picture. Indeed, the closeness between Ω_χ and Ω_b , usually referred to as a cosmic coincidence problem, might suggest a profound similarity between the dark and the ordinary sectors. Indeed, both ρ_χ and ρ_b scale as $1/a^3$ with the expansion of the Universe, and their ratio is independent of time. Why these two fractions are then comparable, if the ordinary and the dark sectors have a drastically different nature and different origin? A hidden parallel sector (mirror world (the idea of a mirror world was suggested before the advent of the standard model (see, e.g., [81, 82]). The idea that the mirror particles might constitute the DM of the Universe was instead discussed in [83, 84])) may shed light on this cosmic coincident problem [85]. Indeed, it is tantalizing to imagine that the dark world could be similarly complex (CP violating and asymmetric), full of forces (e.g., dark electromagnetism), and matter (dominant constituent with a mass around few GeV) that are invisible to us. For a review of mirror dark world; see, for example, [86, 87].

To be more concrete the phenomenology of a complex dark sector, in which the matter fields are charged under an extra $U(1)$ gauge group, is particularly interesting. In this case, the physics of the dark sector in itself can be as complicated as the one of our sector, providing at the same time also a feeble interaction between the two worlds. Indeed, thanks to the following renormalizable Lagrangian:

$$\mathcal{L} = \frac{\epsilon_\phi}{2} F^{\mu\nu} F'_{\mu\nu}, \quad (24)$$

the new $U(1)$ gauge boson ϕ may possess a small kinetic mixing ϵ_ϕ with the ordinary photon. Here $F_{\mu\nu}$ and $F'_{\mu\nu}$ are the field strength tensors of the ordinary and “dark” electromagnetism, respectively. One effect of this mixing is to cause DM particles to couple with ordinary particles with effective millicharge $\epsilon_\phi e$ [88–90], and therefore a Rutherford-like interaction gives rise if the mass of the new $U(1)$ gauge boson is smaller than the typical exchanged momentum in the interaction.

4.1. Derivation of the Main Equations. Apart from the theoretical motivations which are interesting and quite strong, what describes in the nonrelativistic limit the scattering between millicharged DM particles and the protons (notice that the interaction here maximally violates the isospin; e.g., the DM-neutron coupling is zero) is the following Yukawa potential:

$$V(r) = \frac{\epsilon_\phi}{4\pi} \frac{ee_\chi}{r} e^{-m_\phi r}, \quad (25)$$

where $\epsilon_\phi e$ is the effective millicharge of the protons inside the nucleus felt by a DM particle with “dark” charge e_χ . Here m_ϕ is the mass of the dark photon that acts like an electronic cloud which screens the charges of the particles involved in the scattering. The DM-proton matrix element can be then

obtained by performing the Fourier transform of (25) which writes

$$\begin{aligned} \mathcal{M}_p &= 4 m_p m_\chi \int_0^\infty dr 2\pi r^2 \int_{-1}^{+1} d \cos \theta e^{-iqr \cos \theta} V(r) \\ &= c_Y^p(q^2) \mathcal{O}_1^{\text{NR}}, \end{aligned} \quad (26)$$

where $q = (2m_\mathcal{N}E_R)^{1/2}$ is the exchanged momentum, θ is the scatter angle in the centre-of-mass frame, and $c_Y^p(q^2) = 4\epsilon_\phi ee_\chi m_p m_\chi / (q^2 + m_\phi^2)$. Since $\mathcal{O}_1^{\text{NR}} = \mathbb{1}$, the interaction, as already mentioned in Section 2.2, is SI like the usual case but with a coefficient which is instead dependent on the exchanged momentum in the scattering. Summing now over the total number of protons in the nucleus $Z_\mathcal{N}$ and, if the dark sector is made of stable composite particles, over the total number of charge elementary constituents Z_χ , the square of the DM-nucleus matrix element reads

$$|\overline{\mathcal{M}_\mathcal{N}}|^2 = 16m_\mathcal{N}^2 m_\chi^2 \left(\frac{\epsilon_\phi Z_\mathcal{N} e Z_\chi e_\chi}{q^2 + m_\phi^2} \right)^2 F_{\text{Helm}}^2(q^2), \quad (27)$$

where $F_{\text{Helm}}^2(q^2)$ is the usual Helm form factor. Notice that in general this equation should be also multiplied for the form factor of the composite DM particle. For our computation we assume it to be equal to one. Plugging back the DM-nucleus matrix element in (8) the differential cross section will be

$$\frac{d\sigma_\mathcal{N}}{dE_R} = \frac{8\pi m_\mathcal{N}}{v^2} \epsilon_\phi^2 \alpha^2 k_\chi^2 \left(\frac{1}{q^2 + m_\phi^2} \right)^2 Z_\mathcal{N}^2 F_{\text{Helm}}^2(q^2), \quad (28)$$

where $\alpha = e^2/4\pi$ is the electromagnetic fine structure constant and $k_\chi = Z_\chi e_\chi/e$ is a factor that measures the strength of the DM-dark photon coupling.

In order to have a rough comparison with the “standard” picture (SI contact interaction), the differential rate of nuclear recoil can be cast in the following form:

$$\begin{aligned} \frac{dR_\mathcal{N}}{dE_R} &= \frac{\xi_\mathcal{N}}{m_\mathcal{N}} \frac{\rho_\odot}{m_\chi} \left[\frac{m_\mathcal{N}}{2\mu_N^2} A^2 \sigma_{\phi\gamma}^p \mathcal{F}(E_R) F_{\text{Helm}}^2(E_R) \right] \\ &\times \mathcal{G}(E_R), \end{aligned} \quad (29)$$

where

$$\begin{aligned} \sigma_{\phi\gamma}^p &= \frac{16\pi\alpha^2 \epsilon_\phi^2 k_\chi^2}{m_\mathcal{N}^4} \mu_N^2 \\ &\simeq \left(\frac{\epsilon_\phi}{10^{-5}} \right)^2 \left(\frac{k_\chi}{1} \right)^2 \left(\frac{\mu_N}{1 \text{ GeV}} \right)^2 10^{-40} \text{ cm}^2 \end{aligned} \quad (30)$$

is a normalized total cross section that encapsulates all the dependences on the dark sector vertex and the kinetic mixing parameter, and the function

$$\mathcal{G}(E_R) = \frac{Z_\mathcal{N}^2}{A_\mathcal{N}^2} \left[\frac{m_\mathcal{N}^2}{q^2 + m_\phi^2} \right]^2 = \frac{Z_\mathcal{N}^2}{A_\mathcal{N}^2} \left[\frac{m_\mathcal{N}^2}{2m_\mathcal{N}E_R + m_\phi^2} \right]^2 \quad (31)$$

measures the deviation of the allowed regions and constraints compared to the “standard” SI contact cross section. Here the function $\mathcal{G}(E_R)$ is a sort of DM form factors which clearly exhibits two limits.

- (i) Point-like limit ($q \ll m_\phi$): in this regime $\mathcal{G}(E_R) = (Z_{\mathcal{N}}/A_{\mathcal{N}})^2 m_{\mathcal{N}}^4/m_\phi^4$ is independent of E_R and therefore the interaction is of a contact type. Indeed, the rate of nuclear recoil turns out to be proportional to $\alpha^2 \epsilon_\phi^2 k_\chi^2/m_\phi^4$, which plays the same role of the Fermi’s constant in weak interaction. The factor $(Z_{\mathcal{N}}/A_{\mathcal{N}})^2$ shows up the fact that millicharged DM particles only couple with protons. Therefore, it is expected that the allowed regions and bounds in the plane $(m_\chi, \sigma_{\phi\gamma}^p)$ will be rigid shifted of a factor ~ 4 up with respect to the “standard” SI scenario, in which a DM particle symmetrically couples both with neutrons and protons.
- (ii) Long range limit ($q \gg m_\phi$): in this regime $\mathcal{G}(E_R) = (Z_{\mathcal{N}}/A_{\mathcal{N}})^2 m_{\mathcal{N}}^4/(4m_{\mathcal{N}}^2 E_R^2)$ and therefore the differential cross section acquires an explicit dependence on the nuclear recoil energy, and a Rutherford-like cross section gives rise ($d\sigma_{\mathcal{N}}/dE_R \propto 1/q^4$). Experiments with low energy thresholds and light target nuclei (e.g., DAMA and CoGeNT) are therefore more sensitive than the ones with high thresholds and heavy targets (e.g., XENON100). The compatibility among the experiments could therefore be improved.

Considering typical nuclei ($m_{\mathcal{N}} \sim 100$ GeV) and recoil energies (few keV) in the range of interest of the current experiments, the transition between the two limits is obtained for $m_\phi \sim \mathcal{O}(10)$ MeV. Since $q^2 \propto m_{\mathcal{N}}$, increasing $m_{\mathcal{N}}$ the transition occurs at lower m_ϕ . Notice that once the long range regime is reached ($m_\phi \lesssim 10$ MeV), the differential cross section is independent of the mass of the mediator.

4.2. Results. In our analysis we consider as free parameters the normalized total cross section $\sigma_{\phi\gamma}^p$, the mass of the dark photon m_ϕ , and of course one of the DM particle m_χ . The velocity distribution has been assumed to be Maxwell-Boltzmann-like with a velocity dispersion $v_0 = 220$ km/s. For the local DM density we have chosen $\rho_\odot = 0.3$ GeV/cm³. For all the positive results experiments we use a different technique for analyzing the datasets with respect to the one often found in literature. Specifically, we adopt the same approach of [91], in which the null hypothesis is tested. From this kind of statistical test we can then extract the level at which the absence of signal on top of the background in CRESST-II and the absence of modulation in DAMA and CoGeNT is rejected.

In Figure 3 the allowed regions of the positive results experiments and constraints coming from null results in the plane $(m_\chi, \sigma_{\phi\gamma}^p)$ are shown. For a better visualization of the transition from the contact to the long range regime, we have fixed three values of the dark photon mass; namely, $m_\phi = 1$ GeV (left plot corresponding to the contact limit),

$m_\phi = 30$ MeV (central plot), and $m_\phi = 0$ (right plot corresponding to the pure long range regime). In all plots the solid green contours individuate the regions compatible with the DAMA annual modulation [41, 42], without considering the channeling effect. The short-dashed blue contour refers to the region derived from the CoGeNT annual modulation signal data published in [45] (in [46, 47] the collaboration reanalyzed the data finding that the background of surface events was underestimated. In view of that we expect that the CoGeNT allowed regions in the $(m_\chi, \sigma_{\phi\gamma}^p)$ plane will shrink around its best value, like the one reported for the “standard” SI contact interaction (see, e.g., the red contour in the top right-handed plot of Figure 2)). The dashed brown contours individuate the allowed regions compatible with the CRESST-II excess [48]. For each experiment the contour lines cover at least one area in the $(m_\chi, \sigma_{\phi\gamma}^p)$ plane. Specifically, they refer to regions where the absence of annual modulation can be rejected at 7 σ CL (outer region) and 8 σ CL (inner region) for DAMA, and 1 σ CL for CoGeNT. For CRESST-II the absence of an excess is instead excluded at 3 σ CL (outer region) and 4 σ CL (inner region).

Very recently, also the 11 silicon detectors of the CDMS experiment have reported an excess in their counting rate. Since the results presented in Figure 3 are based on [24] published in 2011, we do not include a full statistical analysis of the CDMS-Si datasets. We attempt however an analytical comparison between the results arising from the interaction studied here and the standard SI contact picture (blue regions in the bottom left-handed plot of Figure 2). More precisely, defining $\langle \mathcal{G} \rangle \equiv \mathcal{G}(\langle E_R \rangle)$, where $\langle E_R \rangle \simeq 10$ keV is the average recoil energy of the three events observed [51], the CDMS-Si allowed region in the $(m_\chi, \sigma_{\text{SI}})$ plane can be projected in the parameter space of Figure 3, through the relation $(m_\chi, \sigma_{\phi\gamma}^p) \equiv (m_\chi, \sigma_{\text{SI}}/\langle \mathcal{G} \rangle)$. Recalling now that the best fit value of the SI cross section is $\sigma_{\text{SI}}^{\text{best}} \simeq 2 \times 10^{-41}$ cm², we expect that the CDMS-Si allowed region in the $(m_\chi, \sigma_{\phi\gamma}^p)$ plane will still point towards light DM candidate, but with a normalized total cross section $\sigma_{\phi\gamma}^p = A_{\text{Si}}^2/Z_{\text{Si}}^2 m_\phi^4/m_{\mathcal{N}}^4 \sigma_{\text{SI}}^{\text{best}} \simeq 10^{-40}$ cm² in the point-like regime ($m_\phi = 1$ GeV), and $\sigma_{\phi\gamma}^p = A_{\text{Si}}^2/Z_{\text{Si}}^2 4m_{\text{Si}}^2 \langle E_R \rangle^2/m_{\mathcal{N}}^4 \sigma_{\text{SI}}^{\text{best}} \simeq 3 \times 10^{-47}$ cm² in the long range one ($m_\phi = 0$).

Constraints, derived at 5 σ CL, are shown as dashed gray lines for CDMS-Ge and magenta lines for XENON100. In particular, in order to bracket as much as possible the uncertainties coming from the poor knowledge of the detection efficiency close to the lower threshold; for the XENON100 bound, we adopt two approaches: (i) a case (dotted lines) in which the constraints are computed with the nominal value of the lower threshold of 4 PHE and of the effective luminosity [92], which is a sort of quenching factors in liquid xenon and (ii) another case (dashed lines) in which the constraints are computed by considering a higher threshold of 8 PHE: this is in order to determine a situation which is nearly independent of the poor knowledge of the effective luminosity (especially at very low nuclear recoil) and more important on the statistical distribution of the few PHE collected close to the threshold of the detector. For similar discussions; see [93, 94].

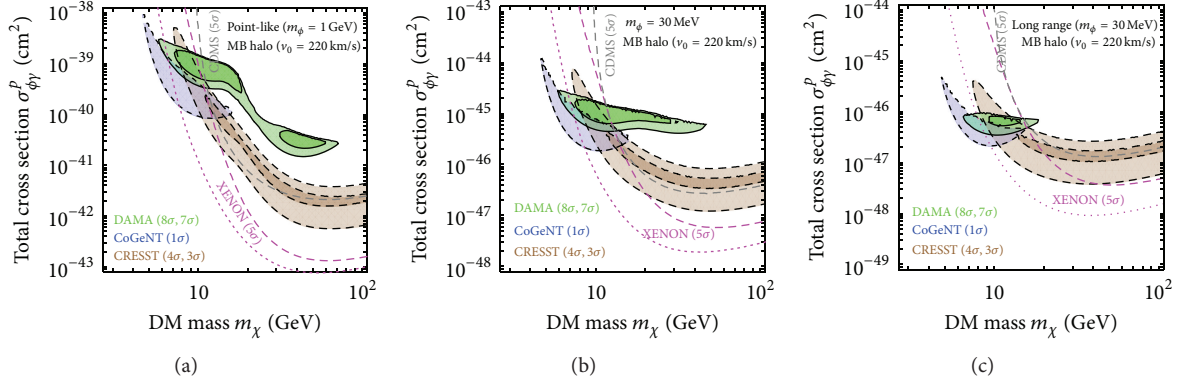


FIGURE 3: Normalized total cross section as a function of the dark matter mass. For a better visualization of the transition from the contact to the long range regime, we have fixed three values of the dark photon mass; namely, $m_\phi = 1$ GeV (a), $m_\phi = 30$ MeV (b), and $m_\phi = 0$ (c). In all plots we show the regions where the absence of annual modulation can be rejected at 7σ CL (outer region) and 8σ CL (inner region) for DAMA (solid green contours) and 1σ CL for CoGeNT (solid green contours). For CRESST-II (solid green contours) the absence of an excess is instead excluded at 3σ CL (outer region) and 4σ CL (inner region). Constraints, derived at 5σ CL, are shown as dashed gray lines for CDMS-Ge and magenta lines for XENON100. These results have been presented in [24, 25].

In October 2013, also the LUX collaboration announced their first DM search results. With the data collected in just 85 live-days, they were able to set the most stringent bound on the SI contact cross section, with respect to the preexisting limits. We do not perform a full statistical analysis of their data, since, as already pointed out, the results in Figure 3 are taken from [24]. Nevertheless, since both XENON and LUX are based on the same double-phase xenon technology, we can estimate the bound on $\sigma_{\phi\gamma}^p$, just by rescaling the magenta lines in Figure 3 with the exposures of the two experiments. Naively, we then expect that the LUX bound will be a factor $w_{\text{LUX}}/w_{\text{XENON100}} \simeq 1.5$ more stringent with respect to XENON100.

We can see, as expected from the discussion above, that the agreement among the positive results experiments increases moving towards long range interaction without being excluded by both the XENON100 and LUX bounds, if our conservative choice for the lower threshold is taken into account. In particular, a common region pointing towards a DM mass around 15 GeV with a normalized total cross section $\sigma_{\phi\gamma}^p \sim 10^{-46}$ cm² has been found. Since the normalized total cross section $\sigma_{\phi\gamma}^p$ depends collectively on the kinetic mixing parameter ϵ_ϕ and on the DM-dark photon coupling encoded in the parameter k_χ (see (30)), keeping fixed, for instance, two values of k_χ , namely, $k_\chi = (1, 10)$; the best fit for the kinetic mixing parameter would then be $\epsilon_\phi \sim (10^{-8}, 10^{-9})$.

On the other hand, the significance of the DAMA region alone gets lower, due to the fact that for pure long range interaction ($q \gg m_\phi$) the $1/q^4$ drop-off of the unmodulated signal rapidly overshoots the measured total rate (see [41, Figure 1]), that of course we treat as an intrinsic constraint in our analysis. This can be appreciated in more details in Figure 4, where again the DAMA allowed regions are shown, but in the (m_χ, m_ϕ) plane. As one can see a 99% confidence level lower bound on the mass of the dark photon

around 10 MeV is possible to be placed. This is due to the fact that the unmodulated signal, unlike the modulated one, is particularly sensitive to the energy drop-off of the cross section, which is typical for Rutherford-like scattering. The situation does not dramatically vary if we change the properties of the dark matter halo. Indeed, if we consider a more physical triaxial halo with the same velocity dispersion in the major axis (right plot of Figure 4), the allowed regions are only slightly enhanced.

Nevertheless, it is worth noticing that, in a dark world filled by more than one species in thermal equilibrium, the DM particles responsible for the annual modulation may possess smaller velocity dispersion. For instance, in the context of mirror DM, the dominant species can be the mirror hydrogen, like our world, while the mass of the DM particles favored by direct detection experiments is around 16 GeV (mirror oxygen). If they are in thermal equilibrium, the relation $v_0 = 1/\sqrt{2} (A_H/A_O)^{1/2} \cdot 220$ km/s ≤ 100 km/s then will hold [21]. In this case the constraints in Figure 4 are less important, because the raise of the total rate for low nuclear recoil energy is under threshold (see, e.g., [21, Figures 5(a) and 5(b)]).

Since, as already stated, the normalized total cross section and in turn the rate depend collectively on the kinetic mixing parameter ϵ_ϕ and on the DM-dark photon coupling k_χ ; in the next section, a complementary class of constraints which are relevant for DM models featured by a long range interaction will be presented.

4.3. Complementary Constraints. A first class of complementary constraints that solely depends on the properties of the dark photon (kinetic mixing parameter ϵ_ϕ and its mass m_ϕ) is the one coming from beam dump neutrino experiments and supernovae observations. In Figure 5 a compilation of the bounds in the (m_ϕ, ϵ_ϕ) plane is shown. Specifically,

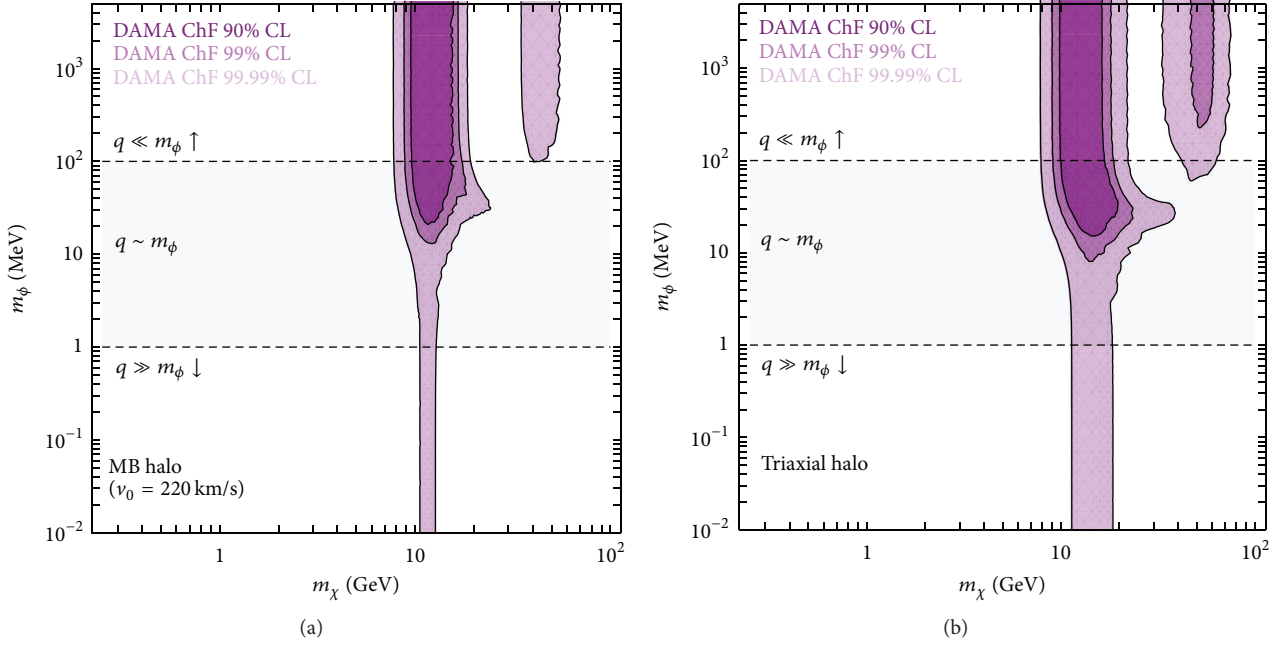


FIGURE 4: The bounds on the mediator mass as a function of the DM one obtained by comparing the DAMA modulated signal with the total rate. The allowed regions are reported for CLs of 90%, 99%, and 99.99% in shaded magenta. In (a) an isothermal sphere with velocity dispersion $v_0 = 220$ km/s and a local DM energy density $\rho_0 = 0.3$ GeV/cm³ has been assumed. In (b) we instead show the allowed regions by considering a more physical triaxial halo with the same velocity dispersion in the major axis and with $\rho_0 = 0.84$ GeV/cm³. These results have been presented in [24, 25].

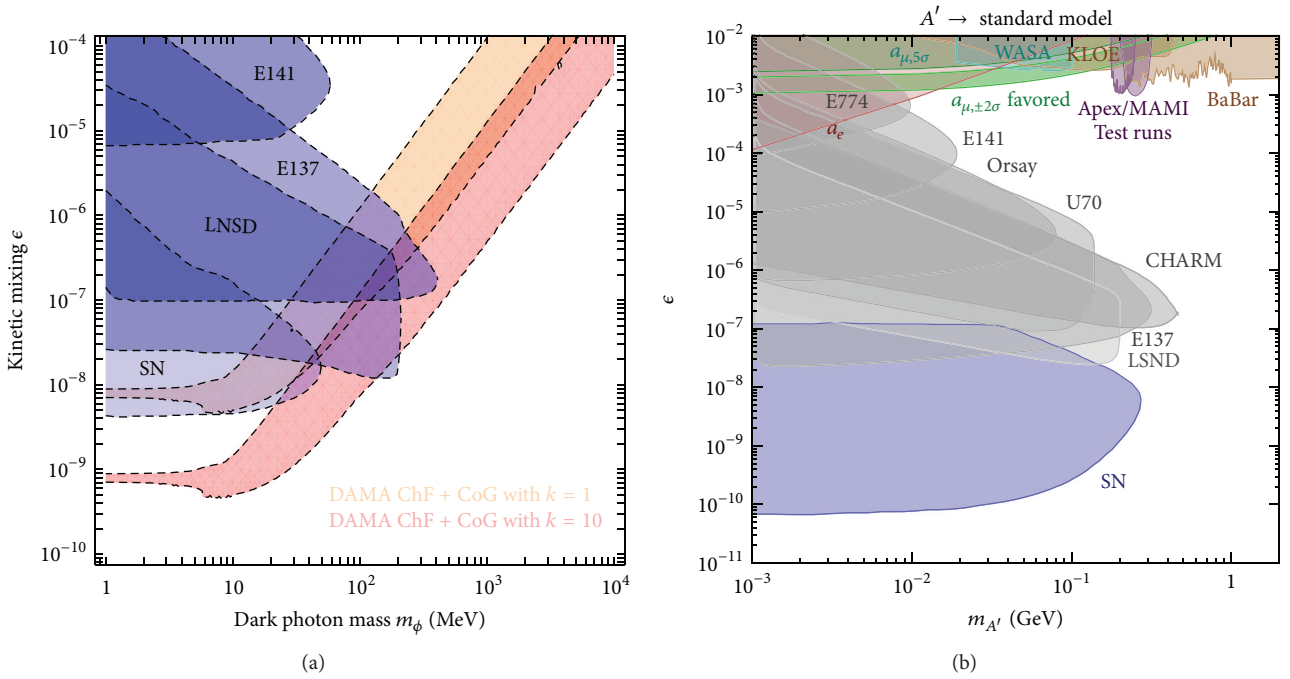


FIGURE 5: Allowed regions and a compilation of constraints in the (m_ϕ, ϵ_ϕ) plane. (a) The upper (orange) and the lower (red) allowed regions are derived by combining the DAMA and CoGeNT annual modulation dataset. Specifically, the absence of modulation is here rejected at 8σ CL. The two regions differ in the choice of parameter k_χ ; namely $k_\chi = 1$ (upper) and $k_\chi = 10$ (lower). In blue are instead represented the constraints coming from beam dumped neutrino experiments and supernovæ observations taken from [95, 96]. (b) A compilation of the latest constraints in the (m_ϕ, ϵ_ϕ) plane. This plot has been taken from the following review [97]. It is worth pointing out that for $m_\phi \leq 10^{-6}$ eV the parameter space of the positive results experiments in direct DM searches is basically unbounded (see, e.g., [97, Figure 7]).

on the left panel the shaded blue regions are taken from [95, 96], while those in the right one represent the latest constraints on the dark photon properties presented in [97] (notice that the labels ϵ and $m_{A'}$ in the plots of Figure 5 stand for the kinetic mixing parameter ϵ_ϕ and the dark photon mass m_ϕ , resp.). As is apparent, the bounds coming from supernovæ observations (namely, the energy loss observed from SN1987a) are the most stringent. They exclude small kinetic mixing parameter and light mass for the dark photon. Indeed, in this case, if dark photons were produced in relevant amount in the centre of a supernova via mixing with the ordinary photon, the subsequent emission of them would shorten so that the predicted neutrinos boost that it would become inconsistent with the measurements made by KamiokaNDE (see, e.g., [95, 98, 99]).

The allowed regions of the DAMA and CoGeNT experiments projected in the (m_ϕ, ϵ_ϕ) plane are instead shown in the left plot of Figure 5. Since, as already stated, the normalization of the rate depends not only on the properties of the dark photon but also on its coupling with the DM particles, we present the results for two benchmark values of k_χ , for example, $k_\chi = 1$ (upper orange region) and $k_\chi = 10$ (lower orange region). We can see that, in the ‘‘symmetric’’ case $k_\chi = 1$, only the dark photons with $m_\phi \gtrsim 100$ MeV can simultaneously satisfy the constraints and give a reasonable fit of the positive results of experiments. On the other hand, for $k_\chi \gtrsim 50$, the whole range is basically unbounded. It is worth stressing that such large values of k_χ can be easily obtained either in models of composite DM particles with large Z_χ (e.g., mirror models) or in those with a strongly coupled dark sector. Furthermore, it is also relevant to point out that, for pure long range interaction ($m_\phi = 0$), the majority of the bounds, and in particular those coming from supernovæ observations, do not apply, being the direct production of dark photon forbidden by kinematical reason (see, e.g., [97, Figure 7]).

A second class of constraints which instead solely depends on the properties on the dark sector itself is the one coming from the self-interactions. Indeed, since for this class of models the DM-DM scattering, given by

$$V(r) = \frac{\alpha k_\chi}{r} e^{-m_\phi r}, \quad (32)$$

is not suppressed by ϵ_ϕ , the self-interactions can easily reach high values, making the dynamics of virialized astrophysical objects affected. This is particularly relevant in the limit $m_\phi \rightarrow 0$; indeed, in this case the self-interaction (32) could be of the same order of the electromagnetic scattering.

A first example of such bounds comes from the observations of colliding galaxy clusters, like the bullet cluster [100], which points towards collision-less DM. In particular a quite robust bound $\langle \sigma_T \rangle / m_\chi \lesssim 1.25 \text{ cm}^2/\text{g}$ on the size of the self-interaction has been placed by [101]. In order to translate such bound in a constraint on the dark photon mass, one has to compute the weighted energy transfer cross section, which

measures the rate at which energy is transferred in the system. It reads

$$\langle \sigma_T \rangle = \iint d^3 v_1 d^3 v_2 f(v_1) f(v_2) \sigma_T(v_{\text{rel}}), \quad (33)$$

where $\sigma_T(v_{\text{rel}}) = \int d\Omega d\sigma/d\Omega(1 - \cos\theta)$ is the two-body energy transfer cross section. Here $f(v)$ is the DM velocity distribution, assumed to be Maxwellian, and $v_{\text{rel}} = |\vec{v}_1 - \vec{v}_2|$ is the relative velocity of the DM particles involved in the scattering. Considering now the typical velocity of collision in the bullet cluster of 4700 km/s, a DM mass of 10 GeV, and two values of $k_\chi = (1, 10)$, the bound of $1.25 \text{ cm}^2/\text{g}$ is exceeded if the mass of the dark photon is smaller than (1, 20) MeV.

A second example of bounds, which is in principle relevant for this kind of models, comes from the fact that quite large self-interaction rapidly drives the DM halo into a spherical configuration, due to the prompt equipartition of the energy in the system. In particular, the efficiency of such process can be roughly estimated by

$$\tau_{\text{rel}} = \frac{1}{\langle \Gamma_T \rangle}, \quad (34)$$

where

$$\langle \Gamma_T \rangle = \iint d^3 v_1 d^3 v_2 f(v_1) f(v_2) n_\chi v_{\text{rel}} \sigma_T(v_{\text{rel}}) \frac{v_{\text{rel}}^2}{v_0^2}, \quad (35)$$

which is telling us the typical time at which the self-interactions affect the dynamics of a virialized astrophysical object with number density n_χ and dispersion velocity v_0 . Indeed, if it is smaller than the age of the object, a spherical configuration will tend to form, making such scenario excluded by few elliptical DM halos observations [102–106]. In particular, in the case of galaxy clusters we get that the relaxation time is always bigger than the age of the object ($\tau_{\text{ob}} \sim 10^{10}$ years), making therefore the mass of the dark photon basically unbounded. On the other hand, if we consider a smaller halo, like the one of dwarf galaxies, which are characterized by larger number density and smaller velocity dispersion, one can in principle put a very stringent lower bound on the mass of the dark photon of the order of 100 MeV (see also [107, 108]).

Nevertheless, it is worth stressing that the derivations of the constraints coming from self-interaction are affected by several uncertainties both from the theoretical and experimental side. Indeed, since the phenomenology of this class of models is completely different compared to the standard one, an N-body/hydrodynamical simulation is needed. This is especially true in the case of multicomponent dark sector, in which the different equipartitions of the energy among the DM particles can generate a sort of dark electric and magnetic fields in the long range regime. Furthermore, since the self-interaction needed to change their dynamics is in general of the order of the Thomson scattering ($\sigma_{\text{em}} \sim 10^{-24} \text{ cm}^2$), from trivial analysis dimension of such large cross section, the following rough estimation yields: the self-interaction is of a long range type in most of the virialized astrophysical objects under the assumption that the DM-dark photon coupling is

of the order of α . In this case, the probability to radiate a dark photon in the scattering process is then different from zero and therefore it might well be possible that the DM sector is dissipative like ours. The time at which energy is transferred in the system (τ_{rel}) is no longer a good indicator, since the relevant quantity that describes the dynamical evolution of the system is now the cooling time: in particular, for a DM sector composed by heavy and light species, the dissipation time due to the soft emission of the dark photon (dark bremsstrahlung) can be smaller than the age of the virialized astrophysical objects (see, e.g., [109–111]). In this scenario the system is no longer stable, and in general it starts to collapse. By virtue of this fact, we do not consider this last class of constraints, since dedicated and careful analysis involving also numerical simulations is needed.

5. Conclusion

Direct DM searches are now characterized by tantalizing results and hints that make this field very active both from the theoretical and experimental side. In particular, in addition to the long standing DAMA results, nowadays there are other experiments, like CoGeNT, CRESST-II and CDMS-Si that are starting to observe anomalies in their counting rates. On the other hand, the increasingly stringent constraints coming from null result experiments put in serious trouble the theoretical interpretation of the data, at least in terms of the simple-minded SI contact interaction. In this work I discussed the *status* of direct DM detection with specific attention to the experimental results and their phenomenological interpretation in terms of DM interaction. In particular, in the first part I presented a new and more general approach to study signals in this field based on nonrelativistic operators. Then I reviewed the experimental results and their interpretation in terms of the “standard” SI interaction pointing out all the uncertainties which enter in this field. In the last part of this work, I investigated a fermionic dark matter particle carrying a small millicharged and analyzed its impact on direct detection experiments. I showed that this kind of long range interaction can accommodate the positive experimental results. By assuming a conservative choice for the lower threshold of the XENON100 and LUX experiments I have demonstrated that this candidate is not ruled out. I also determined the complementary class of constraints which are relevant for millicharged DM particles with long range forces.

Finally, I would like to propose a possible direction to pursue in order to make sense of the current exciting experimental panorama based on the formalism of non-relativistic operators. Indeed, as we have seen in the first part of this work, it allows us to describe the DM-nucleus interactions in terms of a very limited number of relevant degrees of freedom. In this way, it is possible to parametrize the model-dependent part of the rate from the model-independent one encapsulated in a sort of *integrated form factors* that encode all the dependences on the astrophysics, nuclear physics, and experimental details. Therefore, since one is ignorant or agnostic about the underlying theory, I

would like to encourage a synergy between nuclear physicists and experimentalists in order to provide a complete set of *integrated form factors* defined in (23). It would be extremely useful for the community, because, in this way, one can compute the expected number of events for any kind of interaction (e.g., including isospin-violating interactions, momentum-dependent form factors, and velocity-dependent form factors) and compare it directly with the experimental results. Providing the *integrated form factors* will thus be the first step towards a model-independent analysis in direct DM searches.

Conflict of Interests

The author declares that there is no conflict of interests regarding the publication of this paper.

Acknowledgments

The author thanks Marco Cirelli, Eugenio Del Nobile, and Joe Silk for useful discussions.

References

- [1] P. A. R. Ade, N. Aghanim, C. Armitage-Caplan et al., “Planck 2013 results. XVI: cosmological parameters,” <http://arxiv.org/abs/1303.5076>.
- [2] G. Bertone, D. Hooper, and J. Silk, “Particle dark matter: evidence, candidates and constraints,” *Physics Reports*, vol. 405, no. 5–6, pp. 279–390, 2005.
- [3] G. Jungman, M. Kamionkowski, and K. Griest, “Supersymmetric dark matter,” *Physics Report*, vol. 267, no. 5–6, pp. 195–373, 1996.
- [4] J. Berlinger, J. F. Arguin, R. M. Barnett et al., “Review of particle physics,” *Physical Review D*, vol. 86, no. 1, Article ID 01 01, 2012.
- [5] R. Catena and P. Ullio, “A novel determination of the local dark matter density,” *Journal of Cosmology and Astroparticle Physics*, vol. 2010, no. 8, article 4, 2010.
- [6] M. Weber and W. De Boer, “Determination of the local dark matter density in our galaxy,” *Astronomy and Astrophysics*, vol. 509, no. 1, A25, 2010.
- [7] P. Salucci, F. Nesti, G. Gentile, and C. F. Martins, “The dark matter density at the Sun’s location,” *Astronomy and Astrophysics*, vol. 523, no. 5, article A83, 2010.
- [8] D. Lynden-Bell and S. Jin, “Statistical mechanics of violent relaxation in stellar systems,” *Monthly Notices of the Royal Astronomical Society*, vol. 136, no. 1, p. 101, 1967.
- [9] M. Vogelsberger, A. Helmi, V. Springel et al., “Phase-space structure in the local dark matter distribution and its signature in direct detection experiments,” *Monthly Notices of the Royal Astronomical Society*, vol. 395, no. 2, pp. 797–811, 2009.
- [10] Y. P. Jing and Y. Suto, “Triaxial modeling of halo density profiles with high-resolution N-body simulations,” *Astrophysical Journal Letters*, vol. 574, no. 2, pp. 538–553, 2002.
- [11] C. Savage, G. Gelmini, P. Gondolo, and K. Freese, “Compatibility of DAMA/LIBRA dark matter detection with other searches,” *Journal of Cosmology and Astroparticle Physics*, vol. 2009, no. 4, article 010, 2009.
- [12] P. Belli, R. Cerulli, N. Fornengo, and S. Scopel, “Effect of the galactic halo modeling on the DAMA-NaI annual modulation

- result: an extended analysis of the data for weakly interacting massive particles with a purely spin-independent coupling,” *Physical Review D*, vol. 66, no. 4, Article ID 043503, 2002.
- [13] N. Fornengo and S. Scopel, “Temporal distortion of the annual modulation signal of weakly interacting massive particles at low recoil energies,” *Physics Letters B*, vol. 576, no. 1-2, pp. 189–194, 2003.
- [14] A. K. Drukier, K. Freese, and D. N. Spergel, “Detecting cold dark-matter candidates,” *Physical Review D*, vol. 33, no. 12, pp. 3495–3508, 1986.
- [15] K. Freese, J. Frieman, and A. Gould, “Signal modulation in cold-dark-matter detection,” *Physical Review D*, vol. 37, no. 12, pp. 3388–3405, 1988.
- [16] B. A. Dobrescu and I. Mocioiu, “Spin-dependent macroscopic forces from new particle exchange,” *Journal of High Energy Physics*, vol. 2006, no. 11, article 005, 2006.
- [17] A. L. Fitzpatrick, W. Haxton, E. Katz, N. Lubbers, and Y. Xu, “The effective field theory of dark matter direct detection,” *Journal of Cosmology and Astroparticle Physics*, vol. 2013, no. 2, article 004, 2013.
- [18] A. L. Fitzpatrick, W. Haxton, E. Katz, N. Lubbers, and Y. Xu, “Model independent direct detection analyses,” <http://arxiv.org/abs/1211.2818>.
- [19] N. Anand, A. L. Fitzpatrick, and W. C. Haxton, “Model-independent WIMP scattering responses and event rates: a mathematica package for experimental analysis,” <http://arxiv.org/abs/1308.6288>.
- [20] M. Pospelov and T. Ter Veldhuis, “Direct and indirect limits on the electro-magnetic form factors of WIMPs,” *Physics Letters B*, vol. 480, no. 1-2, pp. 181–186, 2000.
- [21] R. Foot, “Mirror dark matter and the new DAMA/LIBRA results: a simple explanation for a beautiful experiment,” *Physical Review D*, vol. 78, no. 4, Article ID 043529, 10 pages, 2008.
- [22] R. Foot, “A CoGeNT confirmation of the DAMA signal,” *Physics Letters B*, vol. 692, no. 2, pp. 65–69, 2010.
- [23] R. Foot, “Mirror & hidden sector dark matter in the light of new CoGeNT data,” *Physics Letters B*, vol. 703, no. 1, pp. 7–13, 2011.
- [24] N. Fornengo, P. Panci, and M. Regis, “Long-range forces in direct dark matter searches,” *Physical Review D*, vol. 84, no. 11, Article ID 115002, 2011.
- [25] P. Panci, <http://arxiv.org/abs/1206.2240>.
- [26] D. E. Kaplan, G. Z. Krnjaic, K. R. Rehermann, and C. M. Wells, “Atomic dark matter,” *Journal of Cosmology and Astroparticle Physics*, vol. 2010, no. 5, article 021, 2010.
- [27] K. Sigurdson, M. Doran, A. Kurylov, R. R. Caldwell, and M. Kamionkowski, “Dark-matter electric and magnetic dipole moments,” *Physical Review D*, vol. 70, no. 8, Article ID 083501, 15 pages, 2004, Erratum in *Physical Review D*, vol. 73, no. 8, Article ID 089903, 2006.
- [28] S. Chang, N. Weiner, and I. Yavin, “Magnetic inelastic dark matter,” *Physical Review D*, vol. 82, no. 12, Article ID 125011, 2010.
- [29] V. Barger, W. Y. Keung, and D. Marfatia, “Electromagnetic properties of dark matter: dipole moments and charge form factor,” *Physics Letters B*, vol. 696, no. 1-2, pp. 74–78, 2011.
- [30] E. Del Nobile, C. Kouvaris, P. Panci, F. San-nino, and J. Virkajarvi, “Light magnetic dark matter in direct detection searches,” *Journal of Cosmology and Astroparticle Physics*, vol. 2012, no. 8, article 10, 2012.
- [31] C. M. Ho and R. J. Scherrer, “Anapole dark matter,” *Physics Letters B*, vol. 722, no. 4-5, pp. 341–346, 2013.
- [32] M. Cirelli, E. Del Nobile, and P. Panci, “Tools for model-independent bounds in direct dark matter searches,” *Journal of Cosmology and Astroparticle Physics*, vol. 2013, no. 10, article 019, 2013.
- [33] R. H. Helm, “Inelastic and elastic scattering of 187-MeV electrons from selected even-even nuclei,” *Physical Review*, vol. 104, no. 5, pp. 1466–1475, 1956.
- [34] R. Bernabei, P. Belli, V. Landoni et al., “New limits on WIMP search with large-mass low-radioactivity NaI(Tl) set-up at Gran Sasso,” *Physics Letters B*, vol. 389, no. 4, pp. 757–766, 1996.
- [35] R. Bernabei, P. Belli, F. Montecchia et al., “Possible implications of the channeling effect in NaI(Tl) crystals,” *European Physical Journal C*, vol. 53, no. 2, pp. 205–213, 2008.
- [36] E. M. Drobyshevski, “Channeling effect and improvement of the efficiency of charged particle registration with crystal scintillators,” *Modern Physics Letters A*, vol. 23, no. 36, pp. 3077–3085, 2008.
- [37] J. Graichen, K. Maier, J. Schüth, A. Siepe, and W. Von Witsch, “Efficiency and directional effects in the detection of low-energy recoil nuclei in a NaI(Tl) single crystal,” *Nuclear Instruments and Methods in Physics Research A*, vol. 485, no. 3, pp. 774–779, 2002, Erratum in *Nuclear Instruments and Methods in Physics Research A*, vol. 501, no. 2-3, p. 630, 2003.
- [38] B. Feldstein, A. L. Fitzpatrick, E. Katz, and B. Tweedie, “A simple explanation for DAMA with moderate channeling,” *Journal of Cosmology and Astroparticle Physics*, vol. 2010, no. 3, article 029, 2010.
- [39] N. Bozorgnia, G. B. Gelmini, and P. Gondolo, “Channeling in direct dark matter detection I: channeling fraction in NaI (Tl) crystals,” *Journal of Cosmology and Astroparticle Physics*, vol. 2010, no. 11, article 019, 2010.
- [40] J. I. Collar, “Quenching and channeling of nuclear recoils in NaI(Tl): implications for dark-matter searches,” *Physical Review C*, vol. 88, no. 3, Article ID 035806, 9 pages, 2013.
- [41] R. Bernabei, P. Belli, F. Cappella et al., “First results from DAMA/LIBRA and the combined results with DAMA/NaI,” *European Physical Journal C*, vol. 56, no. 3, pp. 333–355, 2008.
- [42] R. Bernabei, P. Belli, F. Cappella et al., “New results from DAMA/LIBRA,” *European Physical Journal C*, vol. 67, no. 1, pp. 39–49, 2010.
- [43] P. S. Barbeau, J. I. Collar, and O. Tench, “Large-mass ultralow noise germanium detectors: performance and applications in neutrino and astroparticle physics,” *Journal of Cosmology and Astroparticle Physics*, vol. 2007, no. 9, article 009, 2007.
- [44] C. E. Aalseth, P. S. Barbeau, N. S. Bowden et al., “Results from a search for light-mass dark matter with a p-type point contact germanium detector,” *Physical Review Letter*, vol. 106, no. 13, Article ID 131301, 4 pages, 2011.
- [45] C. E. Aalseth, P. S. Barbeau, J. Colaresi et al., “Search for an annual modulation in a p-type point contact Germanium dark matter detector,” *Physical Review Letters*, vol. 107, no. 14, Article ID 141301, 2011.
- [46] C. E. Aalseth, P. S. Barbeau, J. Colaresi et al., “Search for an annual modulation in three years of CoGeNT dark matter detector data,” <http://arxiv.org/abs/1401.3295>.
- [47] C. E. Aalseth, P. S. Barbeau, J. Colaresi et al., “Search for an annual modulation in a p-type point contact Germanium dark matter detector,” *Physical Review Letters*, vol. 107, no. 14, Article ID 141301, 2011.
- [48] G. Angloher, M. Bauer, I. Bavykina et al., “Results from 730 kg days of the CRESST-II Dark Matter Search,” *The European Physical Journal C*, vol. 2012, article 1971, 2012.

- [49] Z. Ahmed, D. S. Akerib, S. Arrenberg et al., “Dark matter search results from the CDMS II experiment,” *Science*, vol. 327, pp. 1619–1621, 2010.
- [50] R. Agnese, Z. Ahmed, A. J. Anderson et al., “Silicon detector results from the first five-tower run of CDMS II,” *Physical Review D*, vol. 88, no. 3, Article ID 031104, 5 pages, 2013.
- [51] R. Agnese, Z. Ahmed, A. J. Anderson et al., “Silicon detector dark matter results from the final exposure of CDMS II,” *Physical Review Letters*, vol. 111, no. 25, Article ID 251301, 6 pages, 2013.
- [52] J. Angle, E. Aprile, F. Arneodo et al., “First results from the XENON10 dark matter experiment at the Gran Sasso National Laboratory,” *Physical Review Letter*, vol. 100, no. 2, Article ID 021303, 5 pages, 2008.
- [53] E. Aprile, M. Alfonsi, K. Arisaka et al., “Dark matter results from 225 live days of XENON100 data,” *Physical Review Letter*, vol. 109, no. 18, Article ID 181301, 6 pages, 2012.
- [54] D. S. Akerib, H. M. Araujo, X. Bai et al., “First results from the LUX dark matter experiment at the sanford underground research facility,” <http://arxiv.org/abs/1310.8214>.
- [55] E. Behnke, J. Behnke, S. J. Brice et al., “First dark matter search results from a 4-kg CF3I bubble chamber operated in a deep underground site,” *Physical Review D*, vol. 86, no. 5, Article ID 052001, 9 pages, 2012.
- [56] T. Schwetz and J. Zupan, “Dark matter attempts for CoGeNT and DAMA,” *Journal of Cosmology and Astroparticle Physics*, vol. 2011, no. 8, article 008, 2011.
- [57] M. Farina, D. Pappadopulo, A. Strumia, and T. Volansky, “Can CoGeNT and DAMA modulations be due to Dark Matter?” *Journal of Cosmology and Astroparticle Physics*, vol. 2011, no. 11, article 010, 2011.
- [58] P. J. Fox, J. Kopp, M. Lisanti, and N. Weiner, “A CoGeNT modulation analysis,” *Physical Review D*, vol. 85, no. 3, Article ID 036008, 2012.
- [59] D. Hooper and C. Kelso, “Implications of CoGeNT’s new results for dark matter,” *Physical Review D*, vol. 84, no. 8, Article ID 083001, 10 pages, 2011.
- [60] P. Gondolo, P. Ko, and Y. Omura, “Light dark matter in leptophobic ZI models,” *Physical Review D*, vol. 85, no. 3, Article ID 035022, 2012.
- [61] E. Del Nobile, C. Kouvaris, and F. Sannino, “Interfering composite asymmetric dark matter as explanation for DAMA and CoGeNT results,” *Physical Review D*, vol. 84, no. 2, Article ID 027301, 4 pages, 2011.
- [62] C. Arina, J. Hamann, and Y. Y. Y. Wong, “A Bayesian view of the current status of dark matter direct searches,” *Journal of Cosmology and Astroparticle Physics*, vol. 2011, no. 9, article 022, 2011.
- [63] M. T. Frandsen, F. Kahlhoefer, J. March-Russell, C. McCabe, M. McCullough, and K. Schmidt-Hoberg, “On the DAMA and CoGeNT modulations,” *Physical Review D*, vol. 84, no. 4, Article ID 041301, 2011.
- [64] J. L. Feng, J. Kumar, D. Marfatia, and D. Sanford, “Isospin-violating dark matter,” *Physics Letters B*, vol. 703, no. 2, pp. 124–127, 2011.
- [65] D. Hooper, J. I. Collar, J. Hall, D. McKinsey, and C. M. Kelso, “Consistent dark matter interpretation for CoGeNT and DAMA/LIBRA,” *Physical Review D*, vol. 82, no. 12, Article ID 123509, 2010.
- [66] S. Chang, J. Liu, A. Pierce, N. Weiner, and I. Yavin, “CoGeNT interpretations,” *Journal of Cosmology and Astroparticle Physics*, vol. 2010, no. 8, article 018, 2010.
- [67] A. L. Fitzpatrick, D. Hooper, and K. M. Zurek, “Implications of CoGeNT and DAMA for light WIMP dark matter,” *Physical Review D*, vol. 81, no. 11, Article ID 115005, 2010.
- [68] J. Kopp, T. Schwetz, and J. Zupan, “Global interpretation of direct Dark Matter searches after CDMS-II results,” *Journal of Cosmology and Astroparticle Physics*, vol. 2010, no. 2, article 014, 2010.
- [69] P. J. Fox, J. Liu, and N. Weiner, “Integrating out astrophysical uncertainties,” *Physical Review D*, vol. 83, no. 10, Article ID 103514, 12 pages, 2011.
- [70] P. J. Fox, G. D. Kribs, and T. M. P. Tait, “Interpreting dark matter direct detection independently of the local velocity and density distribution,” *Physical Review*, vol. 83, no. 3, Article ID 034007, 12 pages, 2011.
- [71] C. McCabe, “DAMA and CoGeNT without astrophysical uncertainties,” *Physical Review D*, vol. 84, no. 4, Article ID 043525, 6 pages, 2011.
- [72] J. Herrero-Garcia, T. Schwetz, and J. Zupan, “On the annual modulation signal in dark matter direct detection,” *Journal of Cosmology and Astroparticle Physics*, vol. 2012, no. 3, article 005, 2012.
- [73] J. Herrero-Garcia, T. Schwetz, and J. Zupan, “Astrophysics-independent bounds on the annual modulation of dark matter signals,” *Physical Review Letter*, vol. 109, no. 14, Article ID 141301, 5 pages, 2012.
- [74] M. T. Frandsen, F. Kahlhoefer, C. McCabe, S. Sarkar, and K. Schmidt-Hoberg, “Resolving astrophysical uncertainties in dark matter direct detection,” *Journal of Cosmology and Astroparticle Physics*, vol. 2012, no. 1, article 024, 2012.
- [75] P. Gondolo and G. B. Gelmini, “Halo independent comparison of direct dark matter detection data,” *Journal of Cosmology and Astroparticle Physics*, vol. 2012, no. 12, article 015, 2012.
- [76] M. T. Frandsen, F. Kahlhoefer, C. McCabe, S. Sarkar, and K. Schmidt-Hoberg, “The unbearable lightness of being: CDMS versus XENON,” *Journal of Cosmology and Astroparticle Physics*, vol. 2013, no. 7, article 023, 2013.
- [77] E. Del Nobile, G. B. Gelmini, P. Gondolo, and J. H. Huh, “Halo-independent analysis of direct detection data for light WIMPs,” *Journal of Cosmology and Astroparticle Physics*, vol. 2013, no. 10, article 026, 2013.
- [78] N. Bozorgnia, J. Herrero-Garcia, T. Schwetz, and J. Zupan, “Halo-independent methods for inelastic dark matter scattering,” *Journal of Cosmology and Astroparticle Physics*, vol. 2013, no. 7, article 049, 2013.
- [79] E. Del Nobile, G. Gelmini, P. Gondolo, and J. H. Huh, “Generalized halo independent comparison of direct dark matter detection data,” *Journal of Cosmology and Astroparticle Physics*, vol. 2013, no. 10, article 048, 2013.
- [80] E. Del Nobile, G. B. Gelmini, P. Gondolo, and J. H. Huh, “Update on light WIMP limits: LUX, lite and light,” <http://arxiv.org/abs/1311.4247>.
- [81] T. D. Lee and C. N. Yang, “Question of parity conservation in weak interactions,” *Physical Review*, vol. 104, no. 1, pp. 254–258, 1956.
- [82] I. Kobzarev, L. Okun, and I. Pomeranchuk, “On the possibility of observing mirror particle,” *Soviet Journal of Nuclear Physics*, vol. 3, p. 837, 1966.
- [83] S. I. Blinnikov and M. Y. Khlopov, “Possible signatures of mirror particles,” *Soviet Journal of Nuclear Physics*, vol. 36, pp. 472–474, 1982.

- [84] S. I. Blinnikov and M. Khlopov, "Possible astronomical effects of mirror particles," *Astronomicheskii Zhurnal*, vol. 60, pp. 632–639, 1983.
- [85] Z. Berezhiani, "Marriage between the baryonic and dark matters," *AIP Conference Proceedings*, vol. 878, pp. 195–202, 2006.
- [86] R. Foot, "Mirror matter-type dark matter," *International Journal of Modern Physics D*, vol. 13, no. 10, pp. 2161–2192, 2004.
- [87] Z. Berezhiani, "Through the looking-glass: Alice's adventures in mirror world," in *From Fields to Strings: Circumnavigating Theoretical Physics*, M. Shifman, A. Vainshtein, and J. Wheeler, Eds., vol. 3, pp. 2147–2195, World Scientific.
- [88] B. Holdom, "Two $U(1)$'s and ϵ charge shifts," *Physics Letters B*, vol. 166, no. 2, pp. 196–198, 1986.
- [89] R. Foot, H. Lew, and R. R. Volkas, "A model with fundamental improper spacetime symmetries," *Physics Letters B*, vol. 272, no. 1-2, pp. 67–70, 1991.
- [90] R. Foot, A. Y. Ignatiev, and R. R. Volkas, "Physics of mirror photons," *Physics Letters B*, vol. 503, no. 3-4, pp. 355–361, 2001.
- [91] P. Belli, R. Bernabei, A. Bottino et al., "Observations of annual modulation in direct detection of relic particles and light neutralinos," *Physical Review D*, vol. 84, no. 5, Article ID 055014, 2011.
- [92] E. Aprile, F. Arneodo, A. Askin et al., "Dark matter results from 100 live days of XENON100 data," *Physical Review Letter*, vol. 107, no. 13, Article ID 131302, 6 pages, 2011.
- [93] R. Bernabei, P. Belli, A. Incicchitti, and D. Prospero, "Liquid noble gases for dark matter searches: a synoptic survey," <http://arxiv.org/abs/0806.0011>.
- [94] J. I. Collar, "A realistic assessment of the sensitivity of XENON10 and XENON100 to light-mass WIMPs," <http://arxiv.org/abs/1106.0653>.
- [95] J. D. Bjorken, R. Essig, P. Schuster, and N. Toro, "New fixed-target experiments to search for dark gauge forces," *Physical Review D*, vol. 80, no. 7, Article ID 075018, 2009.
- [96] R. Essig, R. Harnik, J. Kaplan, and N. Toro, "Discovering new light states at neutrino experiments," *Physical Review D*, vol. 82, no. 11, Article ID 113008, 2010.
- [97] R. Essig, J. A. Jaros, W. Wester et al., "Dark sectors and new, light, weakly-coupled particles," <http://arxiv.org/abs/1311.0029>.
- [98] J. B. Dent, F. Ferrer, and L. M. Krauss, "Constraints on light hidden sector gauge bosons from supernova cooling," <http://arxiv.org/abs/1201.2683>.
- [99] H. K. Dreiner, J. F. o. Fortin, C. Hanhart, and L. Ubaldi, "Supernova constraints on MeV dark sectors from e^+e^- annihilations," <http://arxiv.org/abs/1310.3826>.
- [100] D. Clowe, M. Bradac, A. H. Gonzalez et al., "A direct empirical proof of the existence of dark matter," *The Astrophysical Journal Letters*, vol. 648, no. 2, pp. L109–L113, 2006.
- [101] S. W. Randall, M. Markevitch, D. Clowe, A. H. Gonzalez, and M. Bradač, "Constraints on the self-interaction cross section of dark matter from numerical simulations of the merging galaxy cluster 1E 0657-56," *Astrophysical Journal Letters*, vol. 679, no. 2, pp. 1173–1180, 2008.
- [102] J. L. Feng, M. Kaplinghat, H. Tu, and H. B. Yu, "Hidden charged dark matter," *Journal of Cosmology and Astroparticle Physics*, vol. 2009, no. 7, article 004, 2009.
- [103] J. L. Feng, M. Kaplinghat, and H. B. Yu, "Halo-shape and relic-density exclusions of sommerfeld-enhanced dark matter explanations of cosmic ray excesses," *Physical Review Letters*, vol. 104, no. 15, Article ID 151301, 2010.
- [104] M. R. Buckley and P. J. Fox, "Dark matter self-interactions and light force carriers," *Physical Review D*, vol. 81, no. 8, Article ID 083522, 9 pages, 2010.
- [105] M. Ibe and H. B. Yu, "Distinguishing dark matter annihilation enhancement scenarios via halo shapes," *Physics Letters B*, vol. 692, no. 2, pp. 70–73, 2010.
- [106] A. Loeb and N. Weiner, "Cores in dwarf galaxies from dark matter with a Yukawa potential," *Physical Review Letters*, vol. 106, no. 17, Article ID 171302, 2011.
- [107] M. Kaplinghat, S. Tulin, and H. B. Yu, "Direct detection portals for self-interacting dark matter," <http://arxiv.org/abs/1310.7945>.
- [108] S. Tulin, H. B. Yu, and K. M. Zurek, "Beyond collisionless dark matter: particle physics dynamics for dark matter halo structure," *Physical Review D*, vol. 87, no. 11, Article ID 115007, 20 pages, 2013.
- [109] J. Fan, A. Katz, L. Randall, and M. Reece, "Double-disk dark matter," *Physics of the Dark Universe*, vol. 2, no. 3, pp. 139–156, 2013.
- [110] J. Fan, A. Katz, L. Randall, and M. Reece, "Dark-disk universe," *Physical Review Letter*, vol. 110, no. 21, Article ID 211302, 5 pages, 2013.
- [111] M. McCullough and L. Randall, "Exothermic double-disk dark matter," *Journal of Cosmology and Astroparticle Physics*, vol. 2013, no. 10, article 058, 2013.

Review Article

Halo-Independent Comparison of Direct Dark Matter Detection Data

Eugenio Del Nobile

Department of Physics and Astronomy, UCLA, 475 Portola Plaza, Los Angeles, CA 90095, USA

Correspondence should be addressed to Eugenio Del Nobile; delnobile@physics.ucla.edu

Received 26 December 2013; Accepted 3 March 2014; Published 1 April 2014

Academic Editor: Anselmo Meregaglia

Copyright © 2014 Eugenio Del Nobile. This is an open access article distributed under the Creative Commons Attribution License, which permits unrestricted use, distribution, and reproduction in any medium, provided the original work is properly cited. The publication of this article was funded by SCOAP³.

We review the halo-independent formalism that allows comparing data from different direct dark matter detection experiments without making assumptions on the properties of the dark matter halo. We apply this method to spin-independent WIMP-nuclei interactions, for both isospin-conserving and isospin-violating couplings, and to WIMPs interacting through an anomalous magnetic moment.

1. Introduction

The presence of dark matter (DM) in the universe is now an established fact that has been confirmed once more by the recent precise measurements of the Planck satellite [1]. Many different particle candidates exist as possible explanations for the DM. A particular class of candidates, the WIMPs (for weakly interacting massive particles), is very actively searched for. WIMPs are particles with weakly interacting cross sections and masses in the $1 \text{ GeV}/c^2$ – $10 \text{ TeV}/c^2$ range. Of particular interest are light WIMPs, with mass around 1 – $10 \text{ GeV}/c^2$.

At present, four direct dark matter search experiments (DAMA [2], CoGeNT [3–5], CRESST-II [6], and CDMS-II-Si [7]) have data that may be interpreted as signals from DM particles in the light WIMPs range. DAMA [2] and CoGeNT [4] report annual modulations in their event rates, compatible with those expected for a DM signal [8, 9]. CoGeNT [3, 5], CRESST-II [6], and CDMS-II-Si [7] observe an excess of events above their expected backgrounds that may be interpreted as due to DM WIMPs.

However, other experiments do not observe significant excesses above their estimated background, thus setting upper limits on the interaction of WIMPs with nuclei. The most stringent limits on the average (unmodulated) rate for light WIMPs are set by the LUX [10], XENON10 [11],

XENON100 [12], CDMS-II-Ge [13], and CDMSlite [14] experiments, with the addition of SIMPLE [15], PICASSO [16], and COUPP [17] for spin-dependent and isospin-violating interactions. CDMS-II-Ge [18] also constrains directly the amplitude of an annually modulated signal.

In order to compare a model for WIMPs with data from direct DM detection experiments, one needs to assume a value for the DM local density and velocity distribution in our galaxy. The Standard Halo Model (SHM) is usually assumed for the DM halo, corresponding to a truncated Maxwell-Boltzmann distribution for the DM velocity (see e.g., [19]). However, the parameters of this model are not known to great accuracy, and the model itself is not supported by data. Actually, quantitatively different velocity distributions are obtained from numerical simulations (see e.g., [20]). Various models and parameterizations for the DM velocity distribution in our galaxy have been proposed as alternatives to the SHM, either derived from astrophysical data or from N-body simulations (see e.g., [9] and references therein). Other authors have attempted to estimate the uncertainty in the determination of the properties of the DM halo and to quantify its effects on the interpretation of DM direct detection data (see e.g., [21–25]). Another approach is that of marginalizing over the parameters of the DM halo when computing bounds and allowed regions from the experimental data (see e.g., [26]). However, all these procedures maintain a certain

degree of model dependence, for example, in the choice of the functional form of the parameterization of the halo. It is very important to notice here that the high velocity tail of the DM velocity distribution plays a crucial role in determining the number of DM particles that is above threshold for a given experiment, and therefore a way to analyze the data without the need to make any assumption on its shape is highly desirable.

The problem of comparing results from different direct detection experiments can indeed be formulated without the need to assume a velocity profile for the DM [27–34]. The basic idea is to factor out from the formulas used to compute the scattering rate all the astrophysical quantities such as the DM velocity distribution function. In this way the rate can be computed, for any model of particle interactions between the DM and the nuclei in the detector, with no need to assume a velocity profile for the DM, while rather allowing using the experimental data to constrain the unknown quantities. Such a “halo-independent” analysis was first proposed in [27], where many of the features of the method were presented, and was further developed in [28] which extended the analysis to annual modulations and [29] which showed how to include detector resolutions. The method was further generalized in [32] to more complicate particle interactions; that is, those where the scattering cross section has a nontrivial dependence on the DM velocity.

The halo-independent analysis is particularly useful to investigate the compatibility of the different experimental results in the light WIMP hypothesis, for which the details of the DM velocity distribution, especially at high velocities, are notably relevant. Here we will review this method, applying it to spin-independent interactions with both isospin-conserving and isospin-violating [35, 36] couplings, and to WIMPs with magnetic dipole moment. We will compare data from DAMA [2], CoGeNT [4], CRESST-II [6], CDMS-II-Si [7], CDMS-II-Ge low threshold analysis [13], CDMS-II-Ge annual modulation analysis [18], CDMSlite [14], XENON10 S2-only analysis [11], XENON100 [12], LUX [10], and SIMPLE [15], following the analysis described in [31–33]. This review summarizes the results presented in [31–33].

2. The Scattering Rate

What is observed at direct DM detection experiments is the WIMP-nucleus differential scattering rate, usually measured in units of counts/kg/day/keV. For a target nuclide T initially at rest, recoiling with energy E_R after the scattering with a WIMP with mass m and initial velocity \mathbf{v} , the differential rate is

$$\frac{dR_T}{dE_R} = \frac{\rho}{m} \frac{C_T}{m_T} \int_{v \geq v_{\min}(E_R)} d^3v f(\mathbf{v}, t) v \frac{d\sigma_T}{dE_R}(E_R, \mathbf{v}). \quad (1)$$

Here m_T is the target nuclide mass and C_T is its mass fraction in the detector, and we denoted by $v = |\mathbf{v}|$ the WIMP speed. $d\sigma_T/dE_R$ is the differential scattering cross section. The dependence of the rate on the local characteristics of the DM halo is contained in the local DM density ρ and the DM velocity distribution in the Earth’s frame $f(\mathbf{v}, t)$, which is

modulated in time due to Earth’s rotation around the Sun [8, 9]. The distribution $f(\mathbf{v}, t)$ is normalized to $\int d^3v f(\mathbf{v}, t) = 1$. In the velocity integral, $v_{\min}(E_R)$ is the minimum speed required for the incoming DM particle to cause a nuclear recoil with energy E_R . For an elastic collision

$$v_{\min} = \sqrt{\frac{m_T E_R}{2\mu_T^2}}, \quad (2)$$

where $\mu_T = mm_T/(m + m_T)$ is the WIMP-nucleus reduced mass.

To properly reproduce the recoil rate measured by experiments, we need to take into account the characteristics of the detector. Most experiments do not measure the recoil energy directly but rather a detected energy E' , often quoted in keVee (keV electron-equivalent) or in photoelectrons. The uncertainties and fluctuations in the detected energy corresponding to a particular recoil energy are expressed in a (target nuclide and detector dependent) resolution function $G_T(E_R, E')$ that gives the probability that a recoil energy E_R (usually quoted in keVnr for nuclear recoils) is measured as E' . The resolution function is often (but not always as the XENON and LUX experiments are a notable exception) approximated by a Gaussian distribution. It incorporates the mean value $\langle E' \rangle = Q_T E_R$, which depends on the energy dependent quenching factor $Q_T(E_R)$, and the energy resolution $\sigma_{E_R}(E')$. Moreover, experiments have one or more counting efficiencies or cut acceptances, denoted here by $\epsilon_1(E')$ and $\epsilon_2(E_R)$, which also affect the measured rate. Thus the nuclear recoil rate in (1) must be convolved with the function $\epsilon_1(E')\epsilon_2(E_R)G_T(E_R, E')$. The resulting differential rate as a function of the detected energy E' is

$$\frac{dR}{dE'} = \epsilon_1(E') \sum_T \int_0^\infty dE_R \epsilon_2(E_R) G_T(E_R, E') \frac{dR_T}{dE_R}. \quad (3)$$

The rate within a detected energy interval $[E'_1, E'_2]$ follows as

$$\begin{aligned} R_{[E'_1, E'_2]}(t) &= \int_{E'_1}^{E'_2} dE' \frac{dR}{dE'} \\ &= \frac{\rho}{m} \sum_T \frac{C_T}{m_T} \int_0^\infty dE_R \\ &\quad \times \int_{v \geq v_{\min}(E_R)} d^3v f(\mathbf{v}, t) v \frac{d\sigma_T}{dE_R}(E_R, \mathbf{v}) \epsilon_2(E_R) \\ &\quad \times \int_{E'_1}^{E'_2} dE' \epsilon_1(E') G_T(E_R, E'). \end{aligned} \quad (4)$$

The time dependence of the rate (4) is generally well approximated by the first terms of a harmonic series,

$$R_{[E'_1, E'_2]}(t) = R_{[E'_1, E'_2]}^0 + R_{[E'_1, E'_2]}^1 \cos[\omega(t - t_0)], \quad (5)$$

where t_0 is the time of the maximum of the signal and $\omega = 2\pi/\text{yr}$. The coefficients $R_{[E'_1, E'_2]}^0$ and $R_{[E'_1, E'_2]}^1$ are, respectively, the unmodulated and modulated components of the rate in the energy interval $[E'_1, E'_2]$.

3. Halo-Independent Method for Spin-Independent Interaction

The differential cross section for the usual spin-independent (SI) interaction is

$$\frac{d\sigma_T}{dE_R} = \sigma_T^{\text{SI}}(E_R) \frac{m_T}{2\mu_T^2 v^2}, \quad (6)$$

with

$$\sigma_T^{\text{SI}}(E_R) = \sigma_p \frac{\mu_T^2}{\mu_p^2} \left[Z_T + \frac{(A_T - Z_T) f_n}{f_p} \right]^2 F_{\text{SI},T}^2(E_R). \quad (7)$$

Here Z_T and A_T are, respectively, the atomic and mass number of the target nuclide T , $F_{\text{SI},T}(E_R)$ is the nuclear spin-independent form factor (which we take to be the Helm form factor [37] normalized to $F_{\text{SI},T}(0) = 1$), f_n and f_p are the effective WIMP couplings to neutron and proton, and μ_p is the WIMP-proton reduced mass. The WIMP-proton cross section σ_p is the parameter customarily chosen to be constrained together with the WIMP mass m for SI interactions, as it does not depend on the detector, and thus bounds and allowed regions from different experiments can be compared on the same plot.

The isospin-conserving coupling $f_n = f_p$ is usually assumed by the experimental collaborations. The isospin-violating coupling $f_n/f_p = -0.7$ [35, 36] produces the maximum cancellation in the expression inside the square bracket in (7) for xenon, thus highly suppressing the interaction cross section. This suppression is phenomenologically interesting because it weakens considerably the bounds from xenon-based detectors such as XENON and LUX which provide some of the most restrictive bounds.

Using this expression for the differential cross section and changing integration variable from E_R to v_{\min} through (2), we can rewrite (4) as

$$R_{[E'_1, E'_2]}^{\text{SI}}(t) = \int_0^\infty dv_{\min} \tilde{\eta}(v_{\min}, t) \mathcal{R}_{[E'_1, E'_2]}^{\text{SI}}(v_{\min}), \quad (8)$$

where the velocity integral $\tilde{\eta}$ is

$$\tilde{\eta}(v_{\min}, t) \equiv \frac{\rho \sigma_p}{m} \int_{v \geq v_{\min}} d^3v \frac{f(\mathbf{v}, t)}{v} \equiv \int_{v \geq v_{\min}} d^3v \frac{\tilde{f}(\mathbf{v}, t)}{v}, \quad (9)$$

and we defined the response function $\mathcal{R}_{[E'_1, E'_2]}^{\text{SI}}(v_{\min})$ for WIMPs with SI interactions as

$$\begin{aligned} \mathcal{R}_{[E'_1, E'_2]}^{\text{SI}}(v_{\min}) &\equiv 2v_{\min} \sum_T \frac{C_T}{m_T} \frac{\sigma_T^{\text{SI}}(E_R(v_{\min}))}{\sigma_p} \epsilon_2(E_R(v_{\min})) \\ &\times \int_{E'_1}^{E'_2} dE' \epsilon_1(E') G_T(E_R(v_{\min}), E'). \end{aligned} \quad (10)$$

Introducing the speed distribution

$$\tilde{F}(v, t) \equiv v^2 \int d\Omega_v \tilde{f}(\mathbf{v}, t), \quad (11)$$

we can rewrite the $\tilde{\eta}$ function as

$$\tilde{\eta}(v_{\min}, t) = \int_{v_{\min}}^\infty dv \frac{\tilde{F}(v, t)}{v}. \quad (12)$$

The velocity integral $\tilde{\eta}(v_{\min}, t)$ has an annual modulation due to Earth's rotation around the Sun and can be separated into its unmodulated and modulated components as was done for the rate in (5)

$$\tilde{\eta}(v_{\min}, t) \simeq \tilde{\eta}^0(v_{\min}) + \tilde{\eta}^1(v_{\min}) \cos[\omega(t - t_0)]. \quad (13)$$

Once the WIMP mass and interactions are fixed, the functions $\tilde{\eta}^0(v_{\min})$ and $\tilde{\eta}^1(v_{\min})$ are detector-independent quantities that must be common to all nondirectional direct DM experiments. Thus we can map the rate measurements and bounds of different experiments into measurements of and bounds on $\tilde{\eta}^0(v_{\min})$ and $\tilde{\eta}^1(v_{\min})$ as functions of v_{\min} .

For experiments with putative DM signals, in light of (8) we may interpret the measured rates $\hat{R}_{[E'_1, E'_2]}^i \pm \Delta R_{[E'_1, E'_2]}^i$ in an energy interval $[E'_1, E'_2]$ as averages of the $\tilde{\eta}^i(v_{\min})$ functions weighted by the response function $\mathcal{R}_{[E'_1, E'_2]}^{\text{SI}}(v_{\min})$

$$\overline{\tilde{\eta}_{[E'_1, E'_2]}^i} \equiv \frac{\hat{R}_{[E'_1, E'_2]}^i}{\int dv_{\min} \mathcal{R}_{[E'_1, E'_2]}^{\text{SI}}(v_{\min})}, \quad (14)$$

with $i = 0, 1$ for the unmodulated and modulated component, respectively. Each such average corresponds to a point with error bars in the $(v_{\min}, \tilde{\eta})$ plane. The vertical bars are given by $\Delta \overline{\tilde{\eta}_{[E'_1, E'_2]}^i}$ computed by replacing $\hat{R}_{[E'_1, E'_2]}^i$ with $\Delta R_{[E'_1, E'_2]}^i$ in (14).

The ΔR^i used here correspond to the 68% confidence interval. The horizontal bar shows the v_{\min} interval where the response function $\mathcal{R}_{[E'_1, E'_2]}^{\text{SI}}(v_{\min})$ for the given experiment is sufficiently different from zero. Following [28, 29, 31, 33] the horizontal bar may be chosen to extend over the interval $[v_{\min,1}, v_{\min,2}] = [v_{\min}(E'_1 - \sigma_{E_R}(E'_1)), v_{\min}(E'_2 + \sigma_{E_R}(E'_2))]$, where $\sigma_{E_R}(E')$ is the energy resolution and the function $v_{\min}(E')$ is obtained from $v_{\min}(E_R)$ in (2) by using the recoil energy E_R that produces the mean $\langle E' \rangle$ which is equal to the measured energy E' . When isotopes of the same element are present, like for Xe or Ge, the v_{\min} intervals of the different isotopes almost completely overlap, and we take $v_{\min,1}$ and $v_{\min,2}$ to be the C_T -weighted averages over the isotopes of the element. When there are nuclides belonging to very different elements, like Ca and O in CRESST-II, a more complicated procedure should be followed (see [28, 29] for details).

To determine the upper bounds on the unmodulated part of $\tilde{\eta}$ set by experimental upper bounds on the unmodulated part of the rate, a procedure first outlined in [27, 28] may be used. This procedure exploits the fact that, by definition, $\tilde{\eta}^0$ is a nonincreasing function of v_{\min} . For this reason, the smallest possible $\tilde{\eta}^0(v_{\min})$ function passing by a fixed point $(v_0, \tilde{\eta}_0)$ in the $(v_{\min}, \tilde{\eta})$ plane is the downward step-function $\tilde{\eta}_0 \theta(v_0 - v_{\min})$. In other words, among the functions passing by the point $(v_0, \tilde{\eta}_0)$, the downward step is the function yielding

the minimum predicted number of events. Imposing this functional form in (8) we obtain

$$R_{[E'_1, E'_2]} = \bar{\eta}_0 \int_0^{v_0} dv_{\min} \mathcal{R}_{[E'_1, E'_2]}^{\text{SI}}(v_{\min}). \quad (15)$$

The upper bound $R_{[E'_1, E'_2]}^{\text{lim}}$ on the unmodulated rate in an interval $[E'_1, E'_2]$ is translated into an upper bound $\bar{\eta}^{\text{lim}}(v_{\min})$ on $\bar{\eta}^0$ at v_0 by

$$\bar{\eta}^{\text{lim}}(v_0) = \frac{R_{[E'_1, E'_2]}^{\text{lim}}}{\int_0^{v_0} dv_{\min} \mathcal{R}_{[E'_1, E'_2]}^{\text{SI}}(v_{\min})}. \quad (16)$$

The upper bound so-obtained is conservative in the sense that any $\bar{\eta}^0$ function extending even partially above $\bar{\eta}^{\text{lim}}$ is excluded, but not every $\bar{\eta}^0$ function lying everywhere below $\bar{\eta}^{\text{lim}}$ is allowed [28].

The procedure just described does not assume any particular property of the DM halo. By making some assumptions, more stringent limits on the modulated part $\bar{\eta}^1$ can be derived from the limits on the unmodulated part of the rate (see [28, 38–40]), but we choose to proceed without making any assumption on the DM halo.

Figures 1 and 2 collect the results of the halo-independent analysis for a WIMP mass $m = 7 \text{ GeV}/c^2$ and $m = 9 \text{ GeV}/c^2$, respectively; the left and right columns correspond to isospin-conserving ($f_n = f_p$) and isospin-violating ($f_n/f_p = -0.7$) interactions, respectively; and the top, middle, and bottom rows show measurements and bounds for the unmodulated component $\bar{\eta}^0 c^2$, for the modulated component $\bar{\eta}^1 c^2$, and for both together, respectively, in units of day^{-1} . The middle row also shows the upper bounds on $\bar{\eta}^0 c^2$ from the plots on the top row.

The bounds from CDMS-II-Ge, CDMS-II-Si, CDMSlite, XENON10, XENON100, and LUX are derived as 90% CL upper bounds using the maximum gap method [41]. The SIMPLE bound is derived as the 90% CL Poisson limit. The crosses show the DAMA modulation signal (green crosses), CoGeNT modulated (blue crosses) and unmodulated signal (plus an unknown flat background, dark red horizontal lines), CRESST-II, and CDMS-II-Si unmodulated signals (black and red crosses, resp.); the CDMS-II-Ge modulation bound is shown as a dark grey horizontal line with downward arrow. Only sodium is considered for DAMA (with quenching factor $Q_{\text{Na}} = 0.3$), as for the DM masses considered here the WIMP scattering off iodine is supposed to be below threshold. For XENON10, limits produced by setting or not setting the electron yield \mathcal{Q}_y to zero below 1.4 keVnr (as in [12]) are obtained (solid and dashed orange line, resp.). For LUX, upper bounds considering 0, 1, 3, and 5 observed events are computed [33], corresponding (from bottom to top) to the magenta lines with different dashed styles in Figures 1 and 2.

The overlapping of the green and blue crosses in Figures 1 and 2 seems to indicate that the DAMA and CoGeNT modulation data are compatible one with the other. On the other

hand, the three CDMS-II-Si points overlap or are below the CoGeNT and DAMA measurements of the modulated part of $\bar{\eta}$. Thus, interpreted as a measurement of the unmodulated rate, the three CDMS-II-Si data points seem largely incompatible with the modulation of the signal observed by CoGeNT and DAMA, since a modulated signal is expected to be much smaller than the respective unmodulated component. For isospin-conserving interactions (left column of Figures 1 and 2), the experiments with a positive signal seem largely incompatible with the limits set by the other experiments, most notably by LUX, and by XENON10 at low v_{\min} values. In fact, only the DAMA, CoGeNT, and CDMS-II-Si data points at very low v_{\min} are below all the bounds. The compatibility of the DAMA, CoGeNT, and CRESST-II data with the exclusion bounds improves slightly for isospin-violating couplings with $f_n/f_p = -0.7$, for which the XENON and LUX limits are weakened (right column of Figures 1 and 2). However, still only the points at low v_{\min} are below the exclusion lines, while the DAMA and CoGeNT modulated data at high v_{\min} are now mostly excluded by the CDMS-II-Ge modulation bound. The improvement is better for the three CDMS-II-Si data that pass all the limits for DM with isospin-violating couplings.

In the top left panel of Figure 1 and the middle right panel of Figure 2, we show the predicted $\bar{\eta}^0 c^2$ (upper line) and $\bar{\eta}^1 c^2$ (lower line) from the SHM (assuming $v_0 = 220 \text{ km/s}$ for the DM velocity dispersion and $v_{\text{esc}} = 544 \text{ km/s}$ for the galactic escape velocity), for particular values of the WIMP-proton cross section. We choose these cross sections so that (a) for the $m = 7 \text{ GeV}/c^2$ isospin-conserving case in the top left panel of Figure 1, the CDMS-II-Si unmodulated data are well explained by the SHM; that is, the $\bar{\eta}^0$ curve passes through the red crosses in the figure (this happens for $\sigma_p = 10^{-40} \text{ cm}^2$) and (b) for the $m = 9 \text{ GeV}/c^2$ isospin-violating case in the middle right panel of Figure 2, the DAMA modulation data are well explained; that is, $\bar{\eta}^1$ passes through the green crosses (this occurs for $\sigma_p = 2 \times 10^{-38} \text{ cm}^2$). These plots show that the $\bar{\eta}^0(v_{\min})$ of the SHM is a very steep function of v_{\min} and thus can be constrained at low v_{\min} values by the CDMSlite limit as well as by other upper limits on the unmodulated rate.

The procedure outlined in this section to compare data from different experiments in a halo-independent way can only be applied when the differential cross section can be factorized into a velocity dependent term, independent of the detector (e.g., it must be independent of m_T), times a velocity independent term containing all the detector dependency. The differential cross section in (6) and (7) is of this form. In the case of a more general form of the differential cross section; instead, we can proceed as described in the following section.

4. Generalized Halo-Independent Method

Here we show how to define the response function $\mathcal{R}_{[E'_1, E'_2]}(v_{\min})$ in (8) so that the halo-independent analysis can be extended to any type of interaction. Changing the order of the \mathbf{v} and E_R integrations in (4), we have

$$\begin{aligned} R_{[E'_1, E'_2]}(t) &= \frac{\rho \sigma_{\text{ref}}}{m} \int_0^\infty d^3 v \frac{f(\mathbf{v}, t)}{v} \sum_T \frac{C_T}{m_T} \end{aligned}$$

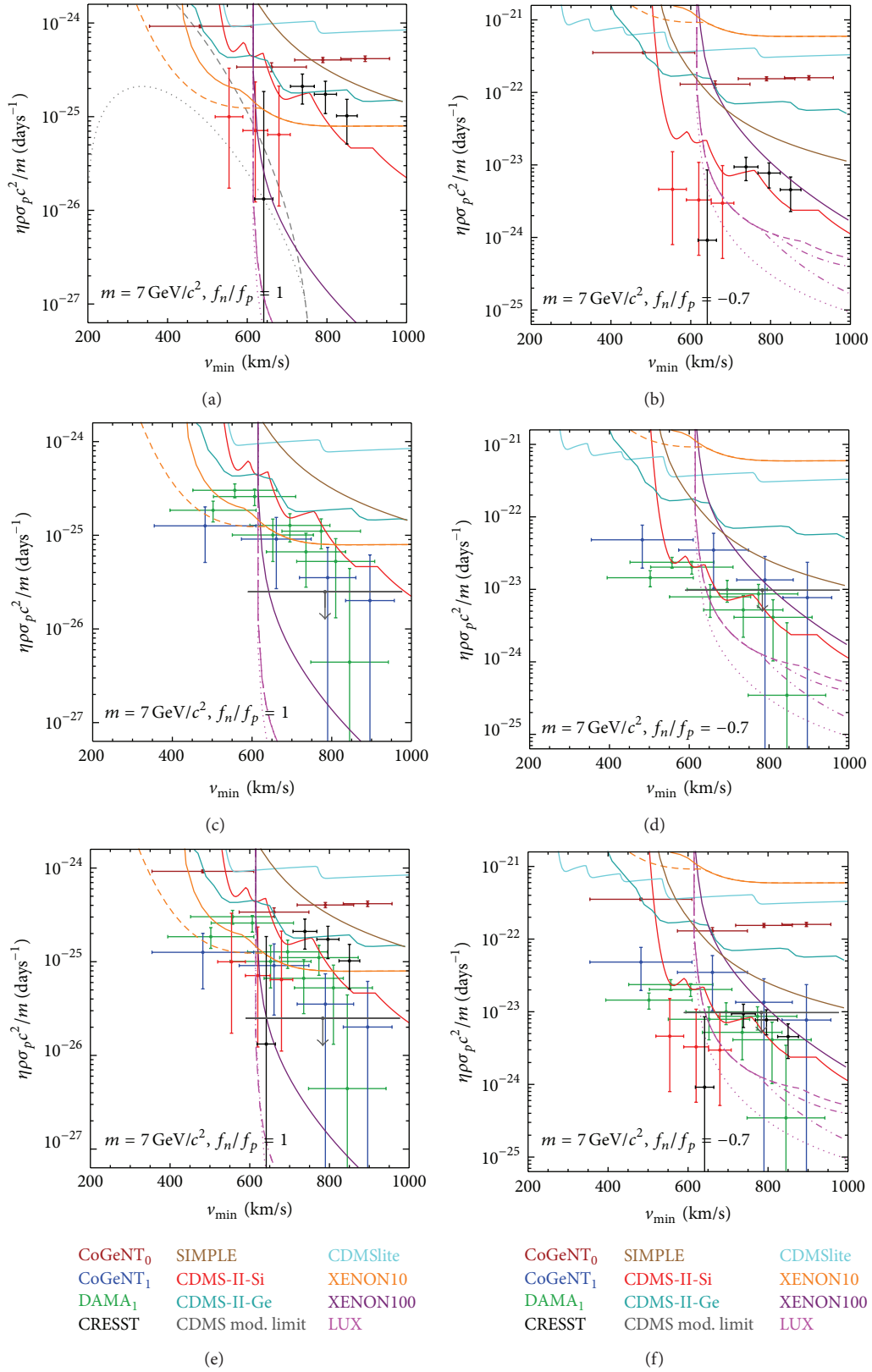


FIGURE 1: Measurements of and bounds on $\tilde{\eta}^0 c^2$ and $\tilde{\eta}^1 c^2$ for $m = 7 \text{ GeV}/c^2$. The left and right columns are for isospin-conserving and isospin-violating interactions, respectively. The dashed gray lines in the top left panel show the SHM $\tilde{\eta}^0 c^2$ and $\tilde{\eta}^1 c^2$ for $\sigma_p = 10^{-40} \text{ cm}^2$ (see text).

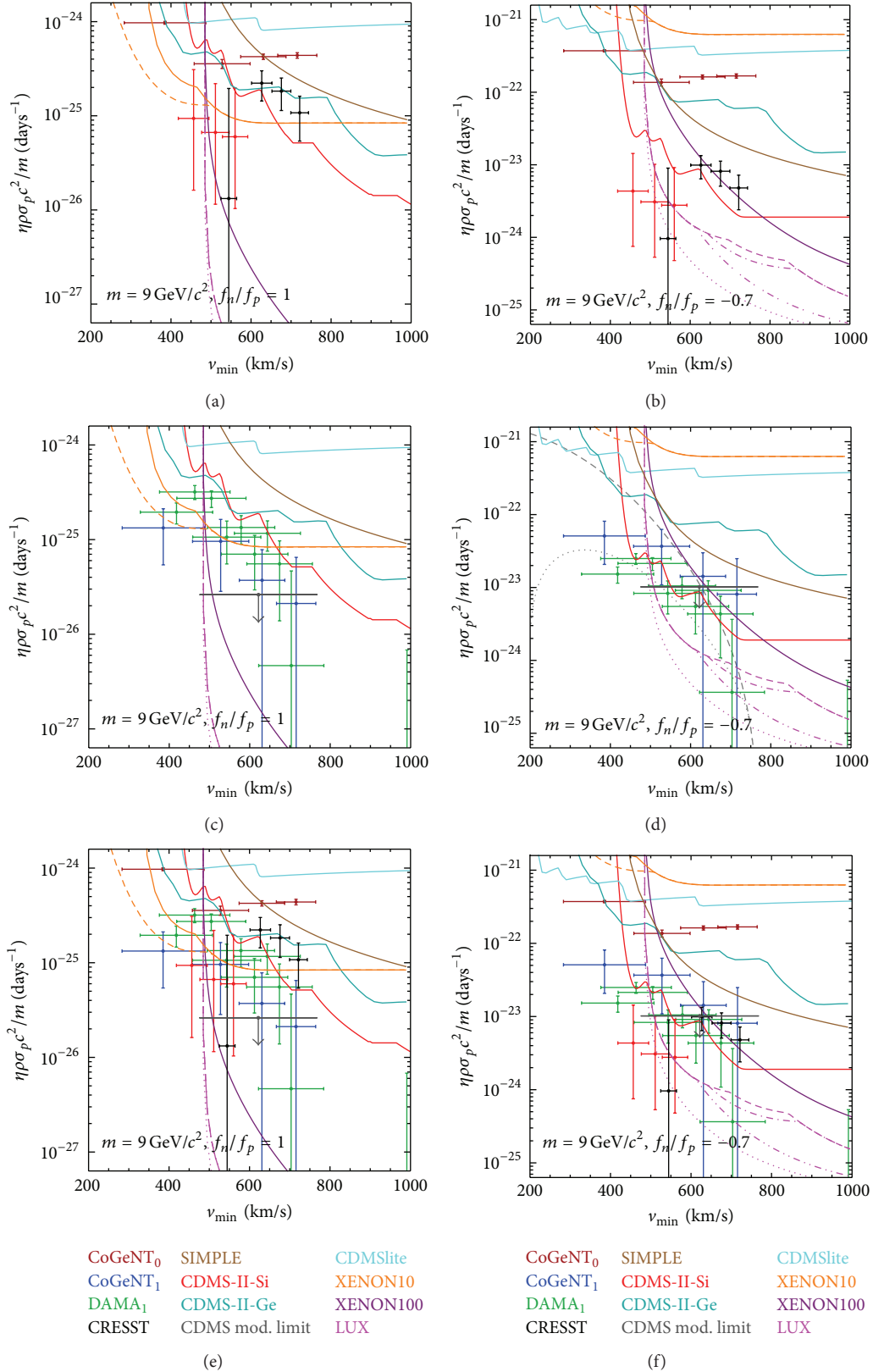


FIGURE 2: Same as Figure 1 but for a DM mass $m = 9 \text{ GeV}/c^2$. The dashed gray lines in the middle right panel show the expected $\bar{\eta}^0 c^2$ (upper line) and $\bar{\eta}^1 c^2$ (lower line) for a WIMP-proton cross section $\sigma_p = 2 \times 10^{-38} \text{ cm}^2$ in the SHM (see text).

$$\begin{aligned} & \times \int_0^{E_R^{\max}(\nu)} dE_R \frac{\nu^2}{\sigma_{\text{ref}}} \frac{d\sigma_T}{dE_R}(E_R, \mathbf{v}) \epsilon_2(E_R) \\ & \times \int_{E'_1}^{E'_2} dE' \epsilon_1(E') G_T(E_R, E'). \end{aligned} \quad (17)$$

Here $E_R^{\max}(\nu) \equiv 2\mu_T^2 \nu^2 / m_T$ is the maximum recoil energy a WIMP of speed ν can impart in an elastic collision to a target nucleus T initially at rest. To make contact with the SI interaction method of the previous section, we have multiplied and divided by the factor $\sigma_{\text{ref}}/\nu^2$, where σ_{ref} is a target-independent reference cross section (i.e., a constant with the dimensions of a cross section) that coincides with σ_p for SI interactions. In compact form, (17) reads

$$R_{[E'_1, E'_2]}(t) = \int_0^\infty d^3v \frac{\tilde{f}(\mathbf{v}, t)}{\nu} \mathcal{H}_{[E'_1, E'_2]}(\mathbf{v}), \quad (18)$$

where in analogy with (9) we defined

$$\tilde{f}(\mathbf{v}, t) \equiv \frac{\rho \sigma_{\text{ref}}}{m} f(\mathbf{v}, t), \quad (19)$$

and we defined the ‘‘integrated response function’’ (the name stemming from (26))

$$\begin{aligned} \mathcal{H}_{[E'_1, E'_2]}(\mathbf{v}) & \equiv \sum_T \frac{C_T}{m_T} \int_0^{E_R^{\max}(\nu)} dE_R \frac{\nu^2}{\sigma_{\text{ref}}} \frac{d\sigma_T}{dE_R}(E_R, \mathbf{v}) \epsilon_2(E_R) \\ & \times \int_{E'_1}^{E'_2} dE' \epsilon_1(E') G_T(E_R, E'). \end{aligned} \quad (20)$$

For simplicity, we only consider differential cross sections and thus integrated response functions that depend only on the speed $\nu = |\mathbf{v}|$ and not on the whole velocity vector. This is true if the DM flux and the target nuclei are unpolarized and the detection efficiency is isotropic throughout the detector, which is the most common case. With this restriction,

$$R_{[E'_1, E'_2]}(t) = \int_0^\infty d\nu \frac{\tilde{F}(\nu, t)}{\nu} \mathcal{H}_{[E'_1, E'_2]}(\nu), \quad (21)$$

where the function \tilde{F} is defined as in (11). We now define the function $\tilde{\eta}(\nu, t)$ by

$$\frac{\tilde{F}(\nu, t)}{\nu} = -\frac{\partial \tilde{\eta}(\nu, t)}{\partial \nu}, \quad (22)$$

with $\tilde{\eta}(\nu, t)$ going to zero in the limit of ν going to infinity. This yields the usual definition of $\tilde{\eta}$ (see (9) and (12))

$$\tilde{\eta}(\nu, t) = \int_\nu^\infty d\nu' \frac{\tilde{F}(\nu', t)}{\nu'} = \int_{\nu' \geq \nu} d^3v' \frac{\tilde{f}(\mathbf{v}', t)}{\nu'}. \quad (23)$$

Using (22) in (21), the energy integrated rate becomes

$$R_{[E'_1, E'_2]}(t) = -\int_0^\infty d\nu \frac{\partial \tilde{\eta}(\nu, t)}{\partial \nu} \mathcal{H}_{[E'_1, E'_2]}(\nu). \quad (24)$$

Integration by parts of (24) leads to an equation formally identical to (8) but which is now valid for any interaction

$$R_{[E'_1, E'_2]}(t) = \int_0^\infty d\nu_{\min} \tilde{\eta}(\nu_{\min}, t) \mathcal{R}_{[E'_1, E'_2]}(\nu_{\min}). \quad (25)$$

The response function is now defined as the derivative of the ‘‘integrated response function’’ $\mathcal{H}_{[E'_1, E'_2]}(\nu)$

$$\mathcal{R}_{[E'_1, E'_2]}(\nu_{\min}) \equiv \left. \frac{\partial \mathcal{H}_{[E'_1, E'_2]}(\nu)}{\partial \nu} \right|_{\nu=\nu_{\min}}. \quad (26)$$

Notice that the boundary term in the integration by parts of (24) is zero because the definition of $\mathcal{H}_{[E'_1, E'_2]}(\mathbf{v})$ in (20) imposes that $\mathcal{H}_{[E'_1, E'_2]}(0) = 0$ (since $E_R^{\max}(0) = 0$).

Similarly to what we did earlier for the SI interaction, we want again to compare average values of the $\tilde{\eta}^i$ functions with upper limits. However, for a differential cross section with a general dependence on the DM velocity, it might not be possible to simply use (14) with $\mathcal{R}_{[E'_1, E'_2]}^{\text{SI}}$ replaced by $\mathcal{R}_{[E'_1, E'_2]}$ to assign a weighted average of $\tilde{\eta}^0$ or $\tilde{\eta}^1$ to a finite ν_{\min} range. This may happen because the width of the response function $\mathcal{R}_{[E'_1, E'_2]}(\nu_{\min})$ in (26) at large ν_{\min} is dictated by the high speed behavior of the differential cross section, and it might even be infinite. For example, if $(\nu^2 d\sigma_T/dE_R)$ goes as ν^n for large ν , with n a positive integer, then $\mathcal{H}_{[E'_1, E'_2]}(\nu)$ also goes as ν^n and $\mathcal{R}_{[E'_1, E'_2]}(\nu_{\min})$ goes as ν_{\min}^{n-1} for large ν_{\min} . Thus, if $n \geq 1$, the response function $\mathcal{R}_{[E'_1, E'_2]}(\nu_{\min})$ does not vanish for large ν_{\min} . This implies that the denominator in (14) diverges.

We can regularize the behavior of the response function at large ν_{\min} by using, for example, the function $\nu_{\min}^r \tilde{\eta}(\nu_{\min}, t)$ with integer $r \geq n$, instead of just $\tilde{\eta}(\nu_{\min}, t)$. Since this new function is common to all experiments, we can use it to compare the data in ν_{\min} space. (While any other function that goes to zero fast enough would be equally good to regularize $\mathcal{R}_{[E'_1, E'_2]}(\nu_{\min})$, as, for instance, an exponentially decreasing function, the power law ν_{\min}^{-r} does not require the introduction of an arbitrary ν_{\min} scale in the problem.) In fact, by multiplying and dividing the integrand in (25) by ν_{\min}^r ,

$$\begin{aligned} R_{[E'_1, E'_2]}(t) & = \int_0^\infty d\nu_{\min} [\nu_{\min}^r \tilde{\eta}(\nu_{\min}, t)] \\ & \times [\nu_{\min}^{-r} \mathcal{R}_{[E'_1, E'_2]}(\nu_{\min})], \end{aligned} \quad (27)$$

we can define the average of the functions $\nu_{\min}^r \tilde{\eta}^i(\nu_{\min})$

$$\overline{\nu_{\min}^r \tilde{\eta}_{[E'_1, E'_2]}^i} \equiv \frac{\hat{R}_{[E'_1, E'_2]}^i}{\int_0^\infty d\nu_{\min} \nu_{\min}^{-r} \mathcal{R}_{[E'_1, E'_2]}(\nu_{\min})} \quad (28)$$

($i = 0$ for the unmodulated and $i = 1$ for the modulated component, see (13)). Notice that exploiting the definition of $\mathcal{R}_{[E'_1, E'_2]}$ in (26), we can write this relation in terms of $\mathcal{H}_{[E'_1, E'_2]}$ instead of $\mathcal{R}_{[E'_1, E'_2]}$ as

$$\overline{\nu_{\min}^r \tilde{\eta}_{[E'_1, E'_2]}^i} \equiv \frac{\hat{R}_{[E'_1, E'_2]}^i}{r \int_0^\infty d\nu \nu^{-r-1} \mathcal{H}_{[E'_1, E'_2]}(\nu)}, \quad (29)$$

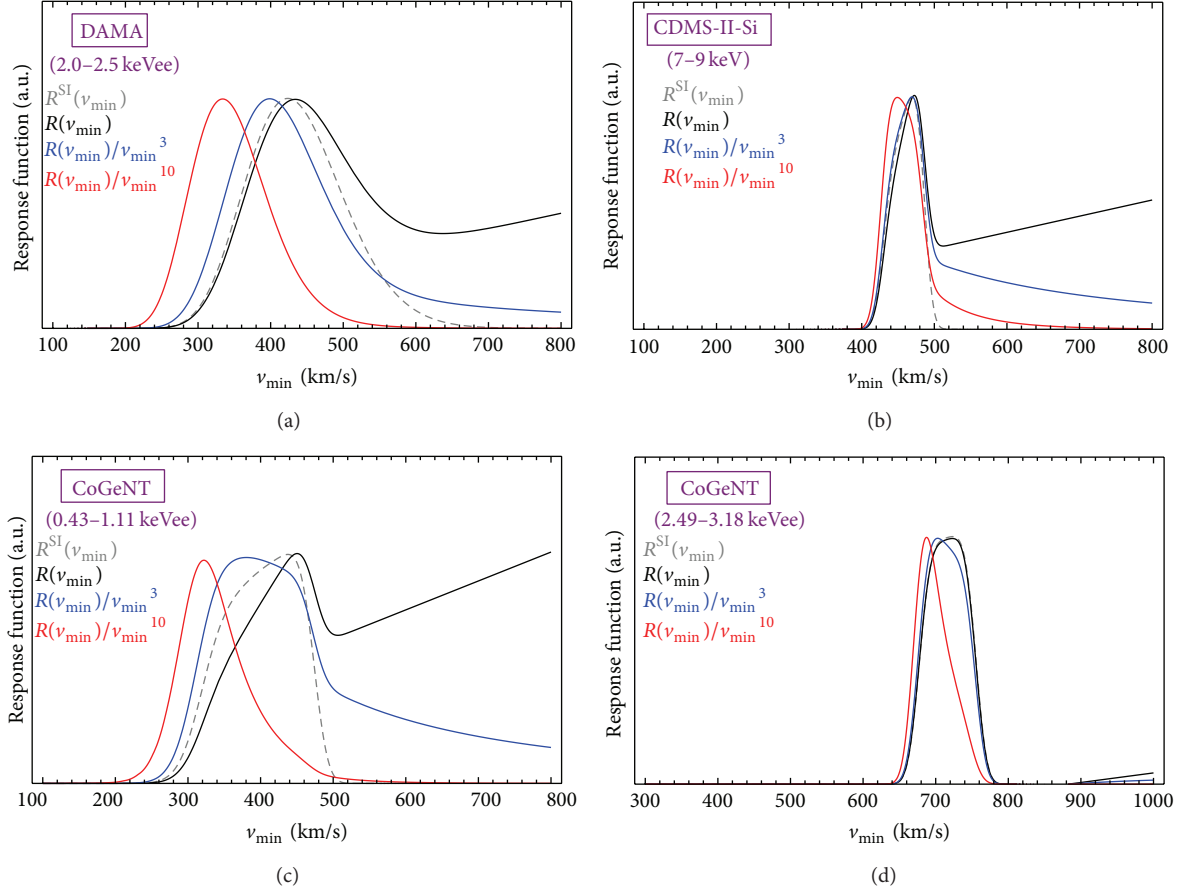


FIGURE 3: Response functions $v_{\min}^{-r} \mathcal{R}_{[E'_1, E'_2]}(v_{\min})$ with arbitrary normalization for several detected energy intervals and detectors for SI interactions (gray dashed line) and for MDM with $m = 9 \text{ GeV}/c^2$.

where in the integration by parts the finite term $[v^{-r} \mathcal{H}_{[E'_1, E'_2]}(v)]_0^\infty$ vanishes since by assumption r has been appropriately chosen to regularize the integral of $v_{\min}^{-r} \mathcal{R}_{[E'_1, E'_2]}(v_{\min})$, that is, $v^{-r} \mathcal{H}_{[E'_1, E'_2]}(v) \rightarrow 0$ as $v \rightarrow \infty$.

Equations (28) or (29) allow translating rate measurements in a detected energy interval $[E'_1, E'_2]$ into averaged values of $v_{\min}^r \tilde{\eta}^i(v_{\min})$ in a finite v_{\min} interval $[v_{\min,1}, v_{\min,2}]$. This is now the interval outside which the integral of the new response function $v_{\min}^{-r} \mathcal{R}_{[E'_1, E'_2]}(v_{\min})$ (and not of $\mathcal{R}_{[E'_1, E'_2]}(v_{\min})$) is negligible. We choose to use 90% central quantile intervals; that is, we determine $v_{\min,1}$ and $v_{\min,2}$ such that the area under the function $v_{\min}^{-r} \mathcal{R}_{[E'_1, E'_2]}(v_{\min})$ to the left of $v_{\min,1}$ is 5% of the total area, and the area to the right of $v_{\min,2}$ is also 5% of the total area. In practice, the larger the value of r , the smaller is the width of the $[v_{\min,1}, v_{\min,2}]$ interval, designated by the horizontal error bar of the crosses in the $(v_{\min}, \tilde{\eta})$ plane. However, r cannot be chosen arbitrarily large, because large values of r give a large weight to the low velocity tail of the $\mathcal{R}_{[E'_1, E'_2]}(v_{\min})$ function, and this tail depends on the low energy tail of the resolution function $G_T(E_R, E')$ in (20), which is never well known. Therefore too large values of r make the procedure very sensitive to the way

in which the tails of the $G_T(E_R, E')$ function are modeled. This is shown more explicitly in Section 5 (see also Figure 3), where we apply this procedure to a particular WIMP-nuclei interaction. In the figures, the horizontal placement of the vertical bar in the crosses corresponds to the maximum of $v_{\min}^{-r} \mathcal{R}_{[E'_1, E'_2]}(v_{\min})$. The extension of the vertical bar, unless otherwise indicated, shows the 1σ interval around the central value of the measured rate.

The upper limit on the unmodulated part of $v_{\min}^r \tilde{\eta}$ is simply $v_{\min}^r \tilde{\eta}^{\text{lim}}(v_{\min})$, where $\tilde{\eta}^{\text{lim}}(v_{\min})$ is computed as described in Section 3 by using a downward step-function $\tilde{\eta}_0 \theta(v_0 - v_{\min})$ for $\tilde{\eta}(v_0)$ to determine the maximum value of the step $\tilde{\eta}_0$. Given the definition of the response function \mathcal{R} in the general case in terms of \mathcal{H} , (26), the downward step-function choice for $\tilde{\eta}^0$ yields

$$\begin{aligned} R_{[E'_1, E'_2]} &= \tilde{\eta}_0 \int_0^{v_0} dv_{\min} \mathcal{R}_{[E'_1, E'_2]}(v_{\min}) \\ &= \tilde{\eta}_0 \mathcal{H}_{[E'_1, E'_2]}(v_0). \end{aligned} \quad (30)$$

From this equation we find the maximum value of $\tilde{\eta}_0$ at v_0 allowed by the experimental upper limit on the unmodulated rate $R_{[E'_1, E'_2]}^{\text{lim}}$,

$$\tilde{\eta}^{\text{lim}}(v_0) = \frac{R_{[E'_1, E'_2]}^{\text{lim}}}{\int_0^{v_0} dv_{\text{min}} \mathcal{R}_{[E'_1, E'_2]}(v_{\text{min}})} = \frac{R_{[E'_1, E'_2]}^{\text{lim}}}{\mathcal{H}_{[E'_1, E'_2]}(v_0)}. \quad (31)$$

In the figures, rather than drawing the new averages $\overline{v_{\text{min}}^r \tilde{\eta}^i c^2}$ and the limits $v_{\text{min}}^r \tilde{\eta}^{\text{lim}}(v_{\text{min}}) c^2$, we may draw $v_{\text{min}}^{-r} \overline{v_{\text{min}}^r \tilde{\eta}^i c^2}$ and $\tilde{\eta}^{\text{lim}}(v_{\text{min}}) c^2$ (in units of day^{-1}), so that a comparison can be easily made with the results obtained for the SI interaction shown in the previous section.

5. Application to Magnetic Dipole Dark Matter

We apply here the generalized halo-independent method to a Dirac fermion DM candidate that interacts only through an anomalous magnetic dipole moment λ_χ (see e.g., [42–61])

$$\mathcal{L}_{\text{int}} = \frac{\lambda_\chi}{2} \bar{\chi} \sigma_{\mu\nu} \chi F^{\mu\nu}. \quad (32)$$

The differential cross section for scattering of a magnetic dipole dark matter (MDM) with a target nucleus is

$$\begin{aligned} \frac{d\sigma_T}{dE_R} &= \alpha \lambda_\chi^2 \left\{ Z_T^2 \left[\frac{1}{E_R} - \frac{1}{v^2} \frac{m_T}{2} \left(\frac{1}{\mu_T^2} - \frac{1}{m^2} \right) \right] \right. \\ &\quad \left. \times F_{E,T}^2(E_R) + \frac{\tilde{\lambda}_T^2 m_T}{v^2 m_p^2} \left(\frac{S_T + 1}{3S_T} \right) F_{M,T}^2(E_R) \right\}. \end{aligned} \quad (33)$$

Here $\alpha = e^2/4\pi$ is the electromagnetic fine structure constant, m_p is the proton mass, S_T is the spin of the target nucleus, and $\tilde{\lambda}_T$ is the magnetic moment of the target nucleus in units of the nuclear magneton $e/(2m_p) = 0.16 (\text{GeV}/c^2)^{-1}$. The first term corresponds to the dipole-nuclear charge coupling, and $F_{E,T}(E_R)$ is the corresponding nuclear charge form factor. We take it to be the Helm form factor [37] normalized to $F_{E,T}(0) = 1$. The second term, which we call ‘‘magnetic’’, corresponds to the coupling of the DM magnetic dipole to the magnetic field of the nucleus, and the corresponding nuclear form factor is the nuclear magnetic form factor $F_{M,T}(E_R)$. This magnetic form factor is not identical to the spin form factor that accompanies spin-dependent interactions, in that the magnetic form factor includes the magnetic currents due to the orbital motion of the nucleons in addition to the intrinsic nucleon magnetic moments (spins). For the light WIMPs considered here, the magnetic term is negligible for all the target nuclei we consider except Na. This term is more important for lighter nuclei, such as Na and Si, but only ^{23}Na has a nonnegligible magnetic dipole moment, $\tilde{\lambda}_{\text{Na}} = 2.218$. The magnetic form factor for this nuclide is taken from [62] as explained in [32].

The spin-independent part of the differential cross section has two terms, with different v dependences. Therefore, had

we computed the rate with the method used to get to (8), we would have obtained two terms in the rate each containing a different function of v_{min} multiplied by detector dependent coefficients. It would have been impossible in this way to translate a rate measurement or bound into only one of the two v_{min} functions. In such a situation, the approach presented in Section 3 cannot be applied and one needs to resort to the generalized method of Section 4. The function $\mathcal{H}_{[E'_1, E'_2]}(v)$ has in this case a v^2 dependence for large values of v , with $\mathcal{R}_{[E'_1, E'_2]}(v_{\text{min}})$ scaling as v_{min} . More precisely we have

$$\begin{aligned} \mathcal{H}_{[E'_1, E'_2]}(\mathbf{v}) &= \sum_T \frac{C_T}{m_T} \int_0^{E_R^{\text{max}}(v)} dE_R \\ &\quad \times \left\{ Z_T^2 \left[\frac{v^2}{E_R} - \frac{m_T}{2} \left(\frac{1}{\mu_T^2} - \frac{1}{m^2} \right) \right] F_{E,T}^2(E_R) \right. \\ &\quad \left. + \tilde{\lambda}_T^2 \frac{m_T}{m_p^2} \left(\frac{S_T + 1}{3S_T} \right) F_{M,T}^2(E_R) \right\} \\ &\quad \times \epsilon_2(E_R) \int_{E'_1}^{E'_2} dE' \epsilon_1(E') G_T(E_R, E'), \end{aligned} \quad (34)$$

where we defined $\sigma_{\text{ref}} \equiv \alpha \lambda_\chi^2$. As a consequence,

$$\begin{aligned} \mathcal{R}_{[E'_1, E'_2]}(v_{\text{min}}) &= 2v_{\text{min}} \sum_T \frac{C_T}{m_T} \int_0^\infty dE_R \\ &\quad \times \left\{ \left[Z_T^2 \frac{\mu_T^2}{m^2} F_{E,T}^2(E_R) + \tilde{\lambda}_T^2 \frac{2\mu_T^2}{m_p^2} \left(\frac{S_T + 1}{3S_T} \right) F_{M,T}^2(E_R) \right] \right. \\ &\quad \times \delta(E_R^{\text{max}}(v_{\text{min}}) - E_R) \\ &\quad \left. + Z_T^2 \frac{1}{E_R} F_{E,T}^2(E_R) \theta(E_R^{\text{max}}(v_{\text{min}}) - E_R) \right\} \epsilon_2(E_R) \\ &\quad \times \int_{E'_1}^{E'_2} dE' \epsilon_1(E') G_T(E_R, E'). \end{aligned} \quad (35)$$

The denominator of (28) is therefore

$$\begin{aligned} &\int dv_{\text{min}} v_{\text{min}}^{-r} \mathcal{R}_{[E'_1, E'_2]}(v_{\text{min}}) \\ &= 2 \sum_T \frac{C_T}{m_T} \int_0^\infty dv_{\text{min}} v_{\text{min}}^{-r+1} \end{aligned}$$

$$\begin{aligned}
& \times \left\{ Z_T^2 \left(\frac{\mu_T^2}{m^2} + \frac{2}{r-2} \right) F_{E,T}^2(E_R(v_{\min})) \right. \\
& \quad \left. + \tilde{\lambda}_T^2 \frac{2\mu_T^2}{m_p^2} \left(\frac{S_T+1}{3S_T} \right) F_{M,T}^2(E_R(v_{\min})) \right\} \\
& \times \epsilon_2(E_R) \int_{E'_1}^{E'_2} dE' \epsilon_1(E') G_T(E_R(v_{\min}), E'), \tag{36}
\end{aligned}$$

where r can be any number larger than 2. To obtain this result, we first integrated the θ term in (35) with respect to v_{\min} and then used (2) to change integration variable from E_R to v_{\min} again.

In Figure 3, we illustrate the effect of various choices of r on the response function $v_{\min}^{-r} \mathcal{R}_{[E'_1, E'_2]}(v_{\min})$ for MDM for several energy bins and experiments: the first energy bin of DAMA/LIBRA [2], 2 to 2.5 keVee, the 7 to 9 keV CDMS-II used for the Si data [7], and the first, 0.43 to 1.11 keVee, and last, 2.49 to 3.18 keVee, of CoGeNT [3, 4]. We also include $\mathcal{R}_{[E'_1, E'_2]}^{\text{SI}}(v_{\min})$ from (10) for the standard SI interaction (gray dashed line) for a comparison. The normalization of each curve is arbitrary. For $r = 0$, the MDM response function is divergent and goes like v at large velocities, given the v^2 behavior of $(v^2 d\sigma_T/dE_R)$ (see discussion after (26)). The divergent behavior is much more pronounced in the low energy bins. The choice $r = 3$ is already enough to regularize the divergent behavior but still yields too large v_{\min} intervals. For growing values of r , the peak of the response function shifts towards low velocities (mostly in the low energy bins), due to the v_{\min}^{-r} factor. This peak, when far from the v_{\min} interval where $\mathcal{R}_{[E'_1, E'_2]}(v_{\min})$ is nonnegligible, is unreliable as it is due to the low energy tail of the detector energy resolution function $G_T(E_R, E')$, which determines the low velocity tail of $\mathcal{R}_{[E'_1, E'_2]}(v_{\min})$ (see (20)) and is never well known. We found the optimum r value by trial and error and for MDM we find that $r = 10$ is an adequate choice (see Figure 3) to get a localized response function in v_{\min} space without relying on how the low energy tail of the energy resolution function is modeled. The choice of r is dictated by the lowest energy bins, where the function v_{\min}^{-r} is largest. Higher energy bins are less sensitive to the choice of r .

Let us remark that this way of comparing data is not an inherent part of the halo-independent method but is only due to the choice of finding averages over measured energy bins to translate putative measurements of a DM signal. So far a better way of presenting the data has not been found, and more work is necessary to make progress in this respect.

Figures 4, 5, and 6 show the measurements of and bounds on $v_{\min}^{10} \tilde{\eta}^0(v_{\min})$ and $v_{\min}^{10} \tilde{\eta}^1(v_{\min})$ for a WIMP with magnetic dipole interactions and mass $m = 6 \text{ GeV}/c^2$, $9 \text{ GeV}/c^2$, and $15 \text{ GeV}/c^2$, respectively. These masses are motivated by previous studies on MDM as a potential explanation for the putative DM signal found by DAMA, CoGeNT, and CRESST-II (see e.g., [57]). The averages (indicated by the crosses) and upper bounds are multiplied by v_{\min}^{-10} so that the vertical axis has the usual $\tilde{\eta} c^2$ units of day^{-1} and the bounds show

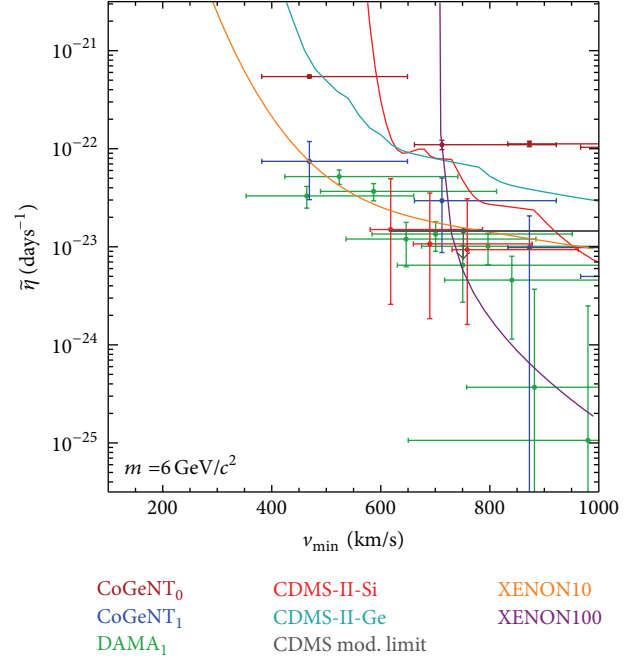


FIGURE 4: Measurements of and bounds on $v_{\min}^{-10} v_{\min}^{10} \tilde{\eta}^0(v_{\min}) c^2$ and $v_{\min}^{-10} v_{\min}^{10} \tilde{\eta}^1(v_{\min}) c^2$ for MDM of mass $m = 6 \text{ GeV}/c^2$.

$\tilde{\eta}^{\text{lim}}(v_{\min})$ (as usual for SI interactions). Figures 4, 5, and 6 include the DAMA modulation signal (green crosses), CoGeNT modulated (blue crosses), and unmodulated signal (plus an unknown flat background, dark red horizontal lines), CDMS-II-Si unmodulated rate signal (red crosses and limit line), CDMS-II-Ge unmodulated rate limit (light blue line) and modulation bound (dark grey horizontal line with downward arrow), XENON100 limit (purple line), and XENON10 S2-only limit without \mathcal{Q}_v suppression below 1.4 keVnr (orange line). The crosses represent the averages $\overline{v_{\min}^{10} \tilde{\eta}^i}$ ($i = 0$ for the unmodulated and $i = 1$ for the modulated parts of the velocity integral) over the v_{\min} intervals indicated by the horizontal bar of each cross multiplied by v_{\min}^{-10} . The lines represent upper limits on $\tilde{\eta}^0(v_{\min})$. The CDMS-II-Ge modulation limit is instead an upper limit on $\overline{v_{\min}^{10} \tilde{\eta}^1}$ multiplied by v_{\min}^{-10} .

The measurements and limits in Figures 4, 5, and 6 for MDM move to larger v_{\min} values as the WIMP mass increases, as expected from the relation (2) between v_{\min} and the recoil energy. As shown in Figure 4, for a WIMP of mass $m = 6 \text{ GeV}/c^2$ the three CDMS-II-Si points are largely below the XENON10 and XENON100 upper limits, but they move progressively above them as m increases to $9 \text{ GeV}/c^2$, see Figure 5, and are almost entirely excluded by them for $m = 15 \text{ GeV}/c^2$ in Figure 6. The addition of the recent LUX bound, which is not shown here, poses however a greater threat to the DM interpretation of the CDMS-II-Si excess even for very low DM masses. Moreover, the three CDMS-II-Si points overlap with or are below the CoGeNT and DAMA measurements of $\tilde{\eta}^1$, and therefore these appear incompatible with the interpretation of the CDMS-II-Si data as a measurement of $\tilde{\eta}^0$, as one usually expects that $\tilde{\eta}^0 \gg \tilde{\eta}^1$. For all three

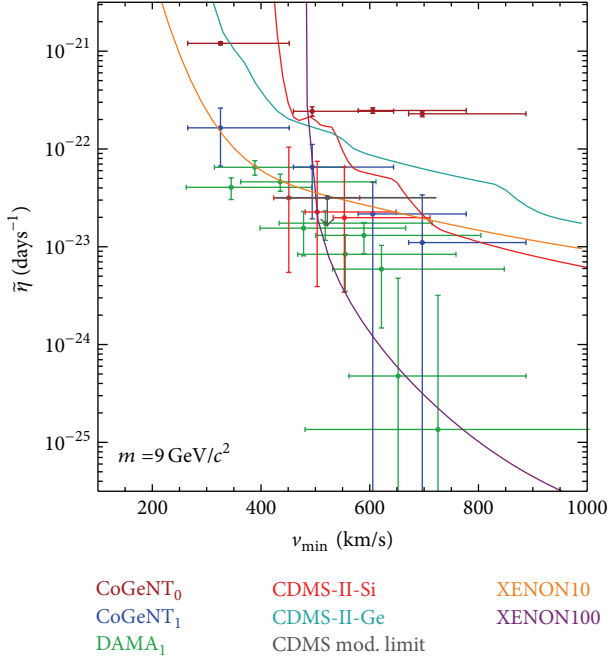


FIGURE 5: As in Figure 4 but for $m = 9 \text{ GeV}/c^2$. All data points have moved to smaller v_{\min} values as expected.

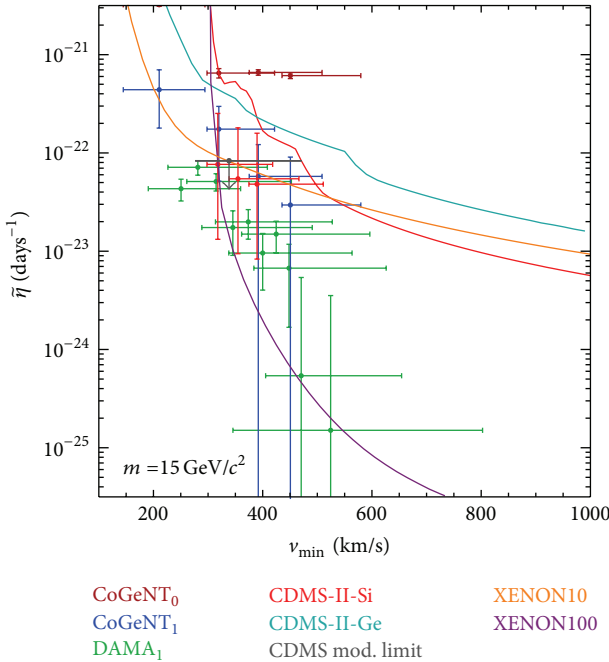


FIGURE 6: As in Figure 4 but for $m = 15 \text{ GeV}/c^2$.

WIMP masses shown in the figures, the DAMA and CoGeNT modulation measurements seem compatible with each other. However, the upper limits on the unmodulated part of the rate imposed by XENON10 and XENON100 (plus CDMSlite and LUX, which are not shown here) reject the MDM interpretation of the DAMA and CoGeNT modulation signal, except for the lowest energy bins.

6. Conclusions

In order to interpret and compare data from different experiments, a model is often (if not always) needed. Concerning direct DM detection experiments, one needs to assume a model of particle interactions between DM particles and nuclei in the detectors, as well as a model for the dark halo, most notably the DM velocity distribution. For light WIMPs with $\sim 10 \text{ GeV}/c^2$ mass, as those pointed by direct detection experiments with positive signals in the assumption of SI interactions and the SHM, the details of the high velocity region of the DM velocity distribution are crucial in comparing positive and negative results. For this reason, a framework to analyze the direct detection data independently on the properties of the DM halo is an important tool to address the compatibility of the different experiments.

In this work we have reviewed the halo-independent method to compare data from direct DM detection experiments, as introduced and developed in [27–34]. We followed closely the treatment in [31–33], which present the most updated analyses of DM direct detection experiment data in the context of the halo-independent method. We applied the halo-independent analysis to SI interactions with both isospin-conserving and isospin-violating couplings. In both cases the situation seems to be of disagreement between most of the experiments with positive signals (DAMA, CoGeNT, and CRESST-II) and those with negative results (most notably LUX, XENON, and CDMS-II). The three CDMS-II-Si events seem however compatible with all the limits for DM with isospin-violating couplings. DAMA and CoGeNT modulation data sets seem to agree with one another, but they appear to be incompatible with the CDMS-II-Si events when these are interpreted as measurements of the unmodulated rate.

We have also shown the results of the halo-independent analysis in the assumption of WIMPs interacting with nuclei only through a magnetic dipole moment. In this case the scattering cross section has a more complicated dependence on the DM velocity, thus requiring a generalized version of the method as it was originally devised. The conclusions for this DM candidate are similar as above, with only the lowest energy data points of DAMA, CoGeNT, and CDMS-II-Si lying below the exclusion bounds. The situation is somewhat better for very light WIMPs ($m \sim 6 \text{ GeV}/c^2$), especially for the CDMS-II-Si events.

The halo-independent analysis is a promising framework to compare different direct detection experiments without making assumptions on the DM halo. This feature is highly desirable given the crucial role played by the DM velocity distribution in the galaxy in determining the total scattering rate at direct detection experiments. This analysis allows to directly compare the recoil spectra measured by different experiments in v_{\min} space, together with bounds from null experiments. These spectra indicate the integrated DM velocity distribution $\bar{\eta}$ favored by the experiments as a function of v_{\min} (see (23)).

At present this framework presents some drawbacks, which could be addressed and improved in future work. For instance, the relation between the $\bar{\eta}$ function that one wants

to fit and the observed rates is an integral equation, (25). So far it has been assumed that $\bar{\eta}(v_{\min}, t)$ is approximately constant in any v_{\min} interval where the response functions $\mathcal{R}_{[E'_1, E'_2]}(v_{\min})$ are significantly different from zero, so that it could be extracted from the integral in the form of the average in (14) or (28) and (29). However, this is not necessarily a good assumption. Secondly, the degree of agreement or disagreement between two data sets cannot be readily quantified (in a statistical sense) in the current halo-independent analysis. Finally, the method provides no information on the consistency of modulated and unmodulated signals, even when these are measured by the same experiment as for CoGeNT. By making some (mild) assumptions, more stringent limits on the modulated part $\bar{\eta}^1$ can be derived from the limits on the unmodulated part of the rate [28, 38–40]. However, with no additional assumptions the only way one can bound the modulated rate with the unmodulated rate is by imposing the most general inequality $\bar{\eta}^0 > \bar{\eta}^1$.

Conflict of Interests

The author declares that there is no conflict of interests regarding the publication of this paper.

Acknowledgments

The author thanks L. Marcus and L. Prosperi for useful discussions. Partial support from Department of Energy under Award no. DE-SC0009937 is also acknowledged.

References

- [1] P. A. R. Ade, N. Aghanim, C. Armitage-Caplan et al., “Planck 2013 results—XVI. Cosmological parameters,” <http://arxiv.org/abs/1303.5076>.
- [2] R. Bernabei, P. Belli, F. Cappella et al., “New results from DAMA/LIBRA,” *European Physical Journal C*, vol. 67, no. 1, pp. 39–49, 2010.
- [3] C. E. Aalseth, P. S. Barbeau, N. S. Bowden et al., “Results from a search for light-mass dark matter with a p -type point contact germanium detector,” *Physical Review Letters*, vol. 106, no. 13, Article ID 131301, 4 pages, 2011.
- [4] C. E. Aalseth, P. S. Barbeau, J. Colaresi et al., “Search for an annual modulation in a p -type point contact germanium dark matter detector,” *Physical Review Letters*, vol. 107, no. 14, Article ID 141301, 5 pages, 2011.
- [5] C. E. Aalseth, P. S. Barbeau, J. Colaresi et al., “CoGeNT: a search for low-mass dark matter using p -type point contact germanium detectors,” *Physical Review D*, vol. 88, no. 1, Article ID 012002, 20 pages, 2013.
- [6] G. Angloher, M. Bauer, I. Bavykina et al., “Results from 730 kg days of the CRESST-II dark matter search,” *The European Physical Journal C*, vol. 72, article 1971, 2012.
- [7] R. Agnese, Z. Ahmed, A. J. Anderson et al., “Dark matter search results using the silicon detectors of CDMS II,” *Physical Review Letters*, vol. 111, no. 25, Article ID 251301, 6 pages, 2013.
- [8] A. K. Drukier, K. Freese, and D. N. Spergel, “Detecting cold dark-matter candidates,” *Physical Review D*, vol. 33, no. 12, pp. 3495–3508, 1986.
- [9] K. Freese, M. Lisanti, and C. Savage, “Annual modulation of dark matter: a review,” *Reviews of Modern Physics*, vol. 85, no. 4, pp. 1561–1581, 2013.
- [10] D. S. Akerib, H. M. Araujo, X. Bai et al., “First results from the LUX dark matter experiment at the Sanford Underground Research Facility,” *Physical Review Letters*, vol. 112, no. 9, Article ID 091303, 7 pages, 2014.
- [11] J. Angle, E. Aprile, F. Arneodo et al., “A search for light dark matter in XENON10 data,” *Physical Review Letters*, vol. 107, no. 5, Article ID 051301, 5 pages, 2011.
- [12] E. Aprile, M. Alfonsi, K. Arisaka et al., “Dark matter results from 225 live days of XENON100 data,” *Physical Review Letters*, vol. 109, no. 18, Article ID 181301, 6 pages, 2012.
- [13] Z. Ahmed, D. S. Akerib, S. Arrenberg et al., “Results from a low-energy analysis of the CDMS II germanium data,” *Physical Review Letters*, vol. 106, no. 13, Article ID 131302, 5 pages, 2011.
- [14] R. Agnese, A. J. Anderson, M. Asai et al., “CDMSlite: a search for low-mass WIMPs using voltage-assisted calorimetric ionization detection in the SuperCDMS experiment,” *Physical Review Letters*, vol. 112, no. 4, Article ID 041302, 6 pages, 2014.
- [15] M. Felizardo, T. A. Girard, T. Morlat et al., “Final analysis and results of the phase II SIMPLE dark matter search,” *Physical Review Letters*, vol. 108, no. 20, Article ID 201302, 5 pages, 2012.
- [16] S. Archambault, E. Behnke, P. Bhattacharjee et al., “Constraints on low-mass WIMP interactions on ^{19}F from PICASSO,” *Physics Letters B*, vol. 711, no. 2, pp. 153–161, 2012.
- [17] E. Behnke, J. Behnke, S. J. Brice et al., “First dark matter search results from a 4-kg CF_3I bubble chamber operated in a deep underground site,” *Physical Review D*, vol. 86, no. 5, Article ID 052001, 9 pages, 2012.
- [18] Z. Ahmed, D. S. Akerib, A. J. Anderson et al., “Search for annual modulation in low-energy CDMS-II data,” <http://arxiv.org/abs/1203.1309>.
- [19] C. Savage, G. Gelmini, P. Gondolo, and K. Freese, “Compatibility of DAMA/LIBRA dark matter detection with other searches,” *Journal of Cosmology and Astroparticle Physics*, vol. 2009, no. 4, article 010, 2009.
- [20] Y.-Y. Mao, L. E. Strigari, R. H. Wechsler, H.-Y. Wu, and O. Hahn, “Halo-to-Halo similarity and scatter in the velocity distribution of dark matter,” *The Astrophysical Journal*, vol. 764, no. 1, article 35, 2013.
- [21] A. M. Green, “Effect of halo modeling on WIMP exclusion limits,” *Physical Review D*, vol. 66, no. 8, Article ID 083003, 9 pages, 2002.
- [22] C. McCabe, “The astrophysical uncertainties of dark matter direct detection experiments,” *Physical Review D*, vol. 82, no. 2, Article ID 023530, 13 pages, 2010.
- [23] A. M. Green, “Dependence of direct detection signals on the WIMP velocity distribution,” *Journal of Cosmology and Astroparticle Physics*, vol. 1010, article 034, 2010.
- [24] A. M. Green, “Astrophysical uncertainties on direct detection experiments,” *Modern Physics Letters A*, vol. 27, no. 3, Article ID 1230004, 20 pages, 2012.
- [25] M. Fairbairn, T. Douce, and J. Swift, “Quantifying astrophysical uncertainties on dark matter direct detection results,” *Astroparticle Physics*, vol. 47, pp. 45–53, 2013.
- [26] C. Arina, “Bayesian analysis of multiple direct detection experiments,” <http://arxiv.org/abs/1310.5718>.
- [27] P. J. Fox, J. Liu, and N. Weiner, “Integrating out astrophysical uncertainties,” *Physical Review D*, vol. 83, no. 10, Article ID 103514, 12 pages, 2011.

- [28] M. T. Frandsen, F. Kahlhoefer, C. McCabe, S. Sarkar, and K. Schmidt-Hoberg, "Resolving astrophysical uncertainties in dark matter direct detection," *Journal of Cosmology and Astroparticle Physics*, vol. 2012, no. 1, article 024, 2012.
- [29] P. Gondolo and G. B. Gelmini, "Halo independent comparison of direct dark matter detection data," *Journal of Cosmology and Astroparticle Physics*, vol. 2012, no. 12, article 015, 2012.
- [30] M. T. Frandsen, F. Kahlhoefer, C. McCabe, S. Sarkar, and K. Schmidt-Hoberg, "The unbearable lightness of being: CDMS versus XENON," *Journal of Cosmology and Astroparticle Physics*, vol. 2013, no. 7, article 023, 2013.
- [31] E. Del Nobile, G. B. Gelmini, P. Gondolo, and J.-H. Huh, "Halo-independent analysis of direct detection data for light WIMPs," *Journal of Cosmology and Astroparticle Physics*, vol. 2013, no. 10, article 026, 2013.
- [32] E. Del Nobile, G. Gelmini, P. Gondolo, and J.-H. Huh, "Generalized halo independent comparison of direct dark matter detection data," *Journal of Cosmology and Astroparticle Physics*, vol. 2013, no. 10, article 048, 2013.
- [33] E. Del Nobile, G. B. Gelmini, P. Gondolo, and J.-H. Huh, "Update on lightWIMP limits: LUX, lite and light," *Journal of Cosmology and Astroparticle Physics*, vol. 2014, no. 3, article 014, 2014.
- [34] E. Del Nobile, G. B. Gelmini, P. Gondolo, and J.-H. Huh, "Direct detection of light anapole and magnetic dipole DM," <http://arxiv.org/abs/1401.4508>.
- [35] A. Kurylov and M. Kamionkowski, "Generalized analysis of the direct weakly interacting massive particle searches," *Physical Review D*, vol. 69, no. 6, Article ID 063503, 12 pages, 2004.
- [36] J. L. Feng, J. Kumar, D. Marfatia, and D. Sanford, "Isospin-violating dark matter," *Physics Letters B*, vol. 703, no. 2, pp. 124–127, 2011.
- [37] R. H. Helm, "Inelastic and elastic scattering of 187-Mev electrons from selected even-even nuclei," *Physical Review*, vol. 104, no. 5, pp. 1466–1475, 1956.
- [38] J. Herrero-Garcia, T. Schwetz, and J. Zupan, "On the annual modulation signal in dark matter direct detection," *Journal of Cosmology and Astroparticle Physics*, vol. 2012, no. 3, article 005, 2012.
- [39] J. Herrero-Garcia, T. Schwetz, and J. Zupan, "Astrophysics independent bounds on the annual modulation of dark matter signals," *Physical Review Letters*, vol. 109, no. 14, Article ID 141301, 5 pages, 2012.
- [40] N. Bozorgnia, J. Herrero-Garcia, T. Schwetz, and J. Zupan, "Halo-independent methods for inelastic dark matter scattering," *Journal of Cosmology and Astroparticle Physics*, vol. 2013, no. 7, article 049, 2013.
- [41] S. Yellin, "Finding an upper limit in the presence of an unknown background," *Physical Review D*, vol. 66, no. 3, Article ID 032005, 7 pages, 2002.
- [42] M. Pospelov and T. ter Veldhuis, "Direct and indirect limits on the electro-magnetic form factors of WIMPs," *Physics Letters B*, vol. 480, no. 1-2, pp. 181–186, 2000.
- [43] H. An, S. L. Chen, R. N. Mohapatra, S. Nussinov, and Y. Zhang, "Energy dependence of direct detection cross section for asymmetric mirror dark matter," *Physical Review D*, vol. 82, no. 2, Article ID 023533, 8 pages, 2010.
- [44] K. Sigurdson, M. Doran, A. Kurylov, R. R. Caldwell, and M. Kamionkowski, "Dark-matter electric and magnetic dipole moments," *Physical Review D*, vol. 70, no. 8, Article ID 083501, 15 pages, 2004.
- [45] K. Sigurdson, M. Doran, A. Kurylov, R. R. Caldwell, and M. Kamionkowski, "Dark-matter electric and magnetic dipole moments," *Physical Review D*, vol. 73, no. 8, Article ID 089903, 2 pages, 2006.
- [46] V. Barger, W.-Y. Keung, and D. Marfatia, "Electromagnetic properties of dark matter: dipole moments and charge form factor," *Physics Letters B*, vol. 696, no. 1-2, pp. 74–78, 2011.
- [47] S. Chang, N. Weiner, and I. Yavin, "Magnetic inelastic dark matter," *Physical Review D*, vol. 82, no. 12, Article ID 125011, 8 pages, 2010.
- [48] W. S. Cho, J.-H. Huh, I.-W. Kim, J. E. Kim, and B. Kyaee, "Constraining WIMP magnetic moment from CDMS II experiment," *Physics Letters B*, vol. 687, no. 1, pp. 6–10, 2010.
- [49] W. S. Cho, J.-H. Huh, I.-W. Kim, J. E. Kim, and B. Kyaee, "Constraining WIMP magnetic moment from CDMS II experiment," *Physics Letters B*, vol. 694, no. 4-5, pp. 496–497, 2011.
- [50] J. H. Heo, "Minimal Dirac fermionic dark matter with nonzero magnetic dipole moment," *Physics Letters B*, vol. 693, no. 3, pp. 255–258, 2010.
- [51] S. Gardner, "Shedding light on dark matter: a Faraday rotation experiment to limit a dark magnetic moment," *Physical Review D*, vol. 79, no. 5, Article ID 055007, 14 pages, 2009.
- [52] E. Masso, S. Mohanty, and S. Rao, "Dipolar dark matter," *Physical Review D*, vol. 80, no. 3, Article ID 036009, 8 pages, 2009.
- [53] T. Banks, J. F. Fortin, and S. Thomas, "Direct detection of dark matter electromagnetic dipole moments," <http://arxiv.org/abs/1007.5515>.
- [54] J. F. Fortin and T. M. P. Tait, "Collider constraints on dipole-interacting dark matter," *Physical Review D*, vol. 85, no. 6, Article ID 063506, 6 pages, 2012.
- [55] K. Kumar, A. Menon, and T. M. P. Tait, "Magnetic fluffy dark matter," *Journal of High Energy Physics*, vol. 2012, no. 2, article 131, 2012.
- [56] V. Barger, W.-Y. Keung, D. Marfatia, and P.-Y. Tseng, "Dipole moment dark matter at the LHC," *Physics Letters B*, vol. 717, no. 1-3, pp. 219–223, 2012.
- [57] E. Del Nobile, C. Kouvaris, P. Panci, F. Sannino, and J. Virkajarvi, "Light magnetic dark matter in direct detection searches," *Journal of Cosmology and Astroparticle Physics*, vol. 2012, no. 8, article 010, 2012.
- [58] J. M. Cline, Z. Liu, and W. Xue, "Millicharged atomic dark matter," *Physical Review D*, vol. 85, no. 10, Article ID 101302, 6 pages, 2012.
- [59] N. Weiner and I. Yavin, "How dark are majorana WIMPs? Signals from magnetic inelastic dark matter and Rayleigh dark matter," *Physical Review D*, vol. 86, no. 7, Article ID 075021, 16 pages, 2012.
- [60] S. Tulin, H. B. Yu, and K. M. Zurek, "Three exceptions for thermal dark matter with enhanced annihilation to $\gamma\gamma$," *Physical Review D*, vol. 87, no. 3, Article ID 036011, 12 pages, 2013.
- [61] J. M. Cline, G. D. Moore, and A. R. Frey, "Composite magnetic dark matter and the 130 GeV line," *Physical Review D*, vol. 86, no. 11, Article ID 115013, 9 pages, 2012.
- [62] T. W. Donnelly and I. Sick, "Elastic magnetic electron scattering from nuclei," *Reviews of Modern Physics*, vol. 56, no. 3, pp. 461–566, 1984.